THE UNIVERSITY
of EDINBURGH

Vegetation root biomechanics and its role in river ecomorphodynamics

Valentina Bau'

Thesis submitted for the

Degree of *Doctor of Philosophy*

THE UNIVERSITY
of EDINBURGH

The University of Edinburgh

School of Engineering

2020

If we take in our hand any volume; of divinity or school metaphysics, for instance; let us ask, Does it contain any abstract reasoning concerning quantity or number? No. Does it contain any experimental reasoning concerning matter of fact and existence? No. Commit it then to the flames: for it can contain nothing but sophistry and illusion.

David Hume *[1748]*

Declaration

This thesis and the work contained herein have been composed solely by the author at The University of Edinburgh, under the supervision of Prof Paolo Perona and Prof Alistair Borthwick. Where others have contributed or other sources are quoted, references are given in full. Parts of this thesis have already been published, as noted in the text, but no part has been submitted previously for any other degree or professional qualification.

Valentina Bau'

June 2020

Abstract

Successful establishment of riparian vegetation on riverbanks and bedforms depends on river hydrology and related flow and sediment erosion processes. Extreme flow-induced erosion events can uproot vegetation, leading in some cases to failure of bank protection and river restoration schemes. This thesis uses experimental, analytical, and numerical approaches to examine key aspects of the mechanisms of vegetation uprooting by flow. First, the ability of riparian vegetation to respond to different water table regimes is investigated in terms of root growth and resistance. To this purpose, small-scale *Salix* cuttings were allowed to grow under different water level regimes. At the end of the growing period, extracted samples, obtained through pullout tests, were analysed in terms of root biomass distribution and resistance to external forces. The results demonstrate the driving influence of water and oxygen availability on the vertical configuration of below-ground biomass and thence on uprooting resistance. Second, a free-body model is derived to predict the critical rooting length – a key parameter that determines the probability of flow-induced uprooting of flexible plants at different erosion stages. Model validation is achieved using laboratory and field-scale data. Third, the dynamics of mobilization of stranded living wood logs from alluvial bedforms is investigated experimentally. Pullout test results are used to assess the root resistance of small-scale wood logs at several stages of growth. Trends in below- and above-ground biomass, together with the free-body model, enable detection of 'biological time windows' within which re-mobilization becomes possible. The results illustrate that uprooting occurs

within two time-lapses, which coincide with particular growth stages of the plant. Finally, a combined analytical and numerical model is derived. This model uses the probability of flow-induced plant uprooting as a proxy to study how perturbations to the natural flow regime may drive riparian ecosystem dynamics towards new and potentially irreversible statistical equilibrium states. The model is applied to an actual case study, in which dam impoundment of a reach of the Maggia River, Switzerland, has led to intense riparian vegetation encroachment with consequent river narrowing. The output of the model sheds light on the type of irreversibility that may arise in riverine ecosystems of severely impounded river basins. The theoretical and experimental results presented in the thesis should be useful to river engineers and managers responsible for river restoration projects, natural flood management schemes, and optimal dam regulation strategies.

Acknowledgements

First and foremost I would like to thank my supervisor Prof Paolo Perona for making this work possible. In particularly I would like to thank him for his constant guidance and encouragement. His unstoppable passion for research and his deep knowledge has always been an essential support, especially during the times I was losing faith in myself. Thank you, Paolo, for sharing your creativity, your rigorous approach to science and your love for research. I would not have made all this way without your constant support!

I cannot find the right words to express my gratitude to my second supervisor Prof Alistair Borthwick, who has always followed my research with interest and to whom I am extremely grateful for revising this thesis report with an extraordinary thoroughness.

I also want to acknowledge the financial support provided by the School of Engineering at The University of Edinburgh.

I wish to thank my Master's thesis supervisor, Prof Andrea Defina, who inspired me and encouraged me to pursue a PhD.

Through this long three and half years I received a lot of support by different people. First of all, my thoughts turn to my parents, who have always believed in me (more than I do) and who always embrace my choices. Rachele and Valentino, thank you for being always my solid pillars. You thought me the perseverance, rigour and moral values, without which I would never have gotten this far.

A huge ‘thank you’ goes to my PhD buddies and office mates from John Muir who greatly enriched my daily life. I want to thank Francesca and Martina for the amazing time spent together and for the solid friendship we built. A huge thanks to Karina and Simone for being the best neighbours and for their constant support and love (for food). To Giulio, for being my best companion of Matlab and beer sessions for 3 consecutive summers! Greta, Laura and Pietro, thanks for being the best friends I have ever asked for in these last 16 years and in the coming. Despite the distance, you have been always able to be by my side. Finally, the journey would not have been as enriching without the countless coffee breaks with Ulises.

Words are not enough to express my infinite gratitude and love to my partner, who unconditionally supported me and found a way to make me smile and being positive every single day. I am forever grateful, Grunde. Tusen takk!

Contents

List of Figures

List of Tables

Nomenclature

α_{BL}	coefficient in bedload transport formula	[-]
α	ratio of dF to dt	$[\mathrm{M} \cdot \mathrm{L} \cdot \mathrm{T}^{-3}]$
$\bar{A}_r$	average root surface area	$[\mathrm{L}^2]$
$\bar{d}$	average diameter	[L]
$\bar{F}_p$	average maximum pullout force	$[\mathrm{M} \cdot \mathrm{L} \cdot \mathrm{T}^{-2}]$
$\bar{l}$	average root depth	[L]
$\bar{L}_s$	average total length of the stems	[L]
$\bar{n}_l$	average number of leaves	[-]
$\bar{n}_r$	average number of roots	[-]
$\bar{Q}_{q>\xi}$	average flow discharge above ξ	$[\mathrm{L}^3 \cdot \mathrm{T}^{-1}]$
$\bar{T}$	average uprooting time	[T]
$\bar{V}_r$	average root volume	$[\mathrm{L}^3]$
β_d	product between λ_d and τ_d	[-]
β_l	ratio between λ_l and η_l	[-]
ΔH	difference between η_v and μ_l	[L]

Δx	longitudinal length scale	[L]
δ	vertical jump of a particle	[L]
$\delta(\cdot)$	Dirac delta function	[-]
$\Delta\tilde{H}$	ratio between ΔH and η_v	[L]
δ_x	characteristic spatial scale of force drops	[L]
$\dot{\eta}$	bed erosion rate	$[\mathrm{L} \cdot \mathrm{T}^{-1}]$
ϵ	significance level	[-]
η	riverbed elevation	[L]
η_l	rate of exponential decay of the water level	$[\mathrm{T}^{-1}]$
η_v	elevation of the plant with respect to the riverbed	[L]
$\Gamma[\cdot,\cdot]$	upper incomplete Gamma function	[-]
$\Gamma[\cdot]$	complete Gamma function	[-]
γ_d	mean height of the pulses of the discharge signal	[L]
γ_l	mean height of the pulses of the water (table) level signal	[L]
γ_w	water specific weight	$[\mathrm{M} \cdot \mathrm{T}^{-2} \cdot \mathrm{L}^{-2}]$
$\hat{F}_d$	dimensionless drag force	[-]
$\hat{R}(L_r)$	dimensionless maximum root resistance	[-]
$\hat{t}$	average duration of the flow erosion process	[T]
λ'_d	frequency of the events above ξ	$[\mathrm{T}^{-1}]$
λ_d	mean rate of the pulses of the discharge signal	$[\mathrm{T}^{-1}]$

λ_g	sediment porosity	[-]
λ_l	mean rate of the pulses of the water (table) level signal	$[\mathrm{T}^{-1}]$
μ_d	average flow discharge in the Poisson process	$[\mathrm{L}^3 \cdot \mathrm{T}^{-1}]$
μ_l	average water stage in the Poisson process	[L]
Ω	normalized cumulative sum of the root surface area	[-]
ω	root surface area per unit length	$[\mathrm{L}^2]$
ϕ	ratio between ξ and γ_d	[-]
ρ^*	modified water density	$[\mathrm{M} \cdot \mathrm{L}^{-3}]$
ρ_f	foliage density	$[\mathrm{M} \cdot \mathrm{L}^{-3}]$
ρ_g	sediment density	$[\mathrm{M} \cdot \mathrm{L}^{-3}]$
ρ_r	root density	$[\mathrm{M} \cdot \mathrm{L}^{-3}]$
ρ_s	stem density	$[\mathrm{M} \cdot \mathrm{L}^{-3}]$
ρ_w	water density	$[\mathrm{M} \cdot \mathrm{L}^{-3}]$
σ	standard deviation	[-]
σ_F	standard deviation	$[\mathrm{M} \cdot \mathrm{L} \cdot \mathrm{T}^{-2}]$
σ_L	standard deviation	[L]
σ_r	tensile breaking stress of the root material	$[\mathrm{M} \cdot \mathrm{L}^{-1} \cdot \mathrm{T}^{-2}]$
σ_s	tensile strength of the soil	$[\mathrm{M} \cdot \mathrm{L}^{-1} \cdot \mathrm{T}^{-2}]$
σ_T	standard deviation	[T]
τ	dummy time variable for integration	[T]

τ^*	dimensionless bed shear stress	[-]
τ^*_{cr}	critical Shield parameter	[-]
τ_1	integral temporal scale of the reference mean event	[T]
τ_d	integral temporal scale of the Compound Poisson Process	[T]
τ_s	shear strength of the soil	$[\mathrm{M} \cdot \mathrm{L}^{-1} \cdot \mathrm{T}^{-2}]$
$\theta(z)$	ratio between root growth and decay rate	[-]
$\tilde{T}$	dimensionless time of uprooting	[-]
$\tilde{x}$	dimensionless coordinate of the cutting	[-]
ξ	POT threshold	$[\mathrm{L}^3 \cdot \mathrm{T}^{-1}]$
A	wet cross sectional area of the river	$[\mathrm{L}^2]$
$a_{1,\dots,9}$	fitting coefficients	[-]
A_{fr}	projected surface area of the upright plant	$[\mathrm{L}^2]$
A_f	surface area of the foliage	$[\mathrm{L}^2]$
A_n	projected area of the plant in the flow direction	$[\mathrm{L}^2]$
A_p	projected area of the stem in the flow direction	$[\mathrm{L}^2]$
A_R	projected area of the roots in the flow direction	$[\mathrm{L}^2]$
A_r	total surface area of roots	$[\mathrm{L}^2]$
A_s	surface area of the stem	$[\mathrm{L}^2]$
A_t	surface area of the plant	$[\mathrm{L}^2]$
B	river width	[L]

b	exponent in the sediment transport formula	[-]
$b_{2,...,9}$	fitting coefficients	[-]
c	maximum value of the logistic curve	[L]
$c_{3,...,9}$	fitting coefficients	[-]
C_D	drag coefficient	[-]
C_f	friction coefficient	[-]
D	diffusion coefficient	$[\mathrm{L}^2 \cdot \mathrm{T}^{-1}]$
$D_{10,s}$	D_{10} of the sand	[L]
$D_{50,p}$	median size of the pebbles	[L]
D_{50}	median grain size of the sediment	[L]
$D_{90,s}$	D_{90} of the sand	[L]
D_p	upright plant diameter	[L]
d_r	root diameter	$[L]$
d_s	stem diameter	[L]
dF	force drop height	$[\mathrm{M} \cdot \mathrm{L} \cdot \mathrm{T}^{-2}]$
dT	force drop intertime	[T]
dt	force drop duration	[T]
F	uprooting force signal	$[\mathrm{M} \cdot \mathrm{L} \cdot \mathrm{T}^{-2}]$
$F_{d,n}$	normal drag force	$[\mathrm{M} \cdot \mathrm{L} \cdot \mathrm{T}^{-2}]$
$F_{d,t}$	tangential drag force	$[\mathrm{M} \cdot \mathrm{L} \cdot \mathrm{T}^{-2}]$

F_n	net buoyancy force	$[\mathrm{M} \cdot \mathrm{L} \cdot \mathrm{T}^{-2}]$
F_p	maximum pullout force	$[\mathrm{M} \cdot \mathrm{L} \cdot \mathrm{T}^{-2}]$
F_{res}	last force recovery in the stess-strain curve	$[\mathrm{M} \cdot \mathrm{L} \cdot \mathrm{T}^{-2}]$
g	gravity acceleration	$[\mathrm{L} \cdot \mathrm{T}^{-2}]$
$G(T)$	time integral of bed erosion randomness	$[\mathrm{L}^2]$
g_t	bed erosion randomness	$[\mathrm{L}^2 \cdot \mathrm{T}^{-1}]$
h_1	distance between soil surface and capillary fringe	[L]
h_2	distance between soil surface and water table level	[L]
h_e	exposed cutting length	[L]
H_p	upright plant height	[L]
k	fitting coefficient	[-]
k_l	logistic growth rate	$[\mathrm{T}^{-1}]$
k_s	equivalent grain roughness height	[L]
Ks_1	Strickler coefficient of the riverbed sediment	$[\mathrm{L}^{1/3} \cdot \mathrm{T}^{-1}]$
Ks_2	Strickler coefficient of the vegetation	$[\mathrm{L}^{1/3} \cdot \mathrm{T}^{-1}]$
L	cutting length	[L]
L_0	main rooting length	[L]
$L_{c,t}$	total critical root length	[L]
L_c	critical rooting length	[L]
$L_{e,t}$	exposed total root length	[L]

L_e	exposed root length	[L]
L_g	optimal root-growth zone	[L]
L_r	total root length	[L]
N_{100}^F	number of force drops in 100% saturation	[-]
N_{60}^F	number of force drops in 60% saturation	[-]
n_r	number of roots	[-]
$p(Q)$	probability density function of the water disharge	$[\mathrm{L}^3 \cdot \mathrm{T}^{-1}]$
$p(z_w)$	probability density function of the water table level	[L]
P_τ	uprooting probability	[-]
$p_\tau(t)$	probability distribution function of time to uprooting	$[\mathrm{T}^{-1}]$
P_ξ	POT probability	[-]
Q	flow rate	$[\mathrm{L}^3 \cdot \mathrm{T}^{-1}]$
$Q_0(\xi)$	initial peak value in reference mean event	$[\mathrm{L}^3 \cdot \mathrm{T}^{-1}]$
Q_{10}	10-year recurrence time discharge	$[\mathrm{L}^3 \cdot \mathrm{T}^{-1}]$
Q_2	2-year recurrence time discharge	$[\mathrm{L}^3 \cdot \mathrm{T}^{-1}]$
$Q_\xi(t)$	reference mean event	$[\mathrm{L}^3 \cdot \mathrm{T}^{-1}]$
Q_{cr}	critical flow rate	$[\mathrm{L}^3 \cdot \mathrm{T}^{-1}]$
Q_s	sediment discharge	$[\mathrm{L}^3 \cdot \mathrm{T}^{-1}]$
R	maximum root resistance	$[\mathrm{M} \cdot \mathrm{L} \cdot \mathrm{T}^{-2}]$
$r(z)$	analytical expression of root profile	[-]

R^2	goodness of fit	[-]
r^2	correlation coefficient	[-]
R_H	hydraulic radius	[L]
Re_D	obstacle Reynolds number	[-]
S	river slope	[-]
T	time of uprooting	[T]
t	time	[T]
T_0	initial time	[T]
t_0	location of the sigmoid's midpoint	[T]
T_ξ^+	mean time above threshold ξ	[T]
T_ξ^-	mean time below threshold ξ	[T]
u	cross-section flow velocity	$[\mathrm{M} \cdot \mathrm{T}^{-1}]$
$V(T)$	time integral of bed erosion rate $\dot{\eta}$	[L]
V_f	foliage volume	$[\mathrm{L}^3]$
V_r	root volume	$[\mathrm{L}^3]$
V_s	stem volume	$[\mathrm{L}^3]$
V_w	water volume	$[\mathrm{L}^3]$
W	uprooting work	$[\mathrm{M} \cdot \mathrm{L}^2 \cdot \mathrm{T}^{-2}]$
w	stream power per unit width	$[\mathrm{M} \cdot \mathrm{L} \cdot \mathrm{T}^{-3}]$
W_{-1}	second limb of the Lambert function	[-]

X_1, X_2	generic plants	[-]
z_c	cutting burial depth	[L]
z_m	maximum root depth	[L]
z_w	water table depth	[L]
${}_1F_1[\cdot;\cdot;\cdot]$	confluent hypergeometric function of the first kind	[-]

Chapter 1

Introduction

1.1 Overview of river ecomorphodynamics

Since the Devonian period, plants with root systems have played a crucial role in shaping fluvial landscapes (Gibling and Davies, 2012). Geological records and isotopic evidence have proven that the development of vascular plants in the Silurian-Devonian boundary has promoted river planform evolution. The stabilizing contribution of roots on riverbanks and bedforms has led to the development of a range of new fluvial styles, such as channelled- and island-braided systems and anabranching planforms (Gibling et al., 2014). Nevertheless, the role of vegetation in controlling fluvial systems has been long undervalued and only recently vegetation has been acknowledged to make an active contribution to the morphodynamic evolution of rivers (Baptist et al., 2007; Rominger et al., 2010).

The structural and biological features of vegetation are complex because they depend on many variables, such as environmental conditions and plant species (Tabacchi et al., 1996). Therefore, the inclusion of vegetation in the branch of morphodynamics has led to many challenging investigations, which have revealed that vegetation contributes to shape river landscapes together with flow and sediment processes.

The discipline that studies the multi-directional interactions between the dynamics of vegetation and river morphology and processes is called river eco-

morphodynamics. The word 'ecomorphodynamics' was introduced for the first time by Marani et al. (2006), who investigated the morphological spatial patterns determined by salt-marsh in the Venice lagoon, Italy. From then on, the term has also been used to describe the interaction between riparian vegetation and river morphodynamics. Even though this discipline denomination was introduced recently, the interest and the research towards the interaction between vegetation and river morphodynamics has been documented a long time before 2006 (e.g. see Bradley and Smith, 1986; Hickin, 1984).

The goals that ecomorphodynamic research aims to achieve are complex, especially given its holistic approach and the modeling processes that operate at different spatial and temporal scales. The component disciplines of river ecomorphodynamics are diverse and predominantly encompass different branches of science, such as hydrology, geomorphology, hydraulics, and ecology. The knowledge fragmentation among these disciplines and the occurrence of diverse niche audience groups often hinder (paradoxically) a mutual collaboration. Furthermore, the use of different approaches and the lack of conformity on certain concepts can confine the cooperation between different scientific communities (Vaughan et al., 2009). An understanding of the feedback mechanisms between hydrology, hydraulics, geomorphology, and ecology is crucially needed in order to comprehend the functioning of the riparian ecosystem, and to foresee and simulate the impacts of natural and anthropogenic changes on riparian corridors.

This Chapter provides an introduction to riparian and river systems. Interactions between vegetation dynamics and fluvial processes are also reviewed, with a particular focus on the mechanics of plant uprooting induced by flow erosion. The research questions, aim and objectives and a synopsis of the thesis are then described.

1.1.1 Riparian and aquatic vegetation

The two types of vegetation that grow and become established in riparian and river systems are classified as riparian and aquatic. The word 'riparian' derives from the Latin adjective *riparius*, and alludes to the transitional area between dryland and water bodies, where both terrestrial and aquatic realms interact (Malanson, 1993). Riparian vegetation comprises the plant communities that establish themselves both along riverbanks and in streams (e.g. vegetated river bars) (Ward, 1998). Aquatic vegetation includes plants that only grow in water, and can be divided into submerged, emergent, and floating leaf plants. However, many different other classifications of aquatic plants can be found in the literature (e.g. see Watson, 1979).

The appearance and development of both riparian and aquatic plants are strongly affected by the frequency and duration of river fluctuations, near-surface groundwater regimes, and soil moisture and composition. Aquatic species show a higher sensitivity to water depth, given their need to be in contact with water (Fischer and Claflin, 1995). The appearance and succession of both plant types respond to fluvial disturbances and water stresses (Malanson, 1993). This leads to the establishment of different plant species across the lateral gradient of the river (Figure 1.1). For instance, the zone closest to flowing water is mainly colonised by young vegetation or by species that are particularly resilient towards high shear stresses and shallow groundwater levels. Meanwhile, at the upper floodplain, in zones that are less inundated, young vegetation gives way to plants at a higher growth stage (Mosner et al., 2011). As riparian areas are transitional zones, hotspot shifts of plant type locations are common and tend to create a mixed vegetation zone among aquatic and terrestrial species (Gurnell, 2014), exhibiting the highest degree of biodiversity.

Both riparian and aquatic vegetation perform and regulate important eco-

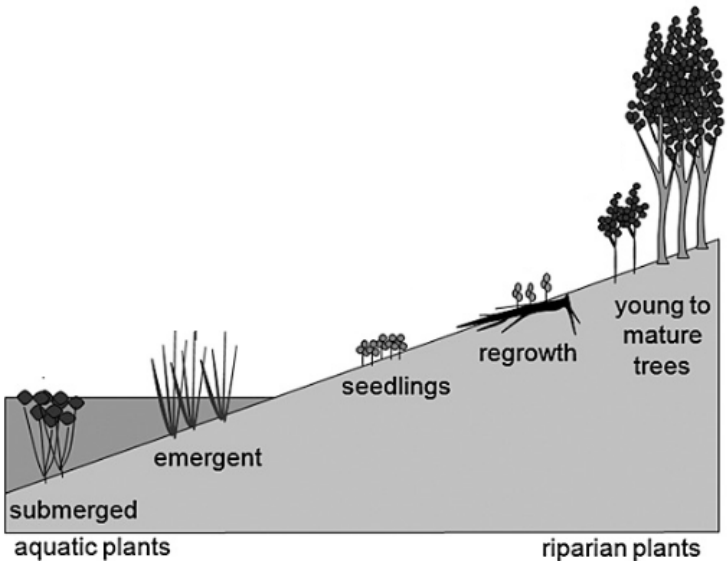

Figure 1.1: Vegetation types and and position of both aquatic and riparian plants along a river transect (modified from Gurnell, 2014).

logical functions for their respective ecosystems (Naiman and Decamps, 1997). Plants are important chemical filters that can absorb pollutants and enhance water quality, with obvious human and ecosystem health benefits (Dosskey et al., 2010; Naiman and Decamps, 1997). As an important carbon sink, vegetation regulates the flow of biogeochemical activities, plays a fundamental role in the cycle of carbon and nitrogen (Beckman and Wohl, 2014; Camporeale et al., 2018; Dybala et al., 2019), and absorbs nitrates from the soil into its root system (Peterjohn and Correll, 1984). The ability of vegetation to store carbon is directly linked to the availability of nitrogen and phosphorus, which have a fundamental role in controlling plant growth (Wieder et al., 2015). However, recent studies have acknowledged that the widespread limitation of nitrogen and phosphorus in the long-term ecosystem development may have a negative impact on plants' response to carbon uptake (Du et al., 2020). As a result, plants may switch from acting as a carbon sink to a carbon source (Penuelas et al., 2013; Wieder et al., 2015). Furthermore, the occurrence of decaying and dead vegetation in rivers

and riparian areas results in a large carbon release, which is further promoted by the higher rate of plant decomposition due to the increase of global temperature (Tabacchi et al., 2000). Vegetation transfers coarse solid organic matter to streams in the form of dead leaves, branches, wood logs, and supplies dissolved organic matter (Knight and Bottorff, 1984). Hence, vegetation is a vital source of nutrition for terrestrial and aquatic organisms (Bis and Higler, 2001; Pusey and Arthington, 2003; Verboom and Pate, 2006). Vegetation regulates light intensity and microclimates by increasing humidity and moderating temperature through evapotranspiration and the provision of shade (Allen, 2016). Microorganisms, insects, animals, fungi benefit from the shelter that vegetation offers against predators (Cook et al., 1974; Weinberger et al., 2019). Vegetation remedies habitat fragmentation, and contributes to maintaining biodiversity (Naiman et al., 1993).

1.1.2 Effect of vegetation on river flow and morphodynamics

The effect of vegetation on river hydrodynamics is well known (Bennett et al., 2008; Camporeale et al., 2019). In rivers, vegetation acts as an additional hydraulic resistance for the flow, causing flow deceleration and deflection across several scales and increasing the local roughness of the riverbed.

According to Baptist et al. (2007), the presence of vegetation in streams provides an additional contribution to the total shear stress, thus conversely decreasing the shear stress of the riverbed and limiting bed erosion processes. However, the momentum absorption of submerged plants depends on their density and shapes (Munar-Martinez et al., 2019). For example, in case of high canopy densities in proximity of the riverbed, the related shear stress decreases (Schoneboom et al., 2010). On the other hand, plants with low leaf density at

higher flow depths trigger a 'sub-canopy flow' dominated by turbulent horseshoe vortexes that increase the bed shear stress (Schnauder and Moggridge, 2009).

The extent of the impact of vegetation on the flow field depends on the morphological and biomechanical properties of the plants. For instance, turbulence intensity is linked to plant community composition. More precisely, turbulence intensity increases when the vegetation is densely concentrated (López and García, 1998), and decreases when vegetation is sparse (Yager and Schmeeckle, 2013).

Many other morphological properties of the plants are capable of modifying the flow field, particularly plant architecture, growth stage, species, plant area exposed to flow, plant flexural bending, and depth of submergence. These last two properties have caught the attention of many researchers (Baptist et al., 2007; Carollo et al., 2005; Duan et al., 2006; Li and Shen, 1973; Musleh and Cruise, 2006; Nepf, 1999; Rubol et al., 2016; Stone and Shen, 2002; Velasco et al., 2003; Wilson et al., 2003). Meanwhile, the biomechanical properties exerted by the root system cannot be neglected, as they provide stability to the plant and resistance to balance hydrodynamic drag (Edmaier et al., 2011). It also well known that the root network consolidates cohesive alluvial sediment and thence increases soil resistance to fluvial disturbance (De Baets et al., 2006).

Vegetation exerts significant influence on sediment transport and deposition processes. Plants enhance trapping of eroded sediment, both from water and wind erosion (Gurnell et al., 2012), leading to the development of pioneer landforms and expansion of riverbanks. Moreover, plants can also trap plant propagules and promote the colonization of other plant species (Gurnell, 2014). By covering bare soil, vegetation decreases erosion and soil moisture content through evapotranspiration, thence reducing the effects of waterlogging processes (Terwilliger, 1990). The local rate of sediment transport is also affected by the presence of vegetation (Gyssels et al., 2005; Ishikawa et al., 2003; Prosser et al., 1995). This is explained by the reductions in flow velocity and bed shear stress that occur

because friction is exerted through the drag force acting on the vegetation. The interaction between vegetation and sediment transport is challenging to frame at field scale. Hence, only a limited number of studies on the direct measurements of sediment transport are available (e.g. Lightbody and Nepf, 2006; Temmerman et al., 2003). On the other hand, the majority of investigations to date have relied on experiments at laboratory scale carried out on both artificial and real vegetation (Barfield et al., 1979; Jordanova and James, 2003; Tollner et al., 1977). Based on the foregoing, vegetation plays an essential role in river ecosystem functioning. For this reason, Gurnell (2014) suggests that vegetation can act as a proper 'river system engineer'.

The study of the effect of vegetation on river morphodynamics has been approached via field observations (Bertoldi et al., 2009; Hupp and Osterkamp, 1996), laboratory experiments (Errico et al., 2019; Gran and Paola, 2001; Tal et al., 2004; Tal and Paola, 2007; Tambroni et al., 2016; Vargas-Luna et al., 2019), and numerical simulations (Bertoldi et al., 2014; Caponi and Siviglia, 2018; Perucca et al., 2007; Siviglia and Crosato, 2016; Wang et al., 2019a) and theoretical models (Bärenbold et al., 2016; Bertagni et al., 2018; Camporeale and Ridolfi, 2006; Perona et al., 2009; Zen and Perona, 2020).

Vegetation is involved in several geomorphological feedback mechanisms (see Camporeale et al., 2013 and Vesipa et al., 2017 for a review). For example, by altering the flow field, vegetation has been found to determine the occurrence of several trends in channel width. Vegetation can induce marked narrowing and deepening of the channel (Gran and Paola, 2001; Hickin, 1984) and, less commonly, can also cause channel widening by deflecting the flow towards the banks (Anderson et al., 2004; Hey and Thorne, 1986). Bank accretion is another frequent morphological feedback from the presence of vegetation in meandering rivers. This phenomenon consists of the natural adjustment mechanism of the river to the formation of new landforms at riverbanks as a result of vegetation

establishment (Beeson and Doyle, 1995; Eschner et al., 1983; Vargas Luna, 2016; Zen et al., 2016). Moreover, vegetation can reduce the degree of river braiding and metamorphose into single-thread planforms. This phenomenon has been observed both at laboratory (Gran and Paola, 2001; Tal and Paola, 2007; Tal and Paola, 2010) and at field scale (Allmendinger et al., 2005). However, the opposite has been found to occur in ephemeral rivers, where vegetation induced an increase in channel formation and flow division into anabranching patterns (Coulthard, 2005; Tooth and Nanson, 2000) . Recent theoretical models serve to support this hypothesis (Crouzy et al., 2016). Vegetation can also trigger shifts between braiding and meandering, according to the stages of growth and density of vegetation in the channel (Millar, 2000).

The action of vegetation on river morphology is not an immediate result of its establishment, but it is rather the outcome of 'temporal adjustments' between fluvial landforms and vegetation succession, as defined by Corenblit et al. (2020). In other words, the biological timing of the plant has an important influence on river morphodynamics. Corenblit et al. (2007) suggest that the most active period during which vegetation competes with river processes is the 'biogeomorphic phase'. This phase represents the period when the interplay between vegetation and river morphodynamic processes starts to determine the evolution of the riparian landscape. Before the onset of this phase, plants undergo a stage of vegetation recruitment whose duration is strongly affected by environmental disturbances (e.g. hydrodynamic forces by waves and currents). Such critical stage was conceptually framed by Balke et al. (2011). Balke et al. (2011) introduced the concept of Windows of Opportunity with the aim of estimating the timescale needed by plants (specifically mangrove seedlings) to successfully establish in a bare substrates without being washed away. This concept was further used as an operational framework by Eichel et al. (2016) and Hortobágyi et al. (2018), who assessed the biogemorphic feedback window

of vegetation establishment along lateral moraines slopes and on alluvial bars, respectively. Recently, Caponi et al. (2019) used the Window of Opportunity concept to model and explain the vegetation development observed on some bars located along the Alpine Rhine river.

1.1.3 Flow impact on vegetation

The previous paragraphs have outlined the main ways in which vegetation influences the morphological evolution of rivers. It should be noted that the interaction between vegetation and river processes is mutual (Camporeale et al., 2013; Camporeale et al., 2019).

Flow and fluvial processes control vegetation dynamics and their successional trajectories through positive and negative feedbacks. In fact, one of the principal actions exerted by rivers is the transport of seeds (hydrochory) and vegetative propagule (e.g. seedlings, vegetative fragments, and drift-wood), which, when water levels recede, are deposited on moist river surfaces and develop into vegetation (Francis et al., 2006; Gurnell et al., 2008; Mahoney and Rood, 1998; Merritt and Wohl, 2002). River fluctuations are also beneficial to the formation of nursery sites, which are suitable areas for vegetation recruitment and establishment (Vesipa et al., 2017). River flow enhances the provision of other matter, such as moisture, organic sediments, chemicals, and nutrients (mainly nitrogen and phosphorus), which are all important for vegetation encroachment and establishment (Asaeda and Rashid, 2014; Sabater, 2000; Stella et al., 2013).

On the other hand, the flow can induce several negative responses by vegetation. An example is the formation of scour and deposition patterns around and behind the plant. The scouring mechanism is driven by enhanced local shear stress and turbulence (Yagci et al., 2016) and its scale depends on the obstacle-diameter-to-sediment-size (Edmaier et al., 2015). As for scouring around

the bridge piers, the higher this scale ratio, the more pronounced the scouring (Manes and Brocchini, 2015; Melville and Sutherland, 1988; Roulound et al., 2005). The erosive power of a river can expose the root system of the plant and make it more susceptible to the actions of external forces. Especially during peak flows, the combination of erosion processes and hydrodynamic forces can cause plant damage and mortality through plant burial, plant anoxia, and plant uprooting. Vegetation burial comprises coverage of the canopy and the stems by post-depositional sediment disturbance (Carter Johnson, 2000; Levine and Stromberg, 2001). The mortality rate induced by burial mechanisms is higher than that induced by scouring (Kui et al., 2014). Plant anoxia is a process triggered by limited capacity for root transpiration due to reduced oxygenation during prolonged submersion (Dixon and Turner, 2006; Kozlowski et al., 1984). Flow-induced uprooting involves a competing-mechanism between root resistance and hydrodynamic forces (Edmaier et al., 2011), and its severity is considered to be the main cause of seedling mortality (Bankhead et al., 2017; Crouzy et al., 2013; Edmaier et al., 2015). Moreover, groundwater level fluctuations have a significant impact on vegetation survival. Extreme drought conditions, due to excessive depth-to-groundwater conditions, can cause the dessication and decay of vegetation (Garssen et al., 2014; Kath et al., 2014). Water level is an important influence factor on root biomass and architecture (Francis et al., 2005; Guilloy et al., 2011; Hughes et al., 1997). Experimental observations have revealed that the root density of riparian vegetation reacts differently according to flow regime alterations (Gorla et al., 2015).

With the advent of ecomorphodynamics, the mechanism of plant uprooting by flow started to receive considerable attention by scientists from different disciplines, including geomorphologists, ecologists, and river engineers. The flow-induced removal of plants is a complex phenomenon that depends, to a large extent, on the resistance exerted by the root system. For this reason, before

illustrating this mechanism, it is sensible to outline key findings concerning root resistance and soil-root interaction.

1.2 Plant roots: 'the hidden half'

1.2.1 Generalities

Known as the 'hidden half' (Waisel and Eshel, 2002), plant roots perform many roles in the terrestrial and aquatic biomes, and knowledge of these roles is useful in predicting vegetation-mediated ecosystem changes. Roots provide nutrition and structure to the plant, affect the resilience of the ecosystem to environmental and anthropological stresses (Fan et al., 2017), transfer carbon to the rhizosphere (Smit et al., 2013), affect the structure of soil and its biological activities (Bertin et al., 2003), and sustain below-ground biodiversity (Bardgett and Van Der Putten, 2014). However, the most important feature in terms of biomechanics is the ability of roots to provide anchorage and stability to the above-ground biomass of a plant subjected to external forces (Ennos and Pellerin, 2000; Fraser, 1962). The resistance exerted by the root system is complex and depends mainly on the root architecture, which is the spatial configuration of primary and secondary roots in the soil and their interconnections (Gregory, 2006).

Due to the high variabilities of plant species, soil, and environmental conditions (Malamy, 2005), several classification systems of plant root architecture have been proposed. Cannon (1949) grouped root types according to the importance of the root emergence process, and distinguished primary and adventious root system (Figure 1.2). According to Cannon (1949), the main root system may be considered monoaxial, and composed of primary roots and secondary roots. The secondary roots are defined as developing from the primary one at first order, second order, etc., of bifurcation. (Adventitious roots, by definition, arise from

the shoot.) Kostler et al. (1968) identified three different architectures (taproots, plate roots, and heart roots) according to the preferential growth direction of the main and secondary roots. The classification proposed by Kostler et al. (1968) is not generic, and is mainly restricted to mature vegetation and especially to trees. Yen (1987) proposed another classification based on the branching pattern of the root system, whereby the root system was grouped into five branching patterns (VH-type, H-type, V-type, R-type, and M-type), according to their primary functions (e.g. soil stabilization, resistance to external forces).

1.2.2 Mechanical anchoring and resistance to uprooting

The mechanical anchoring of plants is rather complicated, owing to the multiplicity of variables involved. Indeed, root morphology (e.g. root diameters and length) and topology (e.g. tortuosity, branching patterns) are the main parameters that affect the rooting resistance. In addition, the soil properties (e.g. grain size distribution and moisture content) and the root-soil ball interface also play an important part (Dupuy et al., 2005; Ennos and Pellerin, 2000; Genet et al., 2005; Pollen, 2007; Schwarz et al., 2010c).

Ennos (1990) was the first to propose a model that expressed the root resistance of a plant with n_r number of roots. Ennos derived three formulae, according to the type of root failure that occurs when a plant is pulled out from cohesive soil. The first formula refers to the resistance of roots to breakage:

$$F = n_r \frac{\pi}{4} d_r^2 \sigma_r. \tag{1.1}$$

The second models the root resistance to pullout:

$$F = n_r \pi d_r L_r \tau_s. \tag{1.2}$$

The third expresses tensile failure at the soil-root ball interface as:

$$F = 2\pi L_r^2 \sigma_s. \tag{1.3}$$

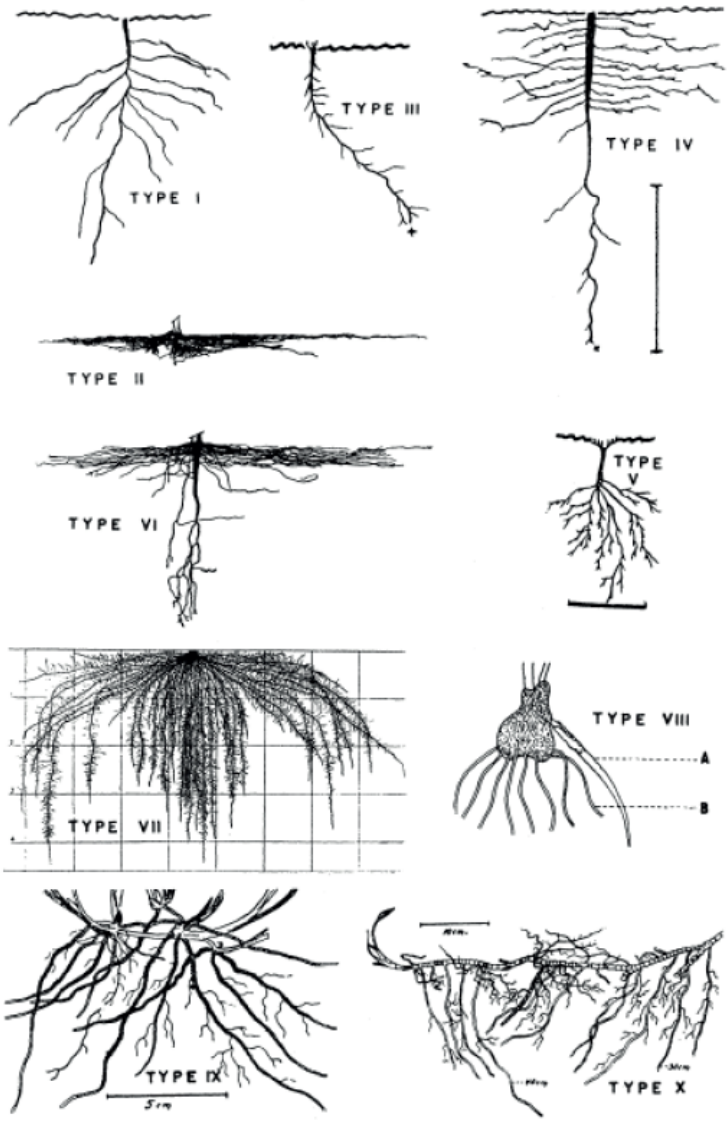

Figure 1.2: Examples of primary and adventitious root systems (after Cannon, 1949). Primary root systems: I - VI, adventitious root systems VII - X.

In the above expressions, L_r is the total length of the roots, σ_r is the tensile breaking stress of the root material, and τ_s and σ_s are the shear and the tensile strength of the soil, respectively. These laws are derived for plants of cylindrical shape and constant diameter d_r. Equation 1.2 describes the conditions often encountered when pulling out plants with short roots or roots subjected to low confining stresses (Gray and Leiser, 1982). However, root breakage occurs most

commonly for longer and weak roots, as confirmed by Schwarz et al. (2010a) who identified a breakage-slippage threshold from a length to diameter plot for different values of branching coefficient. Root branching also has an important influence on uprooting resistance; as reported by Dupuy et al. (2005) and Mickovski et al. (2007), branches can lead to an increase in force resistance by 5 N per branching point. In practice equations 1.1, 1.2, 1.3 are rarely individually applied because the failure of roots occurs as a combination of all three mechanisms (Ennos, 1993). Root failure also depends on soil conditions. For example, moist and soft soils have low shear strength. Hence, in moist soils the tension is transferred slowly into the soil, and failure occurs at high depths. The opposite occurs for dry and hard soils, where the shear strength is higher and failure takes place near the stem base (Smit et al., 2013).

1.2.3 Plant pullout experiments

The approach most used to quantify root reinforcement is based on static uprooting experiments, or more commonly, pullout tests. A pullout test consists of pulling a root out of the soil mechanically or by hand, and registering the pulling force using a load cell. Pullout tests have been carried out at laboratory scale on real plants (Bailey et al., 2002; Bankhead et al., 2017; Ennos, 1989; Ennos, 1990; Liang et al., 2020; Mickovski et al., 2009; Schwarz et al., 2011) and artificial plants (Dupuy et al., 2005; Kamchoom et al., 2014; Mickovski et al., 2007; Stokes et al., 1996), and at field scale (Bankhead et al., 2017; Burylo et al., 2009; Bywater-Reyes et al., 2015; Calvani et al., 2019a; Karrenberg et al., 2003; Liu et al., 2011; Okada and Kurokawa, 2015; Tanaka and Yagisawa, 2009; Tosi, 2007).

Plant pullout tests provide useful information about the ways root morphology, topology, and mechanical properties react to external forces. Generally, the

results of pullout tests have shown that the rooting force correlates well with geometric properties of the roots, such as rooting length and diameter (Edmaier et al., 2014; Ennos, 1989; Mickovski and Ennos, 2002; Yoshioka et al., 1998). Furthermore, Bailey et al. (2002) studied cooperation among roots, and found that the occurrence of secondary roots can influence rooting resistance. However, quantification of the input provided by multiple roots is rather complex, because, contrary to the assumption by Ennos (1993), the resistance exerted by the different root fibers may not be the same, because roots have different lengths and friction properties (Coutts, 1983).

Correlation between pullout force and root architecture is more common in laboratory tests. In field experiments, it can be difficult to recover an intact root system, and so regression laws often rely on parameters that are easier to quantify. In such cases, the force is often linked to the frontal area of the plant, the basal stem, and the plant height (see e.g. Bankhead et al., 2017; Bywater-Reyes et al., 2015; Karrenberg et al., 2003; Liu et al., 2011). In field pullout experiments, the higher heterogeneity of the trajectories of roots in the soil leads inevitably to higher variability in their biomechanical properties (Giadrossich et al., 2017; Riestenberg, 1994; Schwarz et al., 2011; Vergani et al., 2016). For example, it has been found that for the same root diameter, different roots had notably different strength (Loades, 2010; Schwarz et al., 2011). Moreover, water and nutrient availability can affect root morphology and topology and, in turn, root resistance (Markesteijn and Poorter, 2009; Trubat et al., 2006). For instance, soil water suction has been found to influence pullout resistance significantly by modifying the strength properties and the deformation characteristics of the roots (Easson et al., 1995; Edmaier et al., 2011; Ennos, 1990; Schwarz et al., 2011). More force is required to uproot plants growing in less moist sediment, compared with fully saturated sediment (Edmaier et al., 2014; Pollen, 2007; Pollen-Bankhead and Simon, 2010).

1.2.4 Flow erosion experiments

Controlled flow erosion experiments have recently been used to assess the ability of plant root systems to resist external forces (i.e. water-induced drag). In particular, the benefit of controlling the flow erosion processes and plant time removal has made this approach very effective. Edmaier et al. (2015) and Calvani et al. (2019a) used controlled-erosion flume experiments to study the mechanics of flow-induced uprooting of seedlings. The controlled flow regime and the quasi-parallel erosion allowed Edmaier et al. (2015) and Calvani et al. (2019a) to assess the critical rooting length, a variable corresponding to the residual rooting depth of the plant when uprooting occurs. In practice, the critical rooting length is a relevant indicator to assess the percentage of biomass either uprooted or surviving after a flooding event.

Flow-induced uprooting of vegetation has also been investigated through field experiments and observations. Pasquale (2012) tested the resistance of transplanted cuttings to flow erosion processes on a river bar in the Thur River, Switzerland. By monitoring the evolution of above- and below-ground biomass of the cuttings and simulating the morphodynamic evolution of the river, cutting survival was estimated as a function of flow erosion/deposition rates. However, in this case, the challenges associated with tracking river processes and vegetation recovery after uprooting meant that an accurate estimation of the critical rooting length could not be obtained.

Vegetation jet tests comprise another experimental technique that can be used in situ to assess the erosion resistance and cohesive soil reinforcement provided by plant roots. For example, Pollen-Bankhead et al. (2011) used jet-testing measurements to quantify the water erosion resistance of aquatic vegetation established on the margins of the River Blackwater (UK). Pollen-Bankhead et al. (2011) used the critical shear stress of the soil obtained from the tests to estimate

the scour depth that might occur and cause vegetation uprooting. Although this approach has been widely applied (e.g. Hanson, 1990; Hanson and Simon, 2001), its shortcomings need to be taken into account (e.g. comparability between erosion induced by jet dynamics to that determined by river erosion processes).

1.2.5 The role of vegetation roots in soil reinforcement

River bedforms are not the only features affected by the presence of vegetation. Indeed, a major focus has also been on the role of riparian vegetation on the mechanical and hydrological reinforcement of riverbanks and margins (e.g. Burylo et al., 2009; Hughes, 1997; Pollen and Simon, 2005; Pollen-Bankhead and Simon, 2010; Simon and Collison, 2002; Stolzy and Barley, 1968).

Vegetation roots enhance soil fixation and reinforcement against erosion and landslide processes. Plants reduce moisture content in the soil and at its surface through plant canopy interception, evaporation, and transpiration, and through the creation by roots of macropores in the soil across which the water infiltrates at higher rates (Ghestem et al., 2014; Greenway, 1987; Gyssels et al., 2005). However, this increased infiltration capacity may cause the water table level to rise, elevating seepage pressure, and so increasing the risk of landslide (Cammeraat et al., 2005; Collison and Anderson, 1996; Nyssen et al., 2002). The hydrological effect of riparian vegetation is difficult to quantify, given that it is controlled by plant types, soil properties, rainfall intensity and frequency, etc.

Regarding their mechanical effect, roots have been found to reinforce soil due to their high tensile strength and adhesion properties (Ekanayake et al., 1997). Roots are strong in tension but weak in compression. Conversely, soil is generally strong in compression but weak in tension. Hence, root-soil material binds together to create a composite material with enhanced strength (Thorne, 1990). There has been a long debate about the ideal type of roots for streambank

stability. At first sight, fine roots look more suitable for achieving this aim given their small surcharge and their fibrous component, which provides more strength for unit area (Gyssels et al., 2005; Operstein and Frydman, 2000). Although they do not have these advantages, coarse roots can compensate for the shortcomings of their inherent shortness through an ability to penetrate deeply and because of their higher bending stiffness (Bischetti et al., 2007).

The first step in modelling root reinforcement was taken in the late 1970s by Wu (1979) and Waldron and Dakessian (1981) whose simple perpendicular root models were based on an extended version of the Mohr-Coulomb equation, with an enhanced shear strength component representing the root contribution. This method is very simple in that it requires few input parameters. However, the model assumptions are over-simplistic given that they speculate that roots all break simultaneously and are mobilized instantaneously when a bank fails. These assumptions lead to inaccurate overestimation of root reinforcement ability (Preti, 2013). The 'Wu and Waldron model' conditions are not representative of reality by negecting the progressive redistribution of stress on the roots.

To overcome this drawback, Pollen and Simon (2005) devised a fiber bundle model (FBM), called *RipRoot*, which captures the progressive failure of roots, under the hypothesis that the elastic properties of the fibers are the same. The principle of *RipRoot* refers to a basic principle of standard FBM originally proposed by Daniels (1945). FBM assumes that the maximum load withstood by a bundle of fibers is less than the sum of each of the individual strengths. Results obtained by implementing fiber bundle models show better outcomes than obtained using the 'Wu and Waldron model' (Mickovski et al., 2009; Simon and Collison, 2002). However, the foregoing fiber bundle models neglect root-soil interactions, root failure mechanisms, and root geometrical and mechanical properties.

These problems were overcome by Schwarz et al. (2010a), who implemented

an improved Root Bundle Model by introducing a straining step loading method. Recently, Schwarz et al. (2013) proposed another approach, called the Root Bundle Model Weibull (RBMw). This method is novel in that it accounts for variability in the root mechanical properties by using a probabilistic approach (Weibull survival function).

Despite the progress achieved thus far, the foregoing models are only valid for cohesive soils, which are common in riverbanks and hillslopes. The effect of root reinforcement in cohesionless soils, such as comprise river bars and islands, has been practically unexplored and is still based on limited investigations (e.g. Bywater-Reyes et al., 2015; Pollen, 2007; Pollen and Simon, 2005; Simon and Collison, 2002). This is because the mechanism of bonding between soil and roots in cohesionless soil is complicated by the fact that fluvial erosion is regulated by a threshold condition of incipient motion. Hence, once sediment mobilization and transport is achieved, the shear stress on the riverbed induces substrate erosion around the plant that exposes its root system to hydrodynamic forces (Edmaier et al., 2011).

1.3 Mechanisms of plant uprooting by flow

Flow-induced plant uprooting depends on the geometrical and topological properties of roots, soil and moisture characteristics, river hydrology, and related river processes (Edmaier et al., 2011).

The mechanism of plant uprooting by flow was conceptualised by Edmaier et al. (2011), who identified two main types of root erosion mechanisms in non-cohesive soils. Type I uprooting is quantitatively described as an equilibrium between the destabilizing forces (drag and buoyancy forces) and the stabilizing forces (root resistance).

Type I uprooting occurs as soon as the action exerted by flow drag and net

Figure 1.3: Uprooted trees along the Brenta River, a braided river. The photograph was taken in Ponte della Vittoria, Tezze sul Brenta, Italy.

buoyancy force exceeds the mechanical anchoring of the plant (Figure 1.4a). In this case, the process is almost instantaneous and mainly applies to young and weak vegetation, with root systems that are not sufficiently resistant to compete against the action of the flow. The timescales of plant uprooting by flow of Type I were investigated for the first time by Perona et al. (2012a) and by Crouzy and Perona (2012), who discovered that the timescales of pioneer riparian vegetation have a crucial influence on biomass selection induced by floods.

Type II uprooting occurs as a result of the combined action of drag and buoyancy forces and bed erosion processes. In this case, scouring around the plant decreases root resistance and increases the flow-impact area of the plant by exposing part of the root system (Figure 1.4b). Type II uprooting represents

a mechanism of competition between biologic and hydrologic timescales, as its outcome depends on the resilience of the plant to recover and reinforce between two consecutive floods. Hence, unlike its Type I counterpart, Type II uprooting is a time-delayed mechanism that is typical of mature vegetation, or, in general, of plants with a well-developed root apparatus.

Bywater-Reyes et al. (2015) provided a further classification of the uprooting mechanism, noting that uprooting of Type II can occur differently according to the type of process that initiates the scouring. Consequenty, Bywater-Reyes et al. (2015) introduced Type IIa and Type IIb concepts. Type IIa uprooting refers to self-induced local scour resulting from the formation of horseshoe vortexes caused by vibration of the plant stem. Type IIb uprooting occurs as a result of erosion processes extended to larger scale (e.g. bar- and reach-scale). However, the distinction between uprooting of Type IIa and IIb is labile, as very often the two mechanisms occur simultaneously. In fact, as explained in 1.1.3, scouring around the plant depends on the obstacle-to-sediment size ratio. Furthermore, local scour does not occur for plants with a porous structure of leaves and branches because flow penetration through the canopy merely reduces the flow velocity leading to sediment deposition only (Schnauder and Moggridge, 2009).

Before the concept of the uprooting mechanism was developed by Edmaier et al. (2011), vegetation removal was given a marginal role in morphodynamic models. Most investigations focused on vegetation feedback on river morphodynamics, without considering the reverse mechanism. The first studies to include this feedback define plant uprooting using a threshold condition for sediment motion. For example, Bertoldi et al. (2014) developed a numerical model in which vegetation mortality was represented by an exceedance condition of a modified Shields number. A similar approach was used by Oorschot et al. (2016), who proposed that plant mortality by flooding, desiccation, and high flow velocity was determined by a dose-effect law linking vegetation mortality and morphodynamic

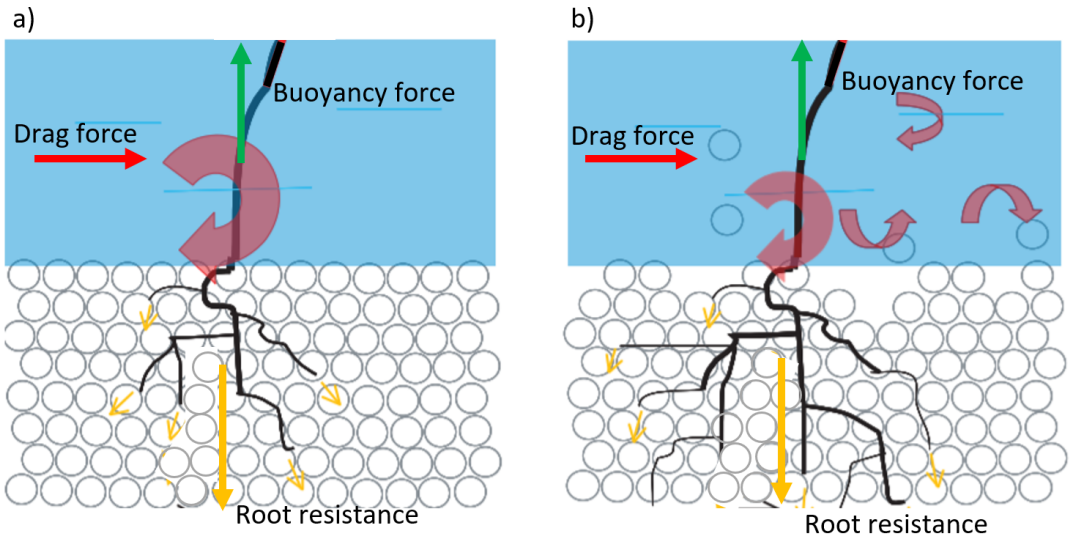

Figure 1.4: Flow-induced plant uprooting mechanisms: a) Type I; and b) Type II. The force components acting on the plant are the drag force (red vector), buoyancy force (green vector), and root resistance (yellow vector) (modified from Edmaier et al., 2011).

pressure. However, these approaches did not succeed in differentiating whether vegetation removal or mortality were occurring as a result of uprooting, burial, or anoxia. Given the strong correlation between uprooting mechanism and root properties (see Section 1.2.3), these approaches were rendered invalid by neglecting the resistance exerted by the roots.

Later, the contribution by vegetation removal was treated as a decay coefficient in the logistic law (e.g. Camporeale and Ridolfi, 2006). However, determination of this coefficient is not trivial because its value depends on the biomechanical properties of the plants. For instance, as an approximate solution, the decay rate was linked to the vegetation growth rate through a coefficient of proportionality (e.g. Bertagni et al., 2018). Nevertheless, the vegetation decay coefficient is closely related to the vegetation species, and there is a lack of experimental data from which to assess a valid relationship between the coefficient and species.

A further step forward was achieved by Crouzy and Perona (2012) who defined

the uprooting probability as a function of the PDF of root resistance, expressed in terms of the root length. Recently, a major advance was made by Perona and Crouzy (2018), who proposed a physically stochastic model to assess the PDF of the uprooting time for the Type IIb uprooting mechanism. Perona and Crouzy's model requires knowledge of the erosion depth, L_e, induced by scouring around the plant, which, assuming the verticality of the root system, coincides with the exposed portion of the root.

A value for the exposed root length can easily be measured in controlled flume experiments (Calvani et al., 2019a; Edmaier et al., 2015) but is difficult to establish in situ. In numerical schemes, approximations are therefore often used, such as by Caponi and Siviglia (2018), who proposed a fixed quantification of L_e. However, given the strong dependency of L_e on the root depth of the plant, soil properties, and root anchoring resistance, the foregoing assumptions may not always be realistic. Another approach was introduced by Calvani et al. (2019a), who determined L_e by expressing a balance between the destabilizing forces acting on the canopy (drag and buoyancy force) and the resisting force of the roots based on the general Mohr-Coulomb criterion for soil resistance.

Despite much recent research effort, knowledge as to how the biomechanical properties of roots (and their related timescales) affect uprooting dynamics still remains very limited.

1.4 Context and research questions

The overview motivates the following research questions:

1. **How do the structure and mechanical resistance of cutting roots depend on local soil characteristics and water level regime, and can the growth of cutting roots be controlled for flume experiments?**

   Section 1.2.5 highlighted that vegetation can increase the mechanical resistance of cohesive soils. However, limited knowledge exists about the mechanism by which roots reinforce non-cohesive soils (e.g. sand). It is therefore important to explore both the growth characteristics and the mechanical properties of candidate plant (e.g. *Salix*) cuttings subject to different soil moisture levels. Furthermore, to date (see Section 1.2.4), flume erosion experiments have been limited to seedlings. Therefore, this research question also paves the way to using *Salix* cuttings as plant prototypes in future flume experiments.

2. **Can plant pullout tests be used to assess the critical rooting length of plants for flow-driven uprooting processes?**

   The critical rooting length is an important variable that enables assessment of the plant uprooting probability (see Section 1.2.4). However, this is not as easy task because the critical rooting length depends on the erosion processes and the residual root resistance of the plant at the time of uprooting. Moreover, Section 1.2.3 revealed that pullout tests are the most effective way to quantify root resistance through the link between uprooting force and plant characteristics (e.g. rooting length). However, the link between static uprooting force and water drag forces is still unknown.

3. **How assessment of the biological timescales can help identification of the 'biological windows' when uprooting of wood logs becomes feasible?**

   Wood logs can deposit on river bars as water levels recede (see Section 1.1.3). The favourable moisture conditions when wood logs strand can promote root development. The likelihood for wood logs to develop roots depends on an interplay between biologic and hydrologic timescales (Section 1.3). Although the dynamics of wood logs has been widely investigated, very little is known about the time needed to re-mobilise them.

4. **How do vegetation roots react to natural flow regime alterations? How does vegetation affect riverine ecosystem resilience to perturbations?**

   As discussed in Section 1.1.3, the roots of riparian plants are highly reliant on groundwater table depth, and can tune their biomass configuration according to water regime alterations (e.g. river impoundments) even under equal climate conditions and for the same vegetation species. However, the sensitivity of the riverine ecosystem towards changes in root configuration (following a hydrologic shift) has not previously been assessed. Likewise, there is a gap in knowledge regarding the signature that the hydrologic adaptation of root systems can leave in terms of riparian landscape succession.

1.5 Aim and objectives

The aim of this thesis is to investigate the biomechanical properties of vegetation roots, their role in controlling the mechanism of vegetation uprooting by flow and erosion processes, and their ultimate contribution to river ecomorphodynamic processes.

To achieve this aim, the research objectives are:

1. To analyse how the root biomass of *Salix* cuttings reacts to different water table regimes, and test how this affects rooting resistance to external forces;

2. To derive a free-body model to predict the critical rooting length, which is a fundamental parameter for assessing the uprooting probability of flexible vegetation by flow-erosion processes;

3. To investigate the biomechanical properties of small-scale wood logs at different growth stages to provide insight, in terms of timescales, into the phenomenon of re-mobilisation of stranded wood pieces from river bars;

4. To derive a combined analytical and numerical model to demonstrate how the uprooting probability of vegetation can be utilised as an important indicator of the statistical equilibrium states of riparian ecosystems when perturbed;

5. To apply the model to a real case of river impoundment for validation purposes.

The diagram in Figure 1.5 illustrates the linkage among the objectives listed above. Objectives 1, 2, and 3 are all essential to reach objective 4, which, in turn, leads to attain objective 5.

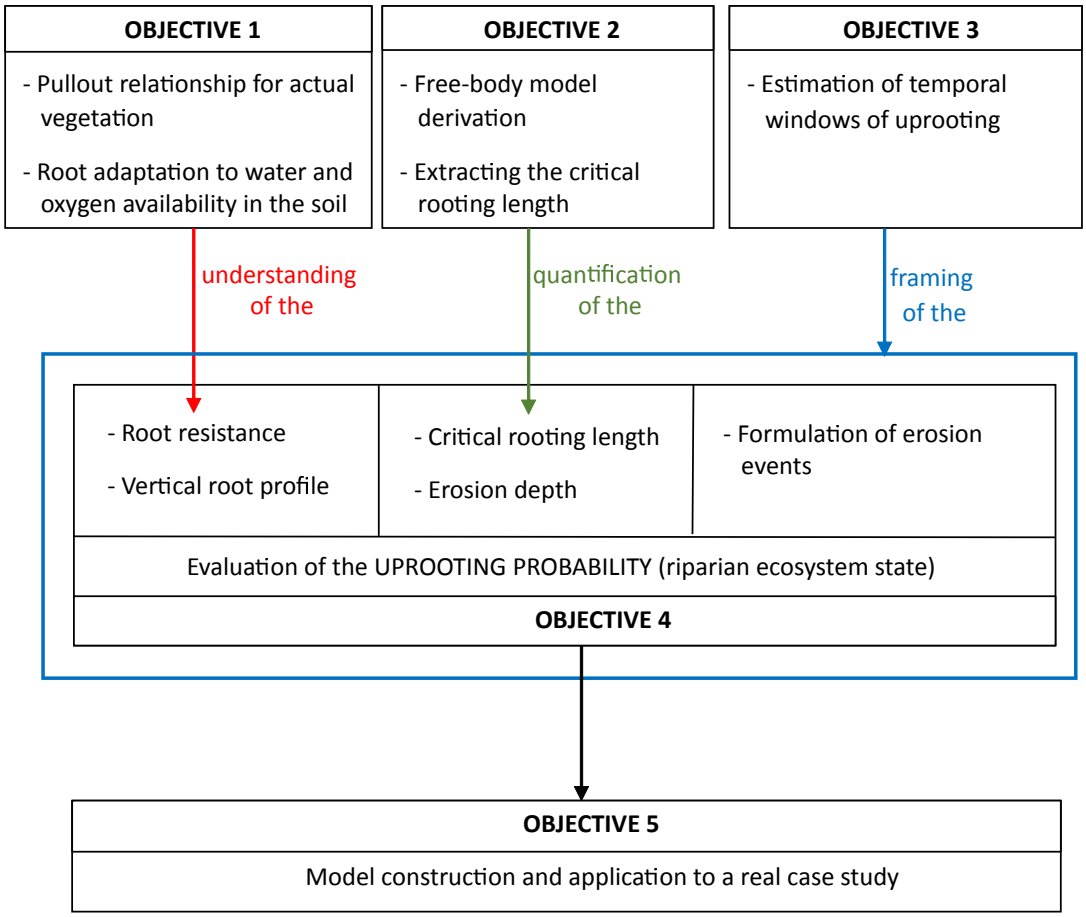

Figure 1.5: Schematic diagram illustrating the linkage among objectives.

In more recent years, riparian ecosystems have been reshaped by anthropogenic pressures, as well as by indirect stressors such as extreme climate and flooding events. As a result, global concerns about the decline of the riparian ecosystem have driven researchers and practitioners to enhance the design and optimization of river restoration strategies. The successful outcome of river restoration projects relies on a complete understanding of the interaction between vegetation dynamics, river flow, and sediment transport, all of which contribute to the riparian landscape evolution. Hence, investigating the biomechanical characteristics of vegetation and its timescales in relation to flow erosion dynamics

represents a fundamental step for the sustainable management of water resources, and the design of bioengineering techniques and urban ecological measures.

This thesis covers several different, but interrelated aspects of river eco-morpohodynamics. In view of recent natural flow regime alterations and river degradations, assessment of the biological and mechanical properties of riparian vegetation is important not only in terms of river restoration, but also in foreseeing impending riverine ecosystem transitions.

1.6 Synopsis

The remainder of the thesis is structured as follows. **Chapter 2** describes the test methodology and results obtained for the growth of 140 cuttings tested under different water table conditions. Particular attention is devoted to statistical analysis of how the decay rate and steadiness of water level affect the root profile and its rooting resistance. The experimental results are used to verify an analytical model. **Chapter 3** presents a detailed derivation of the free-body model, and describes its validation using three data sets obtained from laboratory and field experiments. Important observations are made about the stochastic footprint of the mechanism of flow-induced plant uprooting, through implementation of a physically-based stochastic model. **Chapter 4** explores the dynamics of mobilisation of large fragments of wood pieces after establishment on river bars. Results are presented from pullout tests on 326 small-scale wood logs. Statistical analysis is provided of the below- and above-ground biomass, and the results used to evaluate flow drag force and assess 'biological windows' when uprooting is likely to occur. Particular attention is given to the force-displacement curves obtained from the uprooting signals, from which sequences of force jumps are analyzed to shed light on root resilience and on the mechanism of load redistribution among roots. **Chapter 5** presents a framework for assessing riparian ecosystem dynamics in response to alteration of the natural flow regime, in terms of vegetation resilience to uprooting. A combined numerical and analytical model is developed that computes the uprooting probability in and in between two alternative stable ecosystem states. In **Chapter 6**, the model is applied to a reach of the Maggia River, Switzerland, where aerial images are available pre- and post-dam impoundment. A sensitivity analysis is conducted, and the results interpreted to offer river management recommendations. Lastly, the main findings and the impact of the work, and recommendations for further

research are given in **Chapter 7**.

Journal publications arising from this thesis

1. Bau', V., Zen, S., Calvani, G., and Perona, P., Extracting the critical rooting length in plant uprooting by flow from pullout experiments, *Water Resources Research*, 55(12):10424-10442. https://doi.org/10.1029/2019RR025074.

2. Calvani, G., Perona, P., Zen, S., Bau', V., and Solari, L., Return period of vegetation uprooting by flow, *Journal of Hydrology*, 578, 124103.

3. Bau', V., and Perona, P., Biomechanical properties and resistance to uprooting of laboratory-scale wood logs, *Journal of Geophysical Research: Biogeosciences*, 125(10). https://doi.org/10.1029/2020JG005782.

4. Bau', V., Borthwick A. G. L., and Perona, P., Plant roots steer the resilience of riverine morphodynamic systems to perturbations, (*in preparation*).

Chapter 2

Hydrologic control on root growth

2.1 The role of cuttings in river restoration

Riparian vegetation plays an active, essential role in riverine ecosystems, and so it has been widely cultivated as a strategy towards the sustainable management and restoration of rivers. However, the effectiveness of plants in river engineering largely depends on their root systems. Plant roots are well known to reinforce cohesive soils (see e.g. Mickovski et al., 2009; Millar, 2000; Pollen, 2007), and induce mechanical sediment cohesion in non-cohesive soils such as found in river bars and islands (De Baets et al., 2006; Gyssels et al., 2005; Xie et al., 2006). Despite this, attentive investigations on the role played by the below-ground biomass on soil stabilisation are still scarce, especially for non-cohesive materials, for which root type, growth pattern, and architecture are fundamentally important (Masle, 2002).

The ability of plants to develop adequate rooting resistance depends on several factors. Plant anchorage strength is affected by the depth and the spatial branching density of the root system (Ennos and Pellerin, 2000; Schwarz et al., 2010b) and the moisture and texture of the soil (Pollen, 2007). Hence, the reintroduction of riparian plants in corridor ecosystems requires a full understanding of the candidate plant species and its interaction with river hydrology and geomorphology.

Besides, restoration and propagation of riparian species do not occur sponta-

neously, and so vegetation usually has to be regenerated from seeds or fragments. Even though seed-based regeneration ensures genetic biodiversity and is the most effective approach, germination is strongly influenced by external disturbances (e.g., wind) and may be difficult to control. Therefore, it is instead common to use clonal propagation from dormant and rootless cuttings as a reliable way by which to propagate riparian species (Bentrup, 1998; Cronk and Fennessy, 2016; Pezeshki et al., 2007; Winfield and Hughes, 2002). Clonal propagation of riparian vegetation has become a prominent strand of river management owing to its cost-benefit advantage and likelihood of success.

Salicaceae species are the most common kind of vegetation used to restore rivers because of their fast growth rate on wet subsurface sediments of exposed river bars (Müller and Scharm, 2001) and their ability to adapt to extreme groundwater level configurations (Hupp, 1992; Pasquale et al., 2012; Shields Jr et al., 1995). *Salicaceae* exhibits high tropic response by tuning their below-ground biomass distribution according to river flow fluctuations and oxygen availability (Pasquale et al., 2011). Unlike other species, *Salicaceae* has a particularly solid root system (Karrenberg et al., 2003), is able to survive long periods of inundation periods, and produces adventitious roots to deal with soil anoxia (Vandersande et al., 2001).

Despite the many qualities of *Salicaceae* species, revegetation projects can face difficulties. Although mature *Salix* plants can adapt to drought conditions, the same is not yet true for young transplanted cuttings whose vascular root tissue is still in the early development phase. For example, lack of water can cause plant dessication with a consequent high mortality rate (Rood et al., 1998; Shields Jr et al., 1995; Wolfe, 1992). Hence, once the plant substrate characteristics have been assessed, the water table level and the related plant root depth are crucial parameters in the successful implementation of river restoration projects (Abernethy and Rutherfurd, 1998; Bätz et al., 2016; Simon and Collison, 2001).

Owing to the lack of a standardized approach to the reintroduction of native species, specific assessments are necessary to determine the tolerance of a specific species to different water stresses.

This Chapter presents results from a series of laboratory experiments designed to study the effect of different water table regimes on the root biomass development of *Salix* cuttings at their early stage of growth. The root biomass distribution was compared to the analytical root profile obtained using the model of Tron et al. (2014). A series of pullout experiments were then performed to test whether or not the vertical distribution of the below-ground biomass had a crucial influence on root resistance during the early growth stages (e.g. when cuttings are prone to uprooting). Proper analysis of the establishment of riparian vegetation along river corridors is essential in order to predict the impact of those anthropic disturbances on the river morphology. Thus, a general understanding of the ability of *Salix* cuttings to thrive under shifting hydrological conditions becomes essential for river restoration plans aimed at minimizing the effects of flow regulation actions on groundwater-dependent ecosystems while meeting their functional requirements. Furthermore, the results obtained from these experiments have opened the possibility of using this species as a prototype plant for investigations into plant uprooting by flow.

2.2 Experimental procedure and set up

Three laboratory experiments were undertaken to test the growth response of the below-ground biomass of *Salix* cuttings to different hydrological treatments.

2.2.1 Plant species selection

The samples used in these experiments were harvested from a single tree located on the riverbanks of the Braid Burn, close to the King's Building campus in Edinburgh. The species of the tree were identified as a *Salix fragilis* or more commonly "crack willow". *Salix fragilis* is a perennial plant native to Europe and Western Asia and it is one of Britain's largest native willows. This species colonizes floodplain islands and river bars and riverbanks (Wardle, 1991) and has been widely used to reduce hillslope failure along rivers and mitigate flooding risk (Lester et al., 1994). *Salix fragilis* was chosen for its well-known ability to reproduce from cuttings or broken branches (Howell et al., 1994). Depending on geographical location, other choices are possible. For instance, along the River Thur (Switzerland), the two main species studied are *Salix viminalis* and *Salix Alba* (Gorla et al., 2015; Pasquale et al., 2012), both of which are predominantly spread along the riverbanks and bars of the river.

2.2.2 Cutting recruitment and collection

Cutting acquisition was carried out following guidelines provided by Dirr (1987). Cuttings were selected from tree branch sections that appeared to be roughly at the same stage of development and in a satisfactory state of health and vigor. Branches with flower buds were not considered because they may have grown in preceding seasons. Moreover, only branches that exhibited several buds were selected to ensure successful sprouting. Cuttings, once recruited, were cut into target lengths and then placed into buckets and watered until roots grew about 1 mm long. This practice made it possible to identify, in time, which samples did not produce any roots and would not have been statistically significant in terms of the aim of the experiments.

2.2.3 Cutting planting and extraction

Cuttings were randomly assigned to rhizoboxes and planted vertically at different burial depths. At the time of planting, the soil was dry. Hence, the soil was moistened once the initial water level designed for the treatment had been prescribed. To vary the water table level in the sediment, rhizoboxes were designed to be permeable by placing geotextile layers at their beds. The rhizoboxes were inserted inside a bigger container filled with water, with the water level maintained at a target saturation level in the sand. Each container could hold two rhizoboxes (Figure 2.1). Given the limited size of the rhizoboxes (24 cm x 24 cm in plan, 30 cm deep), only one cutting was planted in each rhizobox to avoid root interactions among the samples.

The soil consisted of a 25 cm layer of washed mineral sand with a mean grain size of $\sim$ 1 mm (see Figure 2.2). This type of sediment was chosen due to its similarity with size classes typically found on riverbanks and bars, and which are particularly favourable for maintaining moisture. The sand used was chemically inert and did not contain any organic material. Cuttings were not treated with nutrient, and so the water was the leading variable influencing plant biomass evolution. Under these circumstances, growth was limited by the internal resources of the plants. The samples grew in an environment with an average ambient temperature of 24°C and maximal diurnal fluctuation of about 4°C.

The above-ground biomass evolution and the state of health of the plants were monitored. The combined length of the stems was measured on average three times per week; here the length of the stems does not include the length of the cutting, but only the length of the branches.

Once each experiment ended, most of the cuttings were removed manually from the soil, with some others uprooted by a pulling mechanism used to test

rooting resistance. Once extracted from the soil, the cuttings were washed in water to remove sand grains.

To obtain the vertical root biomass configuration within the soil, the position of each root was recorded using the following procedure. First, each root was assigned to a depth class determined along the depth axis, taking the soil surface as a reference point. The magnitude of each class interval was set to 2.5 cm, except for the classes just below the soil surface and at the bottom of the rhizobox, each of which were 1.25 cm wide. The interval value of 2.5 cm was convenient for detecting the depth of any roots that grew deeper than the cutting to the bottom of the rhizobox. Roots were scanned at an image resolution of 600 dpi and the root surface area computed using an image analysis system (WinRHIZO BASIC 2009, Régent Instruments Canada, Inc.).

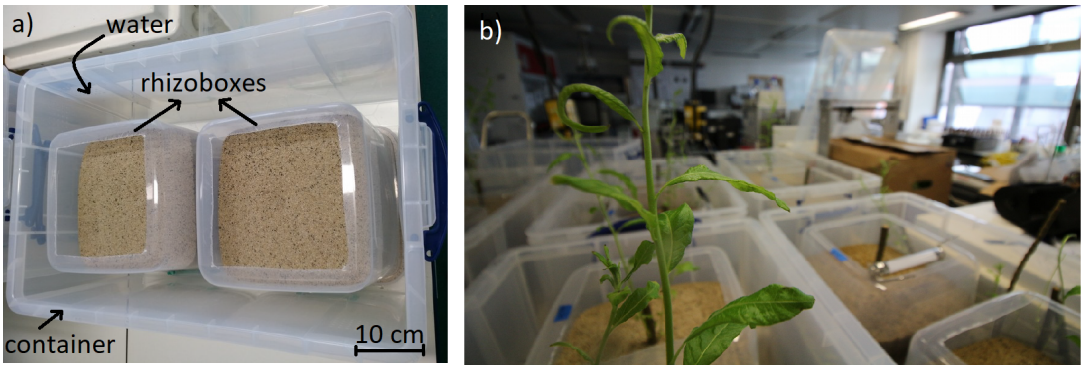

Figure 2.1: Rhizobox experiments: a) experimental setup; b) focus on a full-grown cutting. From the background, it can be seen that each cutting is planted at the center of its rhizobox.

2.2.4 Water level regime

Three experiments were conducted for five different treatments (A, B, C, D, and E) each of them with two water regimes: low and high. The samples used had lengths equal to 10, 15, and 30 cm, with mean diameter, $\bar{d} = 1.27$ cm and

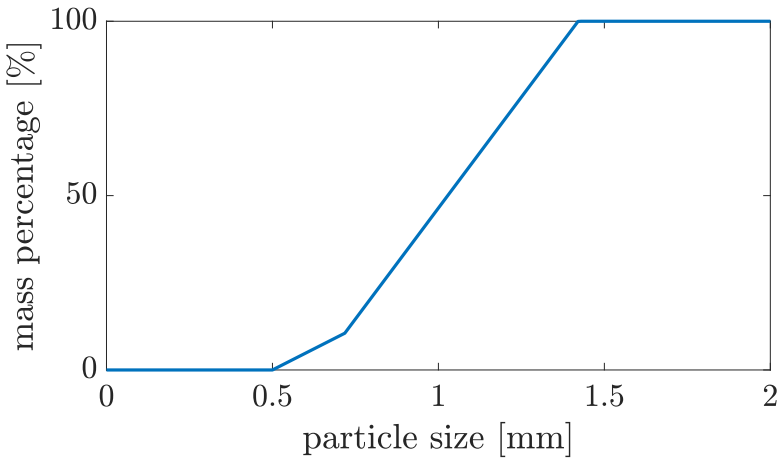

Figure 2.2: Sediment size cumulative distribution for washed mineral sand.

standard deviation, $\sigma_L = 0.18$ cm. Table 2.1 lists the treatment parameters, and Figure 2.3 shows the controlled evolutions in water table level applied for the different treatments.

The use of different water table regimes allows to study the roots' response to variations of the water and oxygen availability in the soil. Given the ability of the phreatophytic roots to redistribute and adjust to lowered water table depths, the use of different rates of water table decline enables to analyse whether, and to what extent, it is possible to guide the root biomass concentration at low depths. Contrarily, adopting high water table conditions allows to recreate the opposite scenario: maintaining the root density near the soil surface. Deep and shallow roots exemplify different root strategies to cope with a lack of water and oxygen in the soil, respectively. These scenarios have already been observed in field experiments (e.g. Pasquale et al., 2012), but it is essential to reproduce them at the laboratory scale, where the water table regime can be monitored. Furthermore, the possibility of reproducing different root biomass configurations at a small-scale would lead to advances in the development of flume erosion experiments aimed at investigating flow-induced plant uprooting.

Table 2.1: Size, growth duration, burial depth (z_c), and number of samples utilized in the different water level treatments.

exp	Treatment	sample size [cm]	growth time [days]	z_c [cm]	number of samples
1^{st}	A	10, 15	30	7, 10	30
1^{st}	B	10, 15	18	7, 10	30
2^{nd}	C	10, 15	36	5	30
2^{nd}	D	10	49	5	30
3^{rd}	E	30	62	25	20

The first two experiments were run using samples with shallow burial depth (5 cm, 7 cm, and 10 cm). The third experiment was undertaken using cuttings that had burial depth equal to sediment depth: 25 cm. The low water table scenarios were designed according to the burial depth of the samples. For low values of z_c, the water level was progressively lowered to a steady-state condition. Hence, different water level control operations were implemented to prevent drought conditions occurring during the very first days of growth. A different approach was used for Treatment E. In this case, cuttings were planted to the bottom of the rhizobox, and so were less likely to suffer adversely from a steady low water level regime.

The first experiment tested 60 cuttings, of which 30 received Treatment A and 30 received Treatment B. In A, the samples were subjected to a progressive decline in water level at a rate of 0.75 cm day^{-1} until the 26^{th} day, after which the level was kept constant at 5.5 cm. On the base of the root biomass allocation obtained from Treatment A, the following water decline rates were adjusted to reach the proposed aim. In B, the water level was lowered using larger steps of equal magnitude (5 cm) albeit at different frequencies. Turning to the high water level scenario: in A, water was lowered gradually to 22 cm, whereas in B the level was kept constant (20 cm) throughout the duration of the experiment.

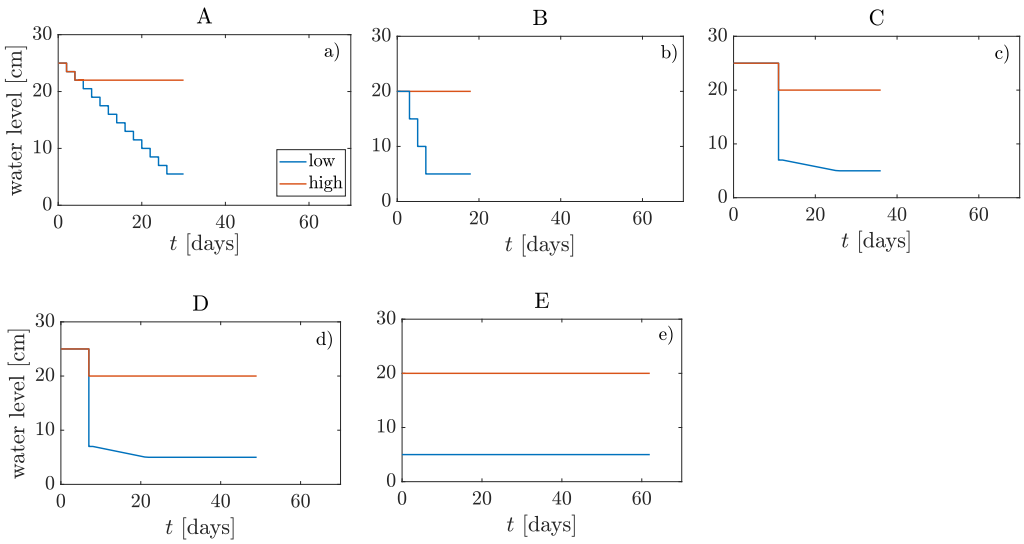

Figure 2.3: Time-histories of water level control operations for each treatment. Both low and high water table scenarios are displayed for: a) Treatment A; b) Treatment B; c) Treatment C; d) Treatment D; and e) Treatment E.

In the second experiment, 60 cuttings were tested: 30 samples subjected to Treatment C and the remainder to Treatment D. Treatments C and D have similar water level regimes. In tests involving low water table conditions, the water level was abruptly lowered by 18 cm on the 11^{th} day in C and on the 7^{th} day in D. In both treatments, steady-state conditions became established after a gradual decline in water level. In high water level scenarios, the levels were dropped to 20 cm synchronously with the respective low water regimes.

In the third experiments, 20 samples were tested. Due to laboratory space limitations at Edinburgh, it was not possible to maintain the same number of samples as in both the first and second experiments. The cuttings tested in E were 30 cm long and buried throughout the whole depth of the sediment layer. Prescribed water levels were maintained constant throughout the experiment: 5 cm for the low water regime, and 20 cm for the high water regime.

2.2.5 Soil moisture regime

Water level variation in the container caused changes to the soil's moisture content, which depends primarily on the texture of the ground material. As expected for fine-grained material, a high rate of capillary rinse was observed. More specifically, the capillary rise led to a capillary fringe of 6 cm and occupied a transition zone, indicated as L_g, of length about 12 cm (Figure 2.4). Whereas the capillary fringe comprises a nearly-saturated zone above the water table (De Marsily, 1986), the transition zone is formed by an unsaturated layer located above the capillary fringe. Here, L_g is considered to be the optimal zone of root water uptake (Loheide et al., 2005; Tron et al., 2014). This is explained by the fact that this layer is located neither very close to the water table, where roots may die of anoxia, nor too far from the water table, where water from the capillary fringe cannot rise further (Naumburg et al., 2005; Orellana et al., 2012).

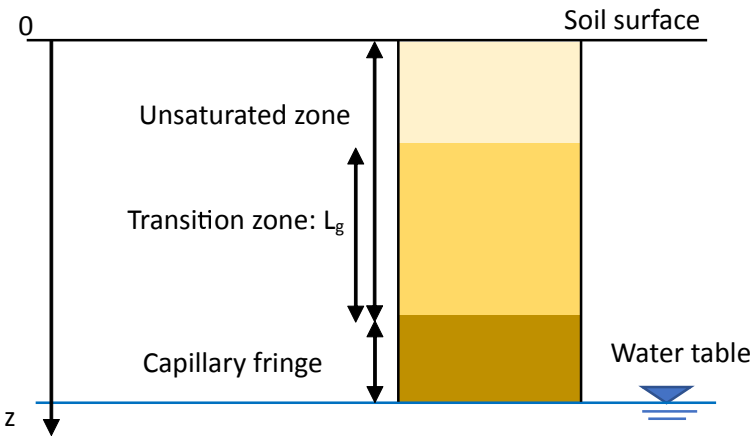

Figure 2.4: Definition sketch of different soil zones occupying the space between the soil surface and the water table. Note that the z-axis is directed vertically downward, with the origin coinciding with the soil surface.

It is well-established that the soil moisture regime plays an important role in roots growth, especially during the initial establishment phase of the plant (Li

et al., 2004; Pezeshki et al., 1998). Therefore, a wide variation in soil moisture regime was selected to test the response of root biomass allocation and the rate at which the roots adjusted their morphology to the newest condition.

2.2.6 Pullout procedures and materials

The pullout mechanism used to extract the samples comprised a motorized pulley system similar to that of Edmaier et al. (2014) (Figure 2.5). Pullout tests were performed on 40 random samples, 24 of which were subjected to Treatment A, and the remaining 16 to Treatment E. Pullout tests were carried out for low and high water level scenarios, except for cuttings with deep burial depths, which were also tested in soil saturated conditions.

Figure 2.5b shows the plant-wire connection system that was designed to apply direct traction. Cuttings were clipped to a double loop nylon wire. The loops were tied using two drawing pins that had been pierced into lateral surfaces of the cutting before planting to avoid disturbing the anchorage of the plant. Cuttings were pulled up at a constant vertical speed of 1.71 mm/s by a computer-controlled motor-encoder (EPOS), which enabled force fluctuations induced by the root system to be recorded. Cuttings were pulled-out mechanically as shown in Figure 2.5a. The vertical uprooting force was recorded at 100 Hz by piezoelectric force sensors (Kistler) with force ranges of $\pm$50 N and $\pm$100 N. The output load cell charge was then routed directly to an external charge amplifier (Kistler) that produced an output voltage signal proportional to the mechanical force.

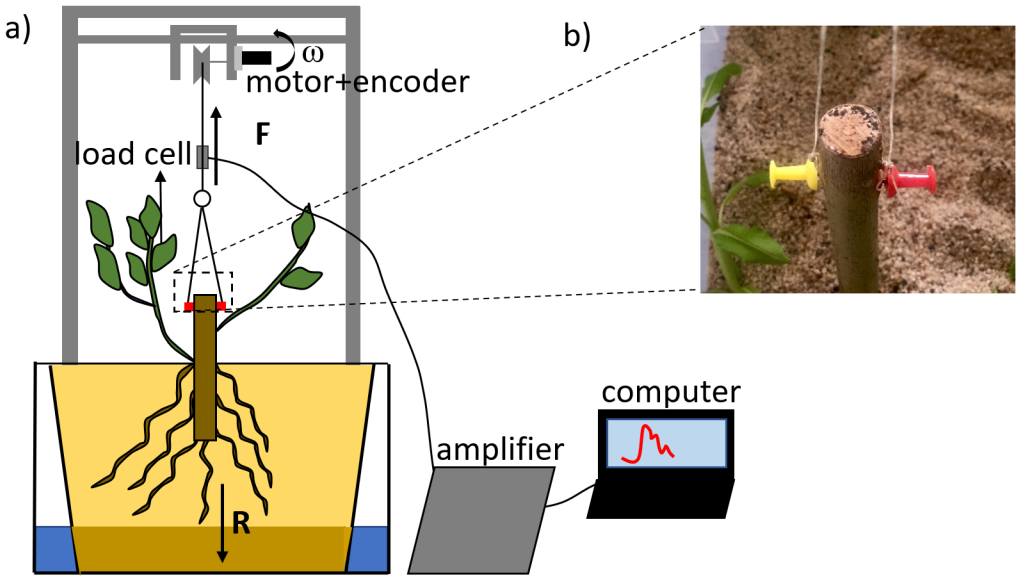

Figure 2.5: Schematic of the pullout experiment. a) Motorized pulley system whereby the cutting is uprooted by an external force applied by a motor whose rotation was measured by an encoder. The exerted force **F** was continuously recorded by a load cell attached to an amplifier that, in turn, was connected to the computer. The modulus of **F** is equal to the anchoring resistance expressed by the vector **R** developed by the root system; b) Photograph showing detail of the plant-wire connection system.

2.3 Results: below-ground biomass

Distributions of below-ground biomass over the soil depth were represented in terms of mean values that were computed according to the amount of biomass contained in each depth class for plants of equal burial depth. Here, the averaged value of biomass is defined by $\bar{A}_r$, the mean surface area of the roots.

An analysis of variance was used to test whether there was a statistical difference within and among treatments. Statistical analysis was undertaken to compare the values of $\bar{A}_r$ at each class over the soil depth where biomass occurred. The test used in most cases was an One-way ANOVA. However, whenever the ANOVA assumptions were violated, data were further tested using a non-parametric Kruskal–Wallis test. The p-value approach to hypothesis

testing was computed with standard statistical tools embedded in Matlab and then compared to a significance level of 5%. Hence, every time the p-value is less than 5% the test proves to be statistically significant. The evolution of $\bar{A}_r$ over the soil depth is discussed for each Treatment and value of z_c.

2.3.1 Treatments A and B

The similar magnitudes of the data presented in Figures 2.6a and 2.6b indicate that neither the low or high water table regimes influenced root biomass significantly except for the 3^{th} class in Treatment B (p-value=0.03). Moreover, use of the different treatments did not affect the way the biomass developed under low and high water level scenarios. The statistical tests support this interpretation, providing p-values higher than the significance level (0.05). In both treatments, biomass is mostly concentrated between the soil surface and the first three classes. The only discernible difference is the mode of the distribution in Figure 2.6b, which reaches higher depth.

Very similar results are presented in Figures 2.7a and 2.7b, where the only noticeable difference from Figure 2.6 is that the biomass extends down to the 5^{th} class and the total root biomass is slightly higher overall. This increase in biomass occurred because the cuttings extended 3 cm deeper into the sand. The results suggest that the influence of z_c in Treatments A and B does not have any statistical effect on the root biomass (p-value > 0.05).

The high concentration of root biomass in the shallow layers of the soil may be related to the high retention capacity of the sand. The low water level control operations performed in Treatments A and B may not have ensured that the decay rate of the zone above the capillary fringe, L_g, was faster than the root growth rate. Almost surely, this may have influenced the preferred direction of growth of the roots. The occurrence of shallow roots may also be explained by

the low values for z_c in the Treatments A and B.

Similar results were obtained by Koch and Kollmann (2012), albeit for a different riparian species. The authors Koch and Kollmann (2012) also subjected cuttings with 5 and 10 cm burial depths to laboratory treatments involving low and high water level regimes. The results showed that survival and biomass production were higher for deeper cuttings, and that the variation in water level was not related statistically to the burial depth of the plant. On the other hand, laboratory experiments carried out by Francis et al. (2005) on *Salix elaeagnos* in sand showed that the root biomass was able to keep up with a water table declining at 1 cm day^{-1}. Better performance was found for the same species, which exhibited a high rate of root elongation for a water table declining at a rate of 3 cm day^{-1} over a duration of 21 days (similar to the present study). This implies that a similar water table decline can nevertheless induce different root biomass reactions for different willow species (Bouma et al., 2001) and that the nutrient supply used by Francis et al. (2005) may also have an important repercussions for biomass development.

2.3.2 Treatments C and D

The results presented in Figures 2.8a and 2.8b exhibit different vertical distributions in root biomass than in Figures 2.6 and 2.7. The fact that deeper roots are produced for a lower value of $z_c = 5$ cm, implies that the value of z_c does not have a substantially limiting effect on the ability of a plant to produce roots at higher depths.

Here, the choice of water level control strategy seems to be the primary influence factor on the development of root biomass. The low and high water level regimes in C do not have a remarkable influence on the biomass distribution, except for the first class (p-value = 0.006).

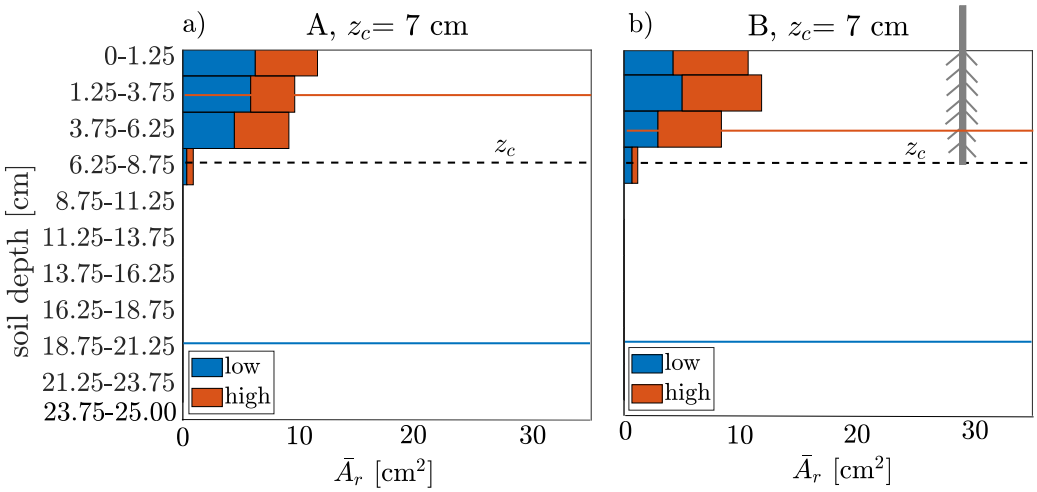

Figure 2.6: Vertical root biomass distribution at each depth class for high and low water table regimes and z_c = 7 cm: a) Treatment A; and b) Treatment B. Orange and blue lines indicate the high and low water levels reached during the last day of treatment. The dashed black line indicates the burial depth of the cutting. Note that the sketch of the cutting is representative for both treatments and that the roots are included solely for illustrative purposes.

This is not the case for Treatment D, where, apart from the first and second classes, the biomass obtained for the low water regime is statistically different from that obtained for the high water regime. The low water level regimes of both treatments have led to a similar root biomass configuration (p-value > 0.05). However, the same does not apply for the high water level regimes. Root biomass has shallower structure when the high water table is maintained at a steady-state level for longer time (see Figure 2.3d). Thus, in light of the similarity between the high water regimes in C and D, the duration of the experiment may have been responsible for the two different biomass distributions.

From Figure 2.8b it is also clear that the high and low water level regimes induce mild oxytropic and hydrotropic responses of the root systems, respectively.

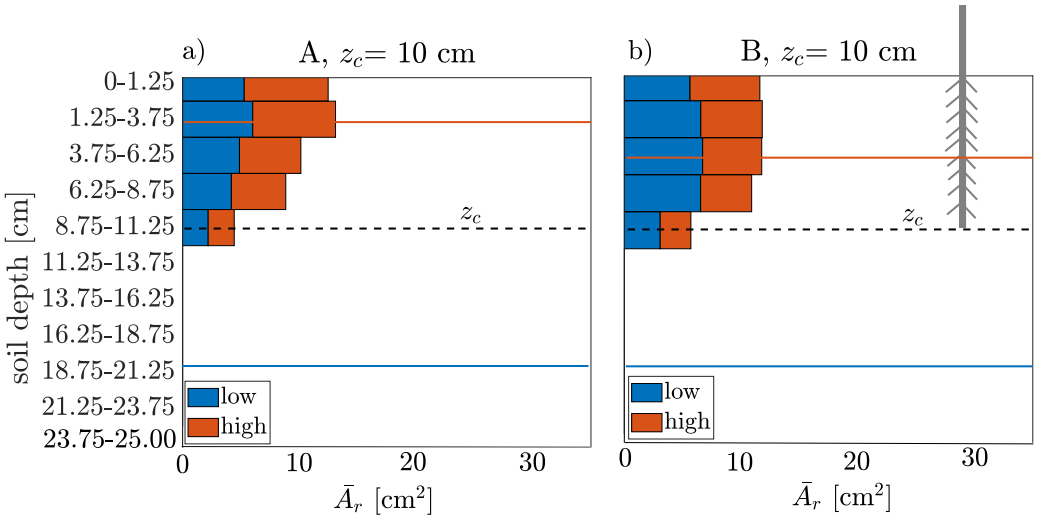

Figure 2.7: Vertical root biomass distribution at each depth class for high and low water table regimes and z_c = 10 cm: a) Treatment A; and b) Treatment B. Orange and blue lines indicate the high and low water levels reached during the last day of treatment. The dashed black line indicates the burial depth of the cutting. Note that the sketch of the cutting is representative for both treatments and that the roots are included solely for illustrative purposes.

Pasquale et al. (2012) observed similar root growth behaviour, with of a shallow root system providing evidence of oxytropism. This behaviour occurred most frequently in cuttings subject to regular inundation. Samples grown in less moist soils exhibited the opposite trend in behaviour. Extension of the duration of the experiment with Treatment D would therefore have probably led to a much more distinctive root tropic response to oxygen and water.

The outputs of Treatments A, B, C and D present opposite behaviour compared to the results obtained by Amlin and Rood (2002), who found that an abrupt decline of the water table had a significant impact on the survival rate of willow cuttings, whereas a gradual decline in water table (between 1 to 2 cm day^{-1}) led to depth-wise elongation of the roots. Such discrepancies may be explained by differences in duration of the experiment, and thickness and

composition of the sediment layer. In the experiments carried out by Amlin and Rood (2002), the duration was longer, and the sediment was about 100 cm deep and contained a percentage of coarse gravel that, almost certainly, had an effect given the reduction in retention capacity.

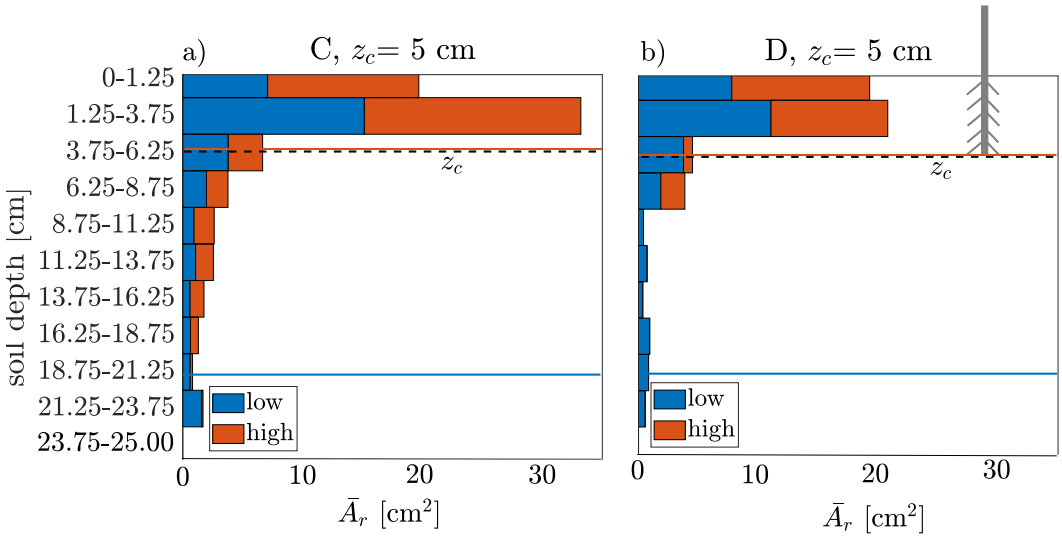

Figure 2.8: Vertical root biomass distribution at each depth class for high and low water table regimes and z_c = 5 cm: a) Treatment C; and b) Treatment D. Orange and blue lines indicate the high and low water levels reached during the last day of treatment. The dashed black line indicates the burial depth of the cutting. Note that the sketch of the cutting is representative for both treatments and that the roots are included solely for illustrative purposes

2.3.3 Treatment E

Hydrotropic and oxytropic behaviour of the root system is particularly evident in Figure 2.9. A steady-state low water level induced high concentration of root biomass towards the lowest depth classes. The converse occurred by maintaining a constant high water level over the entire duration of the experiment. The samples shown in Figures 2.9b1 and 2.9b2 can be considered as representative of the two root biomass configurations.

Both samples also exhibit a similar quantity of root biomass in the middle of the cuttings length, exactly where the two different biomass trends switch. The results of the statistical tests confirm this. ANOVA null hypothesis is invariably rejected, except for depth ranges between 6.25 cm and 13.75 cm. This can be seen, for instance, in the boxplots in Figure 2.10a, where the p-value for the biomass contained in the class 11.25-13.75 cm has a value higher than 0.05. Figure 2.10b shows instead that in the following class, 13.75-16.25 cm, the p-value is much lower than the significance level.

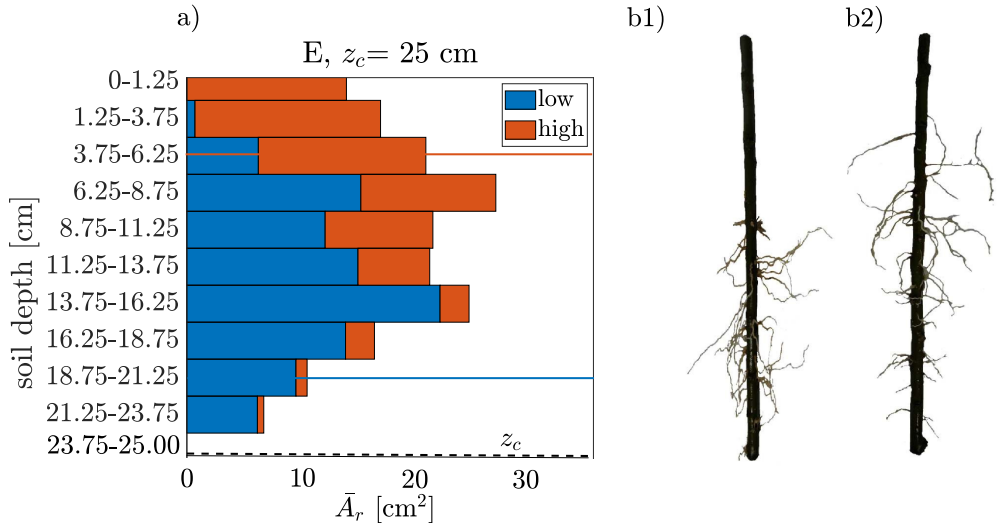

Figure 2.9: Vertical root biomass at each depth class for high and low water table regimes and $z_c = 25$ cm: a) root biomass distribution for roots grown under Treatment E; b1) sample of cutting grown in low water table regime; and b2) sample of cutting grown in high water table regime. Orange and blue lines indicate the high and low water levels reached during the last day of treatment. The dashed black line indicates the burial depth of the cutting.

The biomass distribution obtained for Treatment E is similar to that of Gorla et al. (2015), who found that the root volume of (juvenile *Salix viminalis*) cuttings developed a second mode at high depth values owing to the minimum

flow regime.

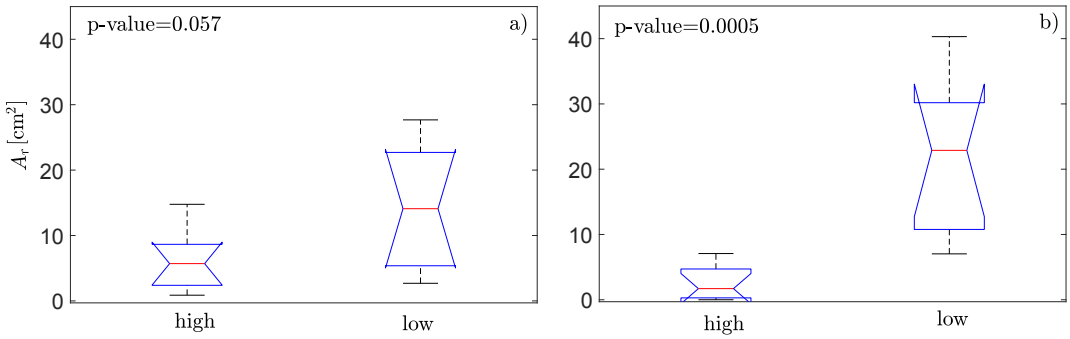

Figure 2.10: Boxplots obtained from the Analysis of Variance of the root surface area for biomass occurring between: a) 11.25 and 13.75 cm; and b) 13.75 and 16.25 cm. 'high' and 'low' stand for high and low water table regimes, respectively.

Such a trend was even more marked in (*Salix alba*) cuttings tested in the field campaign carried out by Pasquale et al. (2012). In this case, cuttings that had grown at higher elevation on the river bar, hence relatively far from the water table, exhibited high root densities at the lowermost part of the stem.

At the light of these results, it becomes clear how cuttings themselves act as primary roots. The deeper the primary root, the greater the likelihood that the plant would produce secondary roots. This explains why the potential occurrence of roots was higher in cuttings of greater burial depth. Even though the root depths in Treatments C and D were higher than those obtained in Treatments A and B, the plant shooting capacity can be still considered almost zero at depths higher than z_c.

A longer duration of the second experiment could have likely induced a root biomass configuration similar to that of Treatment E. However, it is not yet known whether the internal resources of smaller cuttings would have been sufficient to ensure the same rate of root biomass production over longer growth periods. Further experiments are needed to resolve these open questions.

The small timescales considered in the present experiments have revealed the ability of the plants to cope with different soil water conditions during the growth phase (that is most impactful on their establishment and flood survivability). Subjecting cuttings to steady low water level regimes appears not to be detrimental to the health of *Salix fragilis* and has highlighted the important role played by the retention capacity of fine sediment.

The results obtained provide evidence that burial depth and water table configuration influence root distribution in sandy soils. However, the behaviour may be different for other species and even within the same species when reproduced through seedling procedures and under different environmental conditions. These results have also confirmed that the shape of the root biomass of *Salix* cuttings can reveal the availability of oxygen and water in the soil.

2.4 Results: above-ground biomass

Above-ground biomass is represented in terms of the averaged value of the combined length of the stems, $\bar{L}_s$. The average was computed at a set (constant) time for all samples with equal exposed lengths, h_e, and that were subjected to the same water level regimes and treatments.

Growth trends of the above-ground biomass were fitted by logistic curves, which describe the growth of the plant limited by carrying capacity that is represented in the present case by the internal nutrient reserves of the cutting (Hsu et al., 1984; Schimpf et al., 1977). It is important to mention that the logistic law can be considered a reasonable approximation up to a certain stage of plant growth. Due to lack of nutrients, plants undergo resource depletion, during which stage they will start progressively decaying. Given that the aim is to investigate plant properties at the early-stage of growth, the logistic curve provides a representative law for the averaged growth of the stems until all the

resources of the cuttings have been depleted. The logistic curve for $\bar{L}_s(t)$ reads:

$$\bar{L}_s(t) = \frac{c}{1 + e^{-k_l(t-t_0)}} \tag{2.1}$$

where c is the maximum value of the curve, which coincides with the averaged total stem length recorded during the last day of growth, k_l is the logistic growth rate, and t_0 is the location of the midpoint of the sigmoid.

Table 2.2 lists the coefficients k_l and t_0 obtained for each curve.

From the panels in Figure 2.11 it can be seen that there are no substantial differences for the various treatments, except in certain cases where the samples subjected to low water regimes developed longer stems than those under high water regimes. Such situations only occurred for Treatment B when the exposed length was 3 cm, in D, and imperceptibly for Treatment A when the exposed length was 5 cm.

Initially, it may be assumed that high water level regimes can be less favourable to the development of above-ground biomass. However, the opposite behaviour can be identified in Treatment A, when $h_e = 5$ cm, Treatment C and Treatment E. In C, the higher values of $\bar{L}_s$ obtained for high water conditions follow from the exposed length of the tested samples being twice that of samples subjected to low water conditions. On the other hand, in E, the low water conditions may be "too" low to guarantee the same growth rate as that observed for the high water regime. Furthermore, it is evident that, due to the lowest duration of Treatment B, the maximum length of the stems does not represent the carrying capacity of the logistic models, unlike the other cases.

From Table 2.2 it can be seen that the growth rates and the sigmoid midpoints have quite similar values, especially the values of Treatments B and C. The situation is different for Treatment E, where k_l and t_0 have lower and higher values, respectively, compared to the other experiments. This suggests that for plants with large burial depth, the availability of resources expended on stem production is higher than those for shallow burial depths.

Table 2.2: Values assigned to logistic curve parameters, k_l and t_0, for different values of exposed length, h_e, and different water table regime and treatments.

treatment	h_e [cm]	water level regime	k_l	t_0 [days]
A	5	low	0.37	14
		high	0.35	12
	3	low	0.35	15
		high	0.35	15
B	5	low	0.23	14
		high	0.24	14
	3	low	0.25	13
		high	0.25	16
C	5	low	0.24	16
	10	high	0.24	16
D	5	low	0.20	16
	5	high	0.20	16
E	5	low	0.13	23
	5	high	0.13	27

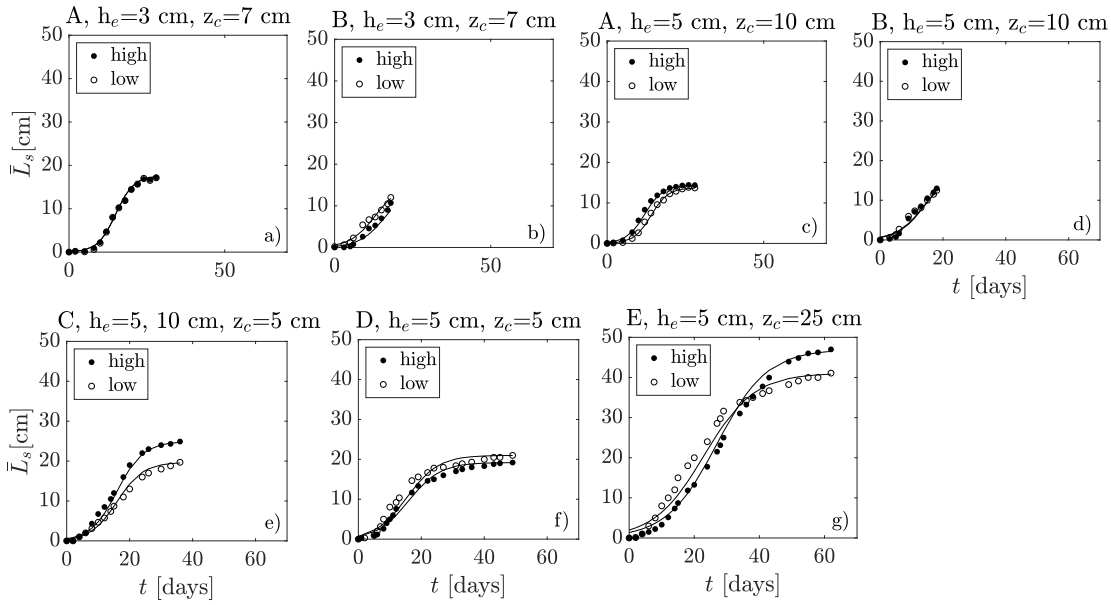

Figure 2.11: Trends in total average stem length, $\bar{L}_s$, for low and high water regimes and for cuttings grown in: a) Treatment A, with $z_c = 3$ cm; b) Treatment B, with $z_c = 3$ cm; c) Treatment A, with $z_c = 5$ cm; d) Treatment B, with $z_c = 5$ cm; e) Treatment C, with $z_c = 10$ and 5 cm; f) Treatment D, with $z_c = 5$ cm; and g) Treatment E, with $z_c = 5$ cm.

2.5 Model-based predictions of vertical root profile

The experimental results presented in the previous section are now compared against theoretical results obtained using the model of Tron et al. (2014). This model is a simple, elegant model that enables predicting, in an analytical manner, the root distribution of phreatophytic vegetation.

The model assumes that roots potentially grow within the zone h_2, which is the maximum distance between the soil surface and the water table depth z_w (Figure 2.12), below which root growth is hindered by anoxic conditions. Root growth is particularly favoured in the so-called 'optimal root-growth zone', L_g, whose water availability is ensured through capillary rise.

This zone, whose thickness is controlled by D_{10} and D_{90} of the sediment, is located a distance $(h_2 - h_1)$ above the water table (see Figure 2.12). The zone L_g, fluctuates according to stochastic oscillation of the groundwater dynamics (Figure 2.12) described as a Compound Poisson Process (Figure 2.13a). Hence, Tron et al. (2014) assumed that the water table moves almost synchronously with the river water stage.

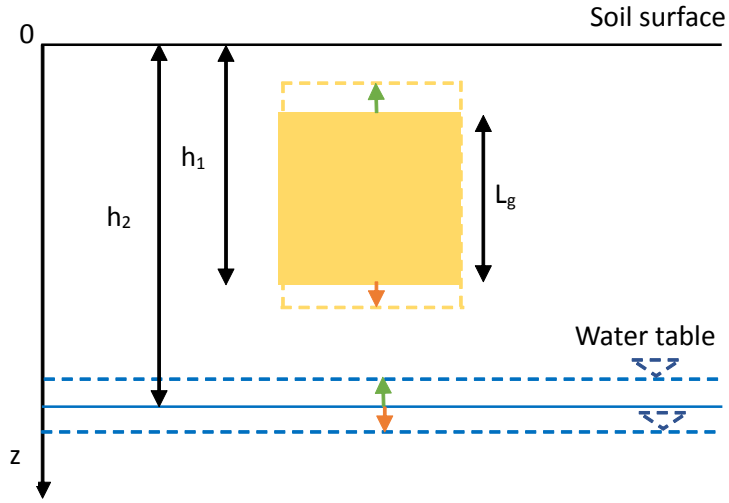

Figure 2.12: Sketch depicting synchronous fluctuations in groundwater level and the L_g zone. Oscillations are indicated by dashed lines: rising in green, lowering in orange.

The Compound Poisson Process (CPP) is a powerful concept that is widely used to represent stochastic systems. CPP is characterized by a sequence of randomly distributed instantaneous jumps and deterministic decays. In the literature, CPP has been used to describe soil moisture dynamics (Rodriguez-Iturbe et al., 1999), snowfall processes (Perona et al., 2007), flood events induced by heavy rainfalls (Todorovic, 1978), and ecomorphodynamics processes (Bertagni et al., 2018; Calvani et al., 2019b). In the present application, the stochastic dynamics of the water table level, z_w, may be expressed:

$$\frac{dz_w}{dt} = \eta_l(h_2 - z_w) - \zeta \tag{2.2}$$

where η_l is the rate of exponential decay in water level signal (Ridolfi et al.,

2011) and ζ is white shot noise. From equation 2.2 it is possible to derive analytically the steady-state probability density function of the water table level (Figure 2.13b) as:

$$p(z_w) = \frac{\gamma_l^{-\beta_l}}{\Gamma[\beta_l]} e^{\frac{z_w - h_2}{\gamma_l}} (h_2 - z_w)^{\beta_l - 1} \tag{2.3}$$

where $\Gamma[\cdot]$ is the Gamma function (Abramowitz and Stegun, 1948), γ_l the mean depth of pulses in water level, and β_l is the ratio between the mean rate of the pulses, λ_l, and η_l.

A more detailed explanation of the Compound Poisson Process and the mathematical derivation of equation 2.3 are available in Appendix A.

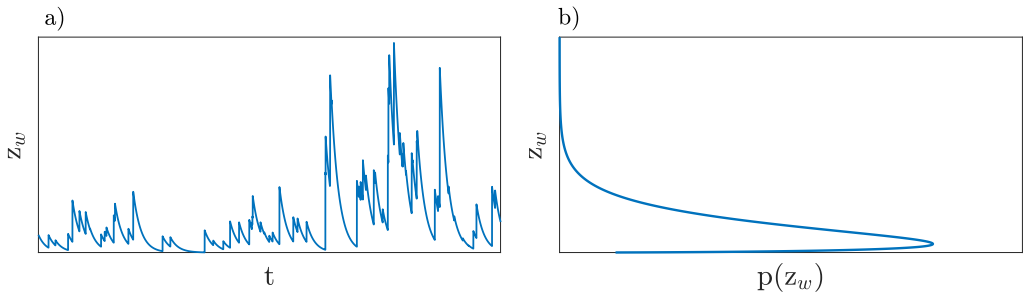

Figure 2.13: Stochastic dynamics of groundwater level: a) simulated Compound Poisson Process for water table level, z_w; and b) probability density function of water table level, $p(z_w)$.

Dynamic behaviour of root growth and decay in L_g is modelled using dichotomous noise (Ridolfi et al., 2011), as this type of noise is commonly used to describe the dynamics of systems that randomly switch between two states (e.g. root growth and decay). The equation representing root dynamics is (for analytical derivation, refer to Tron et al., 2014):

$$r(z) = \frac{2\theta(z)k(z)}{\theta(z) + \theta(z)k(z) + 1 - k(z)}, \tag{2.4}$$

where $\theta(z)$ is the ratio between root growth rate and decay rate, and accounts for root growth being easier over the cutting length and more difficult below it.

$\theta(z)$ is assumed to vary linearly from 1 at the soil surface to 0 at the maximum root depth. The function $k(z)$ expresses the probability that a generic depth, z, is located in the optimal root-growth zone. Hence, when a depth z is located in L_g, root development is enhanced; if z located outside L_g, the roots tend to die of dryness or anoxia. It is assumed that $k(z)$ may be expressed in the following piecewise equation:

$$k(z) = \begin{cases} \left[\Gamma\left(\beta_l, \frac{h_1 - z - L}{\gamma_l}\right) - \Gamma\left(\beta_l, \frac{h_1 - z}{\gamma_l}\right)\right] \cdot \Gamma(\beta_l)^{-1} & -\infty < z < h_1 - L_g \\ \\ 1 - \Gamma\left(\beta_l, \frac{h_1 - z}{\gamma_l}\right) \cdot \Gamma(\beta_l)^{-1} & h_1 - L_g < z < h_1 \end{cases} \tag{2.5}$$

Equation 2.4 was implemented for each scenario analysed in Section 2.3. However, it was found that the analytical expression in equation 2.4 was hardly ever representative of the empirical root distribution observed in the experiments for most of the treatments. The two main reasons for this are discussed below.

The model does not provide for the probability of occurrence of root biomass below the water table. Hence, the experiments could not reproduce the root profiles developed under high water table regimes; this was because the model predicted that the concentration of the whole root biomass occurred in the zone between the soil surface and the water table level. Furthermore, unsteadiness of the water level regimes used in most of the experiments did not comply well with the model assumptions. The biomass distribution was only properly approximated for the samples grown under Treatments A and E (Figure 2.14). Although, unlike Treatment E, the low water level regime in A was not steady, the constant depth and frequency of water decline of Treatment A made it possible to obtain representative values for γ_l and λ_l (Figure 2.14b). Therefore, unsteady water regimes, in some cases, could be approximated by equivalent steady ones by computing temporally-weighted averages for the jumping rate and mean pulse intensities. From Figure 2.14a, it may be discerned that the

root distribution of Treatment E is satisfactorily estimated down to the 8^{th} class, within the unsaturated zone above the water table. The model cannot capture the root biomass in the last two depth classes. This means that, from a stochastic point of view, the probability of biomass occurring in the saturated condition is in fact zero.

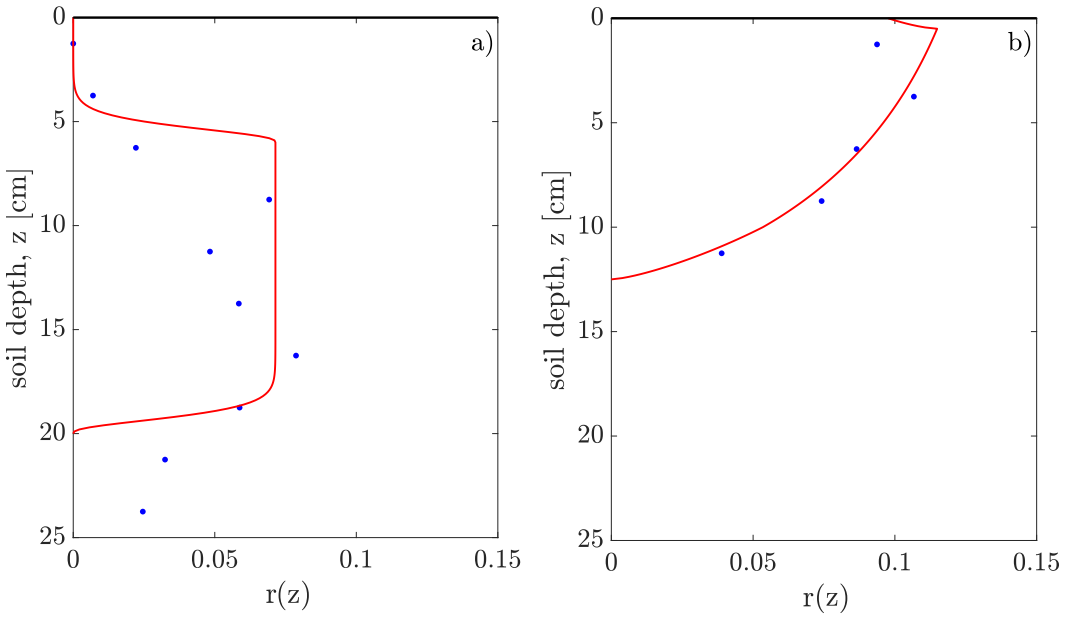

Figure 2.14: Normalized measured (blue dots) and modelled (red lines) root profiles for the low water regime of a) Treatment E and b) Treatment A with z_c=10 cm.

Hence, the model assumptions make it rather difficult for the model of Tron et al. (2014) to simulate reliably experiments that are limited to high water table scenarios, and to reproduce water level regimes that cannot be modelled by a CPP. The results presented in this section explore scenarios and conditions that have not been tested before by the model of Tron et al., 2014.

The present parameter study helps shed light on the predictive power of the model as well as on its limitations when applied to circumstances where the model assumptions are violated.

Another important consideration concerns the growth stage of the vegetation.

It is not certain that the model of Tron et al. (2014) can provide reliable results when applied to vegetation that is still in the early stages of growth. So far, the model has been applied solely to mature plants. For example, sample tests of vegetation along the Rhone river (see Tron et al., 2015) have presented root depths varying between 60 cm to 200 cm. Similar root depths have also been found among plants tested from the Isère and Noce rivers by Serlet (2018). If the willow cuttings had been grown for a longer period, the development of the roots would have been hindered by the lack of space, and the plants would have possibly died for soil anoxia. Hence, in order to apply the model of Tron et al. (2014) to small-scale experiments, it is necessary to set appropriate conditions with respect to the water regime.

2.6 Pullout tests

The values of the burial depths and the different water table regimes set at the start of the experiments appear to indicate that Treatments A and E are the most relevant for studying uprooting resistance. The values of z_c are very different in the two treatments, as well as the low water table control operations. Hence, the aim of the pullout experiments considered in this thesis is to give insight into the impact that burial depth, root biomass distribution, and soil moisture content have on uprooting resistance.

With this in mind, samples from Treatment A were tested under the low and high water level conditions set during the last day of the experiment: 5.5 and 22 cm respectively (see Figure 2.3a). In Treatment E, the samples were further tested under saturated conditions. Consequently, just before running a pullout test, the water level was raised to the soil surface elevation regardless of the water regime used during the growth of the cuttings.

2.6.1 Force-displacement curves

The force-displacement curves represented in Figures 2.16 and 2.17 show the variation in pullout force with vertical displacement of the plants. The labels used in Figures 2.16 and 2.17 indicate the moisture condition of the soil during the pullout tests as follows: *low* stands for low water level and *high* stands for the high water level, encountered at the last day of the experiments, whereas low_{sat} and $high_{sat}$ are their saturated counterparts.

Generally, in the force-displacement curves, three main phases in the process can be identified (Figure 2.15) in accordance with previous findings by other authors (Edmaier et al., 2011; Ennos, 1989). The first phase is the non-linear elastic phase, during which the force increases non-linearly with elastic recovery. This phase coincides with root stretching, when part of the friction between roots and soil is activated (Schwarz et al., 2010a). The second phase, in which all roots are activated, presents linear elastic behaviour until maximum uprooting resistance, F_p, is achieved, corresponding to the highest value of tensile force that the root system can withstand. The third phase is the descending process, where the force decline occurs as a sequence of drops and partial elastic recoveries until uprooting is entirely achieved. Such fluctuations may be explained by a mechanism of progressive load and energy redistribution among roots, which will be thoroughly analysed for the experiments shown in Chapter 4.

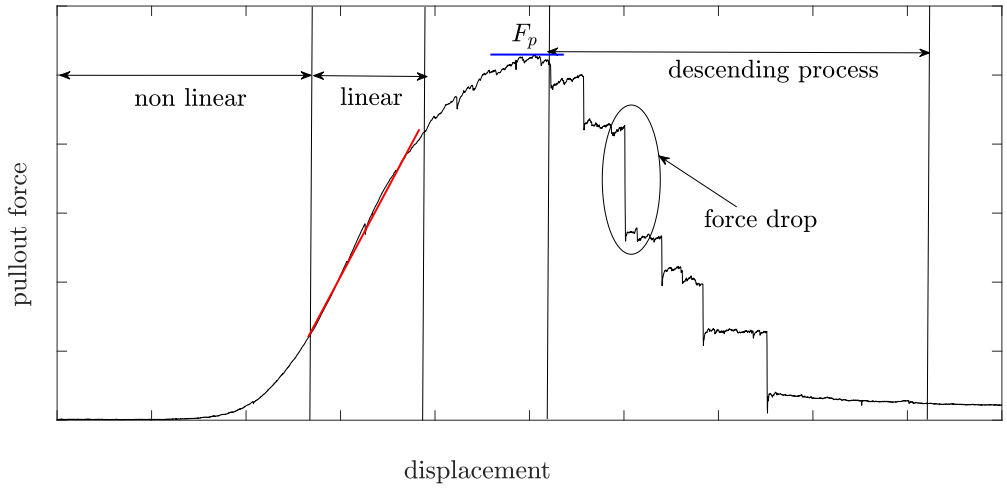

Figure 2.15: Illustration of the different phases of a generic force-displacement curve.

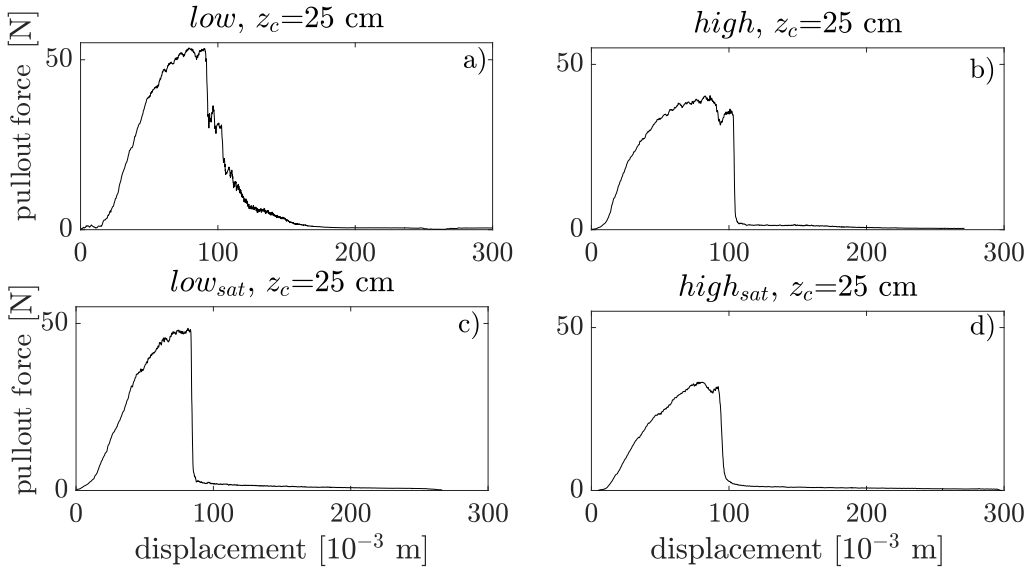

Figure 2.16: Force-displacement curves for samples from Treatment E in: a) low water level regime; b) high water level regime; c) saturated soil for low water level regime; and d) saturated soil for high water level regime.

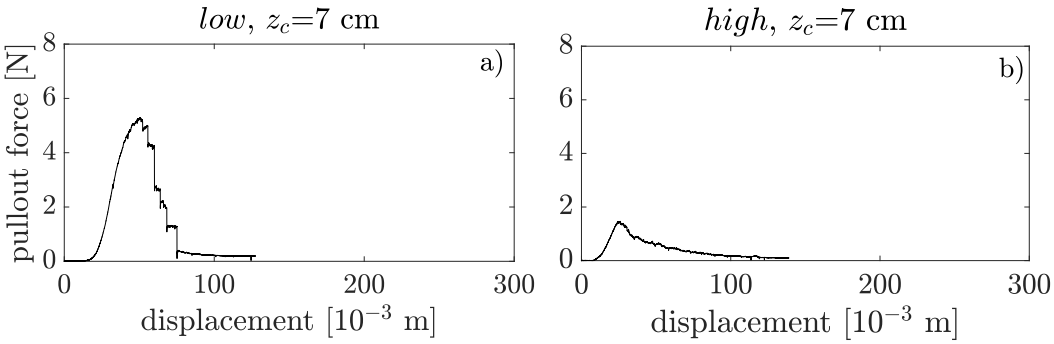

Figure 2.17: Force-displacement curves for samples from Treatment A in: a) low water level regime; and b) high water level regime.

2.6.2 Maximum uprooting force

Figures 2.18 and 2.19 illustrate how F_p varies for the different scenarios considered in each treatment. Figures 2.18a and 2.19a present the mean uprooting force, $\bar{F}_p$, obtained for Treatments E and A. Table 2.3 lists values of the mean and standard deviation of the uprooting force. Notably, the mean uprooting force recorded for cuttings grown under Treatment E are more than 10 times larger than for Treatment A. At first glance, it is apparent that burial depth, growth period, and soil moisture content have a considerable impact on uprooting resistance.

Figure 2.18a is of particular interest because it delivers substantial information on the impacts of biomass distribution and soil moisture conditions on root resistance. The uprooting resistance developed by plants grown in the low water level regime is higher than that in the high water level scenario, independent of soil saturation level and total root biomass. This implies that the root biomass distribution has a major impact on the development of the mechanical anchoring of the plant. Hence, deep roots (representative of hydrotropic conditions) provide greater resistance than shallow roots.

This finding compares well with observations from the field experiments by Pasquale (2012), who found that cuttings with deep root biomass were

less affected by flow removal than shallow root counterparts under the same hydrological conditions.

Different behaviour can be seen in Figure 2.19a. In this case (see Figure 2.6), the distribution of below-ground biomass is not statistically different between low and high water level regimes, and so the soil moisture content is the only variable that can explain the difference in the values of $\bar{F}_p$.

Figures 2.18b and 2.19b, present F_p versus total root surface area, A_r, based on measurements for each sample uprooted. The number of the samples uprooted for Treatment A (Figure 2.19b) are sufficient to establish representative fitting laws. The angular coefficients of the linear regression equations, which are 0.27 for *low* and 0.14 for *high*, prove once again that less force is needed to uproot plants in soil with higher moisture content, for the same overall values of root biomass. In Figure 2.18b, similar values of root biomass correspond to different values of pullout forces. Unfortunately, given the small number of samples, it was not possible to suggest a sensible fitting law.

The foregoing demonstrates that moist soil reduces root resistance, in accordance with similar findings by other authors (Edmaier et al., 2011; Schwarz et al., 2011). An explanation of this phenomenon is provided by Wood (1990) who argues that undrained stress in saturated soil increases pore-water pressure, causing the frictional strength of the soil to reduce. In turn, this mechanism may enhance the sliding of roots among the sediment particles.

Table 2.3: Mean and standard deviation of pullout force under Treatments A and E for different soil saturation conditions.

	Treatment E				Treatment A	
Scenarios	*low*	*high*	low_{sat}	$high_{sat}$	*low*	*high*
$\bar{F}_p$ [N]	50.58	38.16	46.07	31.54	4.53	1.98
σ_F [N]	5.85	3.72	3.24	1.68	1.53	0.74

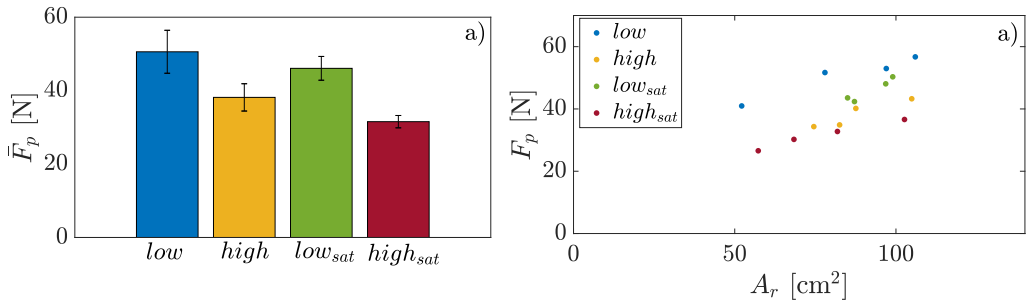

Figure 2.18: Statistics of uprooting force in Treatment E: a) bar chart showing mean uprooting force $\bar{F}_p$ and the respective standard deviation for different saturation conditions; and b) scatter plot of maximum pullout force against total surface area of roots.

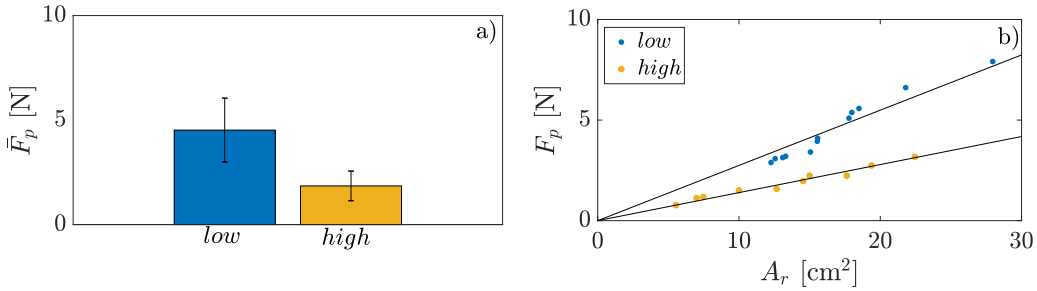

Figure 2.19: Statistics of uprooting force in Treatment A: a) bar chart showing mean uprooting force $\bar{F}_p$ and the respective standard deviation for different saturation conditions; and b) linkage between maximum pullout force and total surface area of roots. The goodness of fit, R^2, is equal to 0.9 for both *low* and *high*.

2.6.3 Roots contribution

The experiments also provided an opportunity to quantify the amount of resistance provided by the root system only. Pulling out a cutting deprived of its roots made it possible to evaluate how the force responds to the sole constraint of the plant's trunk. These tests were carried out only for long cuttings because their length should have ensured greater measurement accuracy.

The bar chart in Figure 2.20a exhibits a similar trend to its counterpart in Figure 2.18a. The force reaches a peak value at low water level conditions and decreases progressively with soil moisture content. However, despite the similarity in trends, the magnitude of $\bar{F}_p$ is lower in the absence of roots. The roots contribution leads to an increase of 46% and 81% in resistance force for cases with low and high water tables, respectively. Moreover, the saturated soil benefitted even more from the presence of the roots, with the resistance force increasing by 170% and 85% in the low_{sat} and $high_{sat}$ cases.

It is also interesting to compare the force-displacement curves obtained with and without roots. To achieve this, the trends in mean pullout force with mean displacement were determined for equal saturation conditions, and for samples with and without roots. From Figure 2.20b,c,d it seems that, for cuttings with roots, the rate of initial increase in resistance force is higher. This may be a consequence of the fact that, during the pulling process, the roots are the first component of the plant to come under tension, hence inducing a rapid increase in resistance force in the initial phase of the test. Another interesting dissimilarity can be discerned in the descending phase of the curve. For cuttings with roots, the final uprooting phase exhibits itself as sudden force drops, associated with the progressive release of roots from the soil (Bailey et al., 2002; Mickovski et al., 2007). For the case without roots present, the descending phase is rather smooth and the force decrease occurs gradually. This is to be expected, given that the contact surface between sand and cuttings decreases linearly with displacement, as does the resisting force (assuming that, at this scale, the normal stress is constant). Conversely, the descending phase for the curves obtained for samples with roots occurs rather rapidly through force drops of higher magnitude. Such discrepancy in the uprooting curve highlights the role of roots in providing additional resistance to the soil.

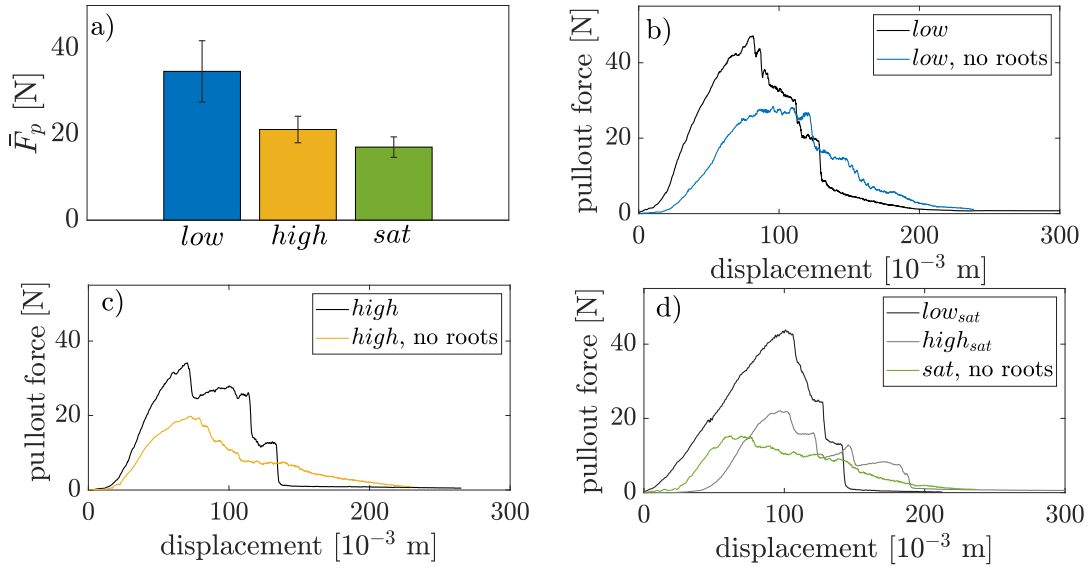

Figure 2.20: Statistical outputs from plant pullout tests with and without roots present: a) bar chart showing mean and standard deviation of resistance force of samples without roots; b) mean force-displacement curves for the low water regime, with and without roots present; c) mean force-displacement curves for high water regime, with and without roots present; and d) mean force-displacement curves obtained in soil saturated conditions, with and without roots present.

2.7 Recommendations

This study has revealed that pull out experiments are useful for assessing: the ability of plants to reinforce and provide stability to soil; and control measures for the distribution and survival of plants in an active floodplain. Furthermore, the results demonstrated the importance of water and oxygen availability as factors influencing root biomass configuration and soil moisture level content that in turn impact on plant uprooting resistance. The results obtained from Treatment E offer a useful starting point from which to design further tests at larger scale or in situ to examine the uprooting efficiency of cuttings when subjected to more variable environmental conditions. The experimental data acquired for

Salix fragilis confirm that this species has good qualities for implementation in river restoration schemes that involve plant species reintroduction and bio-engineering stabilization techniques. *Salix fragilis* was found to have a fast growth rate (even without nutrient supply and in limited space), and exhibited good strength performance and anchorage ability. This makes *Salix fragilis* particularly applicable to soil where the moisture layer is sufficiently deep to promote high concentration of root biomass at depth.

The above findings are likely to be beneficial to river management institutions and organizations involved in planning programmes for species reintroduction and recovery in order to mitigate against river degradation while enhancing flood protection. These encouraging results have revealed that willow cuttings could act as a potential prototype for plant uprooting by flow in an open channel (as initial aim of this thesis). However, due to the laboratory constraints, this hypothesis could not be fully validated. Therefore, it is hoped that these preliminary findings will stimulate further research in this direction.

Chapter 3

A model for the critical rooting length

The material presented in this Chapter appears in:
Bau', V., Zen, S., Calvani, G., and Perona, P., Extracting the critical rooting length in plant uprooting by flow from pullout experiments, *Water Resources Research*, 55(12): 10424-10442. https://doi.org/10.1029/2019WR025074.[1]

3.1 Plant uprooting by flow

The previous Chapter identified that the occurrence of riparian vegetation plays a key role on the ecomorphodynamics of riverbanks and bedforms. However, the establishment and encroachment of vegetation are often threatened by flood events that can lead to plant uprooting and mortality.

Flow-induced uprooting of plants is a complex mechanism that results from interactions between river processes and the bio-mechanical properties of vegetation (Edmaier et al., 2011). The combination of drag forces and bed scouring can expose the root system of a plant and reduce its anchorage resistance until it dislodges. Plant removal triggers processes of habitat desegregation and biodiversity loss (Lake et al., 2007; Palmer et al., 2014) and generates negative feedback

[1]The paper was written in collaboration with the three co-authors, whose contributions are highly appreciated. As the leading author, I was involved in all aspects of the work.

affecting the morphological evolution of riverbed and riverbanks (Bertoldi et al., 2014; Gurnell, 2014). Thus, flow-induced plant uprooting can negatively affect river ecology and morphodynamics. In the light of this, accurate prediction of vegetation removal and mortality has become an objective of many pioneering investigations in river management and restoration. Meanwhile, there are difficult modelling challenges to be faced, especially with regard to complexity of the root system and the stochastic nature of river hydrology and erosion processes (Calvani et al., 2019a; Perona and Crouzy, 2018; Perona et al., 2012a).

In the past decade, many studies have focused on the effect of the above-ground biomass on water dynamics, without yet exploring the below-ground biomass (which provides the stability to the plant). Therefore, studies of the mechanical properties of riparian plant species are of fundamental importance. In particular, static pullout experiments have proved invaluable in assessing the resistance exerted by plant roots. Several investigations have revealed that root-anchoring resistance correlates closely to the plant rooting length (Bailey et al., 2002; Ennos, 1989; Karrenberg et al., 2003).

The rooting length is a useful parameter for representing the anchoring resistance of plants to uprooting (Edmaier et al., 2011; Edmaier et al., 2015; Perona et al., 2012a) for two main reasons. First, the rooting length is relatively easy to quantify. Second, the rooting length concept enables derivation of the so-called critical rooting length (Edmaier et al., 2015; Perona et al., 2012b) defined as the rooting length of a plant when uprooted. In other words, a plant is uprooted at the instant the rooting length becomes critical, and the plant has insufficient resistance to counter the destabilizing forces that act on the above-ground biomass of the plant and its exposed roots. In principle, the critical rooting length can be readily derived by subtracting the vertical length contribution of local erosion processes from the rooting length that the plant had in undisturbed conditions.

Laboratory and field experiments have demonstrated that the critical rooting length directly controls plant uprooting by flow (Calvani et al., 2019a; Edmaier et al., 2015). Thus, the critical rooting length is an important indicator by which to assess the percentage of biomass uprooted by a flood (Perona and Crouzy, 2018). However, challenges related to the spatial scale of erosion and sedimentation processes and the recovery of plants after a flood make it difficult to monitor the response of vegetation to flood disturbance and quantify the critical rooting length.

This Chapter presents a free-body model that enables assessment of the critical rooting length for variable erosion conditions, plant species, and hydrology. In the model, actions that contribute to plant uprooting by flow (hydrodynamic forces) are taken directly into account to balance the anchoring resistance of the root system (from pullout experiments) through consideration of the overall balance of forces. The model is then validated using three different data sets. Finally, the approach proposed by Perona and Crouzy (2018) is used to compute the probability density function of the time to uprooting for the same data sets.

3.2 Model description

The model presented herein is used to reproduce the Type II uprooting mechanism (Edmaier et al., 2011) for flexible plants, and involves assessing the equilibrium of forces between root resistance and drag exerted by the water flow.

Figure 3.1 provides an overview of the different forces acting on the canopy. At initial time, T_0, when bed erosion has not yet occurred (Figure 3.1a), the forces acting on a submerged plant are simply the net buoyancy force $\mathbf{F_n}$ and the normal drag force $\mathbf{F_{d,n}}$. For plants with low flexural rigidity (Calvani et al., 2019a; Nepf, 2012; Yagci et al., 2010), the drag force progressively bends the portion of the plant above the ground until it is parallel to the channel bed

(Figure 3.1b). At incipient uprooting, all the forces have to balance the resistance exerted by plant roots, such that:

$$\mathbf{F_n} + \mathbf{F_{d,n}} + \mathbf{F_{d,t}} = \mathbf{R}. \tag{3.1}$$

where $\mathbf{F_{d,t}}$ is the friction action, and $\mathbf{R}$ represents the resistance exerted by the root system. Plant flexibility enables the physical configuration in Figure 3.1b to be interpreted as a pulley mechanism (Figure 3.1c) (Calvani et al., 2019b). Therefore the vector sum of the destabilizing forces $\mathbf{F_n}$, $\mathbf{F_{d,n}}$, $\mathbf{F_{d,t}}$ is transmitted to the root system and its mechanical resistance $\mathbf{R}$, regardless of the direction of the resultant force acting on the plant.

However, root anchoring is particularly complex to obtain from first principles, given the unknown architecture of the soil-root system. To overcome this problem and quantify the root length resisting the destabilizing forces, it is convenient to recall empirical correlation laws that link resistance force $\mathbf{R}$ to total rooting length L_r. In pullout experiments, $\mathbf{R}$ is generically expressed as follows:

$$\mathbf{R} = \mathbf{R}(L_r). \tag{3.2}$$

As a result, the vertical pullout force $\mathbf{F_p}$ balancing the root resistance at incipient uprooting is directly related to the total rooting length L_r,

$$\mathbf{F_p} = \Phi(L_r), \tag{3.3}$$

where Φ is an empirical fitting relationship extracted from experimental data. Given that the main rooting length, L_0, plays a dominant role in the uprooting process (Edmaier et al., 2014), it is reasonable to approximate L_r by L_0, and equation (3.3) becomes a function of L_0 only:

$$\mathbf{F_p}(L_r) \approx \mathbf{F_p}(L_0). \tag{3.4}$$

The total resistance exerted by a plant at incipient uprooting, $\mathbf{R}$, can be compared to the force $\mathbf{F_p}$ that instantly pulls out a plant with an equal rooting

length in static conditions. Under this assumption, the force balance expressed by equation (3.1) reads:

$$\mathbf{F_n} + \mathbf{F_{d,n}} + \mathbf{F_{d,t}} = \mathbf{F_p} \Longrightarrow \mathbf{F_p} = \mathbf{R}. \tag{3.5}$$

Hence, for a Type II uprooting mechanism, it may be assumed that the critical rooting length coincides with the main rooting length measured in static pullout experiments (Figure 3.1d). Thus, the critical rooting length, L_c, can be assessed as:

$$L_c \approx \Phi^{-1}(\mathbf{F_p} = \mathbf{R}) \tag{3.6}$$

where Φ^{-1} is the inverse function mapping $\mathbf{F_p}$ into L_c.

For the equivalence (3.5) to be valid, the plant species, grain size distribution, and soil saturated conditions are required to be the same for both scenarios of Figures 3.1b and 3.1d.

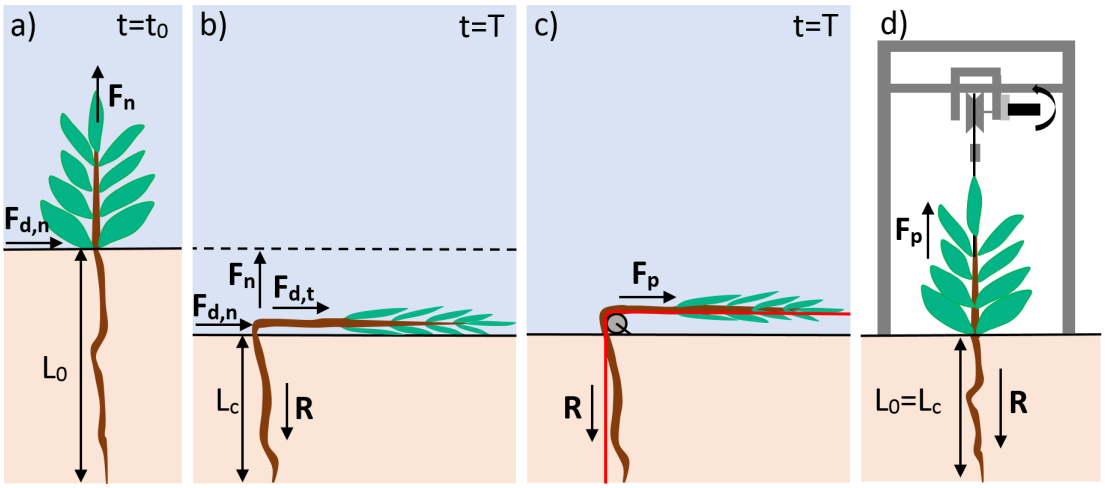

Figure 3.1: Outline of the free-body model. a) Forces acting on an upright seedling at an initial time $t = T_0$, without bed erosion; b) Forces acting on a bent seedling at the uprooting time T; c) Pulley mechanism for flexible plants, where the resultant destabilizing force F_p is balanced by the resisting force R; d) Schematic setup of vertical pullout experiments. The residual resistance exerted by L_c at incipient uprooting coincides with that exerted by L_0 in static uprooting conditions.

The moduli of the vectors in equation (3.5) are expressed in equations (3.7), (3.8), and (3.9). The modulus of $\mathbf{F_{d,n}}$ is:

$$F_{d,n} = \frac{1}{2} C_D \rho_w u^2 A_n. \tag{3.7}$$

where A_n is projected area of vegetation canopy in the flow direction, u the velocity impacting the vegetation element, C_D the drag coefficient, and ρ_w the water density. Similarly, the modulus of the tangential drag force $\mathbf{F_{d,t}}$ depends on the surface area of the plant biomass exposed to the flow, A_t, and the friction coefficient C_f:

$$F_{d,t} = \frac{1}{2} C_f \rho_w u^2 A_t. \tag{3.8}$$

The modulus of the buoyancy force, $\mathbf{F_{d,n}}$, depends on the density of the whole plant and on its volume:

$$F_n = g(\rho_w - \rho_r)V_r + g(\rho_w - \rho_s)V_s + g(\rho_w - \rho_f)V_f \tag{3.9}$$

where V_r, V_s, and V_f are roots, stem and foliage volumes; g is the gravitational acceleration; ρ_r, ρ_s, and ρ_f are roots, stem and foliage densities. In equations (3.7) and (3.8), u can be approximated by the value of the cross-section mean flow velocity or the local flow speed as obtained from numerical simulations for more complex geometries.

The flow resistance of vegetation is influenced by the type, density, shape and flexibility of the plant, the Reynolds number, and the flow depth. The drag coefficient C_d is an empirical parameter that is approximated herein by Schlichting's formula (1962):

$$C_D = \begin{cases} \left(10^3/Re_D\right)^{0.25} & Re_D \leq 10^3 \\ \\ \min\left[0.976 + \left(\frac{10^{-3}Re_D - 2}{20.5}\right)^2 \ , \ 1.15\right] & 10^3 < Re_D < 4 \cdot 10^4 \end{cases} \tag{3.10}$$

where Re_D is the obstacle Reynolds number calculated using the diameter of the root, which is approximated to a cylinder.

Given the foregoing expressions for the force vector moduli, the balancing equation (3.5) becomes:

$$\begin{aligned} F_p(L_c) = \frac{1}{2}C_D\rho^* u^2 A_n + \frac{1}{2}C_f\rho^* u^2 A_t + g(\rho_w - \rho_r)V_r \\ +g(\rho_w - \rho_p)V_p + g(\rho_w - \rho_f)V_f \end{aligned} \tag{3.11}$$

As the water and sediment mixture passing the plant has a density higher than that of pure water, ρ_w has been replaced with a modified density term ρ^*, which reads:

$$\rho^* = \rho_g \left(\frac{V_g}{V_g + V_w} \right) + \rho_w \left(\frac{V_w}{V_g + V_w} \right), \tag{3.12}$$

where ρ_g and V_g are the density and volume of the sediment being moved.

To complete the problem formulation and obtain a relationship for the critical rooting length, the exposed rooting length, L_e, is expressed as the following difference between the main rooting length, L_0, and the critical value, L_c,

$$L_e = L_0 - L_c. \tag{3.13}$$

A_n from equation 3.7 can be approximated as the sum of the projected area of the roots, A_R, and of the stem, A_p, in the flow direction:

$$A_n = A_R + A_p, \tag{3.14}$$

where both A_R and A_p are approximated to the area of a circle.

A_t from equation 3.8 can be decomposed as follows:

$$A_t = A_s + A_f + \pi n_r d_r L_e, \tag{3.15}$$

where A_s is the surface area of the stem and A_f is the surface area of the foliage. The third term is the surface area of the exposed root, whose shape is approximated by a cylinder and n_r is the number of roots exposed to flow (each of diameter d_r).

Expressing the third addend on the right-hand side of equation 3.11 as a function of L_e: $g(\rho_w - \rho_r)\pi n_r L_e \frac{d_r^2}{4}$ leads to an explicit version of equation (3.11) as follows:

$$\begin{aligned} F_p(L_c) = \frac{1}{2}C_D\rho^* u^2 A_n + \frac{1}{2}C_f\rho^* u^2(A_s + A_f) + \frac{1}{2}C_f\rho^* u^2\pi n_r d_r(L_0 - L_c) \\ +g(\rho_w - \rho_r)\pi n_r \frac{d_r^2}{4}(L_0 - L_c) + g(\rho_w - \rho_p)V_p + g(\rho_w - \rho_f)V_f. \end{aligned} \tag{3.16}$$

Equation (3.16) allows L_c to be estimated once a relationship has been established for the static uprooting force, F_p. Note that equation (3.16) is implicit in L_c and so would normally require an iterative numerical solution. However, for the particular case when the static uprooting force has linear form (i.e., when $F_p = kL_c$), equation (3.16) has the following relatively simple explicit solution:

$$\begin{aligned} L_c = \frac{\frac{1}{2}\rho^* u^2 \left[C_D A_n + C_f(A_s + A_f + \pi n_r d_r L_0)\right]}{k + (\pi n_r d_r)\left[\frac{1}{2}C_f\rho^* u^2 + g\frac{d_r}{4}(\rho_w - \rho_r)\right]} \\ + \frac{g\left[(\rho_w - \rho_r)\pi n_r L_0 \frac{d_r^2}{4} + (\rho_w - \rho_s)V_s + (\rho_w - \rho_f)V_f\right]}{k + (\pi n_r d_r)\left[\frac{1}{2}C_f\rho^* u^2 + g\frac{d_r}{4}(\rho_w - \rho_r)\right]} \end{aligned} \tag{3.17}$$

3.3 Model validation

The proposed model was validated using three different data sets available in literature. The first two data sets are taken from Edmaier et al. (2015) and Calvani et al. (2019a), whose aim was to use flume experiments to investigate the dynamics of plant uprooting by flowing water. The third data set, from Bywater-Reyes et al. (2015), refers to results obtained from plant pullout experiments in the field.

3.3.1 Data sets from laboratory experiments

The experiments carried out by Edmaier et al. (2015) and Calvani et al. (2019a) involved similar laboratory set-ups: both experiments were undertaken in a channel with erodible bed and living plants. The plants were cultivated outside the flume in plastic boxes with lateral removable walls. Consequently, after the seedlings had grown for a prescribed time, the boxes were inserted at set locations in the flume and the lateral walls of the boxes removed. Each plant was positioned a certain distance from its neighbors to avoid root-root interactions which could alter the root properties (e.g., root length density, radial spread, and root distribution over density (Smit et al., 2013)). Moreover, during the experiments, a movable downstream wall was lowered at a constant rate, $\dot{\eta}$, (equal to the erosion rate of the channel bed) to obtain quasi-parallel bed erosion. The experimental tests utilised living seedlings of *Avena sativa*, chosen for their simple root structure and small stem size (Figure 3.2a). This type of vegetation differs from the one used in the previous Chapter (*Salix* cuttings). *Avena sativa* plants germinate from seeds and their size and fast germination rates promote their use in flume erosion experiments. Furthermore, given the sediment size used in Edmaier et al. (2015) and Calvani et al. (2019a), the scouring induced by *Avena sativa* is minimal, thus allowing to achieve a condition of quasi-parallel bed erosion. The scale of the experiments allowed records to be taken of the elapse time at which each plant was uprooted, the erosion depth, the amount of root exposed to the flow, and hence the computed critical rooting length. Table 3.1 provides further details of the experimental conditions (e.g., number of samples tested, plant spatial arrangements) and the parameters pertaining to Edmaier et al.'s and Calvani et al.'s data sets.

The simple architecture of *Avena sativa* (Figure 3.2a) enabled straightforward estimation of the geometrical parameters required by the free-body model

of equation (3.16). The plant was decomposed into simple geometric shapes (Figure 3.2b) so that the volume of the seed, grass, and roots and the projected and surface area of the plant could be easily estimated. Given that the stage of growth of the samples did not appear to exert influence on the size of the roots and the seed, the widths of the roots and the seeds were set to constant values. Roots were approximated by cylinders, each of diameter, d_r, equal to 0.6 mm. The shape of the leaves was assumed to be conical; this is reasonable because, when *Avena sativa* plants are exposed to high flow velocities, their leaves roll-up and reconfigured themselves into cones (Järvelä, 2002).

The value of C_d was computed by using the piecewise formula (equation (3.10)) and gives an average value of 1.05 and 1.15 for Edmaier et al.'s data set and Calvani et al.'s data set, respectively. C_f was assigned two different values: 0.6 for leafless seedlings and 1 for seedlings with leaf. Both values were calibrated for one of the four settings considered by Edmaier et al. ($\dot{\eta}$=0.0431 m/s), and then validated for Edmaier et al.'s remaining cases and the data set of Calvani et al. (2019a). The order of magnitude of the resulting projected area of the plant in the flow direction is 10^{-5} m^2, whereas that of the surface area of the plant exposed to flow is 10^{-4} m^2.

Such high values of the friction coefficient may be misleading if compared to the values that are normally associated to the classic formula of Darcy-Weisbach. However, when it comes to vegetated channels and complex plant morphologies, the capability of such approach to provide a valid estimation of C_f has been object of criticism (Rubol et al., 2018). The vortical structures around the canopy generates non-linear dynamics, such as a flapping movement of the plant, which increases vegetation drag and friction forces (Pu et al., 2019). The latter are particularly pronounced when considering the reconfiguration of the plant in the streamline direction. As a result, Darcy-Weisbach approach has been recently abandoned when dealing with channels covered by large roughness elements (see

Wang et al., 2019b). The estimation of the C_f is further complicated for the presence of leaves. The leaves are, in fact, found to contribute between 74% and 98% of the total drag (Västilä et al., 2013). Experimentally attained values of the friction coefficients found by Järvelä (2002) show that C_f may reach values that are three to seven times higher than the leafless samples. Analytical expressions of C_f are now available, but their formulations have been approached in different ways (Järvelä, 2002; Pu et al., 2019; Wang et al., 2019b). Still, the magnitudes obtained for C_f all range from 0 to 7.

The approach flow velocity, u, was calculated using a normal flow approximation using the Manning formula. As mutual interactions among distinct samples were neglected in both data sets, equation (3.11) could be applied independently for every single sample tested.

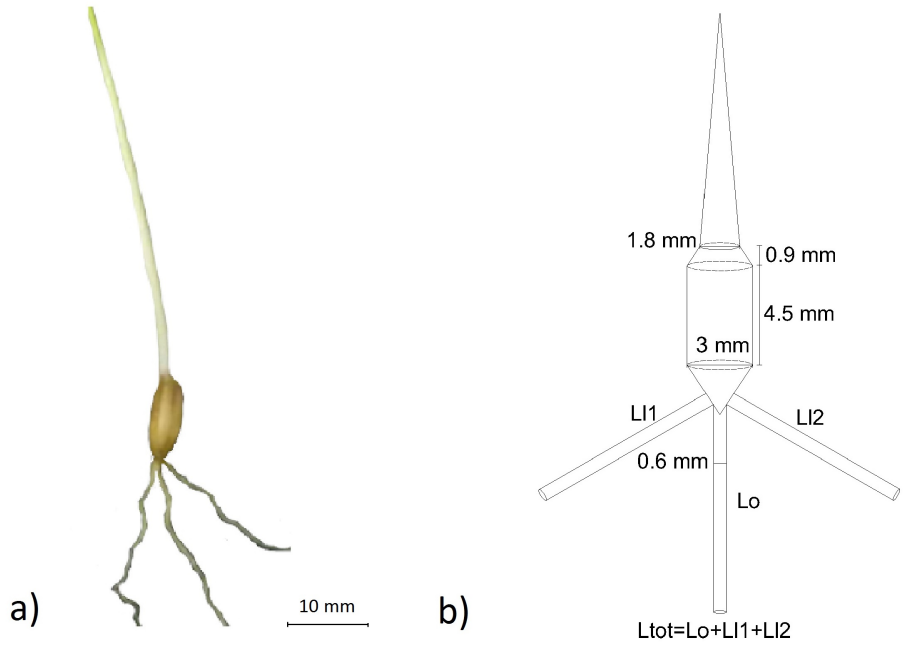

Figure 3.2: *Avena sativa* seedling and its modelled sketch. a) Morphology of a common *Avena sativa* seedling 4 days after seeding; b) The sketch of *Avena sativa* seedling and the different simple geometrical shapes used to approximate its morphology.

Table 3.1: Summary table listing the experimental conditions and the parameters available for each data set used to validate the free-body model.

	(Edmaier et al., 2015)	(Calvani et al., 2019a)
plant species	*Avena sativa*	*Avena sativa*
plan growth conditions	laboratory	laboratory
cultivation time/plant age	48-110 hr	96-144 hr
type of sediment	quartz sand	graded quartz sand
D_{50} [mm]	1.35	0.57
soil moisture	saturated	saturated
type of uprooting	by flow	by flow
uprooting location	artificial flume	artificial flume
number of samples	277 seedlings	87 seedlings
temperature/climate	22.5-26°C	18-21°C
plant spatial arrangement	2 rows of 4 plants	1 or 3 rows of 6 plants
parameters available	L_0, L_e, L_c T 4 different Q 4 different $\dot{\eta}$ static uprooting law	L_0, L_e, L_c T 4 different Q unique $\dot{\eta}$ -

Now that the left-hand side of equation 3.1 has been expressed, it is necessary to define the pullout relationship $F_p(L_c)$ for both data sets. Static pullout data for *Avena sativa* are available from both Edmaier et al. (2012) and Edmaier et al. (2014), for different grain size distribution and soil saturation conditions. A suitable law for the first data set was suggested by Edmaier et al. (2014), who conducted several pullout tests under the same water content and granulometry conditions as used in the flume experiments (Edmaier et al., 2015). The law is

expressed as follows:

$$F_p = a_1 L_c \tag{3.18}$$

with a_1=2.1 [N/m^2] and a goodness of fit, R^2, equal to 0.40.

However, another law had to be used for the second data set, given the different size distribution of the sand used by Calvani et al. (2019a). In this circumstance, an extrapolation of the law proposed by Edmaier et al. (2012) should be fairly representative of the sediment size considered by Calvani et al. (2019a). In this case, the fitting relation is a second degree polynomial equation, which reads as:

$$F_p = a_2 L_c^2 + b_2 L_c \tag{3.19}$$

where a_2=88.4 [N/m^2], b_2=0.65 [N/m], and R^2=0.84.

Expressing F_p by equations (3.18) and (3.19), enables equation (3.16) to be solved explicitly.

3.3.2 Modelled critical rooting length

Edmaier et al.'s data set

Theoretical model values for the critical rooting length were obtained by implementing equation (3.16) for every sample collected during the laboratory tests. Figure 3.3 compares measured (filled circles) and modelled (empty circles) values of critical rooting length as functions of main rooting length for each flow setting. It is evident that the model properly represents the physical link between L_c and L_0 observed at the laboratory scale. Moreover, the Pearson correlation coefficients are higher for the modelled data (r^2=0.99) than the measured data (r^2=0.68, 0.77, 0.87, 0.89). This is due to the simplified description of leaf size used within the model. In fact, the model partially ignores the biological heterogeneity of the plants by assigning an equal value of leaf length to all samples presenting the same rooting length. The reason for this is that the leaves had not

been measured, and so estimation of their length had to rely on the correlation between the below- and above-ground biomass found in Edmaier (2014). This simplification caused a noticeable overlap of modelled critical rooting length values for samples with the same L_0 value. These observations highlight the intrinsic deterministic nature of the model, which leads L_c to be linked to L_0. Figure 3.4 illustrates the correlation between modelled and experimental L_c for all L_c values regardless of flow setting. The high value of the Pearson coefficient (r^2=0.81) suggests that the free-body model provides a good approximation to the experimental data.

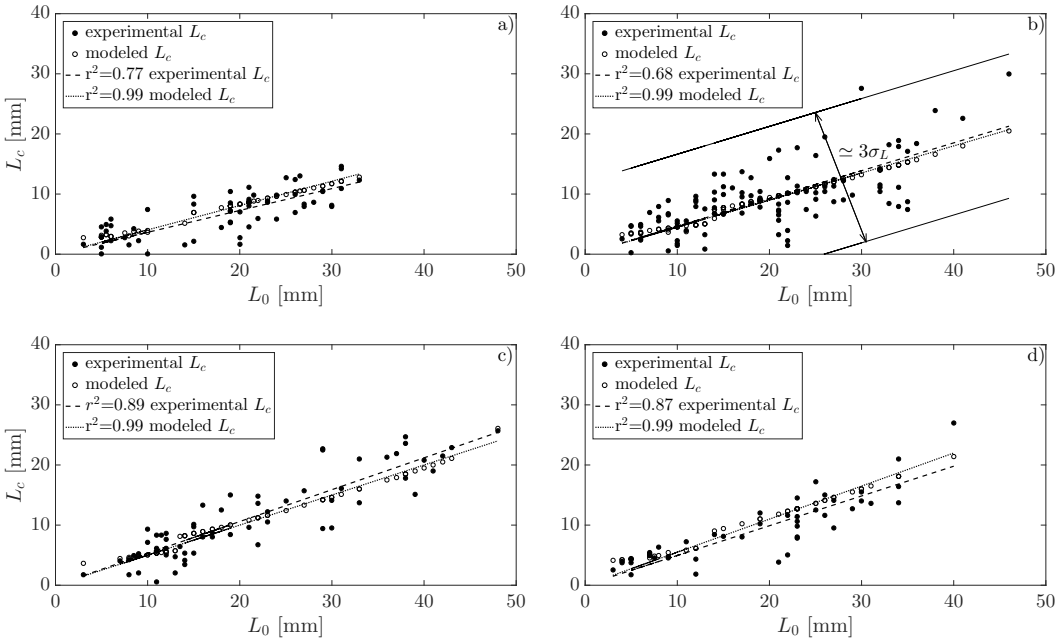

Figure 3.3: Critical rooting length L_c plotted against main rooting length L_0 for the four flow settings considered by Edmaier et al. (2015): a) Q=1.60 l/s and $\dot{\eta}$=0.0431 mm/s; b) Q=1.81 l/s and $\dot{\eta}$=0.058 mm/s; c) Q=1.94 l/s and $\dot{\eta}$=0.076 mm/s; and d) Q=2.15 l/s and $\dot{\eta}$=0.1 mm/s. Model results (empty circles); measurements (filled circles).

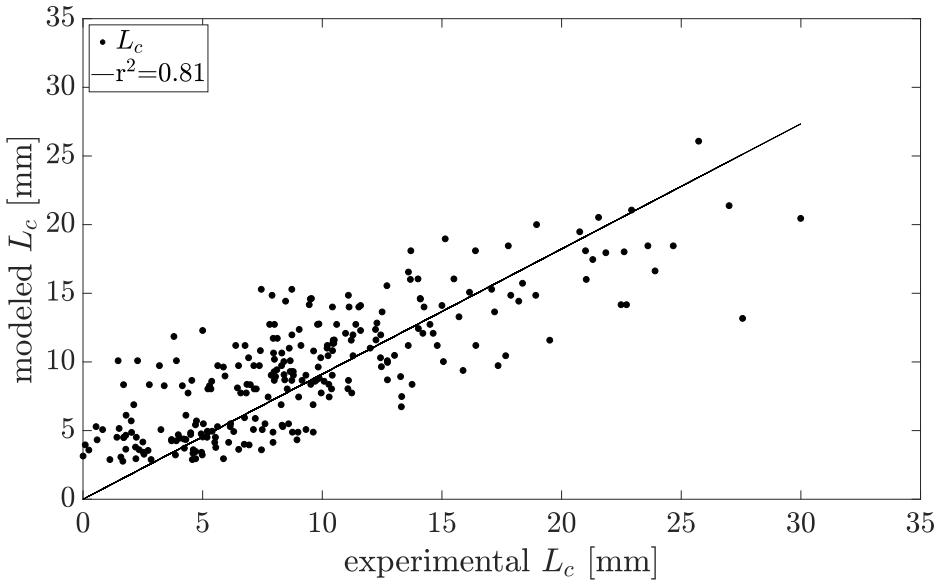

Figure 3.4: Regression plot between modelled and measured critical rooting lengths L_c of samples of *Avena sativa* seedlings tested by Edmaier et al. (2015) for all four investigated flow settings.

Calvani et al.'s data set

Before solving equation (3.16), the data set of Calvani et al. (2019a) was subjected to an outlier elimination procedure. The data set presented some abnormal observations that may have originated from root-root interactions, which are not accounted for in the present model. The method used to detect outliers did not considerably constrain the data set, and involved assigning a threshold value to the data, such that the data considered lay within $\pm 1.5\sigma_L$ where σ_L is the standard deviation obtained at the flow setting that exhibited highest data variability ($\dot{\eta}$=0.058 mm/s, Figure 3.3b). In particular, σ_L was computed for L_c values corresponding to a range of L_0 values varying between 20 and 25 mm. Hence, any data with values of L_c that fell outside of the confidence interval $\pm 1.5\sigma_L$ were discarded. A revised plot of Figure 3.3 is then realized for the data set in the absence of outliers (Figure 3.5a). From Figure 3.5 it can be seen

that the experimental data without outliers exhibit weaker correlation (r^2=0.42) between the main rooting length and its critical value compared to Edmaier et al.'s data set. The lower values may be explained by the poor correlation between the above- and below-ground biomass that occurs for plants at a relatively advanced stage of growth (Pasquale et al., 2014). In fact, the plants tested in the experimental runs by Calvani et al. (2019a) have rooting lengths that are twice as long as those tested by Edmaier et al. (2015). Nevertheless, the regression line for the critical rooting length extracted from laboratory measurements almost completely overlaps that obtained using the model (Figure 3.5a). This suggests that the model can preserve the inter-dependency between L_c and L_0 observed in the experimental data. The weak correlation ($r^2 = 0.47$) between modelled and experimental L_c in Figure 3.5b might be due to the inadequacy of the static uprooting law given by equation 3.19. This law was derived for younger plants, which were characterised by simpler root architecture, and in a soil whose grain size was not exactly the same as that considered by Calvani et al. (2019a).

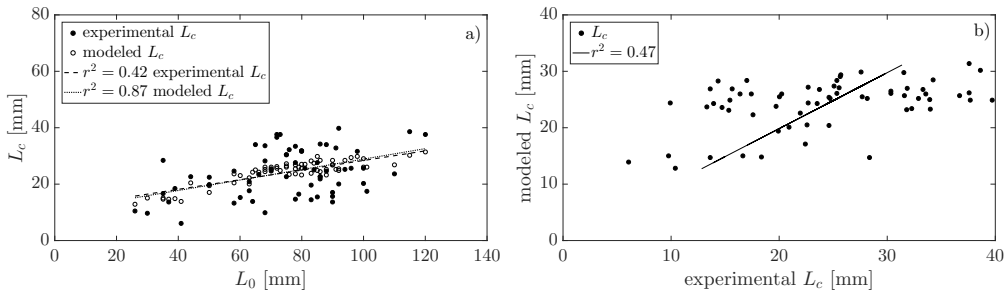

Figure 3.5: Critical rooting length data: a) variation in modelled and Calvani et al.'s experimental values of L_c with L_0 (the flow settings are not distinguished as the $\dot{\eta}$ is constant for every discharge analyzed); and b) variation in modelled L_c with Calvani et al.'s experimental L_c.

3.3.3 Critical rooting length and specific stream power

Furthermore, it is interesting to see how the critical rooting length depends on integral properties of the river channel rather than on its local flow component. Figure 3.6 shows the variation in critical rooting length with the stream power per unit width, w, for different values of the main rooting length. The stream power per unit width is calculated as: $w = \frac{\gamma_w Q h}{B}$, where h stands for the hydraulic head, γ_w is the water specific weight, and B is the width of the channel.

It can be observed that L_c increases with w. Also, L_c increases progressively with L_0 for equal w. The inset panel of Figure 3.6 displays experimental data from Edmaier et al. (2015) and highlights how values of critical rooting length are scattered around the relative average value for each flow setting. It should be emphasised that the four curves do not have any physical meaning when plotted beyond the points for which L_c=L_0. Hence, the curves were truncated at the point where the critical rooting length L_c is equal to average value of L_0. Figure 3.7 shows the dependence of L_c on w for different values of the friction coefficient and for a fixed value of L_0. With w held constant, an increase in friction coefficient is associated with an increase in critical rooting length. This suggests that plants with equal rooting lengths that are subjected to the same water power are more easily uprooted when the friction coefficient is larger.

3.3.4 Data set from field experiments

The free-body model was also applied to a part of the data set reported by Bywater-Reyes et al. (2015). In particular, the model was tested on the results of pullout experiments carried out on the *Populus* species along the Bitterroot River (Montana, USA). The Bitterroot River is an unregulated gravel-bed river with a drainage area of 6500 km^2 and an unregulated nivo-pluvial hydrological regime.

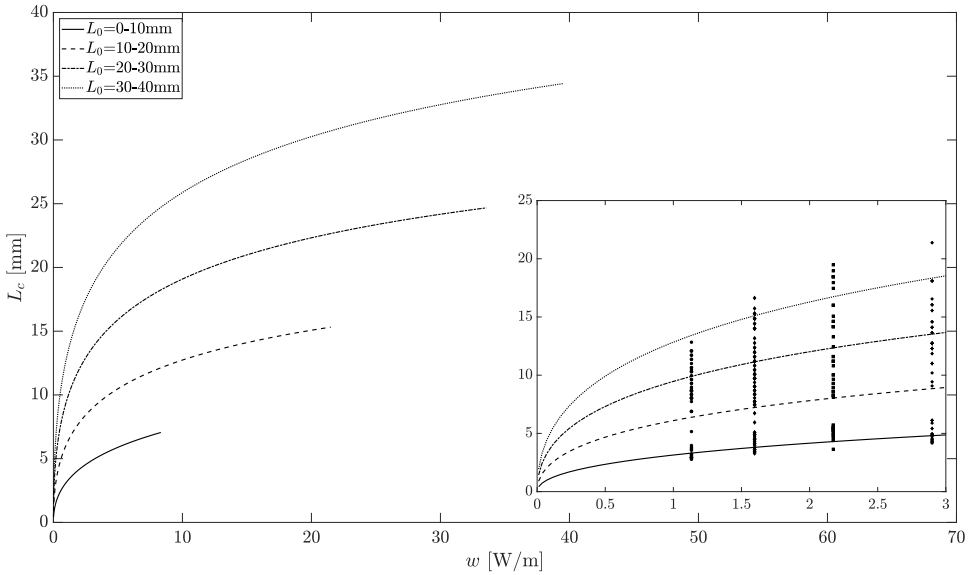

Figure 3.6: Variation in critical rooting length L_c with stream power per unit width w for four different ranges of L_0, when $F_p = a_1 L_c$. The inset panel also displays experimental data from Edmaier et al. (2015).

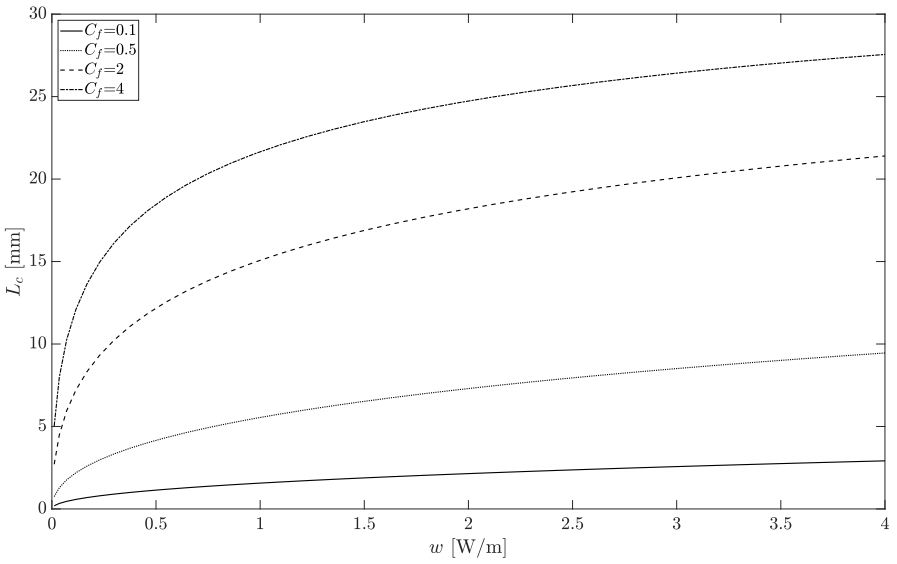

Figure 3.7: Variation of critical rooting length L_c with the stream power per unit width w for four different values of C_f, when $F_p = a_1 L_c$.

The choice of this river was made for practical reasons: the high number of pullout samples and the availability of sufficient streamflow hydrograph data to provide an accurate estimate of average flow duration under movable bed conditions. The samples used in the pull tests were randomly selected and the tests carried out for four different excavated scour depths: 0.1, 0.2, 0.3, and 0.4 m. It was then possible to assess the influence of substrate scour on root resistance, and the likelihood of plant uprooting.

Floods with a recurrence time of two and ten years, Q_2 and Q_{10}, were modelled to determine whether the associated flow speeds would have been sufficient to uproot the plants tested. In their work, Bywater-Reyes et al. (2015) did not estimate the critical rooting length, but they directly linked the scour depth, which coincides with L_e, to the uprooting threshold (represented by the uprooting velocity).

3.3.5 Modelled exposed rooting length

In the absence of values for the critical rooting length, it is necessary to estimate L_e. Combining equation 3.16 with equation 3.11, gives:

$$L_e = \frac{F_p - \frac{1}{2}C_d\rho_w u^2 A_n - \frac{1}{2}C_f\rho_w u^2 A_t}{\frac{1}{2}C_f\rho_w u^2 \pi n_r d_r} \tag{3.20}$$

Using Equation 3.20, it is possible to compare the experimental and analytical values of L_e. It should be recalled that Equation 3.20 was derived under the reasonable assumption that buoyancy forces can be neglected, following Bywater-Reyes et al. (2015) and Calvani et al. (2019a). To be able to calculate L_e, it is necessary to evaluate the equation parameters. In this case, the surface area of the canopy subjected to drag forces, A_t, was difficult to estimate accurately, given the complexity of the geometrical shape of the plants. Moreover, Bywater-Reyes et al. (2015) only provided values for the whole frontal area of the plant, A_{fr}. Hence, with the intention to make use of the only available data, A_t was assumed,

for simplicity, to correspond to a cylinder. Hence, $A_t = \pi(H_p D_p)$, where H_p and D_p are the height and the diameter related to A_{fr}. However, to make this approximation less simplistic, it was considered that not all the surface area of the plant was subjected to flow-induced friction. The contact surface between plant and sediment was presumed to have an angle of approximately 120°, meaning that the effective exposed portion of the plant was about 2/3 of the total surface area. Hence, $\frac{A_t}{A_{fr}} = \frac{2}{3}\pi\frac{HD}{HD} \approx 2$ leads to the term A_t in equation 3.20 being replaced by $A_t \approx 2A_{fr}$. Meanwhile, ρ^* was set to the value of water density ρ_w following Bywater-Reyes et al. (2015), whereas the value of u was provided by Bywater-Reyes et al. (2015) through 1-D numerical simulations.

All the samples tested were divided into three classes according to the value of L_e: 0.1, 0.2, and 0.3 m (the scour depth of 0.4 m was excluded from any statistical analysis because of the small number of samples available). Part of the data was used to calibrate the friction coefficient C_f, whereas the remainder was used to implement equation 3.20. Static uprooting laws F_p for the three scour values were obtained by fitting the maximum pullout forces as functions of plant frontal areas, with an average goodness of fit, R^2 of 0.72. The fitted laws show that more force is needed to uproot a plant with lower L_e (Figure 3.8).

Figure 3.9 illustrates the results of the calibration procedure for C_f. A power law of the type $C_f = a_3 \cdot A_{fr}^{b_3} + c_3$ is found to provide the best approximation to the values of C_f for the three different scour depths considered. The parameters a_3, b_3 and c_3 have values depending on the scour case considered and generate curves that reach almost an asymptotic-constant value for $A_{fr} > 0.06$. As expected, the friction coefficient C_f increases with A_{fr}. However, Figure 3.9 shows that for equal A_{fr}, C_f decreases as L_e increases. This finding agrees with the intuitive concept whereby a lower value of the friction force is needed to uproot a plant whose root system has lost part of its residual anchoring resistance due to scouring around the plant (Edmaier et al., 2011).

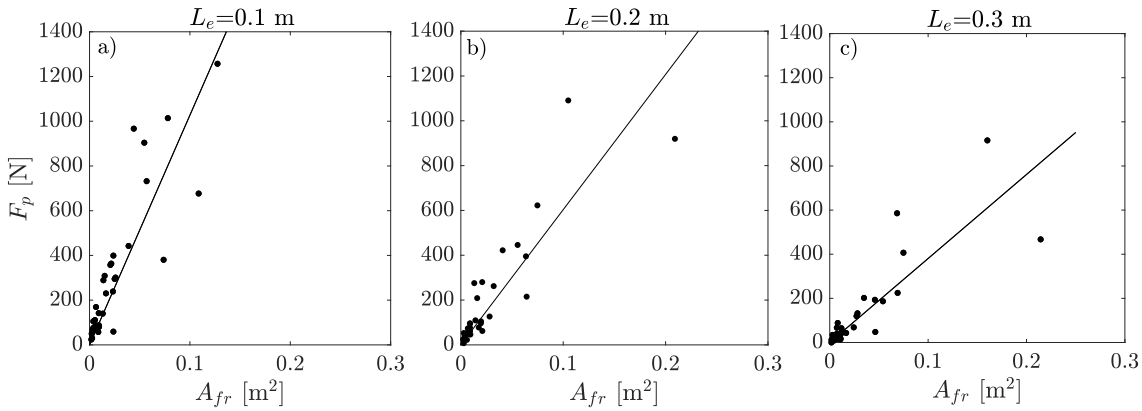

Figure 3.8: Correlation between uprooting force and frontal area of *Populus* samples for: a) L_e=0.1 m; b) L_e=0.2 m; and d) L_e=0.3 m.

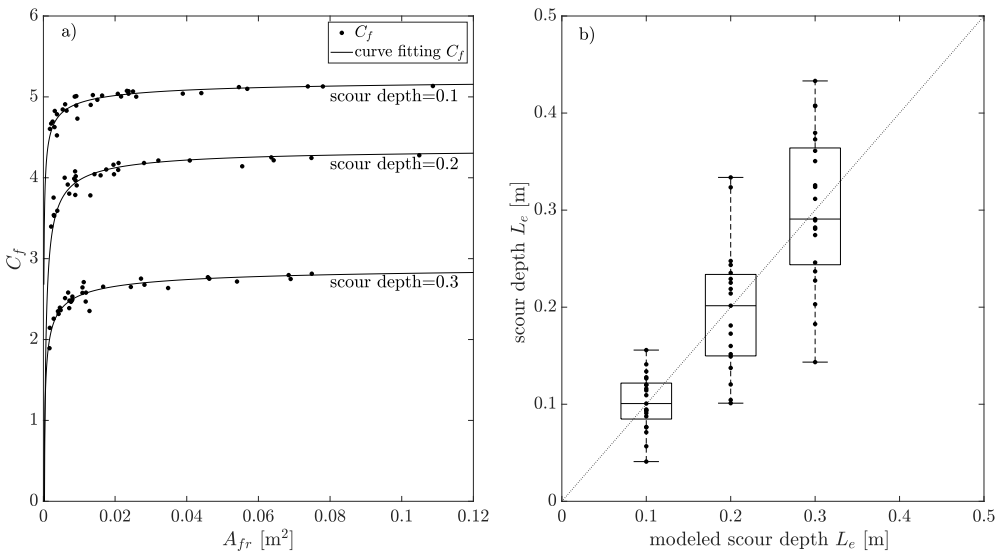

Figure 3.9: a) Power-fitted curve used to determine empirical law of variation in C_f with A_{fr} for three different scour depths; b) L_e defined by Bywater-Reyes et al. (2015) as a function of modelled scour depths. The boxplots highlight the degree of dispersion and skewness of the modelled data about the mean.

Figure 3.9b shows the regression fit between field observations of scour depth and theoretical values obtained using equation (3.20). The box plots show the

degree of agreement between the modelled and observed scour depths, indicating that the mean theoretical values for modelled scour depth are almost the same as the observed values.

3.4 Probability distribution of the time to uprooting

Perona and Crouzy (2018) formulated an analytical expression for the probability density function of the elapsed time to uprooting p_τ:

$$p_\tau(T) = \frac{L_e}{2\sqrt{\pi G(T)^3}} e^{\left(-\frac{(L_e - V(T))^2}{4G(T)}\right)} \left[\frac{g_t(T)}{2} + e^{\left(\frac{(L_e + V(T))^2}{4G(T)}\right)} W(T)\right] \tag{3.21}$$

where g_t describes the random noise in the erosion process, $G(T) = \frac{1}{2}\int_0^T g_t(\tau)d\tau$, $V(T) = \int_0^T \dot{\eta}(\tau)d\tau$, $W(T) = \sqrt{\pi}\text{Erfc}\left[\frac{L_e + V(T)}{2\sqrt{G(T)}}\right]\left(\dot{\eta}(T)\sqrt{G(T)} - \frac{g_t(T)}{2}\frac{V(T)}{\sqrt{G(T)}}\right)$, and τ is the dummy variable.

Assuming that g_t and $\dot{\eta}$ are constant, and $W(T)$=0, equation 3.21 reduces to the following inverse Gaussian distribution:

$$p_\tau(T) = \frac{L_e \exp\left(-\frac{(L_e - \dot{\eta}T)^2}{2g_t T}\right)\left(\frac{g_t}{2}\right)}{2\sqrt{\pi}\left(\frac{g_t T}{2}\right)^{3/2}} \tag{3.22}$$

with mean equal to $L_e/\dot{\eta}$ and variance equal to $\frac{L_e g_t^2}{2\dot{\eta}^3}$.

More details about the model of Perona and Crouzy (2018) are noted in Appendix B.

The analytical expression 3.22 was then implemented for the three data sets. For Edmaier et al.'s and Calvani et al.'s data, the PDF p_τ was used to examine the influence of flow discharge on the statistical uprooting time of plants. In the case of the field experiments, equation 3.22 was used to obtain probability density functions of uprooting time of samples from the Bitterroot river for Q_2 and Q_{10}.

3.4.1 Data sets from laboratory experiments

The PDF of uprooting time p_τ was determined for different values of L_0 and Q, based on the data sets provided by Edmaier et al. (2015) and Calvani et al. (2019a). The variance in uprooting time was computed for a range of L_0 values. The range was kept as narrow as possible to be close to the experimental value while including enough samples for the calculated variance to be representative. In both insets of Figure 3.10, p_τ is plotted against the dimensionless time-to-uprooting: $T/\bar{T}$, where $\bar{T}$ is the average uprooting time obtained for each range of L_0.

By computing the percentage of biomass that survived the flood events, $1 - \int_0^T p_\tau$, it was possible to demonstrate that the model successfully interpreted the random component of the process. For instance, in Figure 3.10b, plants with L_0=75-80 mm subjected to a flow rate of Q=7.4 l/s have less chance of surviving the event than plants with the same range of L_0 subjected to a higher flow rate (Q=10.5 l/s). This implies the level of noise is high compared to the strength of the deterministic drift. The opposite occurs for plants with L_0=28-30 mm (Figure 3.10a), where the percentage of biomass that survives is higher for the lowest value of flow discharge (Q=1.60 l/s). This finding is intuitive and indicates that for L_0 ranging between 28 and 30 mm the dynamics gets closer to the hypothetical condition of a purely deterministic erosion process in the absence of noise. At higher discharges, the probability distribution shifts towards the right, and the likelihood reduces that plants can survive a given flood regardless of the values of L_0.

In order to take into account the variability of the plant characteristics of Calvani et al. (2019a), it is worthwhile to compute the cumulative distribution of the uprooting probability P_τ. Herein, P_τ was obtained by integrating the distribution $p_\tau(\tilde{T})$ of the dimensionless uprooting time: $\tilde{T} = \frac{T\dot{\eta}}{L_0}$.

Figure 3.10 shows there is good correspondence between the theoretical cumulative density function of the time-to-uprooting, P_τ, and the cumulative distribution associated with the data extracted from the laboratory observations of Calvani et al. (2019a). The empirical curve is closely approximated by the theoretical one, except for a short mismatch as P_τ approaches 1. The distribution also exhibits good agreement with data from Edmaier et al.'s data sets (see Perona and Crouzy, 2018).

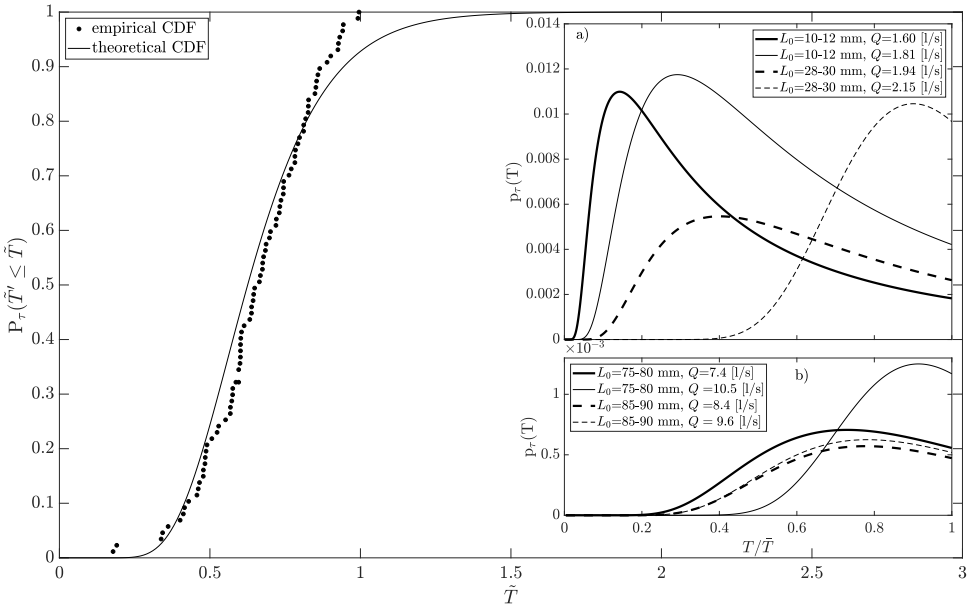

Figure 3.10: Comparison between the theoretical and the empirical (scatter plot) cumulative density functions of the dimensionless time-to-uprooting $\widetilde{T}$=$T\dot{\eta}/L_0$; Insets show probability density functions of time-to-uprooting $p_\tau(T)$ for different ranges of L_0, different flow rates Q, and different magnitudes of process variance and erosion velocity $\dot{\eta}$ for the experimental data sets of: a) Edmaier et al. (2015) ; and b) Calvani et al. (2019a).

3.4.2 Data set from field experiments

Owing to lack information on the uprooting time, the variability in p_τ was assessed by reference to the variance in maximum pullout force of plants at the same scour depth. In fact, the variance in uprooting force can be representative of the variability of the process, being indirectly linked to uprooting time.

However, unlike the laboratory data, Bywater-Reyes et al.'s field data do not provide information on the vertical erosion rate of the channel bed $\dot{\eta}$. The vertical erosion rate is then determined by referring to the definition of sediment mobility provided by Shields (1936). According to Shields' theory, riverbed sediment is mobilized whenever the riverbed shear stress exceeds a threshold value linked to incipient sediment movement. Given that both 2-year and 10-year recurrence time discharges may be considered formative (Doyle et al., 2005), discharge values greater than Q_2 and Q_{10} are assumed capable of inducing morphological change, i.e., scour of the channel bed. The bankfull Shields numbers relevant to Q_2 and Q_{10} (Bywater-Reyes et al., 2015) confirmed that the Bitterroot is a threshold river (Church, 2006) where the limit for bed material transport is exceeded by a moderate amount.

Thus, the time periods for which $Q > Q_2$ and $Q > Q_{10}$ were computed over the historical flood series to obtain values for the mean duration of the flow erosion process, $\hat{t}$, for the two dominant discharges (Figure 3.11). Within the available historical series, the average times for which $Q > Q_2$ and $Q > Q_{10}$, are 73 and 49 hours, respectively. Hence, the vertical erosion rate was computed from:

$$\dot{\eta} \approx \frac{L_e}{\hat{t}} \tag{3.23}$$

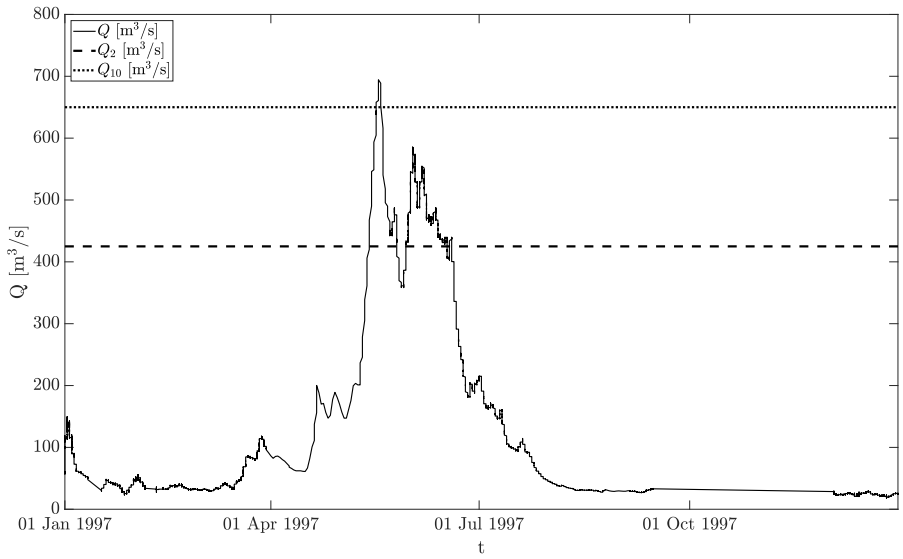

Figure 3.11: Hydrograph of Bitterroot River, Montana, USA, in the year 1997 of the historical flood series. The flow rates Q_2 (dashed line) and Q_{10} (dot line) provide a graphical representation of the period during which the riverbed is morphologically active in 1997.

Figure 3.12 shows the probability density functions of time-to-uprooting for Q_2 and Q_{10} and for different values of L_e. The shapes of the distributions are very similar for both flow rates with increasing L_e. However, the modes of the distributions have remarkably different magnitudes, affecting the probability of uprooting over equal intervals of erosion time.

Application of the analytical model of Perona and Crouzy (2018) to Bywater-Reyes et al.'s data set produces an alternative, valid interpretation of the data compared to that adopted here. Figure 3.13 illustrates this clearly, where uprooting probability is plotted against L_e for both flow rates. From the plot, it can be seen that L_e exerts a fundamental control on the uprooting probability. For a constant value of flow rate, the plant uprooting probability decreases with increasing scour depth.

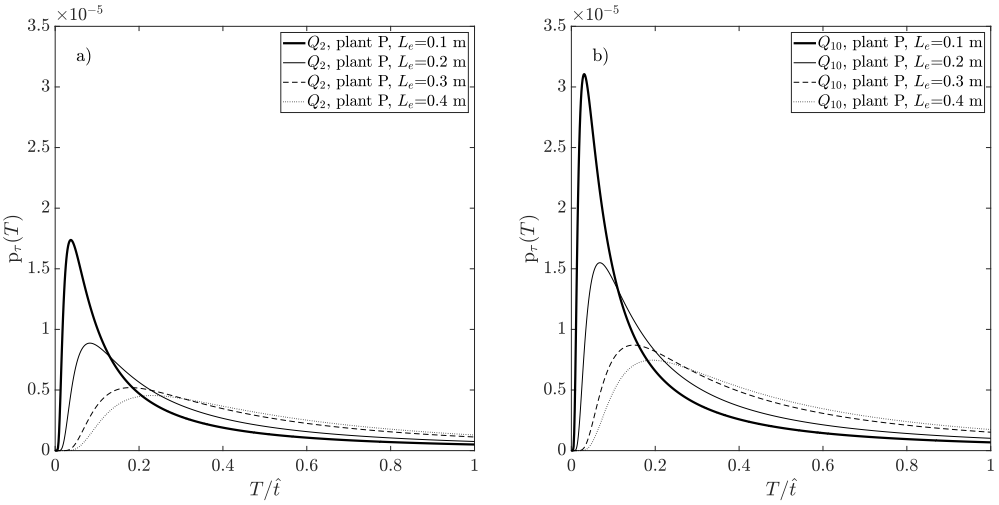

Figure 3.12: Probability density functions of time-to-uprooting $p_\tau(T)$ for *Populus* species in the Bitterroot river, for four different values of scour depths. a) flow rate Q_2; and b) flow rate Q_{10}.

At first glance, this outcome might appear counterintuitive, and so the mechanism requires a more detailed explanation. If two generic plants, X_1 and X_2, with the same total rooting length but different scour depth, are subjected to a flood event of constant magnitude and duration (Figure 3.13), their uprooting probabilities are different. Given that $L_e(X_1) < L_e(X_2)$, the stream has to "work" (i.e., scour) more for plant X_2 than for plant X_1, although $L_{c2} = L_0 - L_e(X_2) < L_{c1} = L_0 - L_e(X_1)$. Due to the limited duration of any flood and the stochastic nature of erosion processes, the probability reduces of reaching the critical scour depth $L_e(X_2)$ and for plant X_2 to be uprooted. Hence, this process is fundamentally different from scouring and lets the stream uproot the plant via drag forces only, leading to the same conclusion found by Bywater-Reyes et al. (2015).

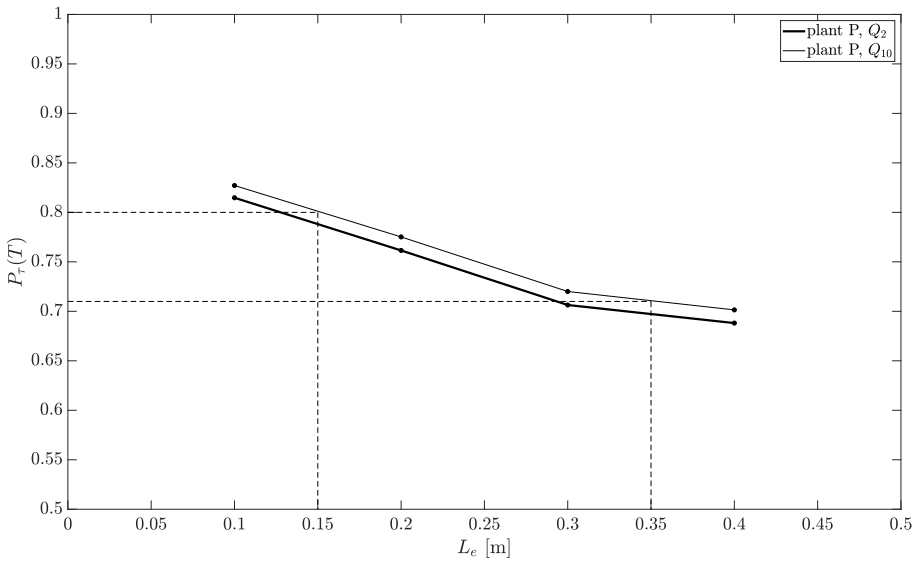

Figure 3.13: Uprooting probability as a function of scour depth in the Bitterroot river for Q_2 and Q_{10}. Here, X_1 and X_2 are two generic plants with scour depths of $L_e(X_1)$=0.15 m and $L_e(X_2)$=0.35 m, respectively.

3.5 Model limitations

Despite the assumptions introduced to tackle the problem analytically, the proposed model provides a satisfactory estimate of critical rooting length (i.e., r^2=0.81, 0.47) even when applied to field cases involving real hydrographs and plants with more complicated morphologies (i.e., leaf shape and root structure). This is a crucial aspect of the model, given that, in actual rivers and channels, the spatial and temporal scales of the process do not allow the critical rooting length to be recorded directly.

Even so, the model has several limitations. The main rooting length has to be known a priori because it forms part of the input data. The main rooting length varies with plant species and age, and so its estimation remains a challenge. For instance, the main rooting length of certain species has been found to be not only dependent on the stage of growth of the plant but also on intra- and

inter-species variability (Cannon, 1949; Köstler et al., 1968) as well as on spatial and seasonal variations (Kiley and Schneider, 2005). On the other hand, in certain circumstances, prediction of the main rooting length from above-ground biomass measurements is still possible. For example, for young *Avena sativa* seedlings (maximal 7-days-old seedlings) estimation of the main rooting length was successfully achieved by Edmaier (2014). However, such correlation laws may be hard to obtain for older plants and for plants with a more complicated morphological structure (see Calvani et al.'s data set). Approximating the root depth with the rooting length, as done previously (e.g., Edmaier et al., 2015), may not reflect what happens in nature. For instance, non-uniform soil texture or thigmotropism may induce roots to change their growth direction (Gregory, 2007).

Other limitations of the model arise from its inherent assumptions, outlined in the first section of this Chapter. The assumption of the bent configuration of the plant under drag loading might not be always be valid in practice. The drag acting on a canopy usually changes with plant bending and exposure time (Nepf, 2012). Another limitation arises from difficulty in estimating the correct value for C_f because of the flapping instability that occurs in plants with relatively long leaves. Such a mechanism was found to increase wake turbulence and generate very marked spikes in the friction factor (Connell and Yue, 2007). Given the primary contribution of the tangential component of the drag force, the flapping mechanism and plant vibration may be responsible for the scatter in the experimental data. Moreover, local fluctuations in the erosion-deposition processes could also provide a source of noise leading to the occurrence of uprooting at different times even under the same initial conditions (Perona and Crouzy, 2018). Randomness emerges also in the correlation law extrapolated from the pull out experiments. Variability in the relationship between F_p and L_0 may be caused by load redistribution among roots (Crouzy and Perona, 2012;

Edmaier et al., 2014) and readjustment of the portion of the soil that adheres to the roots when uprooting occurs. Intrinsic process noise is also generated in the hidden part of the plant, where tortuosity (Schwarz et al., 2010c), and friction between grains and roots play a key role. Even though the present model does not account for the foregoing processes, the limitations can be partly overcome by complementing the free-body model with the stochastic approach proposed by Perona and Crouzy (2018), as indicated in Section 3.4.

By modeling the critical rooting length, insight is provided into the uprooting mechanisms of riparian and aquatic vegetation. The present model has the potential to improve existing numerical models, which rely on assigned values of critical rooting length (such as Caponi and Siviglia, 2018) or adopt an uprooting threshold function of a modified critical Shield number (Bertoldi et al., 2014; Zen et al., 2016) or a dose-response relationship (Oorschot et al., 2016).

Chapter 4

Biomechanical properties of small-scale wood logs

The material presented in this Chapter appears in:
Bau', V., and Perona, P., Biomechanical properties and resistance to uprooting of laboratory-scale wood logs, *Journal of Geophysical Research: Biogeoscience*, 125(10). https://doi.org/10.1029/2020JG005782.

4.1 Wood log dynamics in river corridors

Within riparian zones, the hydrological, geomorphic and ecological processes interact over wide spatial and temporal scales and contribute to bidirectional exchanges of energy and material (Bendix and Hupp, 2000; Hungr et al., 2001; Johnston and Naiman, 1987; Likens and Bormann, 1974; Pinay et al., 2018; Steiger et al., 2005; Wilford et al., 2005). A key material exchange between rivers and adjacent riparian areas involves the transfer of wood logs to stream channels (Latterell et al., 2006; Naiman et al., 2000), a process that often takes place following high magnitude flooding events (Comiti et al., 2016; Mao et al., 2013; Ruiz-Villanueva et al., 2016; Zischg et al., 2018).

The presence of wood material has been recognised to be as fundamental a component of woodland fluvial ecosystem as sediment and riparian vegetation (Abbe and Montgomery, 1996; Anderson et al., 1978; Beckman and Wohl, 2014;

Gregory et al., 2003; Gurnell et al., 2002; Seo and Nakamura, 2009; Tockner et al., 2003; Wohl and Scott, 2017). Moreover, wood logs contribute to the geomorphic and hydrological evolution of riparian ecosystems.

The motion of wood logs involves three main steps: recruitment, transport, and deposition (Gasser et al., 2019).

Recruitment comprises the selection and delivery mechanism of wood logs from riparian buffer strips to streams, and is triggered by geophysical events of stochastic nature such as hillslope failure (Cadol et al., 2009; Comiti et al., 2016; Iroumé et al., 2015; Keller and Swanson, 1979; Nakamura and Swanson, 1993; Rigon et al., 2012), bank erosion (Downs and Simon, 2001; Gurnell et al., 2000; Lassettre et al., 2008; Moulin and Piégay, 2004; Sedell and Froggatt, 1984; Ulloa et al., 2015), snow avalanches (Bebi et al., 2009), stand-replacing events (e.g. tree windthrow (Welty et al., 2002), and wildfires (Benda et al., 2003; Rosso et al., 2007)).

The second wood motion step, transport, refers to the mobilization of wood logs in river corridors. This is also controlled and driven by river morphology, a first-order control on the wood regime (Wohl, 2019), and wood properties (e.g. orientation, size, and density) (Braudrick and Grant, 2000; Gurnell et al., 2002; Ruiz-Villanueva et al., 2016; Wohl, 2011). The transport of wood logs may present a hazard, especially when hindered by obstacles such as infrastructure and urban agglomerates (e.g. bridge piers).

Finally, deposition is the process by which wood logs settle on floodplains and alluvial bedforms such as bars and islands as a result of low flow conditions or narrowing of the river section. The deposition of driftwood entails fundamental ecological functions because driftwood provides niches for aquatic and terrestrial life-forms (Fisher and Likens, 1972), sustains water quality, and provides nutrients and shelter for organisms in a variety of physical habitats (Corenblit et al., 2011; Décamps and Naiman, 1990; Francis et al., 2008; Naiman and Decamps, 1997;

Welber et al., 2012).

Once wood fragments have deposited on moist sediment, there is a high probability that they develop adventitious roots and sprout (Barsoum, 2002; Dewit and Reid, 1992; Galloway and Worrall, 1979; Rood et al., 2003) and promote the formation of stable vegetated patches (Francis, 2007; Gurnell et al., 2005; Gurnell et al., 2012; Montgomery et al., 2003) (Figure 4.1). This, however, does only apply for vegetation that can reproduce asexually and for a limited range of species. For instance, in a study of the riparian forests of the Pacific Coastal Ecoregion, Naiman et al. (2000) report that redwood, willow, poplar, and ash are notable examples of species likely to develop roots from disseminated fragments.

Meanwhile, the success of rejuvenated wood logs in establishing roots on river bedforms depends on competition between the biological timescales of the plants and the frequency and magnitude of the hydrological events that the plant experiences. Hence, knowledge of how the biomechanical properties of wood logs evolve can contribute to assessment of their ability to withstand drag forces and their probability of regeneration on alluvial sediments.

Substantial research has been devoted to understanding the dynamics of recruitment and transport (Bocchiola et al., 2002; Braudrick et al., 1997; Daniels, 2006; Iroumé et al., 2015; MacVicar and Piégay, 2012; Martin and Benda, 2001; Ravazzolo et al., 2015; Ruiz-Villanueva et al., 2014), but has not yet explored the biological timescales and root resistance of the plants when deposited. Hence, investigation into such properties introduces an important new perspective from which to explore the dynamics of wood material in rivers. However, study of the biomechanical properties of wood logs in-situ is not an easy task, and it is therefore necessary to investigate the resilience of wood logs by undertaking controlled laboratory experiments.

Figure 4.1: Examples of regrowth stages of wood logs of different sizes found on river bars: a) Sprouting of a willow branch deposited on a bar in the Sense River, Switzerland (photograph courtesy of V. Ruiz-Villanueva); b) Deposited wood fragments on a bar in the Thur River, Switzerland (photograph: P. Perona) where it can be deduced from the stage of evolution of the branches that the root system of the logs may have developed a certain anchoring resistance; and c) example of sprouting from below the ground.

The aim of this Chapter is to study the growth dynamics of small-scale wood logs and explore their mechanical resistance through pullout experiments. These pullout tests were successfully performed under two different sediment moisture contents and at different growth stages. Particular attention was devoted to the uprooting force-displacement signal, and to the sequence of force drops. Based on the timescale evolution of stems and leaves, the flow-impact areas of the wood logs were computed to estimate the forces exerted by flow and to assess the wood logs resistance to uprooting.

4.2 Experimental procedure and set-up

4.2.1 Plant species selection

The species selected for these experiments is *Salix fragilis*. This species is part of the *Salicacae* family that, according to the literature and to the experiments in Chapter 2, was found to have a high ability to root in adequate soil moisture conditions. Furthermore, the use of cuttings rather than seedlings allowed

processes that occur widely in nature to be simulated, given that wood fragments deposited on river bedforms mainly derive from broken branches or trunks of trees transported during floods. In addition, the cuttings reproduce, at small scale, a tree trunk or wood log and facilitate the design of an upscaling procedure. The samples were harvested from the same tree from which the cuttings used in the previous experiments (Chapter 2) were collected.

4.2.2 Cutting selection and collection

The principle of sample selection was analogous to that outlined in Section 2.2.2. In the present case however, cuttings of similar diameter were carefully selected in order to facilitate the development of up-scaling rules. The resultant mean diameter of all collected samples, $\bar{d}$, was found to be 1.20 cm, with a standard deviation, σ_L, equal to 0.2 cm. Once extracted, the cuttings were pruned into four different standard lengths L: 5, 10, 15, and 20 cm.

4.2.3 Planting of cuttings

Cuttings were assigned randomly to rhizoboxes, but, unlike in Chapter 2, the cuttings were not placed in water before planting to prevent roots developing all over the surface of the trunk. Each sample was planted horizontally, half-embedded in a 16 cm soil layer with moisture content of 60%. The moisture content was also kept at this value for the whole duration of the experiments. The system used to regulate the water table in the sand was analogous to the that adopted previously. Therefore, the present moisture conditions were obtained by maintaining the water at a level 6 cm below the surface of the substrate (Figure 4.2a). Fully saturated conditions were avoided to reduce the risk of anoxia which, in the long term, could have led to the death of the plants.

As before, the sand did not contain any organic material, and cuttings were

not treated with any nutrients. The granulometry of the sediment is the same as illustrated in Figure 2.2.

4.2.4 Plant growth timescales

The duration of each experiment was prescribed according to the growth rates attained by the plants. Here, duration is defined as the period that elapses between the day when a log is planted and the day the log is uprooted. The lower time limit of growth was set to 2 weeks to allow the roots to develop a certain resistance. The maximum time growth was 9 weeks (Table 4.1). The upper growth limit was dictated by the state of health of the plants: it has been observed that after 60 days, plants were likely to weaken and die. It should be noted that, for most alpine rivers, this timescale corresponds to the return period of small to moderate floods able to remobilize the logs (Trush et al., 2000).

On average, every four days, the following measurements were taken for each cutting: the number of stems, their combined length, and the number of living leaves. The measurements were carried out throughout the plants' lifetime using a simple ruler (precision 0.1 cm).

The temperature in the laboratory was recorded to have a mean value of 22°C with a maximal diurnal fluctuation of 4°C.

4.2.5 Uprooting procedure and materials

Once cuttings had reached their specified growth duration, they were extracted from the soil using the motorized pulley system described in Chapter 2 (see also Figure 4.3a). For certain samples, the uprooting was obtained under the moisture conditions used over their growing time (60% of moisture, Figure 4.2a), whereas for the remainder, the water table level was raised to the sediment surface creating a saturated medium (Figure 4.2b). This latter scenario is more

representative of conditions to which pioneer plants are subjected, and it enables determination of the sediment moisture condition of plant uprooting in rivers.

Table 4.1: Summary table listing the length of cuttings tested, time slots of uprooting, and total number of samples pulled out. The uprooting time refers to the elapsed time between when cutting is laid on the sediment and when it is uprooted.

cutting size [cm]	**uprooting time [weeks]**	**total samples**
5, 10, 15, 20	2, 3, 4, 5, 6, 7, 8, 9	326

Figure 4.3b depicts the plant-wire connection system, which only differs from the previous system in the position where the pins were pierced. As Figure 4.3b shows, the extremities of the cuttings were those clipped to the wire. Cuttings were pulled up with the same constant vertical velocity used for vertical cuttings.

Measurements of the root architecture parameters were recorded immediately after the samples were uprooted, to avoid roots losing water content. Roots were gently detached from the log and washed to remove residual soil particles and then scanned using an EPSON Expression 10000 XL.

Starting from a predetermined reference point, the relative position of each root along the cutting was assigned an appropriate interval of 1 cm. Root architecture parameters (e.g., root length, volume, surface area) were computed using WinRHIZO BASIC 2009 root analysis software (Régent Instruments Canada, Inc.) for the total root biomass present in each interval.

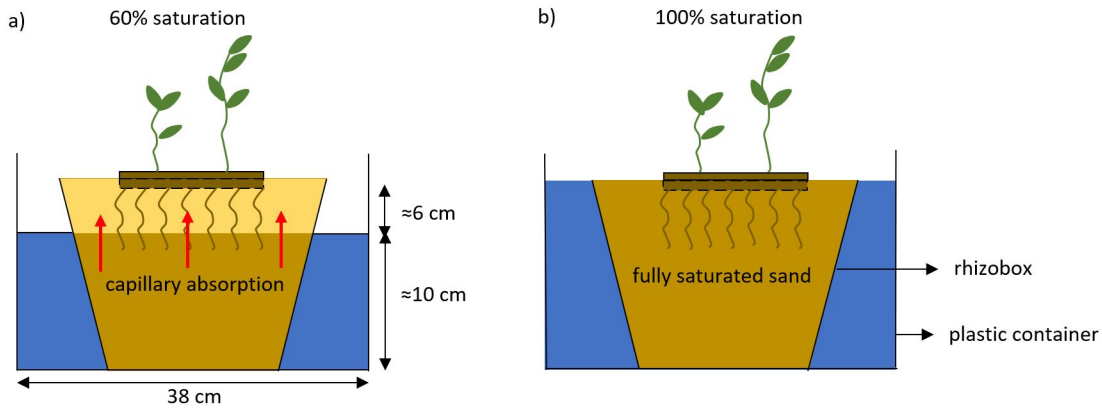

Figure 4.2: Sketches of the containers used in the experiments. a) Water level kept about 6 cm below the sediment surface, corresponding to 60% relative moisture of the unsaturated layer (this setting applied to the growth phase of all the plants); b) Soil moisture conditions when the samples were uprooted (to achieve 100% saturated soil, the water table level was raised to the surface of the sediment).

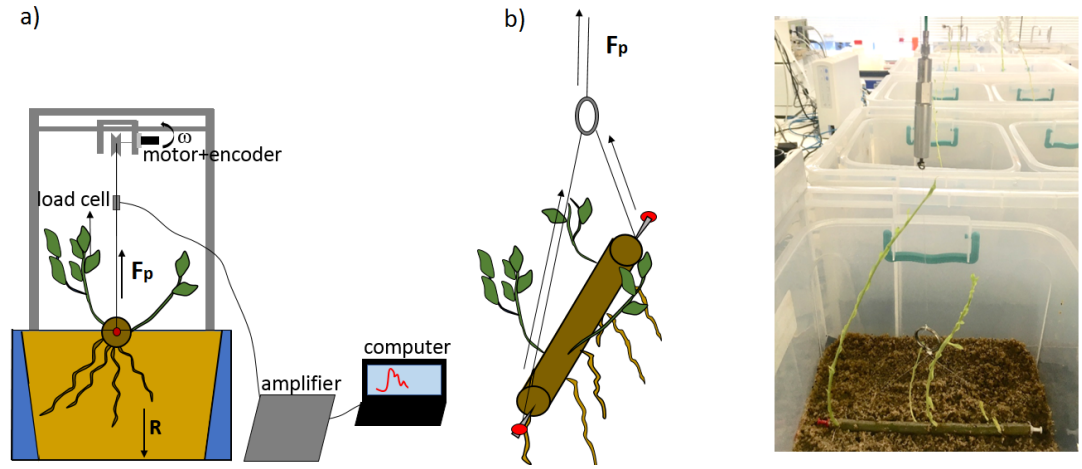

Figure 4.3: Sketch of the pullout experiment. a) Motorized pulley system: cutting is uprooted by an external force powered by a motor whose rotation was measured by an encoder. The exerted force $\mathbf{F_p}$ was continuously recorded by a load cell attached to an amplifier that, in turn, was connected to the computer. The modulus of $\mathbf{F_p}$ is equal to the anchoring resistance **R** developed by the root system; b) Schematic view and a photograph of the plant-wire connection system.

4.3 Plant growth tendencies

The evolution of plant biomass was evaluated in terms of sample averages, whose values were fitted to extrapolated growth laws for parameters representing below- and above-ground biomass. Computation of the averages was almost always undertaken for samples of the same size that were uprooted within the same week.

4.3.1 Below-ground biomass

Statistical analysis of the below-ground biomass focused on specific architectural parameters of the plant that affect uprooting resistance. Study of the development of biomass over the length of the cutting may shed light on possible up-scaling rules.

The scanned photo of the generic sample in Figure 4.4a reveals promising results. The root biomass per unit length, $\omega(x)$, is almost uniformly distributed over the distance coordinate x. Figure 4.4b confirms, overall, a uniform trend in the normalized cumulative distribution of surface area of the roots. The normalized cumulative root surface area is expressed by $\Omega(\tilde{x}) = \int_0^{\tilde{x}} \omega(\zeta) d\zeta$ and is represented over the normalised values of the cutting lengths: $\tilde{x} = \frac{x}{L}$. The normalized cumulative distributions in Figure 4.4b were plotted for all growth stages considered and for all cutting sizes.

A one-sample Kolmogorov-Smirnoff test was run to assess whether the observed data on root biomass were uniformly distributed over the normalized cutting lengths. The results have revealed that the null hypothesis is never rejected for a significance level equal to 0.05. Therefore, the empirical distribution functions are statistically close to the uniform density distribution. This indicates that the logs tend to develop roots at a constant spatial distance independently of their size, which is relevant for up-scaling purposes.

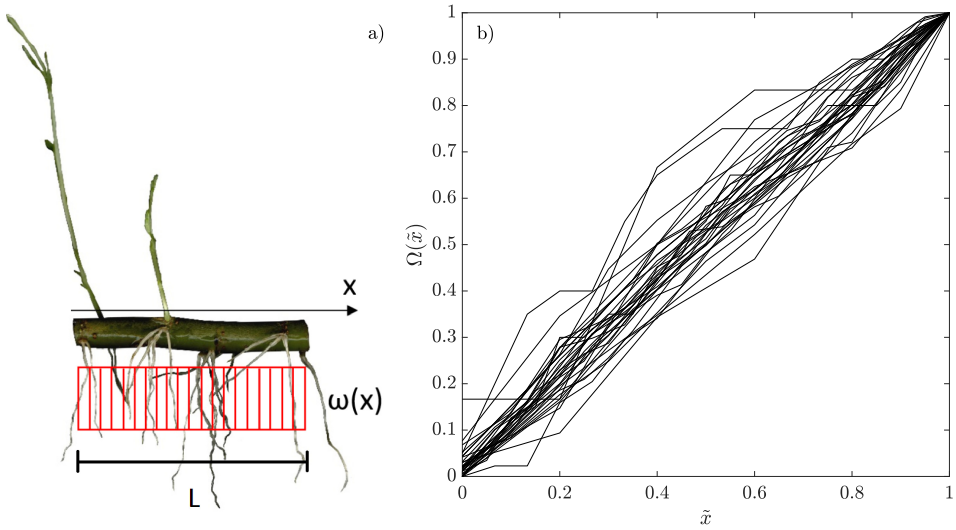

Figure 4.4: Distribution of root biomass over the length of the cuttings. a) Coloured scanned image of a sample of length L (red bars emphasize the uniform distribution of the root biomass over the distance coordinate x); b) normalized cumulative distributions of the total root surface area of the samples.

Figure 4.5a shows that the growth trends of the root lengths tend to follow power laws of the form $\bar{L}_r = a_4 \cdot t^{b_4}$. Similar tendencies can be seen in Figure 4.5b, where the variation in average number of roots, $\bar{n}_r$, is plotted over time. Average values of the number of roots were calculated using the same approach used previously for the total root length; the resulting fitting equations have the form: $\bar{n}_r = a_5 \cdot\ t^{b_5}$.

Once $\bar{L}_r$ and $\bar{n}_r$ were evaluated, the average root depth, $\bar{l}$ was determined by computing the mean value of the ratio of total root length to total number of roots grown in each interval. The values obtained were then further averaged across all the intervals, noting the uniform distribution of the roots along x (Figure 4.4). Values of $\bar{l}$ were determined for all plants uprooted at the same time regardless of their length L. Consequently, eight values of the averaged root

depth were obtained (Figure 4.5c) and fitted by a power law: $\bar{l} = a_6 \cdot t^{b_6}$.

Figure 4.4d depicts the relation between root diameter and total root length of the samples. The root diameter was derived by computing the average of the diameters of all the roots belonging to each sample. Once again, the trend can be expressed by a power law $d_r = a_7 \cdot t^{b_7}$. Table 4.2 lists the fitting coefficients of the power laws of Figure 4.5 and the respective goodness of fit measures, R^2.

On average, the growth trends exhibit power-law behaviour in terms of root length, number of roots, root diameter and depth. However, low values of the goodness of fit do occur, particularly when L= 5 cm (see Table 4.2). This suggests that data variability cannot be neglected. The variability is certainly due to the intrinsic randomness of plant development and the heterogeneity of plant characteristics. Even though cuttings were collected from the same tree, some did not develop roots, others died, and some developed stems faster than others even when subjected to the same external conditions (e.g. sediment, water percentage availability, and stable environment temperature). This variability in the data may also be attributed to the limited availability of samples when computing the statistical averages.

Table 4.2: Fitting coefficients and the goodness of fit R^2 for the power laws fitting $\bar{L}_r$, $\bar{n}_r$, $\bar{l}$, and d_r.

	$\bar{L}_r$			$\bar{n}_r$			$\bar{l}$			d_r		
cutting size [cm]	a_4	b_4	R^2	a_5	b_5	R^2	a_6	b_6	R^2	a_7	b_7	R^2
5	0.05	0.41	0.41	3.19	0.17	0.28						
10	0.08	0.58	0.92	4.08	0.30	0.64						
15	0.04	0.88	0.81	1.78	0.62	0.69	0.02	0.27	0.85	0.004	0.65	0.78
20	0.08	0.81	0.88	3.38	0.56	0.66						

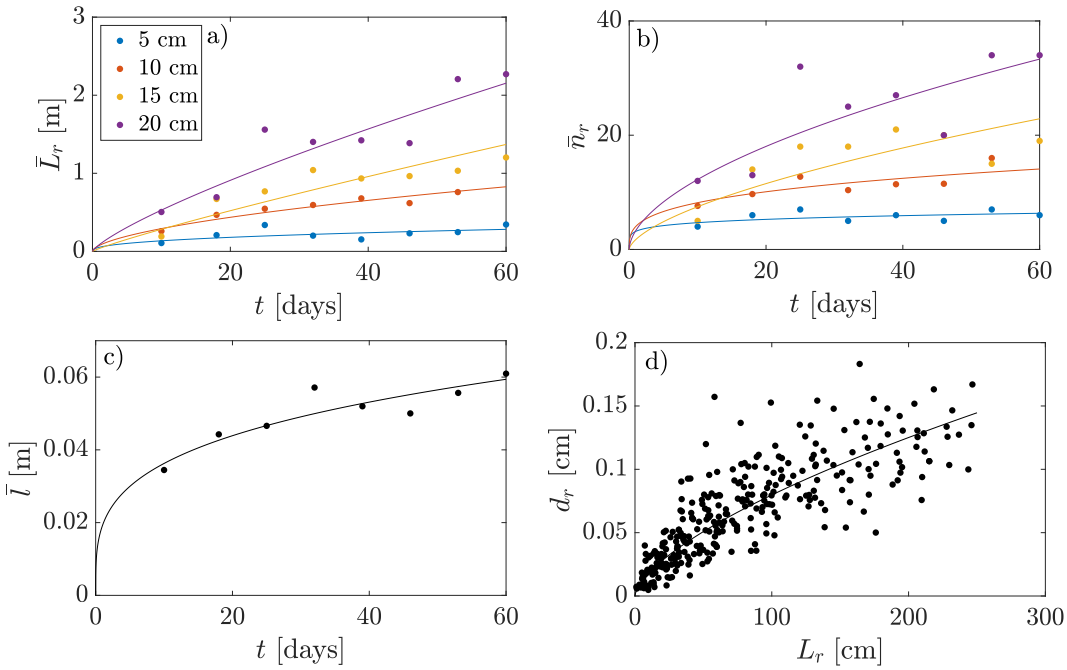

Figure 4.5: Average trends in below-ground parameters. a) Variation in average total root length with time for different sizes of cuttings; b) Variation in average root number with time for different sizes of cuttings; c) Variation in average root depth over time; d) Root diameter against the total root length.

4.3.2 Above-ground biomass

Statistical analysis of above-ground parameters considered growth trends in stem length and number of leaves, which are required in calculating the flow-induced drag forces acting on the plant canopy.

Figures 4.6a and 4.6b show that the stem growth rate alters according to the size of the cutting. As observed before for the root length and root number, this rate increases progressively with trunk size. The mean time needed by the plants to sprout fully is about 25 days (Figure 4.6a). Surprisingly, more time is needed by cuttings of size 20 cm to reach 100% of the sprouting rate. In general, the overall trend is that longer cuttings sprout faster.

Figure 4.6b illustrates the variation in average total length of the stems,

$\bar{L}_s$, with time for each size class. Here, the mean values are obtained as in subsection 2.4: the averages were computed over the total length of the stems that developed in each recording time. The trends of the dots suggest that, as in Chapter 2, the logistic curve (equation 2.1) is a suitable law here. To achieve the best fit, the logistic growth rate, k_l, was set equal to 0.12, independently of L. The sigmoid's midpoint, t_0, was located at 28 for both $L = 5$ cm and $L = 20$ cm and at 30 and 27 for $L = 10$ cm and $L = 15$ cm, respectively. The stems grew to a maximum length whose value represents the carrying capacity of the logistic model. The maximum length reached by the stems depends on the size of the cutting, and increases when L increases (Figure 4.6b). It is worth noting that the logistic curves represented in Figure 4.6b present higher values of the parameter t_o (Table 4.3) than the data listed in Table 2.2 in subsection 2.4. The stems of samples planted horizontally grew more slowly than stems of samples planted vertically. This is not surprising given that the available area for growth is considerably smaller for horizontally planted cuttings.

Figure 4.6c shows that the averaged number of leaves $\bar{n}_l$ correlates linearly with $\bar{L}_s$. Here, the data are fitted by a regression line of the form: $\bar{n}_l = a_8 \cdot \bar{L}_s$ Finally, a correlation between below- and above-ground biomass was also sought.

Figure 4.6d shows the correlation between the total length of the stems and the total root volume developed by the time of uprooting. However, due to the high variability of data, the stem length and root volume were referred to their mean values, $\bar{L}_s$ and $\bar{V}_r$, which were computed for samples at the same growth stage. Data follow a power law with equation: $\bar{L}_s = a_9 \cdot \bar{V}_r^{b_9}$.

A similar fitting law was also obtained in previous experimental studies (Pasquale, 2012). Table 4.3 lists the fitting coefficients for $\bar{n}_l$ and $\bar{L}_s$.

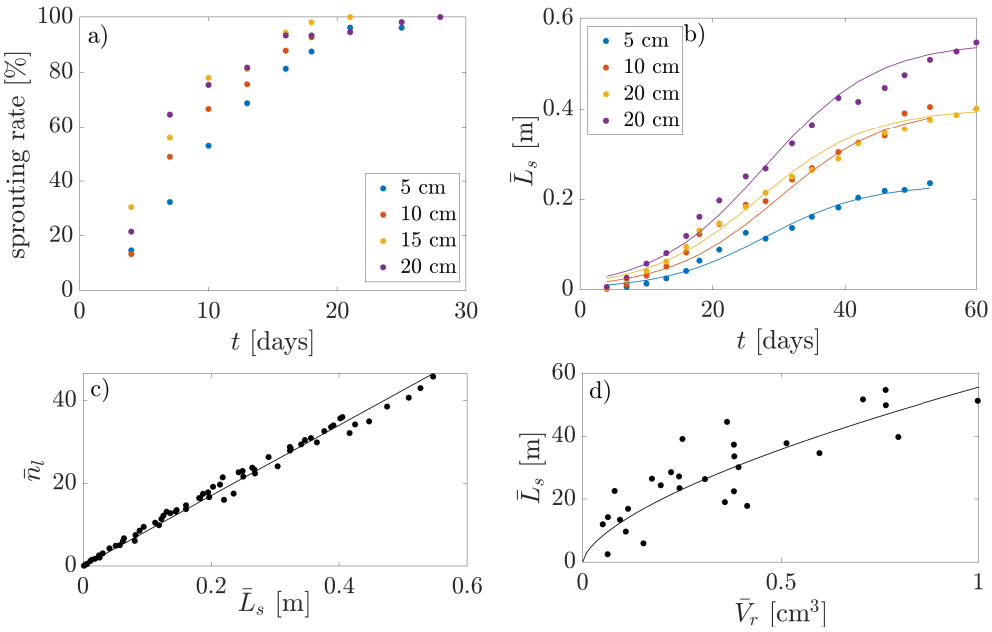

Figure 4.6: Averaged trends in above-ground parameters. a) Sprouting rate of *Salix fragilis* obtained for each cutting size; b) Trends in average value of the total stem length with time for each cutting size c) Average number of leaves versus averaged total length of the stems. d) Average total stem length versus averaged root volume.

Table 4.3: Values of the coefficients k_l and t_0 of the logistic curves, and the fitting coefficients and the goodness of fit R^2 for $\bar{n}_l$ and $\bar{L}_s$.

	logistic curve		$\bar{n}_l$			$\bar{L}_s$		
cutting size [cm]	k_l	$t_0[days]$	a_8	b_8	R^2	a_9	b_9	R^2
5	0.12	28	85	-	0.97	55.58	0.63	0.60
10	0.12	30						
15	0.12	27						
20	0.12	28						

4.4 Resistance to uprooting

4.4.1 Force-displacement curves

The force-displacement curves illustrated in Figure 4.7 present examples of uprooting signals obtained under partially and fully saturated soil conditions. In these plots, the main three phases of the uprooting process outlined in 2.6.1 can be still identified. When comparing the panels in Figure 4.7a to the those of Figure 4.7b, two main differences can be detected. Figure 4.7 not only shows that the maximum force peak reaches higher values in low saturated conditions, but also illustrates certain differences in the descending phase. Typically, in low saturated sand, anchoring forces decay rapidly with large and rapid drops following sharp peaks (Figure 4.7b). This trend is more discernible for 20 cm cuttings and less evident as the size of cuttings diminishes; this is because the load the plant needs to withstand is smaller. For saturated sand (Figure 4.7a), the descending phase is slower and smoother indicating more uniform friction, with smaller post-peak force oscillations. Similar behavior was observed by several authors including (Edmaier et al., 2014; Ennos, 1990; Schwarz et al., 2011) and will be further discussed in the next sections.

4.4.2 Uprooting force

In previous studies, the maximum root resistance exerted by roots was found to increase with the total length of the roots (Bailey et al., 2002; Edmaier et al., 2014; Ennos, 1989; Karrenberg et al., 2003). The same trend can be observed in Figure 4.8, where the maximum pullout force, F_p, increases linearly with the total root length of the samples, L_r, depending on the soil water content. For 100% saturation, the extrapolated law was found to be:

$$F_p = 0.82 \cdot L_r \tag{4.1}$$

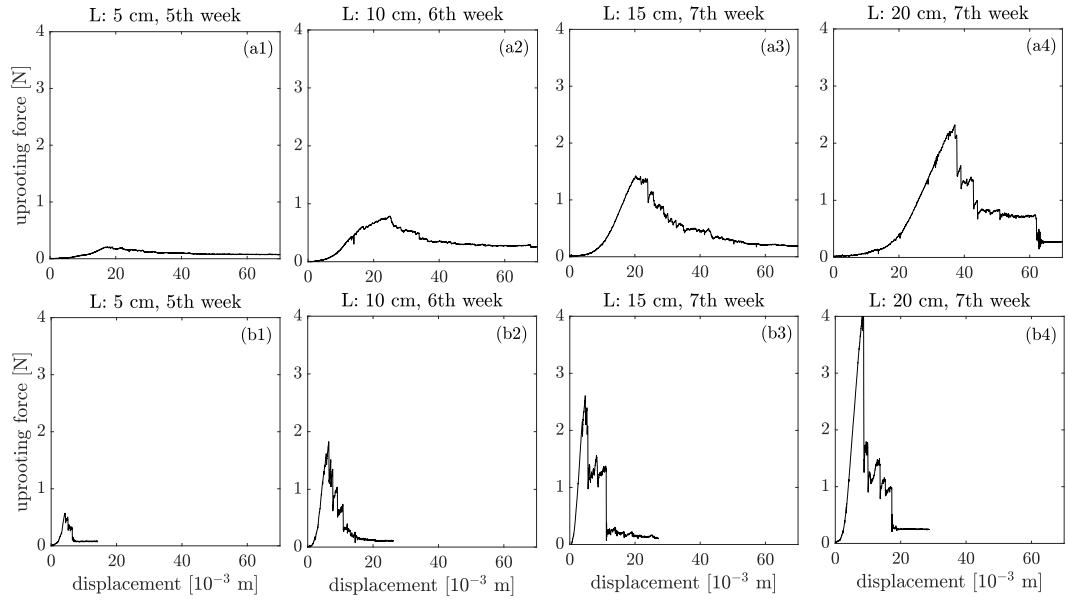

Figure 4.7: Force-displacement curves for *Salix* cuttings of different size L uprooted at different times. Samples illustrated in panels a) are uprooted under 100% saturation conditions, whereas those in b) are uprooted under 60% saturation. The cutting size L and uprooting time for each sample are illustrated as follows: a1) $L = 5$ cm, week = 5^{th}; a2) $L = 10$ cm, week = 6^{th}; a3) L= 15 cm, week = 7^{th}; a4) $L = 20$ cm, week = 7^{th}; b1) L =5 cm and week = 5^{th}; b2) $L = 10$ cm, week = 6^{th}; b3) $L = 15$ cm, week = 7^{th}; b4) $L = 20$ cm, week = 7^{th}.

with $R^2 = 0.67$, and $r^2 = 0.82$. For 60% saturation:

$$F_p = 2.24 \cdot L_r \tag{4.2}$$

with $R^2 = 0.54$, and $r^2 = 0.78$.

By comparing the laws given by equations 4.1 and 4.2, it is obvious that the maximum uprooting force for fully-saturated conditions is more than twice lower than for unsaturated conditions. This is in accordance with the discussion in Section 2.6.2. The uprooting force increases with time, as can be seen by the relationships between total root length and time depicted in Figure 4.5a. Moreover, it can be observed that the maximum uprooting force simply depends

on the size of the cutting via the total rooting length, which, in turn, scales with the cutting size L. This confirms the existence of a possible up-scaling law (given the low variability of the cutting diameters).

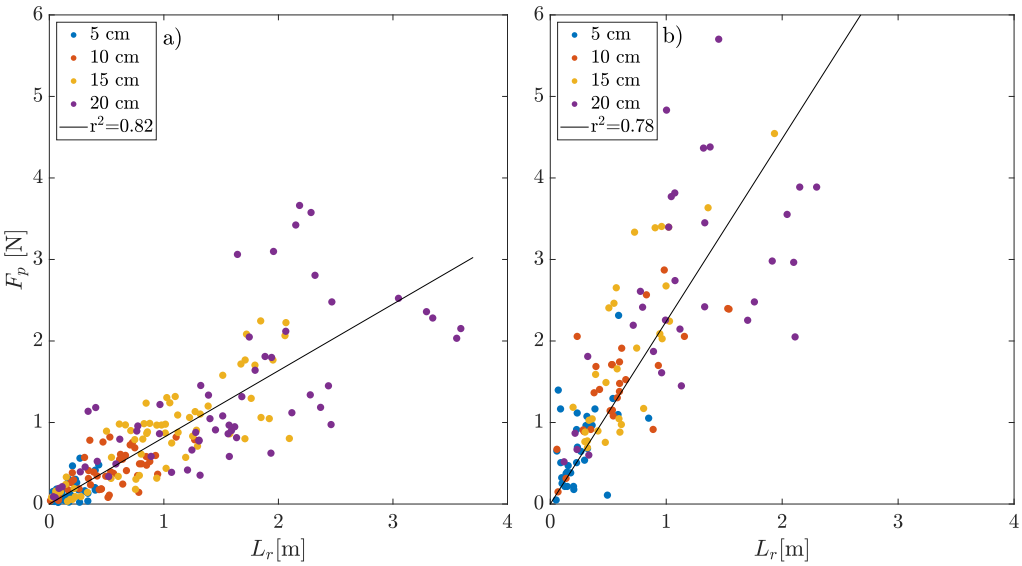

Figure 4.8: Maximum uprooting force plotted against the total root length. a) 100% saturated medium; and b) 60% saturated medium.

4.4.3 Uprooting work

The work done by uprooting (Figure 4.9), obtained by computing the area under the force-displacement curve, reveals valuable information about the resilience to uprooting of the plant. In 100% sediment moisture content (Figure 4.9a), the uprooting work is better approximated by a second-degree polynomial law, whereas for plant uprooted in low saturated sand (Figure 4.9b) the work increases linearly with total root surface area, albeit with a higher variability.

The occurrence of the two different trends in the uprooting work may be explained by examining the post-peak phase of the force-displacement curve in Figure 4.7, where a substantial part of the work takes place. For fully-saturated sand, the uprooting process requires more time to complete than for

low-saturated conditions (compare Figures 4.7a and 4.7b), when roots have less resilience because of the energy loss occurring in shorter time and space.

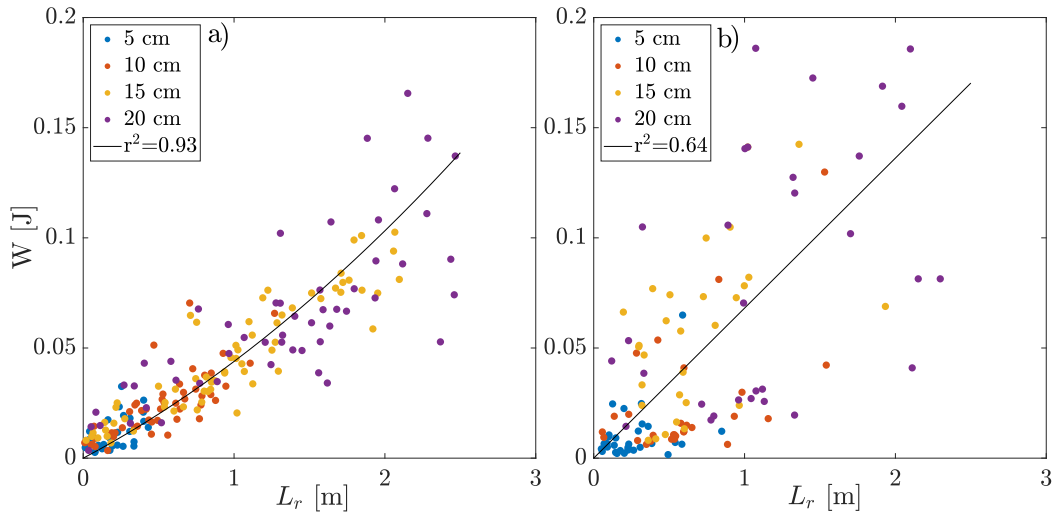

Figure 4.9: Maximum uprooting work plotted against total root length: a) 100% saturated medium, where the fitting law is quadratic such that W=7.7·10$^{-3}L_r^2$+3.6·10$^{-2}L_r$, R^2=0.83, and r^2=0.93 (Spearman coefficient); and b) 60% saturated medium, where the fitting law is linear such that W=6.2·10$^{-2}L_r$, R^2=0.42, and r^2=0.64.

4.5 Force drop analysis

In carrying out statistical analysis of the force drops it is necessary, first, to define what are force drops and classify them quantitatively.

4.5.1 Definition of force drop

Force drops correspond to the monotonic decline of the force-time signal between two successive local maximum and minimum values. However, such monotonic decline may occur with differing mean gradient. Hence, it is necessary to introduce a parameter that can represent the steepness of the force drops and be used for their classification. The parameter is here denoted as α, expressed as the ratio

of local maximum-to-minimum differences of two consecutive values of forces dF to their respective time-lapses dt (Figure 4.10a). By varying α, the force drops can be classified according to size and number.

4.5.2 Force drops under different soil moisture conditions

Figure 4.10b shows the variation in ratios of number of force drops to α in 100% saturated soil, N_{100}^F, and 60% saturated soil, N_{60}^F, when varying α between 0.5 and 1.5. N_{100}^F and N_{60}^F are obtained by computing the average of the number of force drops filtered out from the force signals from plants uprooted at the same time in saturated and unsaturated conditions, respectively.

From Figure 4.10b, it can be seen that the ratio $\frac{N_{100}^F}{N_{60}^F}$ decreases exponentially for $\alpha \geq$0.5-0.9 and becomes almost constant from $\alpha \geq$1. Therefore, $\frac{N_{100}^F}{N_{60}^F}$ becomes independent of α when α is close to 1. This leads to the easy deduction that mild drops are more recurrent when plants are uprooted in saturated soil.

Figure 4.11 illustrates the cumulative relative frequencies of the force drops magnitude computed for plants with similar root length and uprooted at the same time for two different sediment moisture conditions, e.g. as shown in Figure 4.7a4 and 4.7b4. When $\alpha \geq$0.5 (Figure 4.11a), 50% of the force drops for a plant uprooted in saturated sediment have magnitude below 0.017 N, unlike 0.107 N for a plant pulled out from low saturated sediment. For the same value of α in 100% saturated sediment, the force drops have magnitude in a range 4 times larger than in highly saturated sand. A similar trend can be observed when $\alpha \geq$1.5 (Figure 4.11b). Hence, the magnitude of force drops is higher the less saturated is the sediment, suggesting occurrence of stronger adhesion among sediment particles (Edmaier et al., 2011). Therefore, regardless of the size of the sequences of the force drops, the mechanism by which downward jumps occur changes according to the moisture level of the sediment.

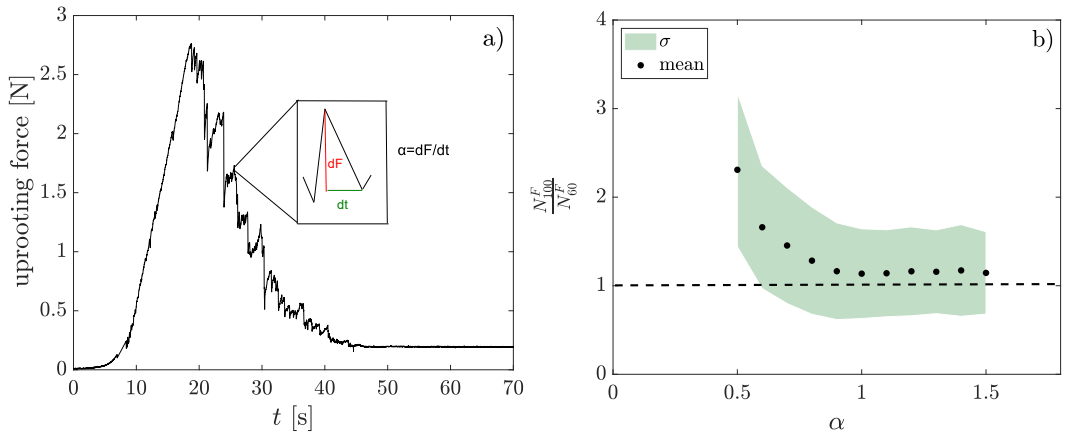

Figure 4.10: Relationships between uprooting force with time and force drop ratio with α: a) Generic force-time curve illustrating the concepts of dF, dt, and α; and b) Averaged ratio of number of force drops in 100% saturated soil to that in 60% saturated soil as a function of α, with standard deviation σ superimposed.

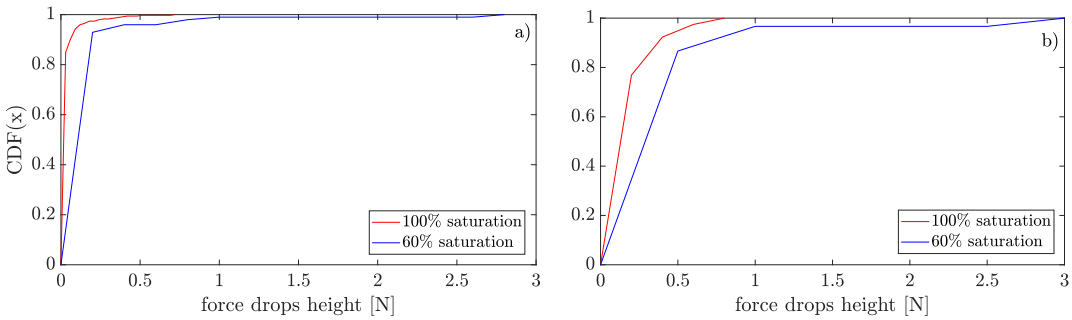

Figure 4.11: Cumulative probability distributions of force drops corresponding to the force-displacement curves in Figure 4.7a4 (100% saturation) and 4.7b4 (60% saturation) when: a) $\alpha \geq 0.5$; and b) $\alpha \geq 1.5$.

4.5.3 Autocorrelation function

It is also instructive to compare the autocorrelation function of the sequences of force drops dF and their inter-time dT.

The formulas to obtain the autocorrelation function are given in Appendix C.

Figure 4.12 shows a series of autocorrelograms, on which are superimposed blue solid lines demarking the confidence bounds. For 100% saturation and

$\alpha \geq 0.5$, the autocorrelograms of the sequence of the force drops, and their respective intertimes show positive, though low, correlations for almost each lag (Figures 4.12a1 and 4.12a3). This is most likely due to rearrangement of sand grains in the soil matrix when roots are sliding. This is not the case in low saturated conditions (Figures 4.12b1 and 4.12b3), where the correlation is not significant.

This discrepancy in the autocorrelograms may be explained as follows: when the medium is entirely saturated, water fills the pores and roots tend to slide between the sand grains. The presence of water modifies the sand grain arrangement around the roots and causes regular force decays to occur (Schwarz et al., 2011). On the contrary, for lower water content in the sediment (60% of water content), the force signal (Figure 4.7b) exhibits steeper force drops (steep loosening). Once roots exceed soil strength, the lower cohesion of sand allows quicker movement of the roots through the grains. Thus, the force drops and the related inter-times between them assume an autocorrelated "white" noise structure. Moreover, the large force drops and the related inter-times appear to have a correlation structure with a spatial scale comparable to the smallest fluctuation in the process, i.e. of the order of sediment grains.

In saturated soil (Figure 4.12a2), the correlation of dT narrows to zero before falling below the bound after the third lag. In low-saturated sand, the loss of correlation in the time signal occurs after the first lag (Figure 4.12b2). Knowledge of the 'constant' uprooting velocity and mean inter-time between force drops allows computation of the average displacement of roots, δx. In 100% saturated soil, $\delta x = 0.08$ mm, whereas in low saturated soil, $\delta x = 0.10$ mm. By multiplying the number of lags (within which correlation subsists) by δx, it is found that in full and low saturated conditions, each steep force drop occurs after a spatial slip of about 4 and 10 grains^{-1}, respectively. This is obtained by assuming that force drops occur at the spatial scale of a sediment grain, following Crouzy

et al. (2014). Hence, in a fully saturated medium, the process is correlated, and the sand matrix continuously manages to readjust throughout root sliding. However, just when roots have slid over 4 sand grains^{-1}, a steep force drop occurs introducing randomness to the signal. On the other hand, under low-saturated conditions, roots slide only when the magnitude of uprooting force is sufficiently high to create gaps among the grains that, without lubrication, cannot readjust and let the root slide. Hence, the spatial scale at which large fluctuations occur changes according to the saturation percentage of the soil. This different behavior would suggest that, for similar root lengths, a steep jump in low saturated soil takes place with higher spatial frequency than in fully saturated conditions albeit in a much shorter amount of time. The opposite is true for saturated soil.

To conclude, the autocorrelation functions provide further insight into the frequency at which force drops occur, so complementing the results illustrated in Figure 4.10.

4.5.4 Residual uprooting force

Finally, it is interesting to analyze the final force recovery event in the force-displacement signal, F_{res}, and compare it to F_p (both parameters are illustrated in Figure 4.13). In the scatter plots in Figure 4.13, two main regions can be identified.

Region I, to the left of the green line, includes mostly small cuttings of which some of the less mature 15-20 cm cuttings have invested all their energy in withstanding the uprooting force. Notably, for fully-saturated soil, the data in the left region are dispersed within a range of $\frac{F_{res}}{F_p}$ that is larger than in low-saturated medium. This agrees with the trends in descending phases observed in Figure 4.7.

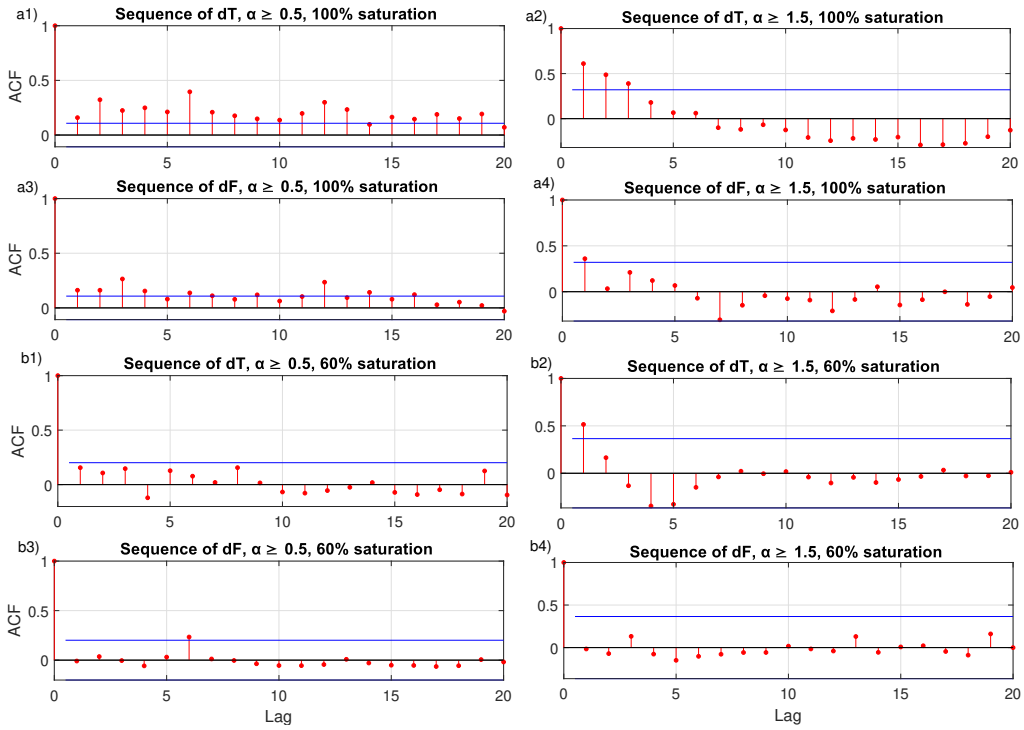

Figure 4.12: Autocorrelation functions of the force drops dF and their respective intertime dT. The blue solid lines demark confidence bounds. Autocorrelation of the force drops intertime dT for 100% saturation when: a1) $\alpha \geq$0.5; a2) $\alpha \geq$1.5; Autocorrelation of the force drops dF for 100% saturation when: a3) $\alpha \geq$0.5; a4) $\alpha \geq$1.5. Autocorrelation of the force drops intertime dT for 60% saturation when: b1) $\alpha \geq$0.5; b2) $\alpha \geq$1.5; Autocorrelation of the force drops dF for 60% saturation when: b3) $\alpha \geq$0.5; b4) $\alpha \geq$1.5.

In 60% saturated soil, the energy loss occurs with large force drops and over shorter time intervals than in 100% saturated soil. This implies that the residual energy of roots may not be sufficient to generate a resistance F_{res} comparable to F_p.

Region II includes cuttings uprooted at a later stage of growth, when $\frac{F_{res}}{F_p}$ is almost constant regardless of the value of F_p. The presence of mature plants in the right hand region indicates that older plants can have higher resilience. A similar division of $\frac{F_{res}}{F_p}$ data into two regions with respect to F_p was also observed

by Crouzy et al. (2014) for *Avena sativa* plants.

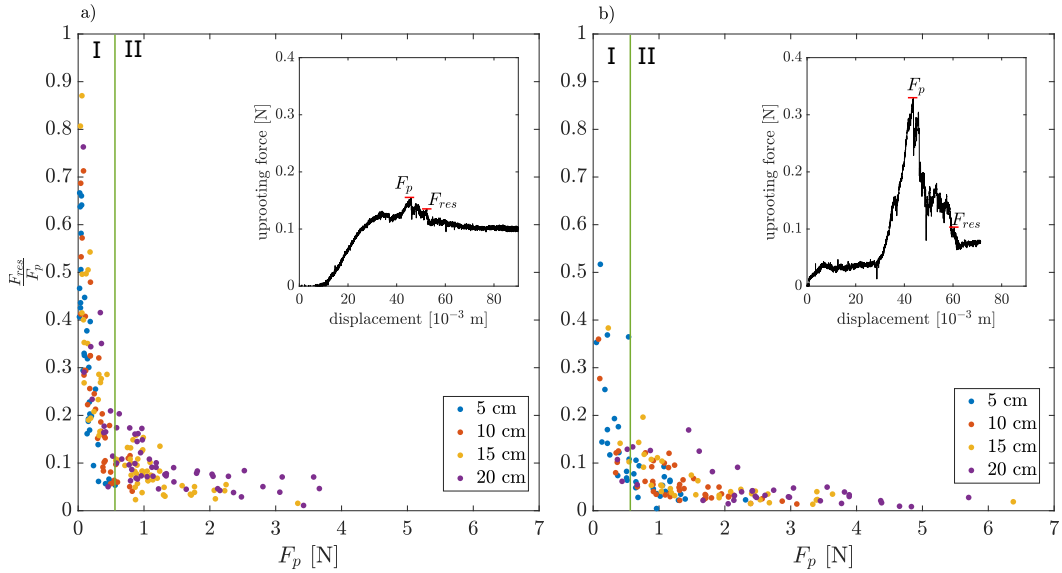

Figure 4.13: $\frac{F_{res}}{F_p}$ versus F_p for uprooting in: a) 100% saturated soil; and b) 60% saturated soil. The inset panels comprise displacement curves on which are marked the maximum uprooting force F_p and the residual force F_{res} that indicates failure of the last plant fiber.

4.6 Uprooting by flow

The likelihood of a wood log being removed by flow does not depend only on its relative elevation on the patch and flood characteristics, but also on the log's biomechanical properties. Whether a wood log is uprooted or not depends on the stage of growth that the plant has reached by the time the flood arrives. By studying the statistics of plant growth, it is possible to assess the trend in drag force over different plant growth phases and compare the trend with the evolution of root resistance derived from pullout experiments. Given that the root resistance law was determined in the previous section (equation 4.1), it only remains to compute the drag force. The coefficients in equation 4.1 are selected

to simulate soil conditions typical of a scenario of a flooding event.

4.6.1 Drag force computation

In the previous Chapter, it has been established that the forces destabilising a submerged plant comprise the water drag forces and the net buoyancy force. By neglecting the contribution by buoyancy, the force balance for overall drag on a log are described by the following equation:

$$\mathbf{F_d} = \mathbf{F_{d,n}} + \mathbf{F_{d,t}} \tag{4.3}$$

where the modulus of the normal component $\mathbf{F_{d,n}}$ and tangential component $\mathbf{F_{d,t}}$ of the drag force are expressed by equations 3.7 and 3.8. The projected area of the trunk of the log in the flow direction, A_n, depends on the orientation of the trunk towards the flow. In this case, it was assumed that the impact between the flow and the longitudinal cross-section of the log is perpendicular, hence analyzing the worst-case scenario. The surface area exposed to the flow, A_t, was set equal to: $A_s + A_f$, which is the sum of the total surface area of stems, A_s, and the total area of leaves, A_f, exposed to flow. C_d and C_f were each assigned a representative value of 1 (Järvelä, 2002), thus being also in line with the values obtained in Chapter 3.

Following the approach used in Chapter 3, estimation of the projected and surface areas A_n, A_s and A_f, was made possible by approximating the shapes of the trunk, stem and leaves by geometric shapes. In these circumstances, A_n, A_s, and A_f were approximated by a rectangle, a cylinder, and a rhombus, respectively. The modulus of the drag force then becomes:

$$F_d = \frac{1}{2} C_D \rho_w u^2 \left(A_n\right) + \frac{1}{2} C_f \rho_w u^2 \left(A_s + A_f \bar{n}_l\right) \tag{4.4}$$

By expressing A_s in average terms and using the fitting laws of $\bar{n}_l$ extracted

in section 3.3.2, equation 4.4 becomes:

$$F_d = \frac{1}{2} C_D \rho_w u^2 \left(\frac{L\bar{d}}{2} \right) + \frac{1}{2} C_f \rho_w u^2 \left(\pi d_s \bar{L}_s + A_f a_8 \bar{L}_s \right) \tag{4.5}$$

where $\frac{L\bar{d}}{2}$ is the projected area of the wood log in the flow direction and d_s is the diameter of the stem.

Graphically, uprooting takes place when the drag surpasses the root maximum resistance curve. In order to be able to plot the drag forces and the resistance law $R(L_r)$, the drag force components in equation 4.4 have to be written as functions of the total root length L_r. Consequently, both the total surface area of the stem A_s and the total surface area of the leaves A_f must also be expressed in terms of L_r.

Using the fitting law for $\bar{L}_s$:

$$\begin{aligned} F_d = \frac{1}{2} C_D \rho_w u^2 \left(\frac{L\bar{d}}{2} \right) + \frac{1}{2} C_f \rho_w u^2 \pi d_s \left(\frac{c}{1 + e^{-k_l (t - t_0)}} \right) \\ + \frac{1}{2} C_f \rho_w u^2 A_f a_8 \left(\frac{c}{1 + e^{-k_l (t - t_0)}} \right) \end{aligned} \tag{4.6}$$

By invoking the link between time and average root length from Figure 4.5a and, under the reasonable assumption that $\bar{L}_r \approx L_r$, equation 4.6 can be rewritten as follows:

$$\begin{aligned} F_d = \frac{1}{2} C_d \rho_w u^2 \frac{L\bar{d}}{2} + \frac{1}{2} C_f \rho_w u^2 \pi d_s \left(\frac{c}{1 + e^{[-k_l ((\frac{L_r}{a_4})^{\frac{1}{b_4}} - t_0)]}} \right) \\ + \frac{1}{2} C_f \rho_w u^2 A_f a_8 \left(\frac{c}{1 + e^{[-k_l ((\frac{L_r}{a_4})^{\frac{1}{b_4}} - t_0)]}} \right) \end{aligned} \tag{4.7}$$

Figure 4.14a displays the trends in dimensionless drag force, $\hat{F}_d$, and maximum root resistance, $\hat{R}(L_r)$, with increasing L_r. The plot refers to a cutting with $L = 20$ cm and a fixed value of impact velocity u. The dimensionless forms were obtained by dividing equations 4.1 and 4.7, respectively, by the product: $\frac{1}{2} C_f \rho_w u^2 \bar{d}^2$, such that the drag force is parametrized by L and the root resistance scales with u.

It is obvious that uprooting occurs within two temporal windows. The first one, I, is located at the very early stage of plant growth when the root length is still small and the curve of the drag forces is convex. The second window, II, occurs in the section of the curve that coincides with the terminal growth stage of the plants. The occurrence of biological time windows reminds of the concept introduced by Balke et al. (2011), who studied the threshold for the establishment of mangrove seedling on tidal flats.

Figure 4.14b shows the trend in dimensionless drag force with root length for all values of cutting length L. Here, $\hat{R}(L_r)$ is plotted for increasing values of u (gray lines). It can be observed that the curves representing $\hat{F}_d$ cross the L_r=0 axis at different ordinate values. This is due to the fact that, when wood logs have not yet developed any above- and below- ground biomass, the drag force acts only on that portion of the trunk exposed to the flow. Over a certain range of low flow velocities, wood logs can provide resistance to drag forces without any contribution from root resistance. Importantly, this means that the present model is applicable both to species able to reproduce asexually, and to species incapable of resprouting.

On the other hand, the drag force curves interrupt at different values of L_r, with the maximum values reached by L_r depending on L, as seen in Figure 4.5a. Moreover, unlike the root resistance curves in Figure 4.8, the trends in drag forces are affected by the size of the cuttings.

In other words, Figure 4.14 displays the timescales for which stranded wood logs can be threatened by flooding events.

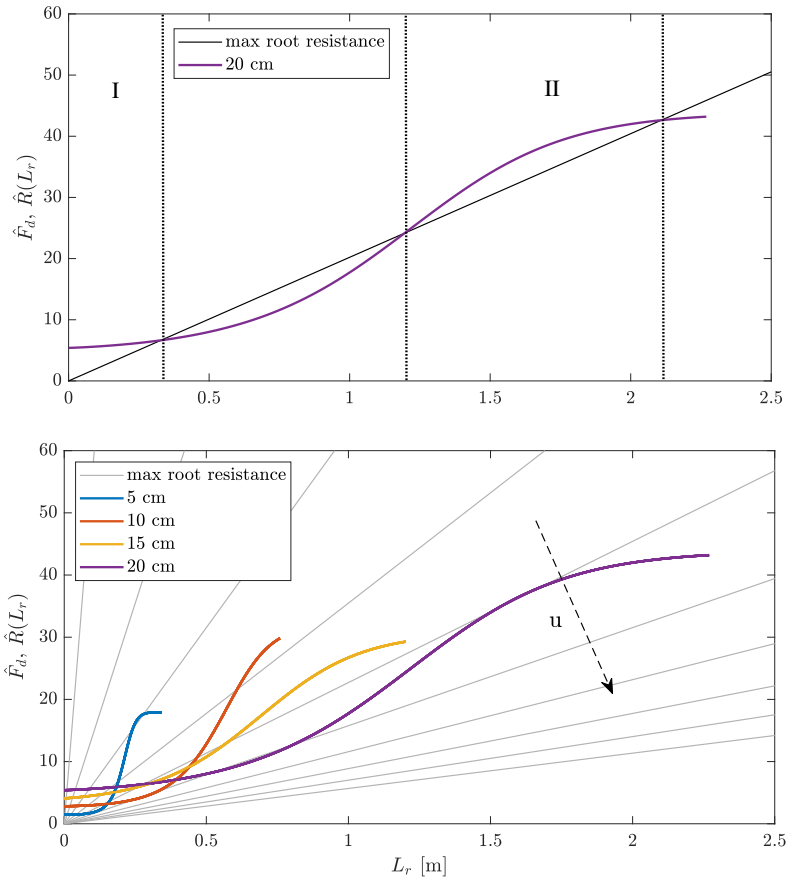

Figure 4.14: Relationship between dimensionless drag force and maximum root resistance: a) for $L = 20$ cm and a fixed value of u; b) for all cutting sizes L and different values of u.

4.7 Strengths and shortcomings of the current application

The results presented in this section have demonstrated the versatility of the free-body model presented in Chapter 3. In particular, the findings in the previous Section confirm that the free-body model can be suitably applied to wood logs. It should be noted however that scouring processes, accounted in the free-body model in Chapter 3, were not considered here. As a consequence, the type of uprooting simulated here is of Type I. This simplification is nevertheless

consistent with the young growth state of the samples considered. In practice, when the scour depth is known, equation 4.6 can be rewritten by adding the contribution of the force acting on L_e, by following the approach suggested by equation 3.15, which also takes into account the surface area of exposed roots.

Another aspect to consider is the assumption concerning the impact angle of flow-cutting. When computing the drag force, the cases solely considered flow impact perpendicular to the longitudinal cross-section of the log. More complex scenarios, which involve impacts at other angles, were not examined.

The present experiments and analysis have enabled light to be shed on limitations that were not identified in the previous Chapter. The main constraint arises from having expressed the maximum uprooting force as a function of total rooting length. This implies that the strength exerted by a long root results from the summed individual root strength, assuming perfect cooperation among roots (Ennos, 1993). However, it may be thought that the pullout force is not built up by the individual and simultaneous contribution of all roots. Roots are not pulled in parallel, but uprooting is a "slightly cumulative process", as described by Edmaier (2014), where a root is strained just after loosening of another root that was previously under tension. Nonetheless, it should be noted that the calculation of maximum root resistance included contributions provided by root hairs and secondary roots, whose cooperation is significant in multi-root systems (Bailey et al., 2002; Ennos, 1989).

To conclude, despite the aforementioned limitations, the present analysis provides a useful tool to inform new flood protection measures and to understand the contribution of wood logs to river ecology, management, and restoration. It is hoped that the present experiments will be further reproduced at larger scales in order to develop up-scaling rules that would be useful in predicting such complex dynamics.

Chapter 5

The role of vegetation roots in riverine ecosystem resilience

5.1 Flow regime shifts in riparian ecosystems

Riparian ecosystems are highly dynamic systems that serve as transitional bodies between land and water through an exchange of energy, materials, and biota (Helfield and Naiman, 2001; Naiman and Decamps, 1997; Ward, 1989). This connectivity takes place over a very large spatial extent, and such complex interaction makes riparian ecosystems vulnerable to perturbations of the natural flow regime. Riparian ecosystems have therefore become one of the most threatened ecosystems globally (Theobald et al., 2010).

The 'master variable' that shapes and regulates the process rates and the dynamics of riparian ecosystems (Power et al., 1995) is the flow regime. According to Poff et al. (1997), the flow regime has five relevant components (magnitude, frequency, timing, duration, and rate of change) that together contribute to regulate the ecological dynamics of the riverine ecosystem and its geomorphological assets. The natural river flow variability enables the occurrence of many physical and biogeochemical processes that are essential for the correct functionality of the ecosystem (Karr, 1991; Poff et al., 1997; Richter et al., 1997). For instance, the natural intermittence of magnitude and frequency between high and low flows ensures a proper balance between seed dispersal and sediment (induced

by high flow) and vegetation recruitment (induced by low flow). Hence, the life cycles and functionality of biota are regulated and have adapted to the natural variability of the flow components (Bunn and Arthington, 2002; Lytle and Poff, 2004).

However, in recent decades, riverine landscapes have been subjected to human-induced perturbations that have altered the structure and functions of local ecosystems to accommodate human needs. Irrigation systems, groundwater exploitation, dams, and other forms of river adaptations have triggered serious alterations to the natural flow regime, which, in turn, have had detrimental repercussions on the equilibrium of the riparian ecosystem, leading to its ecological degradation (Bunn and Arthington, 2002; Petts, 1984; Poff et al., 1997; Rosenberg et al., 2000). However, anthropogenic activities are not the only flow regime stressors; the quantity and pattern of streamflow are also affected by erratic hydroclimatic drifts (e.g. intense precipitation) (Campbell et al., 2011). Therefore, anthropogenic activities and climate change are jointly responsible for hydrologic shifts in free-flowing river systems.

Disruption of the dynamic equilibrium of natural flow regimes has a visible impact on the geomorphic asset of the river and the ecological services offered by river biomes. Hence, it is important to design works that alter the flow regime to mitigate their impact on the riverine ecosystem services. For instance, tracking the response of different ecological indicators to river flow alterations may help to detect possible early warning signals and hence prevent future hydrological shifts (Vigiak et al., 2018). Several studies have proposed a qualitative analysis of the ecological response of different taxonomic identities towards different types of flow alterations (e.g. Bunn and Arthington, 2002; Poff and Zimmerman, 2010). However, tracking ecologic indicators and their feedback to hydrologic stressors is not an easy task. Ecological indicators are in fact scattered across environments characterized by different spatial and temporal scales, and may also be influenced

by local environmental conditions (Lloyd et al., 2004). Furthermore, accurate forecasting of the effects of flow regime shifts is further hindered by the fact that flow regime alterations may not systematically occur as a direct consequence of landscapes and climatic drifts, towards which flow regimes exhibit a certain level of resilience (Botter et al., 2013). In such cases, qualitative ecological indicators are unable to respond immediately to ecosystem change. Consequently, it is important to combine qualitative ecological investigations with analytical models, which use measurable indexes to provide a continuous signal of the ecosystem state in response to flow regime shifts, in order to plan suitable mitigation strategies for water resources management.

5.1.1 Ecological and geomorphological impacts caused by river dam regulation

Dams are the most obvious disruptor responsible for altering the natural flow regime of a river (Poff et al., 1997). After a river is dammed, its flow magnitude and frequency characteristics dramatically change, and seasonal patterns of water discharge evolution can vanish being replaced by persistent low flow periods disrupted by a few high flow peaks (Magilligan and Nislow, 2005). The onset of a low flow regime also has a direct effect on the groundwater table dynamics, which is also subjected to level drops (Williams and Wolman, 1984). As a result of dam installation, riverine biota communities, which rely on and are synchronized with certain patterns of water and nutrient availability, have to develop new strategies to adapt to the new water stress regime (Lytle and Merrit, 2004). Reduced flood flows create stagnant pools and limit connectivity with other floodplain areas. This hinders the existence of pathways for dispersing organisms (Kondolf et al., 2006; Naiman and Decamps, 1997), and reduces the mobility of aquatic animals and their ability to have access to adjacent habitats. Water stratification

in reservoir upstream of a dam lowers the level of dissolved oxygen, which can induce anaerobic reactions that may promote release of ammonia and hydrogen sulfide (Canter, 2018). Eutrophication is another common biogeochemical process that affects reservoirs. Eutrophication occurs as a result of influxes of nutrient salts (such as nitrogen and phosphorus), which increase the proliferation of algae and aquatic plants (Bergkamp et al., 2000). Low oxygen levels, together with eutrophication and increased sediment concentration can induce a higher rate of turbidity, and alter water quality at the expense of many species (Hwang and Jeong, 2006). High water turbidity, in turn, inhibits plankton growth and reduces the amount of light penetration, thus damaging the aquatic food web and decreasing the rate of plant photosynthesis (Bergkamp et al., 2000).

The high rate of sediment retention upstream of the dam affects sediment transport and deposition processes downstream of the dam (Da-Chuan et al., 2008; Maingi and Marsh, 2002). Downstream sediment deprivation may impact on river physical processes; this may include reduction in the formation of river meanders (Johnson et al., 1976), constrained channel migration, and accelerated mechanisms of bar deposition and delta subsidence (Li et al., 2017). When the sediment inflow is interrupted by a dam, the sediment-carrying capacity of the river drops, leading to reduction in the bankfull width of the river and incision and entrenchment of the channel (Brandt, 2000; Gurnell et al., 1994). These geomorphic transformations of the river can have negative repercussions on the ecological status of base flow stream habitats (Shields et al., 1994) and promote disconnection between the channel and the floodplain (Wohl, 2004).

Hence, after a dam closure, the river system goes through a relaxation period - the 'transient phase' (Petts, 1987) - of physical and ecological adjustment that lasts until a new dynamic equilibrium is reached. According to Petts (1987), the timescales of the 'transient phase' depend on several factors (e.g. channel type and the mobility of the channel boundary sediment) and can even reach hundreds

of years (Petts, 1984). Moreover, after the introduction of dams, habitats are not only affected by alterations to water quality and runoff discharge but also by the presence of a physical barrier that impedes the movement of organic matter, nutrients, and even blocks migration routes for certain habitat features causing fragmentation of the habitat (Matzinger et al., 2007; Porto et al., 1999).

5.1.2 Response of riparian vegetation to dam impoundment

The drastic change in flow regime brought about by the impoundment of a river also has significant implications for the dynamics of the downstream riparian vegetation. In general, vegetation dynamics and rejuvenation are strongly modulated by the seasonal pattern of the hydrological cycle. However, the onset of dam-induced low-water periods causes intense encroachment of riparian vegetation to occur on the former banks and bed of the channel, thus further promoting river narrowing and incision (Gordon and Meentemeyer, 2006; Hadley and Emmett, 1998; Shafroth et al., 2002a). This inhibition of river morphodynamics also promotes vegetation colonization and stabilization of bars (OHare, 1995). However, the increase in downstream vegetation abundance is accompanied by low species diversity, mainly because certain riparian species are incapable of adapting to lower groundwater levels encountered in such hydrological conditions (Magilligan et al., 2003; Osterkamp et al., 1998; Wyżga et al., 2016).

The survival of the plants depends on their ability to deepen their roots to reach the new water table level, causing the below-ground biomass to become more concentrated at greater depths (Gorla et al., 2015). Hence, physiological and biochemical adaptions of the root system to water availability stresses determine vegetation encroachment and survival (Ravanbakhsh et al., 2017). The establishment of vegetation during a post-dam period is also fostered by reduced

plant removal due to uprooting by flow (Perona et al., 2009). Plants, besides being subjected to less frequent flood disturbances, can increase their resilience to uprooting in the inter-arrival time between events of large return periods, thus reducing their probability to be washed away. The development of deeper roots was found to influence the ability of a plant to withstand erosion processes and increase the plant survival probability with respect to flow-induced plant uprooting (Docker and Hubble, 2008; Pasquale et al., 2014; Pasquale et al., 2012; Pollen and Simon, 2005; Simon and Collison, 2002). Hence, the plant rooting depth can serve to enhance riparian ecosystem resilience to pressures such as hydrological alterations and flow erosion processes.

Many sources in the literature have confirmed the occurrence of a phenomenon of intense vegetation establishment in the downstream area of a dam. Choi et al. (2005) found that the greatest establishment of vegetation (willow communities) on previously active bar surfaces was strongly related to riverbed degradation after a dam was constructed in the Hwang River. Friedman et al. (1996) and Burkham (1972) observed that the formation of in-channel benches was linked to the growth of woody riparian vegetation. By analysing sequences of historical aerial photographs, Gordon and Meentemeyer (2006) found a substantial contraction occurred in bankfull width, along with increased vegetation coverage (72%), during the post-dam period in Dry Creek, USA. Allred and Schmidt (1999) and Grams and Schmidt (2002) found that channel narrowing of the Green River, USA, was followed by tamarisk species colonization. Schumm (1969) reported a drastic reduction in channel width from over 1200 m to 46 m of the Green River below the Flaming Gorge Dam, associated with the establishment of trees.

The percentage of vegetation in the floodplain was also found to depend on the channel type, as exemplified by the Missouri and Platte Rivers (Johnson, 1998). These cases provide examples of the very different ways in which vegetation responds and adjusts after dam impoundment. Braided rivers show a

remarkable increase in pioneer woodland compared to meandering rivers that do not exert influence on floodplain vegetation coverage, mainly because of the lack of point bars. Therefore, different river geomorphological patterns can lead to two opposing feedback mechanisms in terms of floodplain vegetation coverage (Johnson, 1998). A similar event to that of the Platte River has been documented for another briaded river: the Maggia River in Switzerland. A series of aerial photographs of the Maggia floodplain taken during and after dam construction in 1953 have facilitated monitoring and analysis of the evolution of the vegetation distribution in the floodplain of the river. Image analysis revealed a strong increase in floodplain forest and successive vegetation coverage from herbaceous vegetation to softwood and hardwood plants (Molnar et al., 2008; Perona et al., 2009). Increases in riparian vegetation following the construction of a dam have been confirmed in the literature by other authors (Erskine, 1985; Fergus, 1997; Graf, 2006; Williams and Wolman, 1984).

In short, it is clear that riparian vegetation is one of the most sensitive biotic factors to hydrological alteration and can be considered a good indicator of ecosystem change caused by dam operation (Nilsson and Berggren, 2000). Hence, understanding the response of plant roots to anthropogenic and natural disturbances is fundamentally important in terms of ecosystem restoration and management.

This Chapter presents a model that enables us to examine and explain how riparian ecosystems respond to alterations of the hydrologic regime caused by dam disruptions. The model provides the uprooting probability of the downstream riparian vegetation at a point and permits examination of the steady-state evolution of the ecosystem between pre- and post-dam scenarios. The model also offers a means for analysing the possibility of the system recovering to its

original state if the natural flow regime is re-established, and identification of the conditions for which this can occur. In addition, the role played by roots in the regime transition is thoroughly examined. Finally, in Chapter 6, the model is applied to a real case scenario, where dam impoundment has had a severe impact on the dynamics of riparian vegetation communities.

5.2 Modelling ecomorphodynamic state transition in response to natural flow regime shifts

5.2.1 Uprooting probability as an ecosystem state

Root depth and root configuration exert direct control on the probability of plant removal by flow-erosion processes (e.g. see Chapter 3 and Section 5.1.2). This suggests that uprooting probability can be used as a proxy variable to represent the ecosystem state and its evolution between the pre- and post-dam scenarios.

As discussed in Chapter 3, the uprooting probability can be given by time integration of the probability density function (equation 3.21), and is repeated below:

$$p_\tau(T) = \frac{L_e}{2\sqrt{\pi G(T)^3}} e^{\left(-\frac{(L_e - V(T))^2}{4G(T)}\right)} \left[\frac{g_t(T)}{2} + e^{\left(\frac{(L_e + V(T))^2}{4G(T)}\right)} W(T)\right] \tag{5.1}$$

To evaluate equation 5.1, it is necessary to have information on the scour depth, L_e, the deterministic and stochastic components of the erosion process, $V(T)$ and $G(T)$, and the function $W(T)$. However, these parameters are unknown as they are directly linked to the plant properties and to the erosion process dynamics. To address this issue, the model of Perona and Crouzy (2018) is coupled with other existing models and approaches. In particular, the scour depth is calculated by implementation of a combination of the model of Tron et al. (2014) and the free-body model developed in Chapter 3. The time integral

$V(t)$ is expressed using the probabilistic approach used by Calvani et al. (2019b). Likewise, the remaining terms, $G(t)$ and $W(t)$, are computed once the stochastic component of the erosion process, g_t, has been determined.

The approach used in the present model is mostly stochastic, whereas its treatment is analytic at almost every step. Hydrologic variability is addressed using Compound Poisson Process (CPP) and Peak Over Threshold Theory (POT) methods. The first method is used to generate synthetic hydrologic signals for the pre- and post-dam states. The second is used to assess the mean flow erosion event above a certain threshold at which plant uprooting occurs.

Although the Peak Over Threshold is one of the most common approaches used in hydrology for the analysis of extreme events, its key points are illustrated in Appendix D.

In order to make the derivation of the model easier to follow, the following paragraph uses a step-by-step approach to outlines the model structure.

5.2.2 Model structure and implementation

Figure 5.1 illustrates the procedure used to implement the model step-by-step.

1. CPP of the water discharge time series

In order to proceed analytically, the first step consists in generating the hydrologic signals (of the pre- and post-dam periods) using a Compound Poisson Process (see Figure 2.13), already discussed in Chapter 2. The evolution equation for the flow rate variable Q is:

$$\frac{dQ}{dt} = \zeta(t) - \frac{Q}{\tau_d}, \tag{5.2}$$

where t is time, and τ_d is the integral temporal scale obtained by solving the integral of the autocorrelation function of Q, and $\zeta(t)$ is white shot noise of mean

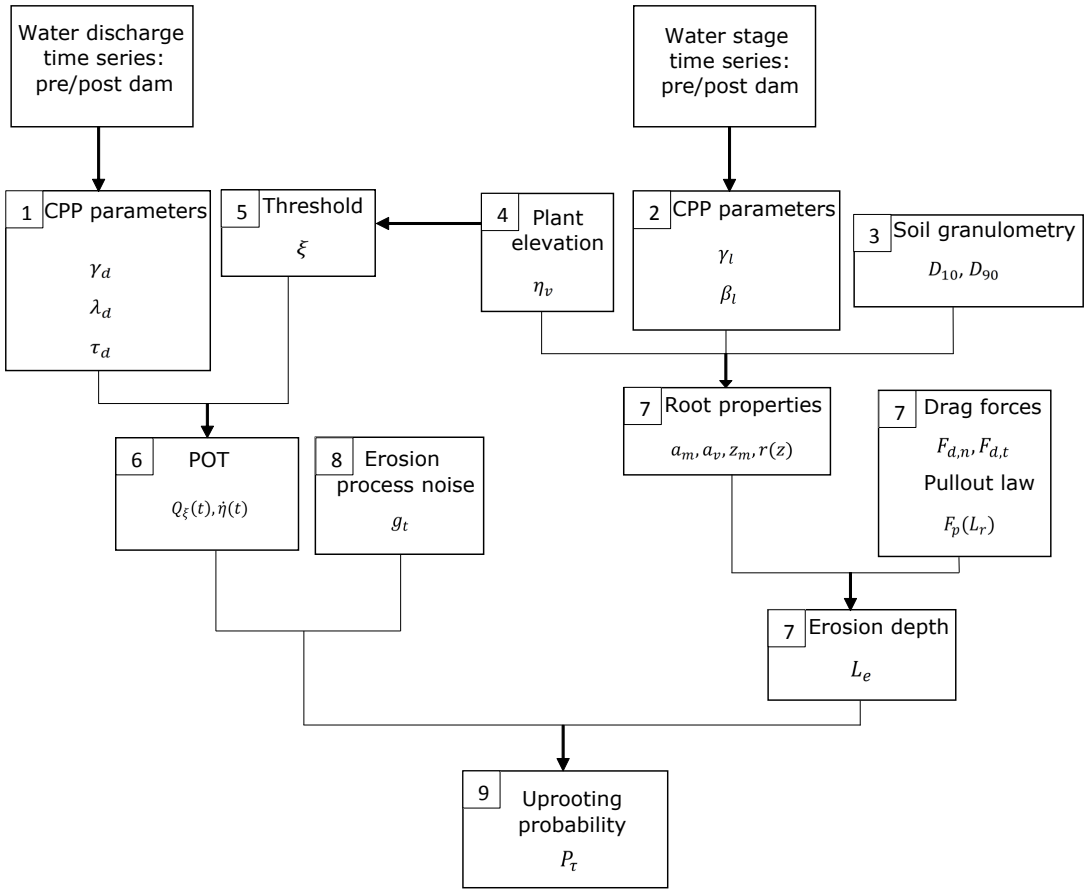

Figure 5.1: Diagram illustrating the main computational steps of the model.

intensity γ_d and rate of accuracy λ_d. The probability distribution of Q is:

$$p(Q) = \frac{1}{Q\Gamma[\beta_d]} e^{(-Q/\gamma_d)} \left(\frac{Q}{\gamma_d}\right)^{\beta_d}, \tag{5.3}$$

where β_d is the product between λ_d, the mean rate of the pulses, and τ_d.

2. Compound Poisson Process for water stage time series

In order to derive the steady-state of root profile using the model of Tron et al. (2014), it is necessary to know the PDF of water stage (see equation 2.4), whose solution requires knowledge of the γ_l and β_l parameters, which are analogs of γ_d and β_d for the water stage series (see also Section 2.5).

In the event that the water level data series is not available, the Chézy equation provides an effective way to extrapolate the rating curve to obtain the fluctuations of the water stage from the flow rate. The non-linear transformation between water discharge and water level does not allow the properties of the Compound Poisson Process (CPP) to be satisfied also for the water stage. However, when the effect of the distortion of the signal is negligible, then the resulting time series and its statistical distribution can still be approximated with a CPP.

3. Defining the grain size distribution

Soil texture is another important input parameter used in computing the root biomass profile in the soil. It is sufficient to know the values of D_{10} and D_{90}, as these parameters enable assessment of the 'optimal root-growth zone', L_g of the model of Tron et al. (2014). Given the sediment retention capacity of a dam, a change in grain size distribution must be expected to occur between the pre- and post-dam scenarios (Yang et al., 2014).

4. Setting the position of the plant on the riverbank

The position of the plant along the riverbank, η_v, is another input parameter required for computation of the root profile and plant uprooting probability. It is convenient to express the position of the plant in terms of elevation above the riverbed. Once the soil texture is known, it is then easy to compute the maximum depth that can be reached by the roots, z_m, from the soil surface (see Figure 5.2).

5. Determining the threshold value ξ

Peak Over Threshold Theory (POT) provides an estimate of the distribution of values of a hydrologic series that exceed a certain fixed threshold value ξ. Following the approach of Calvani et al. (2019b), POT is here used to estimate

Figure 5.2: Sketch of a generic river section. The plant on the riverbank is located at an elevation η_v vertically above the riverbed. z_m is the maximum depth reached by the roots from the soil surface at the plant location.

the mean value of erosion rate able to induce uprooting of vegetation. However, the first step necessary to implement POT is to assign a value for the threshold ξ. In this case, it is assumed that the value of ξ coincides with the water stage at the plant elevation level. In this way, uprooting by flow at a given location can only occur for all flooding events that reach or exceed that location, i.e. for values that lie above ξ (see red part of the signal in Figure 5.3). For values of Q below ξ, the plant is not subjected to flow drag or erosive action, and so the probability that the plant is uprooted by flow-erosion processes is equal to zero.

Note that the assumptions used here differ from those used by Calvani et al. (2019b), who considered the erosion event to be represented also by the falling limb of the signal included between ξ and Q_{cr}. This approach is not implemented here because it would lead to an overestimate of the uprooting probability at specific locations.

6. Computing the mean erosion rate

Following Calvani et al. (2019b), the mean erosion rate is the value computed for the reference mean event, $Q_\xi(t)$, which is the statistical average of all events in the temporal series that exceed the threshold ξ (Figure 5.4).

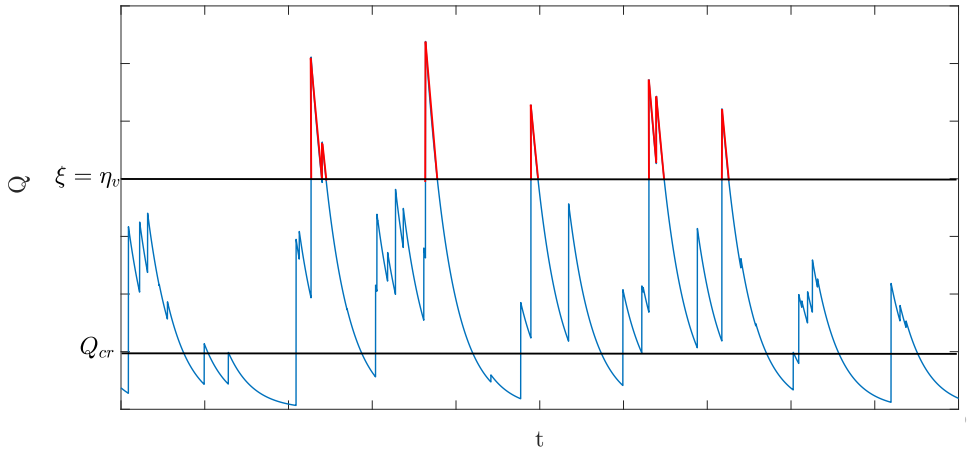

Figure 5.3: Setting of threshold ξ to implement Peak Over Threshold Theory for the Compound Poisson Process time series. The red portion represents flow events that may lead to plant uprooting by flow. The lower horizontal line represents the critical flow discharge for incipient erosion Q_{cr}. The upper horizontal line represents the threshold value ξ, which coincides with the plant elevation η_v.

The reference mean event is expressed as follows:

$$Q_\xi(t) = Q_0(\xi)e^{-t/\tau_1}, \tag{5.4}$$

where $Q_0(\xi)$ is the peak event occurring at time t (see Figure 5.4a) and τ_1 is the integral temporal scale of the reference mean event and is equal to:

$$\tau_1 = \frac{-T_\xi^+}{\frac{\xi}{\bar{Q}_{q>\xi}} + W_{-1}\left[\frac{-\xi}{\bar{Q}_{q>\xi}}e^{-\xi/\bar{Q}_{q>\xi}}\right]} \tag{5.5}$$

where W_{-1} is the second limb of the Lambert function (Corless et al., 1996) and $\bar{Q}_{q>\xi}$ is the average flow discharge above ξ:

$$\bar{Q}_{q>\xi} = \frac{\mu_d}{\beta_d}\frac{\Gamma[1+\beta_d, \phi]}{\Gamma[\beta_d, \phi]} \tag{5.6}$$

where μ_d is the average flow discharge in the Poisson process: $\mu_d = \gamma_d\beta_d$, ϕ is the ratio between ξ and γ_d, and $\Gamma[\cdot,\cdot]$ is the upper incomplete Gamma function. T_ξ^+

is the upcrossing time (the time average over which the signal is above ξ). The formulation of T_ξ^+ is known in a closed form (Laio et al., 2001), which reads:

$$T_\xi^+ = \frac{1}{\lambda_d} {}_1F_1[1; 1+\beta_d; \phi] \frac{\Gamma[\beta_d, \phi]}{\Gamma[\beta_d] - \Gamma[\beta_d, \phi]} \tag{5.7}$$

where ${}_1F_1[\cdot;\cdot;\cdot]$ is the confluent hypergeometric function of the first kind.

Once the reference mean event has been assessed, it is possible to compute the respective erosion rate $\dot{\eta}(t)$. The erosion rate can be obtained by combining the time-varying flow discharge to the 1D-Exner equation and sediment transport relationship (Meyer-Peter-Müller type formula) (Calvani et al., 2019b). The sediment transport relationship reads:

$$Q_s = \alpha_{BL}(\tau^* - \tau^*_{cr})^b D_{50} \sqrt{\frac{\rho_g - \rho_w}{\rho_w} g D_{50}} B, \tag{5.8}$$

where α_{BL} is the coefficient in the bedload formula, τ^* is the dimensionless bed shear stress, τ^*_{cr} is the critical Shields parameter, b is the exponent in the sediment transport formula, D_{50} is the median grain size of the riverbed sediment, and B is the width of the river. The Exner equation reads:

$$\frac{\partial \eta}{\partial t} = -\frac{1}{(1-\lambda_g)B} \frac{\partial Q_s}{\partial x}, \tag{5.9}$$

where η is the riverbed elevation, λ_g is the sediment porosity, Q_s is the sediment discharge, and x is the coordinate in the streamline direction.

By considering the difference in sediment transport fluxes between two consecutive sections $\left(\frac{\Delta Q}{\Delta X} = \frac{1}{\Delta x}\int_1^2 dQ_s\right)$ and assuming a condition of net bed erosion, the upstream sediment discharge becomes negligible (Perona and Crouzy, 2018) and equation 5.9 reduces to:

$$\dot{\eta}(t) = \frac{1}{(1-\lambda_g)B\Delta X} Q_s, \tag{5.10}$$

where Δx is the longitudinal scale along the river where bed erosion takes place (Calvani et al., 2019b).

By combining equation 5.8 with equation 5.10 it results:

$$\dot{\eta}(t) = \frac{1}{(1-\lambda_g)\Delta X}\alpha_{BL}(\tau^* - \tau^*_{cr})^b D_{50}\sqrt{\frac{\rho_g - \rho_w}{\rho_w}gD_{50}}. \tag{5.11}$$

The dimensionless bed shear stress, τ^*, can be expressed as follows:

$$\tau^* = \frac{\rho_w g R_H S}{\rho_w g D_{50}(\frac{\rho_g - \rho_w}{\rho_w})}, \tag{5.12}$$

where R_H is the hydraulic radius.

As R_H is related to the flow rate $Q_\xi(t)$ through the Gauckler-Manning formula:

$$R_H = \left(\frac{Q_{\xi(t)}}{A\sqrt{S}K_s}\right)^{3/2}, \tag{5.13}$$

equation 5.11 becomes:

$$\dot{\eta}(t) = \frac{1}{(1-\lambda_g)\Delta X}\alpha_{BL}\left(\frac{\left(\frac{Q_\xi(t)}{A\sqrt{S}K_s}\right)^{3/2}S}{D_{50}(\frac{\rho_g-\rho_w}{\rho_w})} - \tau^*_{cr}\right)^b D_{50}\sqrt{\frac{\rho_g - \rho_w}{\rho_w}gD_{50}}, \tag{5.14}$$

where K_s is the Strickler coefficient and A is the wet cross sectional area of the river.

Note that, for a wide rectangular river cross-section, the expression of 5.14 reduces to the one illustrated in Calvani et al. (2019b). Figure 5.4a shows the trend in average erosion event $\dot{\eta}(t)$ with time.

7. Assessment of erosion depth that determines plant uprooting by flow

To obtain the scour depth, L_e (see Figure 5.5), it is necessary to combine the free-body model of Chapter 3 with the model of Tron et al. (2014). To achieve this, values are required for the proportionality constant, a_m, that links the total root length L_r (which is needed for the computation of the drag forces) to the biomass density of the root profile, and the coefficient a_v that accounts for the

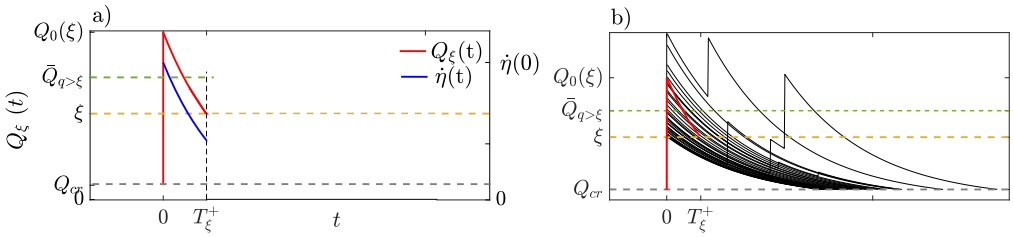

Figure 5.4: Reference mean event $Q_\xi(t)$ (red line) and erosion event $\dot{\eta}(t)$ (bue line) as functions of time. a) Reference mean event $Q_\xi(t)$ and related bed erosion rate $\dot{\eta}(t)$ for a given threshold ξ. b) Sequence of events, generated by a CPP, that lie above threshold ξ. The statistical average of all the events shown here is the mean reference event (red line) (modified from Calvani et al., 2019b).

dependence between L_r and the plant species (Cannon, 1949). This implies that different plant species yield different L_r for equal hydrologic conditions.

Once the value of a_v has been assigned, the value of a_m can be obtained by solving the following equation:

$$a_m = \frac{L_r}{a_v \int_0^{z_m} r(z)dz} \tag{5.15}$$

where integral $\int_0^{z_m} r(z)dz$ expresses the root biomass density underneath the vertical root profile $r(z)$, and L_r is the total rooting length that is obtained by solving the balance (equation 5.16) between the pullout law and the drag forces acting on the plant:

$$\frac{1}{2}C_D\rho_w u^2 A_n + \frac{1}{2}C_f\rho_w u^2(A_s + A_f) + \frac{1}{2}C_f\rho_w u^2\pi d_r(L_r) = F_p(L_r) \tag{5.16}$$

Note that equation 5.16 can be solved once the pullout law, the geometric properties of the canopy, the flow velocity, the drag and the friction coefficients have been determined. With a_m evaluated, L_e is readily determined by solving:

$$L_{e,t} = a_m \int_0^{L_e} r(z)dz \tag{5.17}$$

where $L_{e,t}$ is the exposed total root length, obtained by subtracting the total critical rooting length from the total rooting length of the plant:

$$L_{e,t} = L_r - L_{c,t} \tag{5.18}$$

where $L_{c,t}$ is obtained in the same way as L_r:

$$\frac{1}{2}C_D\rho_w u^2 A_n + \frac{1}{2}C_f\rho_w u^2(A_s + A_f) + \frac{1}{2}C_f\rho_w u^2\pi d_r(L_r - L_{c,t}) = F_p(L_{c,t}) \tag{5.19}$$

Figure 5.5 illustrates the link between $L_{e,t}$ and the L_e for two different vertical root profiles.

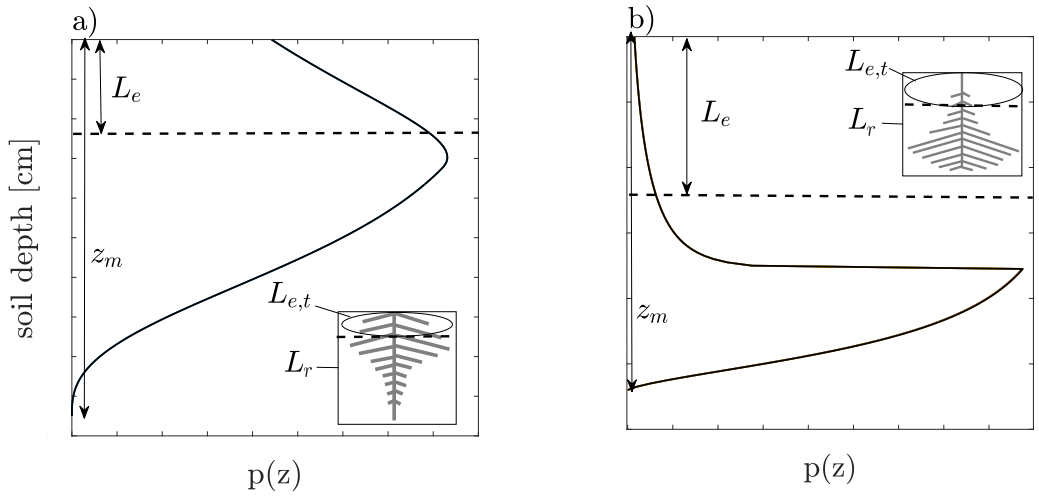

Figure 5.5: Illustration of the scour depth L_e for two different root profiles. a) Marked development of root biomass close to the soil surface. The total root length exposed that corresponds to L_e is labelled as $L_{e,t}$. b) Root biomass highly concentrated in depth. The amount of total root length exposed is therefore lower than in a) even though the erosion depth is larger.

8. Fluctuations in the erosion process

The final term required to integrate equation 5.1 is $G(t)$, the time integral of g_t. In developing their model, Perona and Crouzy (2018) assume that the erosion process occurs following a Gaussian diffusion with drift (Ornstein-Uhlenbeck

stochastic process, Uhlenbeck and Ornstein (1930)), where the diffusion coefficient is: $D(t) = g_t(t)/2$, which, for the sake of simplicity, is assumed constant with respect to time: $D = g_t/2$. This expression for the diffusion coefficient is well known from Einstein's theory of diffusion (Einstein, 1905). Einstein (1905) relates D to the smallest fluctuations influencing the process and to the time over which such fluctuations take to manifest, i.e.:

$$D = \frac{\delta^2}{2t} \tag{5.20}$$

where δ is the vertical jump of a particle. Rearranging:

$$g_t = 2D = \frac{\delta^2}{t}, \tag{5.21}$$

For the layer of well packed spheres of mean diameter D_{50}, shown in Figure 5.6, t can be taken as the time a particle takes to free its space such to generate a vertical jump δ. So, t can be expressed as:

$$t = \frac{D_{50}}{8.5u_*} \tag{5.22}$$

Equation 5.22 is obtained under the assumption that the particle has a longitudinal velocity equal to that of the fluid at vertical elevation $y = k_s = D_{50}$, where k_s is the equivalent grain roughness size. The term $8.5u_*$ derives from the the classic logarithmic expression of the velocity profile: $\frac{\bar{u}}{u_*} = 8.5 + 5.75log(y/k_s)$ (Papanicolaou et al., 2002). So, using equation 5.22, equation 5.21 becomes:

$$g_t = \frac{\delta^2}{D_{50}} \frac{8.5u_*}{1} = 8.5 \frac{\delta^2}{D_{50}} u_*. \tag{5.23}$$

It remains to link δ to the size of particles mobilized during the process. Without loss of generality, and assuming that the particles are almost spherical, it is found that $\delta = D_{50}$ (see Figure 5.6). Hence, equation 5.23 can be simplified as follows:

$$g_t = 8.5 D_{50} u_*, \tag{5.24}$$

Once g_t is has been obtained, the expression for p_τ can be finally implemented.

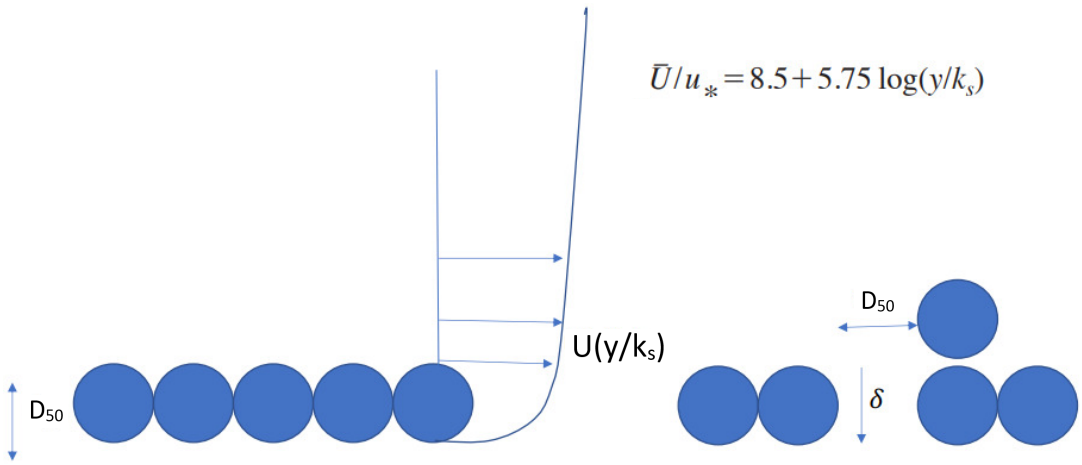

Figure 5.6: Longitudinal velocity profile of a particle, and similarity between the spatial scale of a particle and its median size D_{50}.

9. Calculation of uprooting probability distribution P_τ

Given that the variables needed to solve equation 5.1 are now available, the uprooting probability, P_τ, is determined by solving the time integral of equation 5.1.

Table 5.1 lists the model input parameters.

Table 5.1: Model input parameters.

Input parameters		
γ_d	mean height of the pulses of the discharge signal	[m^3]
λ_d	mean interval between the pulses of the discharge signal	[$days^{-1}$]
τ_d	autocorrelation time	[days]
γ_l	mean height of the pulses of the water level signal	[m]
β_l	ratio between λ_l and η_l	[-]
ξ	threshold flow discharge	[m^3]
B	river width	[m]
A	wet cross sectional area of the river	[m^2]
R_H	hydraulic radius	[m]
u	flow velocity	[m s^{-1}]
K_s	Strickler coefficient	[$m^{1/3}s^{-1}$]
S	riverbed slope	[-]
ρ_g	sediment density	[Kg m^{-3}]
λ_g	sediment porosity	[-]
ΔX	longitudinal length scale of bed erosion	[m]
α_{BL}	coefficient in bedload transport formula	[-]
b	exponent in sediment transport formula	[-]
τ^*_{cr}	critical Shields parameter	[-]
g_t	erosion process noise	[m^2 $days^{-1}$]
D_{10}	grain size value corresponding to cumulative size distribution at 10%	[m]
D_{90}	grain size value corresponding to cumulative size distribution at 90%	[m]
D_{50}	grain size value corresponding to cumulative size distribution at 50%	[m]
C_d	drag coefficient	[-]
C_f	friction coefficient	[-]
d_r	root diameter	[m]
A_s	total surface area of the stem	[m^2]
A_f	total surface area of the foliage	[m^2]
A_n	projected area of the plant in the flow direction	[m^2]
$F_p(L)$	pullout law	[Kg m s^{-2}]
η_v	elevation of the plant with respect to the riverbed	[m]
a_v	coefficient of plant species	[-]

5.2.3 Expected results

Before considering a real case study, it is worth examining application of the model to the transition a river undertakes after an hydrological shift. Figure 5.7 presents a sketch illustrating the main features of the model output. The plot is purely conceptual; the application to real data will be presented in the next Chapter. Figure 5.7 summarises the different regime transitions that are expected to occur when a river is dammed. The plot presents curves relating the ecosystem state (uprooting probability) against the driver, $\Delta H = \eta_v - \mu_l$, where η_v is the plant elevation and μ_l is the mean value of the water stage. In Figure 5.7, three different solid curve segments can be detected. The curve segment that links P1 to P2 represents the regime shift that the system undergoes after the dam is constructed. Whereas P1 stands for the equilibrium of the system under the natural flow regime, P2 represents the unstable equilibrium that the system reaches just after the abrupt shift in hydrology. In P2, the ecosystem has not yet adapted to the altered flow regime, because the plants have not yet changed their below-ground biomass configuration. This state is therefore representative of the start of the 'transient phase' (Petts, 1987), which slowly brings the system to a new equilibrium state in P3. When the state is in P3, the ecosystem has finally adjusted to the post-dam hydrologic regime, because the root biomass has shifted deeper into the soil. The curve between P1 and P3 represents steady state equilibrium points due to a quasi-static transformation. In other words, this segment of the curve can be compared to quasi-static processes occurring in thermodynamics, where the system remains in internal equilibrium.

The availability of time series for discharge and water stage covering both pre- and post-dam periods enables computation of the uprooting probability for the respective ecosystem equilibrium states, P1 and P3. However, to be able to represent the steady-state transition of the system, it is essential to vary

the parameters γ_d, λ_d, and τ_d. Given that the growth rate of these parameters is unknown, a simple, linear relation can be assumed. The reverse regime describes the transition between P3 and P4, during which time the system exhibits hysteresis in response to the reversal of the hydrologic regime. However, the ecosystem state is not significantly affected by this alteration because the roots are resilient to a reverse change. This explains the occurrence of an irreversible state between P4 and P1. Hence, if the dam were to be removed, the vegetation coverage and community would not be much affected, leading to a long-term impact on vegetation succession (Hobbs et al., 2009). Furthermore, intensive establishment of mature vegetation during the post-dam period increases the stability of the riverbanks, thus also making it difficult for the river morphology to reestablish its natural pattern (Shafroth et al., 2002a). Therefore, restoration of the vegetation pattern and coverage of the pre-dam period can be achieved by the occurrence of an unquantifiable flood or by the intervention of deforestation and river restoration. Only in this way it is possible to bring the system back to its pre-existing equilibrium.

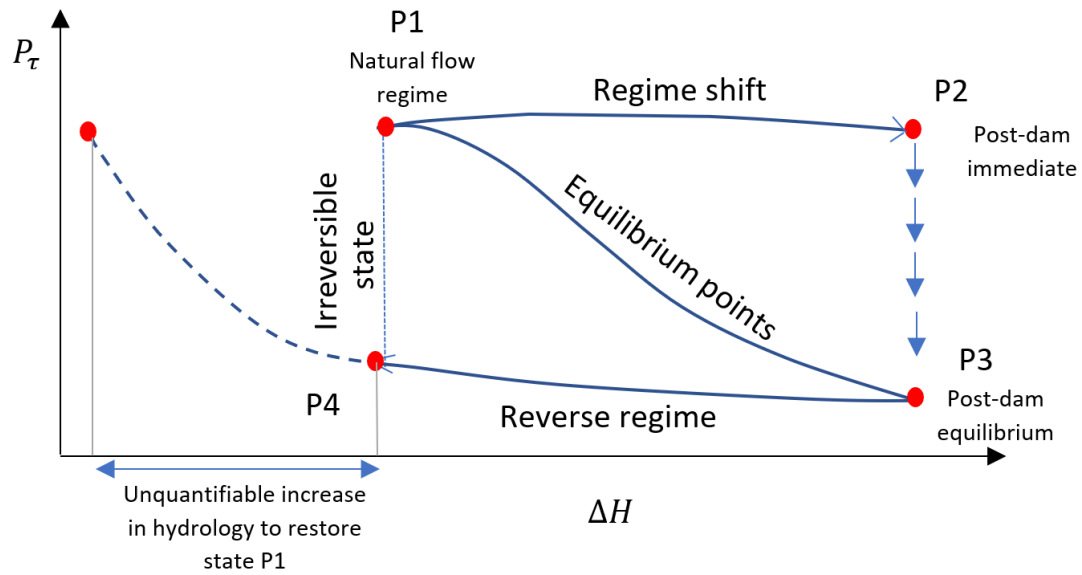

Figure 5.7: Detailed sketch of the different regime transitions of the ecosystem state.

Chapter 6

Application of the model to a case study

6.1 The Maggia River floodplain

The Maggia River is a gravel-bed stream located in the Canton of Ticino, in the southern rim of the Swiss Alps (Figure 6.1). Its springs are located near the Cristallina mountain and the river flows through Sambuco, Lavizzara, and Maggia Valleys before merging into Lake Maggiore to form a delta. The river has three main tributaries: Lavizzara, Bavona, and Rovana. The Maggia River basin covers a surface area of 592 km^2 at an altitude ranging between 200 and 3300 m.a.s.l.

The hydrological regime of the Maggia basin can be described as glacial-nival-pluvial with a typical snowmelt peak in June. Snow precipitations during the winter and the partial melting of the glaciers of Basodino and Cavagnoli during the summer contribute to the hydrological variability of the river. The steep slopes and the geologic composition of the valley (granite and gneiss) lead to a rapid catchment response to fast and intense surface runoff. The floodplain of the main valley is characterized by the presence of large gravel and sand (Ruf, 2007). The most interesting part of the Maggia valley is located between Riveo and Giumaglio (Figure 6.2). Here, the total surface area covered by the floodplain is about 58 km^2 and the river strait is approximately 3 km long.

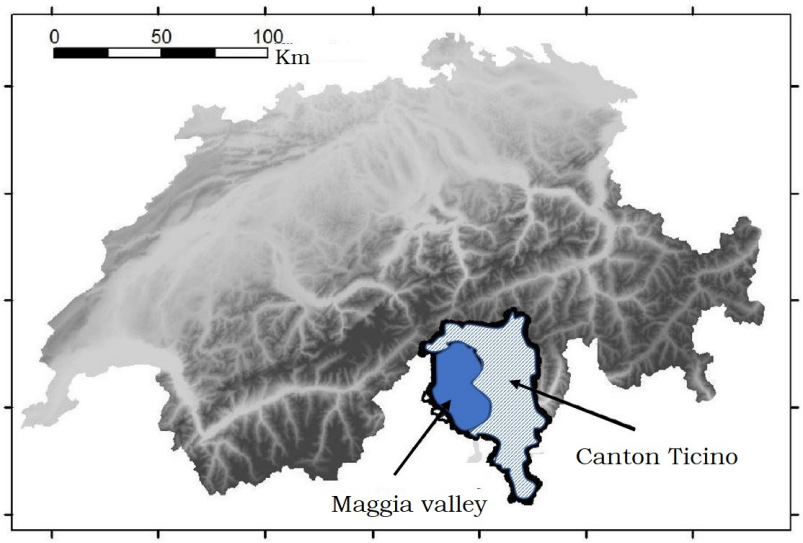

Figure 6.1: Location of Canton Ticino and Maggia Vally in the Southern part of Switzerland. Canton Ticino is represented by the light blue area on the map. The study area (Maggia Valley) is indicated in dark blue (modified from Foglia et al., 2004).

This braided area of the river is particularly active from the geomorphological point of view, given the presence of intense interaction dynamics between flow processes and vegetation. This reach is equally interesting for its response to the impoundment of the river by the large hydro-power system put in place in 1953 (Molnar et al., 2008). The installation of 8 artificial reservoirs and a lack of sustainable construction operations caused the reach almost to dry out.

The river alterations induced a sudden change in magnitude and interannual variability of the streamflow. Comparing the pre- and post-dam hydrographs in Figure 6.3, it can immediately be seen that in the post-dam hydrographs the seasonal component disappears giving way to a base flow that is interrupted by occasional flow peaks. The consequent drop of groundwater to a critical level and the reduction in sediment supply have stimulated vegetation encroachment, thus interrupting the preexisting balance between vegetation destruction and regeneration. In the post-dam period, vegetation growth was found to be mostly reliant on groundwater and lateral hillslope fluxes (Ruf, 2007).

Figure 6.2: Braided reach of the Maggia river between the villages of Riveo and Giumaglio.

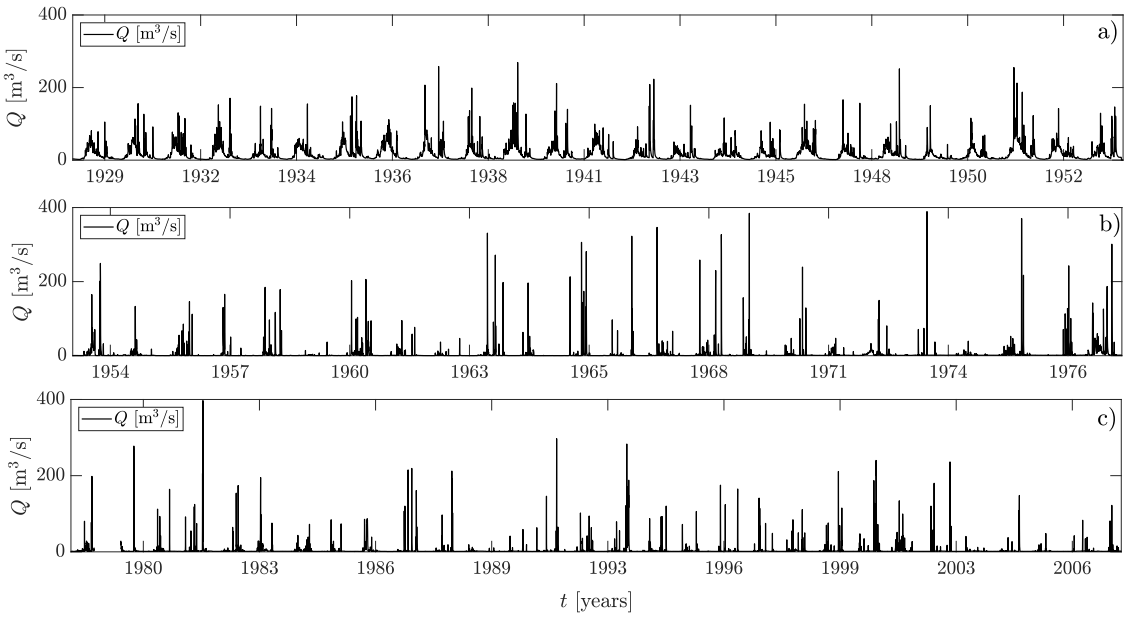

Figure 6.3: Hydrographs showing the daily streamflow at Bagnasco station: a) pre-dam period (1929-1953); b) post-dam period (1954-1977); and c) post-dam period (1978-2007).

In the pre-dam period, the vegetation coverage comprised a typical spatial arrangement of riparian species, where tolerance to inundation, erosion processes, and soil texture are driving factors inducing plant species distribution. According to Bayard and Schweingruber (1991), in the pre-dam period, the riverbed areas and the embankment zones close to the river where the gravel sediments are dominant, were populated by sagebrush and willows. Sandbanks, as well as high waterfronts of the river islands, were covered by softwood species dominated by the following types of willow bushes: lavender willow (*Salix elaeagnos*), purple willows (*Salix purpurea*) and black poplars (*Populus nigra*). Low sandbank areas were covered by gray alder bushes. Irregularly flooded river terraces and areas further distant from the banks were populated by hardwood species such as small-leaved lime trees (*Tilia cordata*), common oaks (*Quercus robur*), and ash trees.

The availability of aerial photos in different years (1933, 1944, 1962, 1977, 1978, 1989, 1995, 1999, 2001, 2004, and 2006) allowed investigation of the long-term impact of vegetation dynamics on river morphodynamics, thus documenting the evolution of vegetation. The georeferentiation of the photographs enabled classification of vegetation according to their type: grass, shrubs, young trees and old trees (Figure 6.4). A general comparison between the aerial photographs of the Maggia floodplain in 1933 and 2006 (Figure 6.4), shows an intense change in the spatial distribution pattern of the vegetation (Favre, 2004; Sturzenegger, 2005). In 2006, a higher percentage of vegetation at the high stage level can be detected compared to 1933. The herbaceous surfaces that used to characterize the sandbanks in the pre-dam period (Figure 6.4a) have become a wood surface in Figure 6.4b, which corresponds, intuitively, with non-alluvial areas. Furthermore, areas watered by the river decreased noticeably after 1933. New vegetation that colonized the river floodplain in the pre-dam period (herbaceous plants) contributed to populate the mature vegetation patch, mostly characterized by

softwood and hardwood forest (Ruf, 2007). Meanwhile, pioneer plants used to colonize the floodplain after flooding events have disappeared or evolved to more mature alluvial ligneous plants. Bearing this in mind, it is interesting to examine the overall ecosystem transition between pre- and post-dam system, from the perspective of the evolution of the plant uprooting probability due to flow erosion processes.

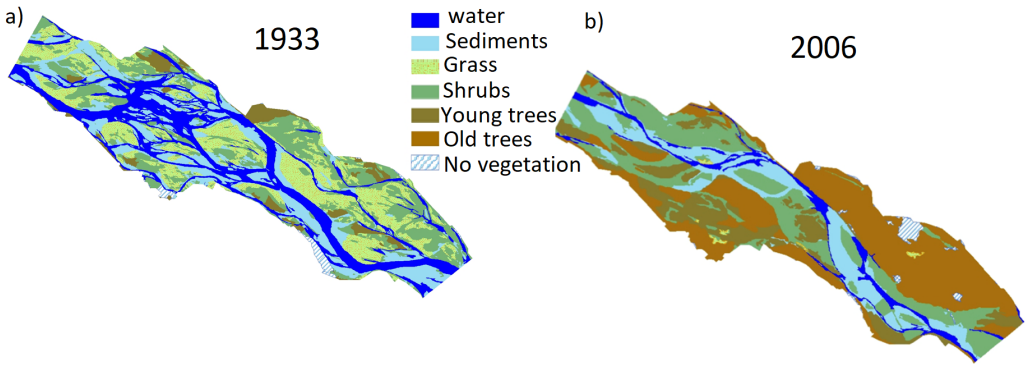

Figure 6.4: Vegetation classification mapped from aerial photography of the braided area between Riveo and Someo. The different shades of green and brown color represent different types of vegetation. Areas covered by sediment and water are colored in light blue and blue, respectively. (Based on Savina et al., 2008).

6.2 Input Parameter Values

Compound Poisson Process parameters

Flow discharge time series for the pre- and post-dam periods were reconstructed using historical daily streamflows recorded at the Bignasco station located upstream of the braided reach of the river. Figure 6.3 shows the flow rate time series. The pre-dam hydrograph commences in January 1933 and ends in December 1953 (see Figure 6.3a). The post-dam hydrograph refers to the period between January 1954 and December 2007 (see Figures 6.3b and 6.3c). The

mean flow rate is 16.50 m^3/s in the pre-dam period, and reduces to 4 m^3/s in the post-dam period. Table 6.1 lists the representative hydrological parameters for the pre- and post-dam states. It can be seen that the mean flow discharges of the CPP signals, μ_d, coincide with the average values of the actual hydrographs. Due to the lack of water stage series, the variation in water level was estimated using the Chézy equation. Table 6.1 lists values of the mean depth and rate of the water level pulses for both scenarios.

Table 6.1: Values of parameters defining Compound Poisson Process of flow discharge and water levels at Bignasco Station, Maggia River, Switzerland.

Parameter	Pre-dam	Post-dam
γ_d	23	50
λ_d	0.22	0.05
τ_d	3.31	1.60
γ_l	18.70	46.70
β_l	1.97	0.19

Furthermore, from Table 6.1, it appears that switching between the hydrologic signals before and after dam impoundment led to a decrease in τ_d and λ_d and an increase in γ_d. This is confirmed by comparing the hydrographs in Figure 6.3, where, in the post-dam case, the flow peaks have higher intensity and occur with a lower frequency. In other words, during the post-dam period, the hydrologic events have become less correlated, more infrequent, and larger. Figure 6.5 also shows the similarity achieved between corresponding portions of the CPP signal and hydrograph (extracted from Figure 6.3). It is evident that the signal generated from a CPP can simulate the overall characteristics of real hydrology. Even so, it should be emphasized that the CPP cannot simulate the hydrologic seasonality. Therefore, for the pre-dam case, the artificial signal is not always

able to reproduce the actual time series.

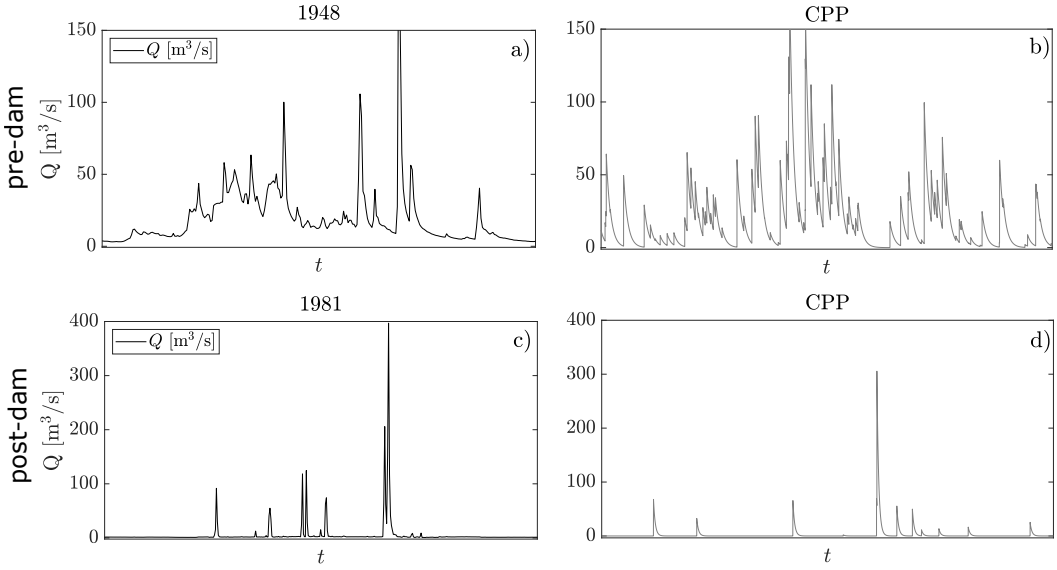

Figure 6.5: Comparison between real and artificial flow rate time series, Q, for: a) the pre-dam period in the year 1948, with the CPP signal obtained by assigning γ_d=23 m^3, λ_d=0.22 days^{-1}, and τ_d=3.31 days; and b) post-dam period in the year 1981, with the CPP signal obtained by assigning γ_d=50 m^3, λ_d=0.05 days^{-1}, and τ_d=1.60 days.

The CPP parameters for the flow discharge in Table 6.1 are only representative of the conditions of the ecosystem equilibrium. Hence, as mentioned previously, in order to represent the steady-state transition between the two extreme scenarios, γ_d, λ_d, and τ_d are prescribed to vary linearly. This differs from the parameters of the water stage, which were instead computed at each equilibrium point by fitting the probability density function of the water stage.

Channel geometry and hydraulic parameters

The cross-section representative of the braided reach of the river was approximated by a trapezoidal geometry with external angle, α_s, equal to 5° and a minor base, B, equal to 50 m (Figure 6.6). The channel slope was set to 5‰, which is within the range outlined by Ruf (2007).

The water level in the river was computed by using Engelund's method for different values of the Strickler coefficient for the vegetated ($K_{s,1} = 6$) and non-vegetated part of the river ($K_{s,2} = 20$). The vegetated area coincides with the riverbanks, whereas the unvegetated area comprises the channel bed.

For the parameter concerning the bed-load transport, the critical Shields parameter for incipient motion, τ^*_{cr}, was set equal to 0.03 (Parker et al., 2007). The sediment porosity, λ_g, was set to 0.2, the exponent in the sediment transport formula, b, was given a value of 1.5 following Van Rijn (Van Rijn, 2013), and the sediment density, ρ_g, was set to 2600 kg/m^3. The coefficient of the bed-load transport formula, α_{BL}, was set to 3.97 following Wong and Parker (2006). A representative value for ΔX, which is the erosion length scale, is difficult to assign. So, following Calvani et al. (2019b), ΔX was assumed to be equal to $6 \cdot B$, which is about the length scale of a bar according to Leopold and Wolman (1957).

Parameters of soil texture

The grain size distribution of the riverbank soil is unknown. Hence, the values assigned to $D_{10,s}$ and $D_{90,s}$ are only indicative. Furthermore, given the sediment retention capacity of the dam, it was appropriate to account for a shift in the sediment size between the pre- and post-dam periods. The change in the sediment supply and the resulting decrease in bed mobility downstream of the dam led to the intuitive assumption that, in the post-dam period, the size of the sediments increased. Therefore, $D_{90,s}$ and $D_{10,s}$ were prescribed to vary from 0.12 to 0.24 mm and from 0.03 to 0.06 mm between the two states, respectively.

Concerning the grain size distribution of the riverbed sediment, Ruf (2007) provided a median value for the pebbles, $D_{50,p}$, which is about 100 mm. The value of $D_{50,p}$ in the pre-dam scenario was chosen equal to 65 mm, as the real

value is unknown. The variation in sediment size was assumed to be linear, as for the CPP parameters for flow discharge. In the case of the bed material, the variation in median size of the pebbles was also assigned to drive a variation of the critical flow rate between the pre- and post-dam period.

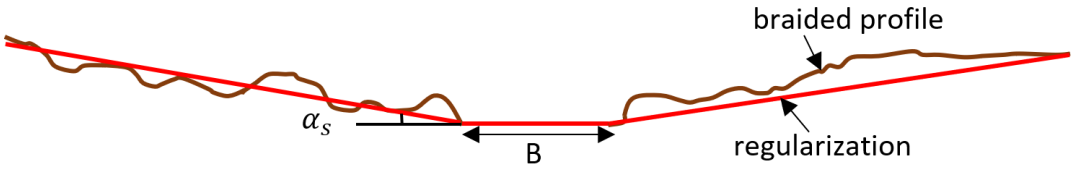

Figure 6.6: Regularization of the braided profile of the river.

The input data are summarised in Table 6.2, where values of the remaining variables (e.g., parameters defining the uprooting law and plant properties) are also given. It should be noted that the species and the growth stage of the vegetation were not included in this model. Therefore, the maximum depth that the root can reach, z_m, is not constrained by vegetation type and age and solely depends on plant elevation, soil texture, and water table level.

The application of the free-body model to represent the flow resistance of more mature plants deserves some more comments. As seen in Chapter 3, the model has only been validated on young seedlings. As a result, the model's applicability is restricted to the cases of flexible plants, which, at the time of uprooting, adopt a reconfiguration in the streamline direction. Therefore, this assumption may not be realistic and should not be used when considering the rigid-structure of large and woody plants. Rather, in these circumstances, the level of submergence of the plant and its degree of deflection should be assessed, because the drag force would predominantly be represented by its normal component ($F_{d,n}$). Given the above considerations, it is worthwhile to mention that the plants in the Maggia river that are likely to be uprooted are the ones that are still in their intermediate stage of growth, and thus flexible.

Apart from the information obtained by Bayard and Schweingruber (1991)

about the main types of plant species populating the banks of the Maggia Valley, there is no data available about plant allometric relationships, pullout laws and descriptions about the types of root systems. Given the lack of definite input values, the free-body model has been applied without revisiting its assumptions and sensible values have been assigned to the coefficients and variables of equations 5.16 and 5.19.

Hence, in this complex context, the dynamics of plant flow interaction has been set in an idealized framework, in which also the assumptions of the model of Tron et al. (2014) plays a key role. In fact, the steady-state conditions used in Tron et al. (2014) assume that the above-ground biomass of the plants does not change over time. As a result, the surface area of the canopy and its projected area on the flow direction are constant between the pre- and post- dam scenarios. Rather, the time development of the plant is taken into account by the pullout law, for which the increase of anchoring resistance is driven by the growth of the roots.

As seen in Table 6.2, the pullout law follows a polynomial trend, as such law was found to be appropriate for plants at a high stage of growth (like equation 3.19). The drag coefficient, C_D, was assigned the representative value of 1, which agrees with what found in Chapter 3 and, on average, with the range of values found in the literature (e.g. see Vargas-Luna et al., 2015). The value set for the friction coefficient has a higher value (C_f=3) than the one calibrated in Chapter 3 according to complex plant geometry (i.e. a higher number of branches and leaves and their configuration). The surface area of the plant exposed to flow, $A_s + A_f$, was given a value of 1 m^2, whereas the projected area of the stem and branches in the flow direction, A_n, was set to $5{\cdot}10^{-1}$ m^2. The average diameter of a single root was taken to be equal to $3{\cdot}10^{-3}$ m.

Table 6.2: Input data to the combined model.

Input parameters	pre-dam	post-dam
B	50 m	50 m
$K_{s,1}$	20 $m^{1/3}s^{-1}$	20 $m^{1/3}s^{-1}$
$K_{s,2}$	6 $m^{1/3}s^{-1}$	6 $m^{1/3}s^{-1}$
S	5‰	5‰
ρ_g	2600 kgm^{-3}	2600 kgm^{-3}
λ_g	0.2	0.2
b	1.5	1.5
ΔX	300 m	300 m
α_{BL}	3.97	3.97
τ^*_{cr}	0.03	0.03
g_t	0.18 m^2 day^{-1}	0.18 m^2 day^{-1}
$D_{10,s}$	$3.4{\cdot}10^{-5}$ m	$6{\cdot}10^{-5}$ m
$D_{90,s}$	$1.2{\cdot}10^{-4}$ m	$2.4{\cdot}10^{-4}$ m
$D_{50,p}$	$6.5{\cdot}10^{-2}$ m	$1{\cdot}10^{-1}$ m
C_d	1	1
C_f	3	3
d_r	$3{\cdot}10^{-3}$ m	$3{\cdot}10^{-3}$ m
$A_s + A_f$	1 m^2	1 m^2
A_n	$5{\cdot}10^{-1}$ m^2	$5{\cdot}10^{-1}$ m^2
η_v	1.2 m	1.2 m
a_v	1	1
a^*_r	0.025	0.025
b^*_r	0.6	0.6

$*$ coefficients of the static pullout law: $F_p = a_r x^2 + b_r x$

6.3 Model Ouput

6.3.1 General considerations

With respect to the procedure outlined in Section 5.2.2, it is convenient also to refer to Figure 6.7, which presents a sketch of the modeling framework. As a starting point for the discussion, consider a generic plant species positioned on the banks of the river at an elevation, η_v, equal to 1.2 m above the riverbed. In Figure 6.7a, the water level is set to a certain elevation h, which is typical of the natural flow regime of the river before impoundment. This condition is meant to be representative of the equilibrium state of the ecosystem in the pre-dam period, which is referred to as P1. Figure 6.7b represents the equilibrium state for the same plant in the post-dam period, and is indicated as P3. As the water level has decreased, the root system has adapted to lower groundwater levels by displacing its biomass towards greater depths, as predicted by the model of Tron et al. (2014) and recognised in the literature.

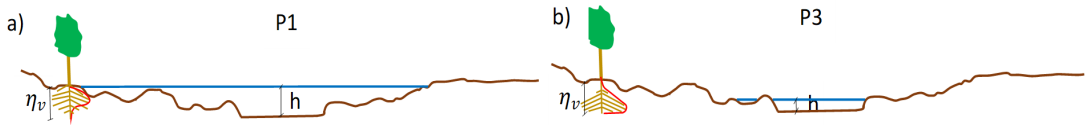

Figure 6.7: Sketch of the modeling framework: a) pre-dam state (P1), where h is the water depth in the river in its natural flow regime, with a shallow root distribution of riverbank vegetation; and b) post-dam state (P3), where h is the water depth in the river in its low flow regime, with a deep root distribution of riverbank vegetation.

Figure 6.8 shows the uprooting probability for these two equilibrium states, P1 and P3, and links the ecosystem state (uprooting probability) to ΔH (which is expressed as difference between the plant elevation and the mean level of the water stage, such that $\Delta H = \eta_v - \mu_l$). In P1, the uprooting probability is about equal to 88%, whereas in P3 the values of P_τ decreases to about 10%. Such a decline in P_τ is associated with the change to the root profile of the plant.

The root profile in the pre-dam system is shallower, exhibiting an oxytropic response. Conversely, the root profile in the post-dam equilibrium is highly developed over the depth, suggesting an hydrotropic response to the lowering water table (Figure 6.9a). This tropic response of the plants is in accordance with the experimental findings discussed in Chapter 2.

Returning to Figure 6.8, the blue dots connecting equilibrium states P1 and P3 represent the steady-state points resulting from a quasi-static change in hydrologic conditions between P1 and P3. (This is equivalent to changing the driver in infinitesimally small steps, giving sufficient time to the system to adjust). This part of the curve represents the condition at which the root system progressively adjusts to the progressive lowering of the water stage by changing its shape and depth (see also Figure 6.9b).

The grey dots, meanwhile, delineate a curved limb that relates to unstable transient states, in which P2 represents a scenario occurring just after the new regime has commenced. In P2 the uprooting probability is hardly affected, given that the root cannot instantly adapt to a sudden drop in water table. However, P2 is in a condition of unstable equilibrium that eventually leads the system to reach P3. In other words, the unstable equilibrium point in P2 represents the start of an 'adjustment period', which ceases when the root system of the plant has reached higher depths according to the position of the water table in the new regime.

The third curve limb (orange dots) represents the reverse regime, which is obtained by returning back to the hydrologic conditions starting from P3. The trajectory of this curve indicates that the system undergoes an irreversible process, for which it is not possible to restore the initial conditions in P1. In fact, the uprooting percentage in P4 turns out to be less than half that obtained in natural flow regime conditions. Hence, the system exhibits a certain resistance to reestablishing the condition in P1. Moreover, this result suggests that the initial

state conditions may only be restored by the occurrence of an hydrologic event of a much larger return period or by the clearance of the riparian vegetation through deforestation.

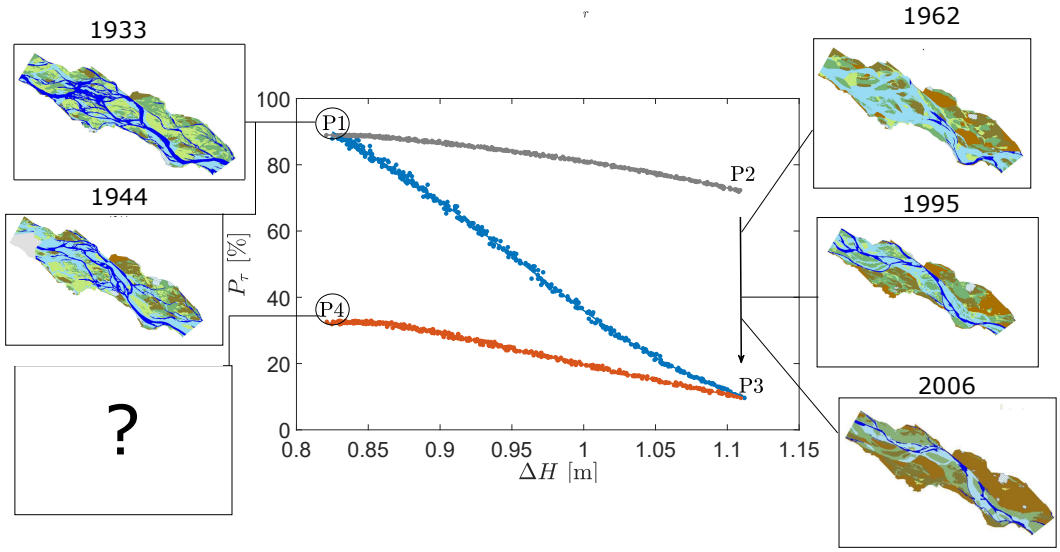

Figure 6.8: Uprooting probability, P_τ, plotted against ΔH, for a plant elevation, η_v, equal to 1.2 m. The insets show the morphological evolution of the river floodplain in 1933, 1944, 1962, 1995, and 2006.

The model output accords with the four aerial images displayed in Figure 6.8 that show the morphological changes experienced by the riverine system and the trends shown in Savina et al. (2008).

The image representative of point P1 dates to 1933 and 1944, before the construction of the impoundment. At this stage, the river was still in its natural regime, and areas covered by vegetation were confined to the riverbanks and terraces. The abundance of young vegetation suggests that the uprooting percentage was particularly high, promoting equilibrium between vegetation removal and regeneration. The images below point P2 are representative of the 'transient phase' of the system, which started in 1953. The first aerial image shows the morphological condition of the river 9 years after impoundment. The consequences are already visible a few years later. Water is much less prevalent,

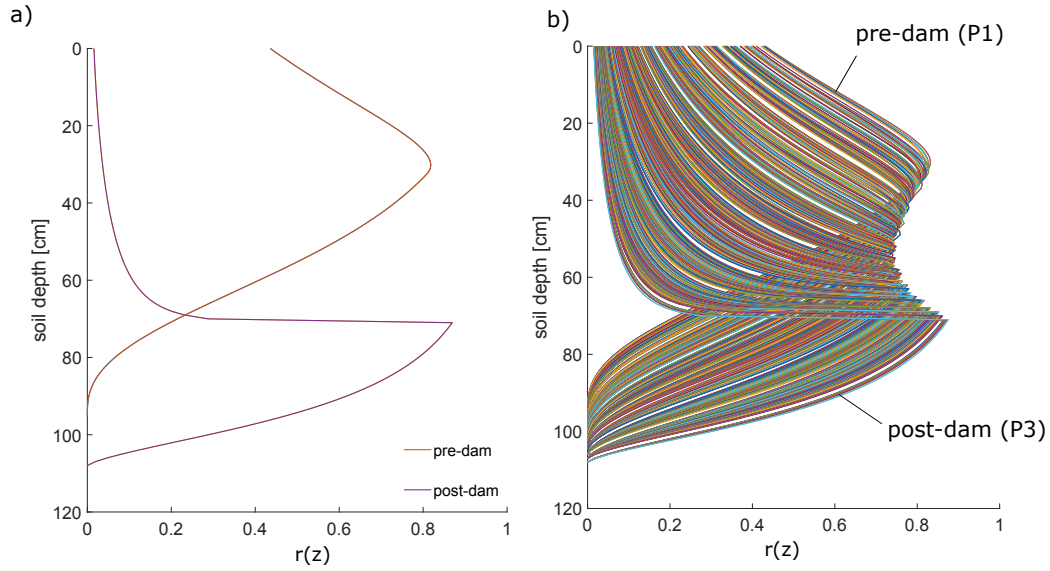

Figure 6.9: Vertical root profiles for $\eta_v = 1.2$ m: a) at pre- and post-dam equilibrium points; and b) at equilibrium points in and between P1 and P3.

giving space to a wide area of sediment and vegetation. The area of grass has widely decreased. This is because flood reduction has caused the uprooting percentage to decrease. In turn, this has encouraged the vegetation to evolve and reach further maturity. The middle image relates to 1995, and shows a more marked phenomenon of vegetation development that consists mainly of an increase in dark green and brown patches (shrubs and trees). On the other hand, the image from 2006 indicated that the morphology of the river has again changed. In particular, it can be seen that areas previously covered by sediment have been taken over by shrubs and forest. It is obvious that the conditions of the system in 1962, 1995, and (most probably) 2006 were transient compared to how the system evolved once the equilibrium state had been reached (P3). Unfortunately the unavailability of a processed aerial image after 2006 has made it impossible to ascertain whether the system has now reached an equilibrium. The image relating to P4 is instead reported with a question mark, as this represents an unknown condition.

6.3.2 System dynamics

Figure 6.8 raises certain important considerations regarding the type of regime transition that occurs when a new regime commenced. To improve the clarity of the foregoing concept, it is convenient to examine the time series of the driver and ecosystem state.

In Figure 6.10a the shift in driver (hydrology) is manifested through a jump in the hydrologic signal at the time t^*, which is further stressed by the trend in averaged flow rate value μ_d. Here, t^* is representative of the year 1953, when the river is dammed. However, Figure 6.10b shows that the ecosystem state, here represented in terms of braiding index, exhibits a slow progressive change after t^*. The aerial images provide an overview of the morphological evolution undertaken by the braided reach of the river, thus complementing the trend of the P_τ - ΔH curve. It should be noted that the plot was originally obtained by plotting P_τ against t and by re-adapting the initial value of P_τ (horizontal curve segment), given that this would undoubtedly cause a discontinuity in t^*. The time lapse over which the curve decreases is denoted as the 'relaxation period' of the system – the time needed by the ecosystem state to adapt to the new equilibrium. It is evident that the reaction timescale of the ecosystem state differs from that of the driver. This is evident in both Figure 6.10a and Figure 6.10b where it is obvious that the ecosystem state and the driver are not linearly linked. By comparing these plots with the classification of the regime transitions proposed by Andersen et al. (2009), an unexplored ecosystem scenario arises. In fact, Andersen et al. (2009) do not report any case where a direct link does not exist between the driver and the ecosystem state. Interestingly, the dashed area in Figure 6.10c provides an indication of the use of resources of the system due to hysteresis. Such resources can be interpreted as that used by the plants to develop longer roots and hence adapt to the hydrologic shift, and the effort that the system

would require to return to the pre-dam equilibrium state.

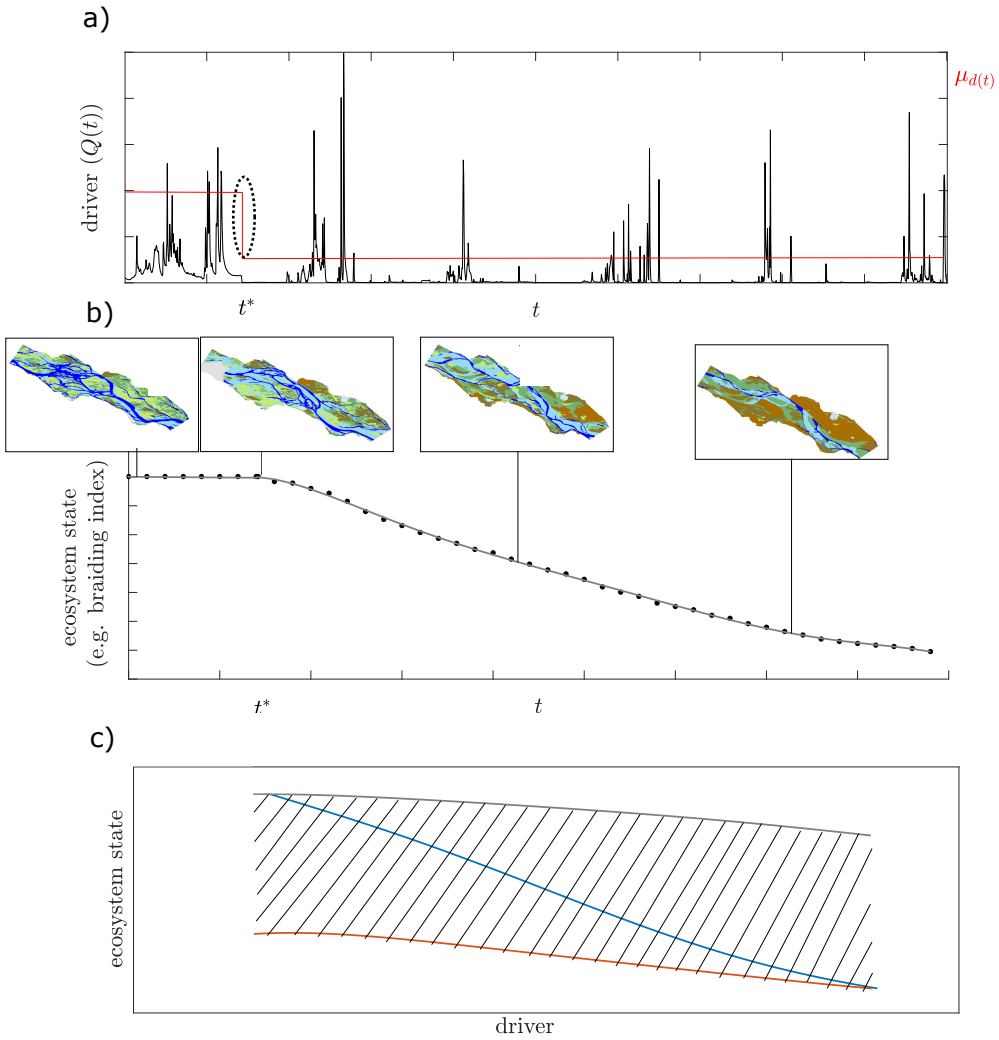

Figure 6.10: Differences between driver and ecosystem state transitions: a) Time series of the driver (flow discharge). Note that the value of the average flow rate, μ_d, does not reflect actual values for the Maggia River. b) Time series of the ecosystem state (braiding index). The aerial images, from left to right, are from 1933, 1944, 1989, and 2006. c) The graph of Figure 6.8 is repeated to highlight the area (energy) enclosed by the three curves.

6.3.3 Role of plant elevation

The curves in Figure 6.8 were produced for a plant elevation of 1.2 m above the riverbed. Hence, it still remains to observe how the uprooting probability changes for other plant elevations. Figure 6.11 shows the equilibrium curves obtained from a plant of elevation varying between 0.8 to 2 m. In this case, the uprooting probability was plotted against $\Delta\tilde{H} = \frac{\Delta H}{\eta_v}$. The minimum value of η_v was set to 0.8 m because lower values of 0.8 m would have led the threshold ξ to be below Q_{cr}, thus going against the POT assumptions.

From Figure 6.11 it is evident that, at the state points P1 and P3, the uprooting probability decreases as the plant elevation increases and vice-versa. This is quite intuitive for the post-dam period, when the plants approaching the riverbed are those with more chance of being uprooted given the long periods of low flow conditions. Conversely, plants at higher elevation are only inundated by sporadic flooding events that cannot be contained by the dam (see Figures 6.3b and 6.3c). Meanwhile, the same logic can be applied to the pre-dam period, where plants with higher probability of being stressed by drag forces are inundated also for low flow conditions occurring in winter periods (see Figures 6.3a).

Figure 6.12a examines the variation in probability of plant uprooting with plant elevation on the riverbank. Figure 6.12a is particularly useful in illustrating to what extent the elevation of the plant influences the uprooting percentage at points P1, P2, P3, and P4. It is clear that the uprooting percentages in P1 and P3 decrease as the plant elevation increases. The uprooting percentage in P3 decreases more rapidly with the plant elevation than in the pre-dam point P1. Hence, the low flow conditions of the post-dam scenario have a greater impact on uprooting probability. The way the percentage varies in P2 (Figure 6.12a) is closer to that in P1, even though there is a inflexion in the trend at a plant elevation of 1.5 m. In P4 the percentage also declines, at a rate that is particularly

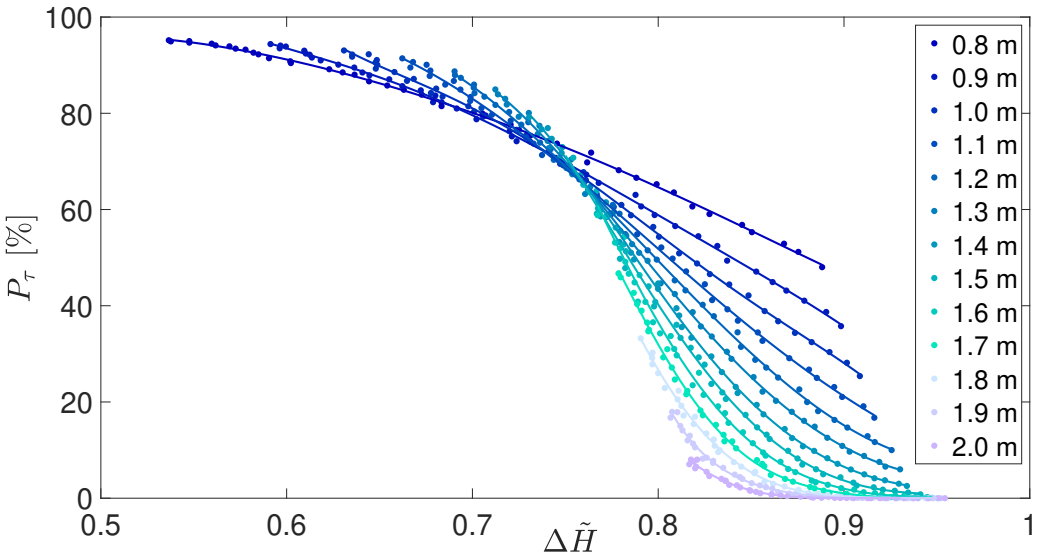

Figure 6.11: Uprooting probability, P_τ, plotted against $\Delta\tilde{H}$, for a range of plant elevations between 0.8 and 2 m.

high for plant elevations greater than 1.2 m.

Figures 6.12b, 6.12c, and 6.12d illustrate the differences in uprooting percentage, ΔP_τ, obtained between the points P1 & P3, P2 & P3, and P1 & P4 for different plant elevations. In these cases, the trends for certain traits resemble a parabola, where plants at different elevations display the same response in terms of ecosystem shift (Figure 6.12b), adaptation to post-dam equilibrium (Figure 6.12c), and ability to re-establish pre-dam conditions (Figure 6.12d). However, it is important to note that these seemingly similar reactions by plants at different elevations have different causes. This can be shown, for instance, by comparing Figure 6.12b to Figure 6.12a. For plants located at elevations lower than 1.3 m, the uprooting probability in P3 decreases much more rapidly than in P1. The vice-versa is observed in the trend of the uprooting probability for plants at elevations between 1.4 and 1.7 m, where the rapid decrease in P_τ occurs in P1.

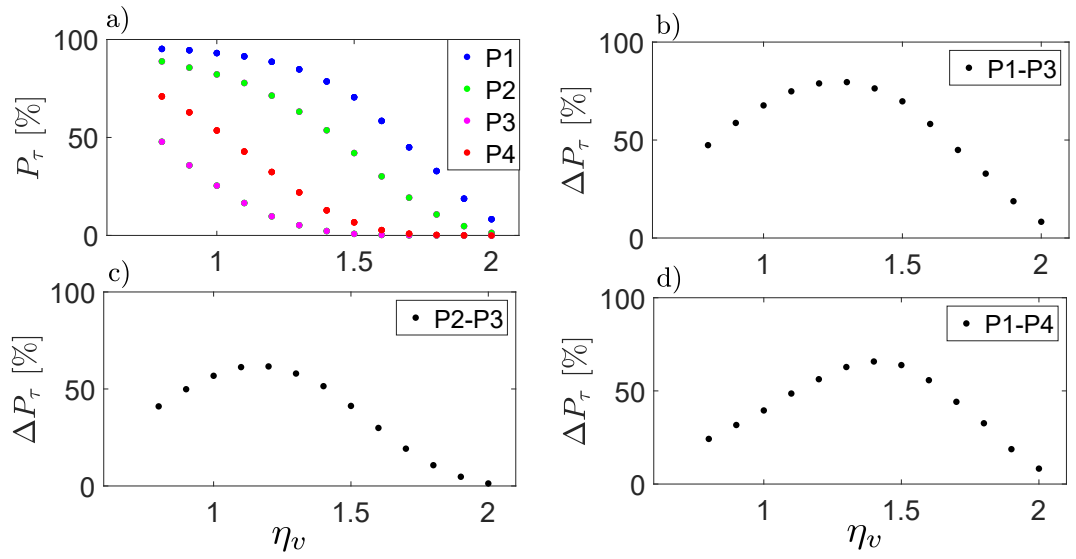

Figure 6.12: Uprooting probability as a function of plat elevation: a) Variation in uprooting probability P_τ with plant elevation on the riverbank in P1, P2, P3, and P4. Variation in difference in the uprooting probability with plant elevation on the riverbank for different values of η_v between: b) P1 & P3, c) P2 & P3, d) P1 & P4.

6.3.4 Role of soil parameters

Figure 6.13 represents the same curves as Figure 6.11, the only difference being that, in this case, the values assigned to $D_{10,s}$ and $D_{90,s}$ are kept constant between P1 and P3. In other words, this is a scenario that would occur if the dam had no impact on the sediment supply downstream. Although this might not happen naturally, it could be expected if sediment continuity was artificially maintained. Figure 6.13 shows that such change can considerably affect the uprooting probability. Specifically, P_τ reached higher values in the post-dam periods than in Figures 6.11 for equal plant elevations. The trends of P_τ in P1 and in P2 (Figure 6.14a) are almost the same as those represented in Figure 6.12a. However, this is not the case for P3 and P4.

A comparison between Figure 6.14 and Figure 6.12 reveals that maintaining $D_{10,s}$ and $D_{90,s}$ constant mostly affects the uprooting probability of plants with

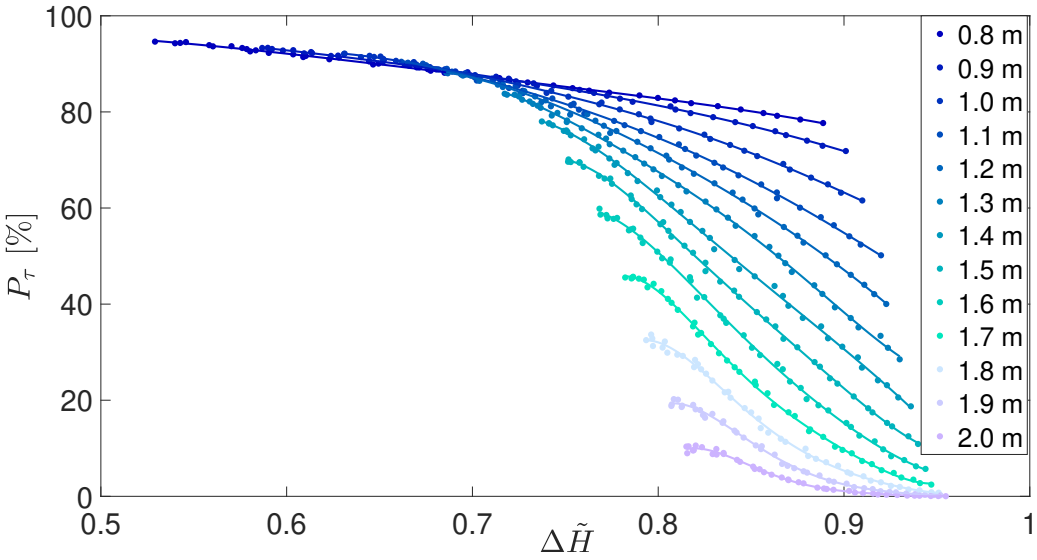

Figure 6.13: Uprooting probability, P_τ, plotted against $\Delta\tilde{H}$, for a range of plant elevations and for constant values of $D_{10,s}$ and $D_{90,s}$.

elevation lower than about 1.5 m. By maintaining the same soil texture between P1 and P3, the retention capacity of the soil remains unchanged as well. Hence, compared to what seen before in Figure 6.11 and Figure 6.12, now in P3 the roots do not have to propagate towards deeper layers to reach the water table. This implies that plants can reach the equilibrium point in P3 and approach point P4 more easily. This does not apply equally for plants that grow at higher elevations, where ΔP_τ appears almost independent of soil texture (compare Figures 6.14a and 6.14b to Figures 6.12a and 6.12b).

When analysing the uprooting probability at the equilibrium points, P1 and P3, the respective reference mean events are constant, and so the PDF of the uprooting times comes to depend solely on the scour depth L_e. To examine the effect of L_e on the variation of the uprooting probability, $D_{10,s}$ and $D_{90,s}$ were varied, as these parameters control the biomass density of the root profile when γ_l and β_l are constant.

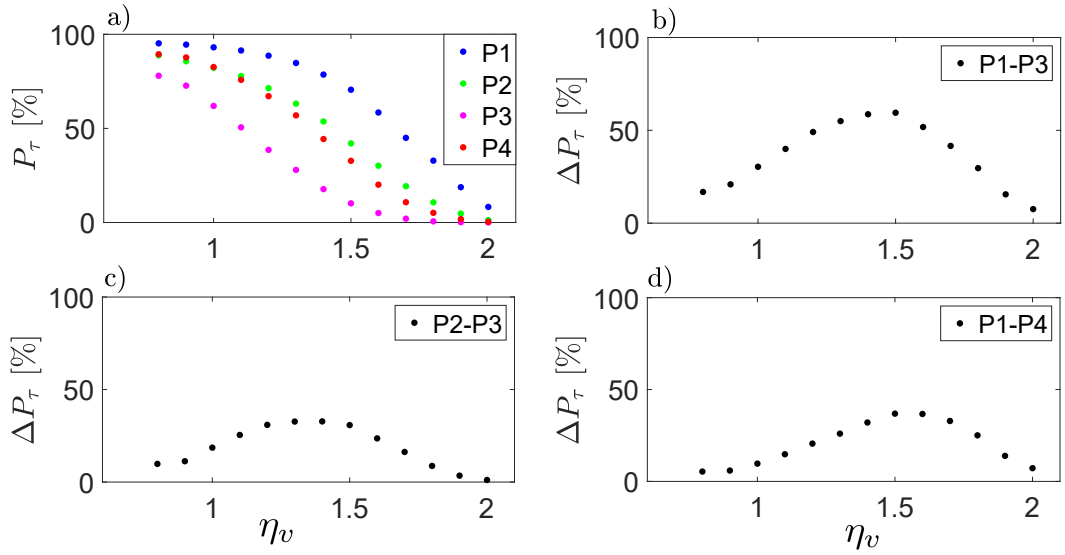

Figure 6.14: Uprooting probability with plant elevation. a) Variation in uprooting probability P_τ with plant elevation on the riverbank in states P1, P2, P3, and P4 , while keeping the value of soil texture constant between P1 and P3. Variation in difference in the uprooting probability with plant elevation on the riverbank for different values of η_v and constant values of $D_{10,s}$ and $D_{90,s}$ between: b) P1 & P3, c) P2 & P3, d) P1 & P4.

Figures 6.15 and 6.16 reveal the effect of variation in $D_{10,s}$ and $D_{90,s}$ on the root profile. An increase in $D_{10,s}$ leads to a decrease in the L_g zone, thus affecting considerably root density and changing its shape. On the other hand, increasing $D_{90,s}$ induces a reduction of the capillary fringe thickness, which drives the roots to reach higher values of z_m.

Figure 6.17 shows how the uprooting probability changes when varying $D_{10,s}$ and $D_{90,s}$ by $\pm 50\%$ with respect to the values used to implement the curves in Figure 6.8. From Figure 6.17 it emerges that, for both hydrologic conditions, the uprooting probability rises as $D_{10,s}$ and $D_{90,s}$ decrease. It is also obvious that the effective particle size impacts more on P_τ than $D_{90,s}$, especially in the post-dam period.

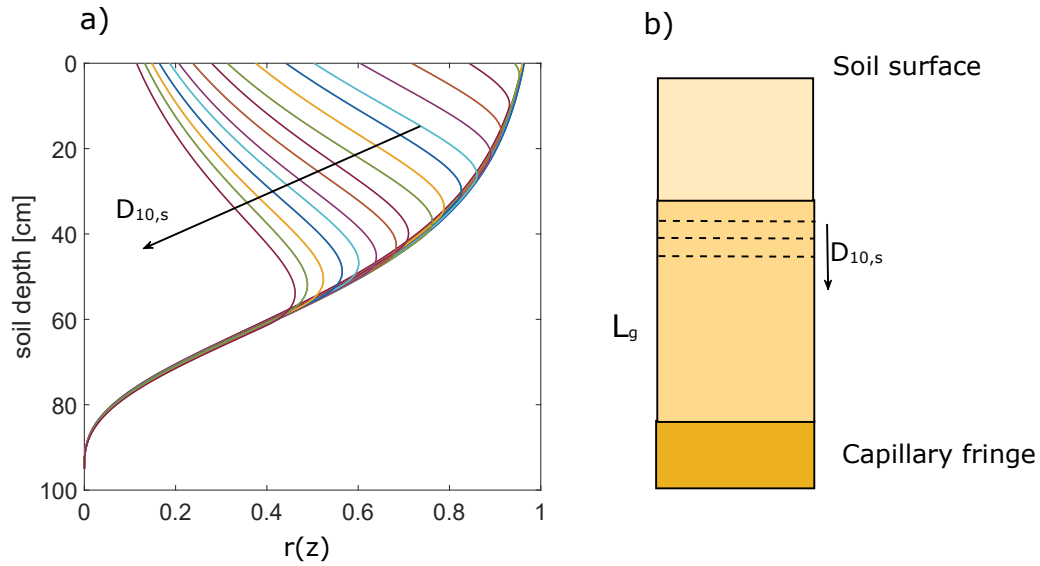

Figure 6.15: a) Vertical root profiles obtained for different values of $D_{10,s}$ and b) related change in L_g thickness.

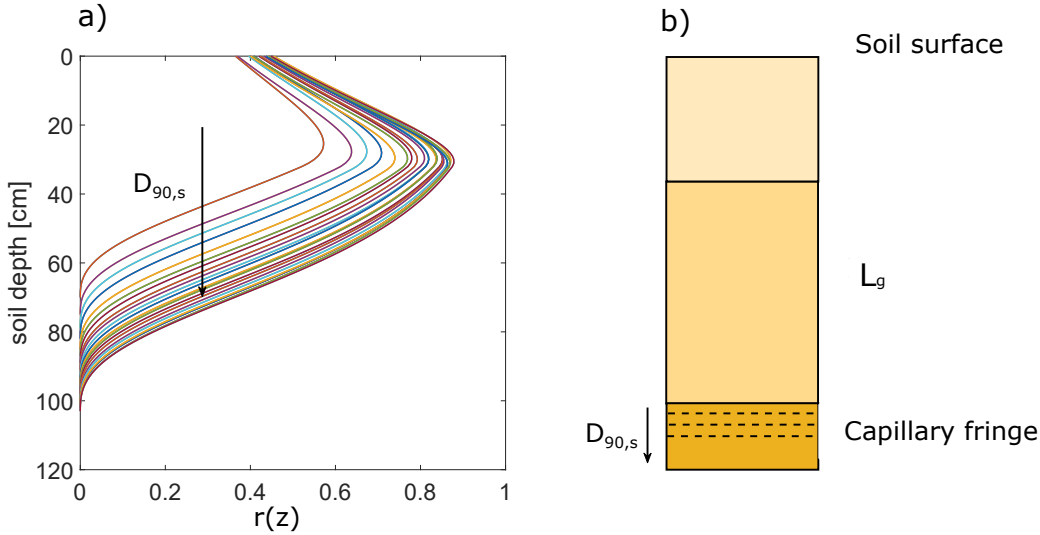

Figure 6.16: a) Vertical root profiles obtained for different values of $D_{90,s}$ and b) related change in L_g thickness.

Given the substantial influence of $D_{10,s}$ on P_τ, Figure 6.17a was replotted for two extreme conditions, namely when η_v is equal to 0.8 and 2 m (see Figures 6.18a and 6.18b). For an elevation of 0.8 m, the minimum difference in uprooting probability between P1 and P3 reaches 24%. However, for certain values of $D_{10,s}$,

this difference reduces further when considering a plant elevation of 2 m.

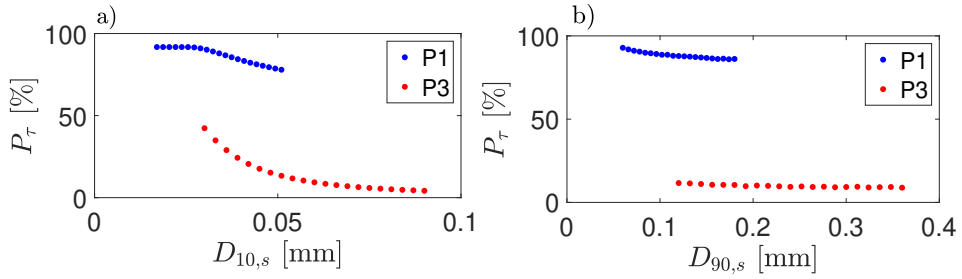

Figure 6.17: Variation in uprooting percentage of P1 and P3 with a) $D_{10,s}$ and b) $D_{90,s}$ (over a range of ±50%) for a plant elevation equal to 1.2 m .

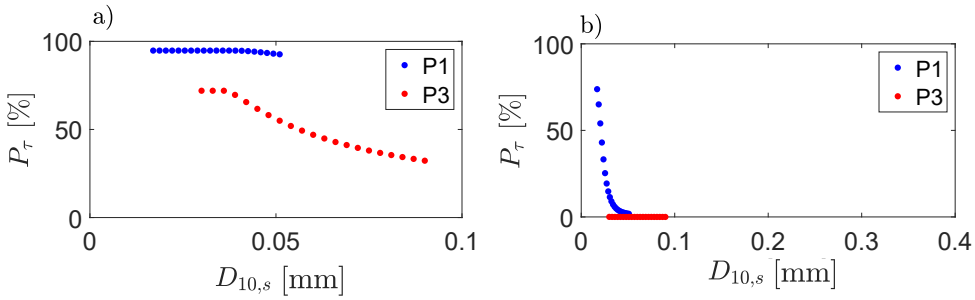

Figure 6.18: Variation in uprooting percentage of P1 and P3 with $D_{10,s}$ (over a range ±50%) for a plant elevation equal to: a) 0.8 m; and b) 2m.

In conclusion, for a plant elevation of 1.2 m, the variation in fine percentage of the soil is insufficient to change the overall configuration of the system triggered by the hydrological shift. However, this conclusion does not apply for the two extreme plant elevations (0.8 and 2m), for which, in certain cases, the soil texture parameters are primary factors of influence.

6.4 Overall interpretation and recommendations

The model was validated for a real case scenario concerning the effect of dam impoundment on a reach of the Maggia river, Switzerland. The model proved

useful at identifying the regime dynamics of the system. Similar dynamics have also been documented in the literature. For instance, Auble et al. (2007) found that vegetation recovery following removal of a dam is complex and does not follow a reversal response, leading to the necessity for a river restoration intervention. Another important observation was made by Shafroth et al. (2002a), who suggested that the persistent occurrence of transient phases after dam construction has a determinant impact on the duration life of mature vegetation (e.g. forest), which could persist for even more than a century. In practice, mature vegetation cannot easily be removed by flow erosion processes. This conforms with Shafroth et al. (2002a) who found that, in the post-dam period, trees commonly decay because of anoxia caused by prolonged inundation or the richness of toxic substances in the soil. Shafroth et al. (2002a) also emphasised how the removal of dams, especially in systems with low sediment transport, may result in negligible downstream changes.

Previous analysis has shown that the effective particle size of the fine sediment plays an important role in uprooting probability (Section 6.3.4). Hence, replenishment of fine sediments could offer a potential way of maintaining the uprooting percentages of the post-dam conditions at levels closer to those of the pre-dam conditions. Such a goal could be achieved for instance by inducing artificial floods, a well-established technique used to reduce river morphological changes after dam impoundment. In the present application, artificial flooding should be controlled to ensure that the increase in frequency of peak events would bound the erosion rate so as to hinder river narrowing and incision, and stream-bank erosion (Stähly et al., 2019). This strategy could also be adopted to reduce the accumulation of fine sediment upstream of a dam, whose presence considerably limits the storage capacity of the reservoir. The input of fine sediment would not only benefit the shape of the river but also its biodiversity, thus preventing the riparian system from drifting to alternative states (Arheimer et al., 2018). In

terms of uprooting probability, the release of flood pulses would enhance scouring while increasing the percentage of fine sediment that, as observed previously, raises the likelihood of plant uprooting by inducing a shift in the root profile. The artificial flooding strategy appears to be the most promising in terms of effectiveness compared to alternative approaches, such as sediment bypassing and artificial sediment supply. This is also confirmed by results obtained by Perona et al. (2009), who used a lumped model to predict that adding an artificial disturbance each year would lead to increases of 10% in both sediment and water area in the Maggia River reach considered herein. Nevertheless, artificial floods require careful control because such floods can have significant consequences for water quality and fauna (Grimardias et al., 2017).

The combined model presented in this Chapter has shed light on the type of ecosystem shift that occurs when a river is impounded by a dam. The results obtained by applying the model to data from an existing river system compared well with the actual regime dynamics. Furthermore, testing the hysteretic behaviour of the river system also motivated the following questions: what would the floodplain look like if a higher return period flood occurred? Would the model predict such a scenario correctly?

To conclude, the novel combined method can identify and complement dam regulation strategies, which in turn could promote sustainable solutions to preserve riparian ecosystems.

Chapter 7

Conclusions

This final Chapter presents a brief summary of the main findings of the thesis. The potential research impact is also identified in the context of river restoration. Recommendations for future work are also made.

7.1 Summary of findings

The main conclusions of this work are listed as follows:

- The experiments presented in Chapter 2 provided high quality data which should prove particularly useful for informing the reintroduction of riparian species to river systems and for wider bio-engineering and research purposes (e.g. the use of cuttings to stabilize and reinforce riverbanks and river bedforms; guidance in flume erosion experiments). *Salix fragilis* were demonstrated to exhibit an optimum tolerance to high water stress and prolonged drought conditions. Furthermore, the rate of decay of water table level was found to be the most important influence factor on vertical root biomass distribution. Hence, soil retention capacity (e.g. such as that of sand) should be selected such that a layer is created where a good balance between oxygen and water is achieved enabling *Salicacae* species to develop without experiencing anoxic or hypoxic conditions. It was also found that soil moisture percentage influences the rooting resistance of *Salicacae* cuttings. In particular, a higher saturation level in the soil

corresponded to a lower root resistance, and vice-versa. Even short *Salicacae* cuttings were capable of developing roots and surviving, albeit their reduced supply of internal resources. This suggests that micro-cuttings may also be considered to be a suitable technique for riverbank stability, as recently also demonstrated by Desrochers et al. (2020). Furthermore, the presents experiments have paved to way to the possibility of using more realistic types of vegetation in future flume erosion experiments.

- The free-body model proved to be a valuable tool in assessing the critical rooting length. The model validation study showed that the framework adopted can adequately describe the physical process of uprooting, for different types of seedlings, at different stages of growth, and for different magnitudes of scouring events. The free-body model revealed that the tangential component of the drag force plays the leading role among the destabilizing forces acting on the canopy, and that the drag exposed surface area of the plant significantly contributes to the modulus of the friction force. However, these observations result from having assumed a reconfiguration of the plant in the streamline direction. For less flexible and rigid vegetation, the normal component of the drag force would likely make the most significant contribution. Furthermore, morphologic and topologic variability among intra-species, evident in the data sets, could not be detected by the free-body model. Inclusion of an improved description of the effect of hydrodynamic instabilities (e.g. flapping mechanism) and turbulence on the canopy and leaves would contribute to extending the range of validity of the model.

- Pullout tests carried out for *Salix fragilis* (see Chapter 4) revealed that soil moisture percentage has a significant influence on the pullout mechanism. From the results, it was found that the maximum root resistance increases

with the total length of the roots and with time, but is independent of the size of the logs. This response demonstrates that the statistics obtained are relevant for developing up-scaling rules. The outputs of the statistical analysis of the below-ground biomass also proved relevant for the up-scaling, given that the root biomass was observed to be uniformly distributed along the trunks. The regression laws describing the growth of the above-ground biomass and the link between the maximum pullout force and total root length allowed computation of the drag forces acting on the logs and detection of 'biological windows' when mobilization of the logs is likely to occur. These fundamental findings shed light on the competition between the frequency and magnitude of flood disturbances and the temporal evolution of the biomechanical properties of vegetation.

- A regime dynamics model has been established (see Chapter 5) that enables examination of the regime transitions that riparian floodplains undergo when a dam impoundment alters the hydrological flow regime of a river. The model uses uprooting probability as a proxy to describe how the ecosystem evolves according to the continuous adjustment of the root profile within the soil. A conceptual representation was proposed for all possible regime transitions that a riparian ecosystem could experience after river impoundment.

- The regime dynamics model was validated for a reach of the River Maggia, Switzerland, where damming had taken place. It was found that the hydrological shift induced by a dam impoundment can lead to a new type of ecosystem regime transition characterised by irreversibility. Even if the ecosystem driver (hydrology) exhibits a down-shift in time, the ecosystem state (uprooting probability) might change smoothly with time and not necessarily undergo a sharp shift. However, the ecosystem state may

experience irreversible dynamics when the initial hydrologic regime is re-established. This dynamics is entirely driven by vegetation root tropism responses (e.g. hydrotropism) to changing river hydrology. Analysis of different scenarios (e.g. involving different plant elevations and grain size distributions) showed that plants close to the river bed are the most likely to be removed and that an increase in effective particle size of the soil can affect the ecosystem state significantly. Finally, comparison between the scenarios presented by the aerial images of the reach of the Maggia River and the modeled output suggests that uprooting probability is a suitable proxy to examine and foresee the consequences of hydrologic shifts in riparian ecosystems.

7.2 Research impact

For decades, riparian systems have been subjected to intensive anthropogenic actions that have disrupted and damaged river systems by altering the natural flow regime to accommodate human needs. Riparian areas have thus drastically changed from pristine conditions to give way to intensive agriculture, energy production and urban development. For example, progressive loss of braided patterns in certain river systems was caused by the onset of flow regime regulation and deforestation.

Growth of awareness of the state of health of riparian areas and the increasing occurrence and severity of extreme events (e.g. flooding and rainfall events) have encouraged environmental organizations and government agencies to promote river rehabilitation and restoration programmes. Conservation and restoration of river ecosystems are now crucially important and urgently needed. One of the many goals of river restoration projects is to reestablish the natural processes of rivers through the development of natural biogeomorphic river structures and the

reintroduction and establishment of natural riparian species. However, the lack of adequate design criteria for enhancing the formation and recovery of floodplain vegetation have led to unsuccessful outcomes (Wohl et al., 2005). The 2015 State of the Environment Report found that only less than half of the rivers achieved "good ecological status" in 2015 (EEA, 2015). The foregoing confirm that not enough has been done, and that river processes might suffer an irreversible mechanism. This thesis helps shed light on the cause of such irreversibility (e.g. vegetation root re-adaptation following flow regime perturbation).

In this context, vegetation removal due to flow and erosion processes plays a significant part in the morphologic and ecologic evolution of rivers and is an issue of great importance for the adequate realization and maintenance of river restoration schemes. Although relevant research studies have been carried out on the interaction between vegetation and river dynamics, limited research has been conducted on how the biomechanical properties of vegetation and the related timescales interact with fluvial processes and river hydrology, and how vegetation roots can be considered as an important ecological indicator of ecosystem alterations.

To help answer the foregoing questions, this thesis has presented a novel holistic approach that links river hydraulics, hydrology, geomorphology, biology and, to some extent, ecology. From a practical perspective, it is important to emphasise that the success of this novelty rests on a very careful designed framework that includes the use of intersecting models (e.g. Calvani et al., 2019b; Perona and Crouzy, 2018; Tron et al., 2014) and high fidelity customised input values. Moreover, the two data sets obtained from the experiments presented in Chapter 2 and in Chapter 4 represent a relevant resource that can be shared with interested parties and used to design future laboratory and field investigations, as discussed below.

This work has led to three additional important discoveries. Firstly, despite the

large variability of vegetation characteristics, experimental and theoretical results have demonstrated that the average trends in vegetation growth characteristics and responses to external forces are statistically significant and can be considered as representative. Secondly, the experimental results confirmed that knowledge of the biologic timescales of vegetation is fundamentally important when analysing the balance between vegetation growth and mortality in relation to hydrologic disturbance. Finally, vegetation roots play a relevant part in engineering the resilience of a riverine ecosystem to hydrologic disturbance and perturbations of both climatic and anthropic origin.

Hence, mechanisms of plant-river interactions together with elaborate species distribution models (e.g. Ogle and Barber, 2008; Smolik et al., 2010) and guidance on plant species specification should be integrated in morphodynamic and computation fluid dynamics models. Furthermore, as a result of the irreversibility of ecomorpohodynamic processes in the face of flow regime alterations, it is crucial that strategies be developed to optimize the design of mitigation measures (such as dam re-operation and river restoration schemes). Reconceptualization of river and green engineering practices would be aid decision makers responsible for maintaining the floodplain morphology, without incurring irreversible regime transitions.

7.3 Recommendations for future work

This thesis has provided insight into the role of vegetation in river restoration, and also motivates new research directions, several of which are discussed below.

- More realistic flume experiments should be carried out to investigate flow-induced uprooting of *Salix fragilis*, given its promising performance as seedlings in the idealised experiments described in Chapter 2. Based on the results of these further experiments, it should then be possible to optimise

the water table regime for different biomass configurations and specific scenarios. It is also recommended that the flume tests be undertaken for *Salix fragilis* cuttings instead of seedlings. This would enable investigation of the phenomenon of local erosion, induced by a large obstacle-to-sediment size ratio (Melville and Sutherland, 1988). To date such dynamics have only been studied (to the author's knowledge) in the context of fluid-obstacle interactions (Kirkil and Constantinescu, 2010; Manes and Brocchini, 2015; Roulound et al., 2005). It would be interesting to discover the effect of local erosion on uprooting probability and uprooting time.

- Analysis should carried out on the ability of *Salix fragilis* to reinforce river-bank stability for heterogeneous soils and different river flooding regimes.

- The free-body model results (Chapter 3) indicate the need for allometric laws to be derived for the most common riparian species. This is an essential prerequisite for making precise estimates of the plant area experiencing drag and of the main rooting length. At the time of writing, the free-body model has only been tested on isolated vegetation. Hence, it is recommended that the model undergo further tests to examine its reliability when applied to different geometrical arrangements of porous vegetation.

- Statistical analysis of small-scale wood logs in Chapter 4 revealed the possibility of mechanical similarity at a larger scale. To achieve this, investigation needs to be made of the growth requirements (e.g. soil moisture condition, light and nutrient availability) at field scale and specific to the site of interest.

- It is recommended that the regime dynamics model presented in Chapter 5 be validated for other fluvial systems that have experienced regime transitions similar to those of the Maggia River (e.g. Santa Maria and Bill

Williams Rivers, see Shafroth et al., 2002b).

- The Maggia River study demonstrated that satellite and detailed field observation campaigns are essential for the analysis of river regime dynamics. Hence, more detailed, comprehensive digital monitoring of the riparian landscape is required. Such information would provide more accurate model input data on the evolution of the grain size distribution of the bed and banks and bars of a given river. Likewise, more consistent tracking of vegetation coverage and type over longer periods would improve assessment of ecosystem evolution over time.

- From a holistic point of view, closer transdisciplinary cooperation between river engineers, geomorphologists, and ecologists is needed to preserve and save the terrestrial and aquatic ecosystems before planetary boundaries are reached (Steffen et al., 2015). The present thesis offers a starting point for such cooperation, given that its methodology and results pave a way for new research that would benefit greatly from concerted effort at the intersection between different disciplines to yield results of higher fidelity, and thus also of higher research and societal value.

Appendices

Appendix A

A.1 Compound Poisson Process

The Compound Poisson Process (abbreviated as CPP) is a signal characterized by a sequence of stochastic instantaneous pulses followed by exponential deterministic decays. CPP signal can be used as a synthetic signal for the water table dynamics. The CPP signal is governed by the Langevin equation of the form (see also equation 5.2):

$$\frac{dz_w}{dt} = \eta_l(h_2 - z_w) - \zeta \tag{A.1}$$

where z_w is the water table depth and h_2 is the maximum distance from the soil surface to the water table. The first term on the right-hand side of equation A.1 expresses the deterministic component of the signal (exponential decay) with decay rate η_l. ζ is the state variable representing the stochastic counterpart in which the pulses are modeled as a white shot noise with mean rate, λ_l. The expression of ζ reads:

$$\zeta(t) = \sum_{i=1}^{\infty} h_i(t)\delta(t - t_i) \tag{A.2}$$

where $h_i\delta(0)$ is the size of the pulses and $\delta(\cdot)$ is the Dirac delta function.

The probability distribution of the random pulses is exponential with mean γ_l: $p_H(h) = \frac{1}{\gamma_l}e^{-h/\gamma_l}$.

As the quantity h_2 is a constant shift in z-axis, equation A.1 can be simply rewritten referring to a generic variable s. This allows to facilitate the derivation of the probability density function of the water table level (see equation 2.3) from equation A.1.

Hence, the Langevin equation for s becomes:

$$\frac{ds}{dt} = \eta_l(s) - \zeta \tag{A.3}$$

Assuming that the variable s at the time t is $s(t)$ and that in a small interval dt the probability that no jumps occurs is $(1 - \lambda_l dt) + o(dt)$:

$$s(t + dt) = s(t) - \Delta s, \tag{A.4}$$

where:

$$\Delta s = \int_t^{t+dt} \eta_l(s(\tau))d\tau = \eta_l(s(t))dt + o(dt) \tag{A.5}$$

where $o(dt)$ represents an infinitesimal of higher order.

The probability that a pulse takes place in dt is $\lambda_l dt + o(dt)$. In this case:

$$s(t + dt) = s(t) + h - \Delta s \tag{A.6}$$

As a result, the probability that the process takes a value in $(s, s + ds)$ at the time $t + dt$ reads:

$$\begin{aligned} p(s, t + dt)ds &= (1 - \lambda_l dt)p(s + \Delta s, t)d(s + \Delta s) \\ &+\lambda_l dt \int_0^s p(u + \Delta u, t)p_H(s - u; u)d(u + \Delta u)ds, \end{aligned} \tag{A.7}$$

where the second term on the right-hand side takes into account the condition for which the process reaches s due to a instantaneous pulse. If equation A.5 is substituted into equation A.7 and the terms of order $o(dt)$ are neglected:

$$\begin{aligned} p(s, t + dt)ds &= (1 - \lambda_l dt)p(s + \eta_l(s)dt, t)d(s + \eta_l(s)dt) \\ &+\lambda_l dt \int_0^s p(u + \eta_l(u)dt, t)p_H(s - u; u)d(u + \eta_l(u)dt)ds \\ &= (1 - \lambda_l dt)\left(p(s, t) + \eta_l(s)dt\frac{\partial}{\partial s}p(s, t)\right)\left(1 + \frac{\partial}{\partial s}\eta_l(s)dt\right) \\ &+\lambda_l dtds \int_0^s p(u, t)p_H(s - u; u)du. \end{aligned} \tag{A.8}$$

Dividing equation A.8 by ds, subtracting the quantity $p(s,t)$ from both sides, dividing by dt, and for dt approaching 0, we obtain the Chapman–Kolmogorov equation (master equation):

$$\frac{\partial p(s,t)}{\partial t} = \frac{\partial}{\partial s}[p(s,t)\eta_l(s)] - \lambda_l p(s,t) + \lambda_l \int_0^s p(u,t)p_H(s-u;u)du. \tag{A.9}$$

Given that the distribution of the jump sizes, $p_H(h)$, is exponential with mean γ_l, the general form of the solution of equation A.9 is:

$$p(s) = C\frac{1}{\eta_l(s)}e^{\left(-\frac{s}{\gamma_l}+\lambda_l\int_s\frac{du}{\eta_l(u)}\right)}. \tag{A.10}$$

By solving the integral in equation A.10, we obtain:

$$p(s) = C\frac{1}{\eta_l(s)}e^{-\frac{s}{\gamma_l}}(s)^{\frac{\lambda_l}{\eta_l}-1} \tag{A.11}$$

where C is the normalization constant. Hence, the constant C can be obtained by imposing the integral of $p(s)$ equal to 1:

$$\int_0^\infty \left(C\frac{1}{\eta_l(s)}e^{-\frac{s}{\gamma_l}}(s)^{\frac{\lambda_l}{\eta_l}-1}\right)ds = 1. \tag{A.12}$$

The expression for the constant C resulting from the normalizing condition of equation A.12 is:

$$C = \frac{\gamma_l^{-\lambda_l/\eta_l}}{\Gamma[\frac{\lambda_l}{\eta_l}]}\eta_l(s) \tag{A.13}$$

where $\Gamma[\cdot]$ is the complete Gamma function. By being $\frac{\lambda_l}{\eta_l} = \beta_l$ and by substituting the value of the constant C in equation A.11, we obtain:

$$p(s) = \frac{\gamma_l^{-\beta_l}}{\Gamma[\beta_l]}e^{-\frac{s}{\gamma_l}}(s)^{\beta_l-1} \tag{A.14}$$

If we reestablish the variables of equation A.1, we obtain:

$$p(z_w) = \frac{\gamma_l^{-\beta_l}}{\Gamma[\beta_l]}e^{\frac{z_w-h_2}{\gamma_l}}(h_2-z_w)^{\beta_l-1}, \tag{A.15}$$

thus obtaining equation 2.3.

Appendix B

B.1 Perona and Crouzy's model

Perona and Crouzy's model uses a probabilistic frame to define the plant resilience to uprooting induced by flow-erosion processes (uprooting of Type II). The model is built on the concept that the rooting depth of a plant, L, is the main responsible variable for the root mechanical anchoring. L is time dependent because the plant is subjected to the evolution of the riverbed elevation due to erosion and deposition processes. The variation of L is expressed with the Langevin equation:

$$\frac{dL}{dt} = -\dot{\eta}(L,t) + g_t(t)\psi(t), \quad t > 0 \tag{B.1}$$

The first term on the right-hand side of the equation describes the mean erosion dynamics (mean erosion rate), whereas the second term accounts for the local fluctuations of the erosion and deposition processes. As stated in Chapter 3, g_t describes the random noise in the erosion process and $\psi(t)$ indicates the strength of a Wiener process.

Plant anchoring is reduced by scouring dynamics that are taken into account as alternating deposition and erosion trajectories (see Figure B.1). Uprooting occurs when the trajectory is lost, that is when the rooting depth L reaches the critical one L_c.

Given the stochastic nature of the process, the probability density function

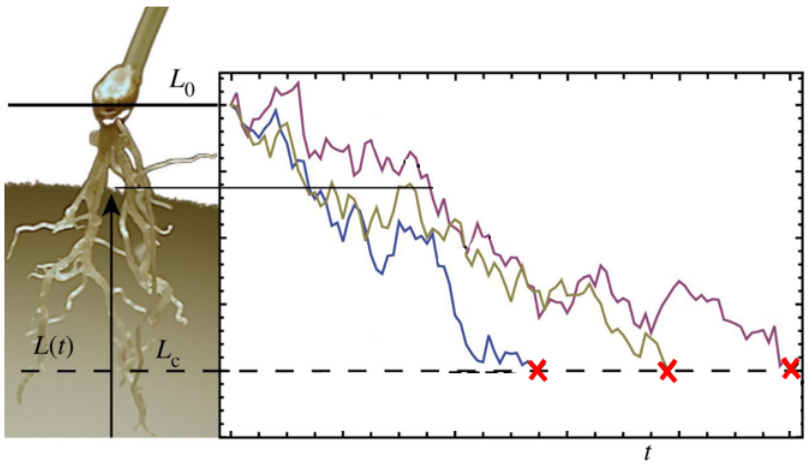

Figure B.1: Illustration of the approach described by equation B.1. Uprooting occurs when the scouring trajectories are lost and, specifically, when the critical state L_c is achieved (modified from Perona and Crouzy, 2018).

of the rooting depth is also obtained and reads:

$$p(L,t) = \frac{1}{\sqrt{4\pi G(t)}}\left(e^{(-(L+V(t)-L_0)^2)/4G(t)}\right) + \frac{1}{\sqrt{4\pi G(t)}}\left(-e^{(V(t)(L_0-L_c)/G(t))-((L+V(t)-2L_c+L_0)^2)/4G(t)}\right). \tag{B.2}$$

Equation B.2 is obtained by solving the Fokker-Planck equation via the methods of images (see Perona and Crouzy, 2018).

In equation B.2, $G(t) = \int_0^t (g_t(\tau)/2)d\tau$, and $V(t) = \int_0^t \dot{\eta}(\tau)d\tau$, where τ is the dummy variable of integration. The integration of equation B.2 generates the *survivor function*, which provides the survival percentage of a plant during the uprooting process:

$$P(t) = \int_{L_c}^{+\infty} P(L,t)dL. \tag{B.3}$$

If equationB.3 is derived in time: $\frac{-dP(t)}{dt}$, we obtain the probability density function of the uprooting time, which is the PDF of the first mean passage time T through the boundary when $L = L_c$ (Perona and Crouzy, 2018):

$$p_\tau(T) = \frac{L_e}{2\sqrt{\pi G(T)^3}} e^{\left(-\frac{(L_e-V(T))^2}{4G(T)}\right)}\left[\frac{g_t(T)}{2} + e^{\left(\frac{(L_e+V(T))^2}{4G(T)}\right)}W(T)\right] \tag{B.4}$$

where G and V are the functions that have been defined previously for $t = T$, and $W(T) = \sqrt{\pi}\text{Erfc}\left[\frac{L_e+V(T)}{2\sqrt{G(T)}}\right]\left(\dot{\eta}(T)\sqrt{G(T)} - \frac{g_t(T)}{2}\frac{V(T)}{\sqrt{G(T)}}\right)$. If g_t and $\dot{\eta}$ are constant, then $W(t) = 0$ and $p_\tau(T)$ becomes an inverse Gaussian distribution (see equation 3.22).

Appendix C

C.1 Autocorrelation function

The autocorrelation function (abbreviated as ACF) reveals the correlation between the lagged values of a temporal series (Box et al., 2015). The autocorrelation function is used to ascertain randomness in a data set. Autocorrelation is weak when data are random, conversely, data have significant autocorrelation when data are not random. In the case of non-random data, ACF can be used to detect a certain time series model.

The mathematical expression of the autocorrelation function, r_k, reads:

$$r_k = \frac{\frac{1}{N}\sum_{t=1}^{N-k}(X_t - \bar{X})(X_{t+k} - \bar{X})}{\frac{\sum_{t=1}^{N}(X_t - \bar{X})^2}{N}}, \tag{C.1}$$

where X_t and X_{t+k} are the lagged values of the time series of the variable, k indicates the time lag, and N the number of observations.

The plot that represents r_k against k is called autocorrelogram (Figure C.1).

If the signal of the autocorrelation function falls below the confidence bounds (see horizontal blue line in Figure C.1), it means that there is no autocorrelation between adjacent values.

The confidence bounds were here obtained as follows:

$$\pm z_{1-\epsilon/2}\sqrt{\frac{1}{N}(1 + 2\sum_{i=1}^{k} X_i^2)}, \tag{C.2}$$

where z is the cumulative distribution function of the standard normal distribution and ϵ is the significance level that, in Chapter 4, has been set to 5%.

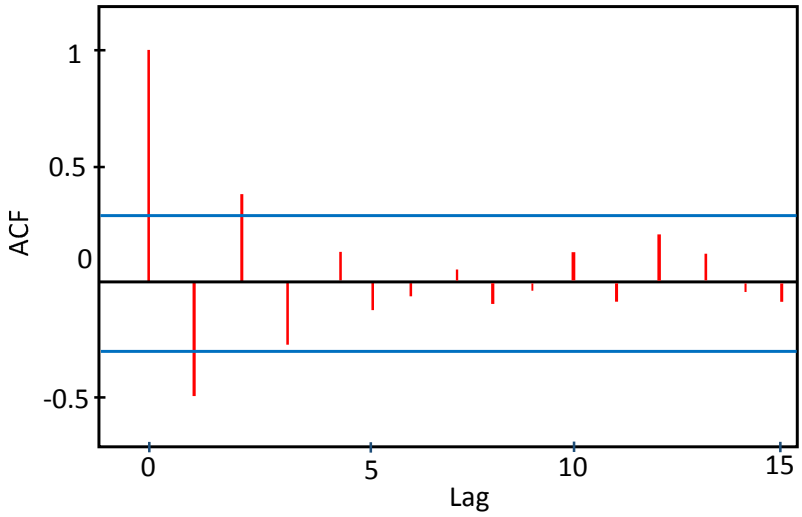

Figure C.1: Example of sample autocorrelation plot.

Appendix D

D.1 Peak Over Threshold Probability

Peak Over Threshold (POT) is a methodology used in extreme value analysis that was developed by Todorovic (1970) and widely applied in flood frequency analysis (Bezak et al., 2014; Castillo, 2012; Claps and Laio, 2003). Specifically, POT evaluates the exceedance probability of the local maxima of a time series over an assigned threshold ξ (see Figure 5.3 for a graphical representation). The applicability of POT relies on a time series that is composed of independent and identically distributed values.

In the context of this thesis, the peak events are represented by the local maxima of the daily discharge time series, $Q(t)$, whose signal is generated by a Compound Poisson Process. Hence, POT is used to assess the return period, $T(\xi)$, of the discharge events that exceed ξ:

$$T(\xi) = \frac{1}{1 - P_\xi}, \tag{D.1}$$

where P_ξ is the POT probability (i.e. the probability of events occurring above the selected threshold.) The classic expression of the POT probability, P_ξ, can be obtained by applying the following mathematical steps.

Generally, for high thresholds ($\xi \to \infty$), the distribution of the peaks is Poissonian (Cramér and Leadbetter, 2013). Hence, the number of the peaks occurring in a period of time T is governed by the Poisson distribution:

$$p(j) = \frac{(\lambda'_d T)^j}{j!} e^{-\lambda'_d T}, \tag{D.2}$$

where j is the generic number of occurrences ($j = 0, 1, 2, ...\infty$) and λ'_d is the frequency of the events that are above ξ. λ'_d is expressed as follows:

$$\lambda'_d = \frac{1}{T_\xi^+ + T_\xi^-}, \tag{D.3}$$

where T_ξ^+ is the average time above the threshold and T_ξ^- is the average time below the threshold. The expression of T_ξ^+ has already been given in equation 5.7.

T_ξ^- is given by:

$$T_\xi^- = \frac{1}{\lambda_d} {}_1F_1[1; 1 + \beta_d; \phi] \tag{D.4}$$

where $\beta_d = \lambda_d \tau_d$ is the product between the mean rate of the pulses, λ_d, and the autocorrelation time, τ_d, and ${}_1F_1[\cdot;\cdot;\cdot]$ is the confluent hypergeometric function of the first kind.

Equally, λ'_d can be simplified to:

$$\lambda'_d = \frac{e^{-\phi}\phi^{\beta_d}}{\tau_d \Gamma[\beta_d]}, \tag{D.5}$$

where, as seen in Chapter 5, $\phi = \frac{\xi}{\gamma_d}$ is the ratio between threshold and the mean rate of the pulses, γ_d, and $\Gamma[\cdot]$ is the complete Gamma function.

By considering the probability of occurrence $p(j)$, the POT probability, P_ξ, corresponds to the cumulative distribution of the events j:

$$P_\xi = \sum_{j=0}^{\infty} p(j)(P_\xi^-)^j, \tag{D.6}$$

in which $(P_\xi^-)^j$ represents the non-exceedance probability of j where $P_\xi^- = 1 - P_\xi^+$ and P_ξ^+ is the above-threshold probability.

Substituting the expression in D.2 into D.6, we obtain:

$$P_\xi = \sum_{j=0}^{\infty} \frac{(\lambda'_d T)^j}{j!} e^{-\lambda'_d T} (P_\xi^-)^j. \tag{D.7}$$

After some simple mathematical steps and by recalling that:

$$e^z = \sum_{j=0}^{\infty} \frac{z^j}{j!}, \tag{D.8}$$

equation D.7 becomes:

$$P_\xi = e^{-\lambda'_d T} e^{\lambda'_d P_\xi^- T} = e^{-\lambda'_d T(1-P_\xi^-)}, \tag{D.9}$$

which, for a unit time interval ($T = 1$), gives the classic relation of the Peak Over Threshold probability:

$$P_\xi = e^{-\lambda'_d (1-P_\xi^-)} = e^{-\lambda'_d P_\xi^+}. \tag{D.10}$$

Bibliography

Abbe, T. B., & Montgomery, D. R. (1996). Large woody debris jams, channel hydraulics and habitat formation in large rivers. *Regulated Rivers: research & management*, *12*(2-3), 201–221.

Abernethy, B., & Rutherfurd, I. D. (1998). Where along a river's length will vegetation most effectively stabilise stream banks? *Geomorphology*, *23*(1), 55–75.

Abramowitz, M., & Stegun, I. A. (1948). *Handbook of mathematical functions with formulas, graphs, and mathematical tables* (Vol. 55). US Government printing office.

Allen, D. C. (2016). Microclimate modification by riparian vegetation affects the structure and resource limitation of arthropod communities. *Ecosphere*, *7*(2), e01200.

Allmendinger, N., Pizzuto, J., Potter, N., Johnson, T., & Hession, W. (2005). The influence of riparian vegetation on stream width, eastern Pennsylvania, USA. *Geological Society of America Bulletin*, *117*, 229–243.

Allred, T. M., & Schmidt, J. C. (1999). Channel narrowing by vertical accretion along the Green River near Green River, Utah. *Geological Society of America Bulletin*, *111*(12), 1757–1772.

Amlin, N. M., & Rood, S. B. (2002). Comparative tolerances of riparian willows and cottonwoods to water-table decline. *Wetlands*, *22*(2), 338–346.

Andersen, T., Carstensen, J., Hernández-García, E., & Duarte, C. M. (2009). Ecological thresholds and regime shifts: Approaches to identification. *Trends in Ecology Evolution*, *24*(1), 49 –57.

Anderson, N. H., Sedell, J. R., Roberts, L. M., & Triska, F. J. (1978). The role of aquatic invertebrates in processing of wood debris in coniferous forest streams. *American Midland Naturalist*, 64–82.

Anderson, R. J., Bledsoe, B. P., & Hession, W. C. (2004). Width of streams and rivers in response to vegetation, bank material, and other factors. *JAWRA Journal of the American Water Resources Association*, *40*(5), 1159–1172.

Arheimer, B., Hjerdt, N., & Lindström, G. (2018). Artificially induced floods to manage forest habitats under climate change. *Frontiers in Environmental Science*, *6*, 102.

Asaeda, T., & Rashid, M. H. (2014). Modelling of nutrient dynamics and vegetation succession in midstream sediment bars of a regulated river. *International journal of river basin management*, *12*(2), 123–133.

Auble, G. T., Shafroth, P. B., Scott, M. L., & Roelle, J. E. (2007). Early vegetation development on an exposed reservoir: Implications for dam removal. *Environmental management*, *39*(6), 806–818.

Bailey, P. H., Currey, J., & Fitter, A. (2002). The role of root system architecture and root hairs in promoting anchorage against uprooting forces in Allium cepa and root mutants of Arabidopsis thaliana. *Journal of Experimental Botany*, *53*(367), 333–340.

Balke, T., Bouma, T. J., Horstman, E. M., Webb, E. L., Erftemeijer, P. L., & Herman, P. M. (2011). Windows of opportunity: Thresholds to mangrove seedling establishment on tidal flats. *Marine Ecology Progress Series*, *440*, 1–9.

Bankhead, N. L., Thomas, R. E., & Simon, A. (2017). A combined field, laboratory and numerical study of the forces applied to, and the potential for removal of, bar top vegetation in a braided river. *Earth Surface Processes and Landforms*, *42*(3), 439–459.

Baptist, M., Babovic, V., Rodríguez Uthurburu, J, Keijzer, M, Uittenbogaard, R., Mynett, A, & Verwey, A. (2007). On inducing equations for vegetation resistance. *Journal of Hydraulic Research*, *45*(4), 435–450.

Bardgett, R. D., & Van Der Putten, W. H. (2014). Belowground biodiversity and ecosystem functioning. *Nature*, *515*(7528), 505–511.

Bärenbold, F., Crouzy, B., & Perona, P. (2016). Stability analysis of ecomorphodynamic equations. *Water Resources Research*, *52*(2), 1070–1088.

Barfield, B., Tollner, E., & Hayes, J. (1979). Filtration of sediment by simulated vegetation I. Steady-state flow with homogeneous sediment. *Transactions of the ASAE*, *22*(3), 540–0545.

Barsoum, N. (2002). Relative contributions of sexual and asexual regeneration strategies in Populus nigra and Salix alba during the first years of establishment on a braided gravel bed river, In *Ecology and evolutionary biology of clonal plants*. Springer.

Bätz, N, Colombini, P, Cherubini, P, & Lane, S. (2016). Groundwater controls on biogeomorphic succession and river channel morphodynamics. *Journal of Geophysical Research: Earth Surface*, *121*(10), 1763–1785.

Bayard, M, & Schweingruber, F. (1991). Ein Baumgrenzstandort: Das Wildwasserbett der Maggia im Tessin, Schweiz. Eine dendroökologische Studie. *Botanica helvetica*, *101*(1), 9–28.

Bebi, P., Kulakowski, D., & Rixen, C. (2009). Snow avalanche disturbances in forest ecosystems-State of research and implications for management. *Forest ecology and Management*, *257*(9), 1883–1892.

Beckman, N. D., & Wohl, E. (2014). Carbon storage in mountainous headwater streams: The role of old-growth forest and logjams. *Water Resources Research*, *50*(3), 2376–2393.

Beeson, C., & Doyle, P. (1995). Comparison of bank erosion at vegetated and non-vegetated channel bends. *JAWRA Journal of the American Water Resources Association*, *31*(6), 983–990.

Benda, L., Miller, D., Sias, J, Martin, D, Bilby, R, Veldhuisen, C, & Dunne, T. (2003). Wood recruitment processes and wood budgeting, In *American fisheries society symposium*. American Fisheries Society.

Bendix, J., & Hupp, C. R. (2000). Hydrological and geomorphological impacts on riparian plant communities. *Hydrological processes*, *14*(16-17), 2977–2990.

Bennett, S. J., Wu, W., Alonso, C. V., & Wang, S. S. (2008). Modeling fluvial response to in-stream woody vegetation: Implications for stream corridor restoration. *Earth Surface Processes and Landforms: The Journal of the British Geomorphological Research Group*, *33*(6), 890–909.

Bentrup, G. (1998). *The Practical Streambank Bioengineering Guide: User's Guide for Natural Streambank Stabilization Techniques in the Arid and Semi-arid Great Basin and Intermountain West*. USDA Natural Resources Conservation Service, Plant Materials Center.

Bergkamp, G., McCartney, M., Dugan, P., McNeely, J., & Acreman, M. (2000). Dams, ecosystem functions and environmental restoration. *Thematic review II*, *1*, 1–187.

Bertagni, M. B., Perona, P., & Camporeale, C. (2018). Parametric transitions between bare and vegetated states in water-driven patterns. *Proceedings of the National Academy of Sciences*, *115*(32), 8125–8130.

Bertin, C., Yang, X., & Weston, L. A. (2003). The role of root exudates and allelochemicals in the rhizosphere. *Plant and soil*, *256*(1), 67–83.

Bertoldi, W., Gurnell, A., Surian, N., Tockner, K., Zanoni, L., Ziliani, L., & Zolezzi, G. (2009). Understanding reference processes: linkages between river flows, sediment dynamics and vegetated landforms along the Tagliamento River, Italy. *River Research and Applications*, *25*(5), 501–516.

Bertoldi, W., Siviglia, A., Tettamanti, S., Toffolon, M., Vetsch, D., & Francalanci, S. (2014). Modeling vegetation controls on fluvial morphological trajectories. *Geophysical Research Letters*, *41*(20), 7167–7175.

Bezak, N., Brilly, M., & Šraj, M. (2014). Comparison between the peaks-over-threshold method and the annual maximum method for flood frequency analysis. *Hydrological Sciences Journal*, *59*(5), 959–977.

Bis, B, & Higler, L. (2001). Riparian vegetation of streams and the macroinvertebrate community structure. *International Journal of Ecohydrology and Hydrobiology*, *1*(01).

Bischetti, G. B., Chiaradia, E. A., Simonato, T., Speziali, B., Vitali, B., Vullo, P., & Zocco, A. (2007). Root strength and root area ratio of forest species in Lombardy (Northern Italy), In *Eco-and ground bio-engineering: The use of vegetation to improve slope stability*. Springer.

Bocchiola, D., Catalano, F, Menduni, G., & Passoni, G. (2002). An analytical–numerical approach to the hydraulics of floating debris in river channels. *Journal of Hydrology*, *269*(1-2), 65–78.

Botter, G., Basso, S., Rodriguez-Iturbe, I., & Rinaldo, A. (2013). Resilience of river flow regimes. *Proceedings of the National Academy of Sciences*, *110*(32), 12925–12930.

Bouma, T. J., Nielsen, K. L., Van Hal, J., & Koutstaal, B. (2001). Root system topology and diameter distribution of species from habitats differing in inundation frequency. *Functional Ecology*, *15*(3), 360–369.

Box, G. E., Jenkins, G. M., Reinsel, G. C., & Ljung, G. M. (2015). *Time series analysis: Forecasting and control*. John Wiley & Sons.

Bradley, C. E., & Smith, D. G. (1986). Plains cottonwood recruitment and survival on a prairie meandering river floodplain, milk river, southern alberta and northern montana. *Canadian Journal of Botany*, *64*(7), 1433–1442.

Brandt, S. A. (2000). Classification of geomorphological effects downstream of dams. *Catena*, *40*(4), 375–401.

Braudrick, C. A., & Grant, G. E. (2000). When do logs move in rivers? *Water resources research*, *36*(2), 571–583.

Braudrick, C. A., Grant, G. E., Ishikawa, Y., & Ikeda, H. (1997). Dynamics of wood transport in streams: A flume experiment. *Earth Surface Processes and Landforms: The Journal of the British Geomorphological Group*, *22*(7), 669–683.

Bunn, S. E., & Arthington, A. H. (2002). Basic principles and ecological consequences of altered flow regimes for aquatic biodiversity. *Environmental management*, *30*(4), 492–507.

Burkham, D. (1972). *Channel changes of the Gila River in Safford valley, Arizona, 1846-1970* (Vol. 655). US Government Printing Office.

Burylo, M, Rey, F, Roumet, C, Buisson, E., & Dutoit, T. (2009). Linking plant morphological traits to uprooting resistance in eroded marly lands (Southern Alps, France). *Plant and Soil*, *324*(1-2), 31.

Bywater-Reyes, S., Wilcox, A. C., Stella, J. C., & Lightbody, A. F. (2015). Flow and scour constraints on uprooting of pioneer woody seedlings. *Water Resources Research*, *51*(11), 9190–9206.

Cadol, D., Wohl, E., Goode, J. R., & Jaeger, K. L. (2009). Wood distribution in neotropical forested headwater streams of La Selva, Costa Rica. *Earth Surface Processes and Landforms*, *34*(9), 1198–1215.

Calvani, G., Francalanci, S., & Solari, L. (2019a). A physical model for the uprooting of flexible vegetation on river bars. *Journal of Geophysical Research: Earth Surface*, *124*(4), 1018–1034.

Calvani, G., Perona, P., Zen, S., Bau', V., & Solari, L. (2019b). Return period of vegetation uprooting by flow. *Journal of Hydrology*, *578*, 124103.

Cammeraat, E., van Beek, R., & Kooijman, A. (2005). Vegetation succession and its consequences for slope stability in SE Spain. *Plant and Soil*, *278*(1-2), 135–147.

Campbell, J. L., Driscoll, C. T., Pourmokhtarian, A., & Hayhoe, K. (2011). Streamflow responses to past and projected future changes in climate at

the Hubbard Brook Experimental Forest, New Hampshire, United States. *Water Resources Research*, *47*(2).

Camporeale, C., Perucca, E., Ridolfi, L., & Gurnell, A. (2013). Modeling the interaction between river morphodynamics and riparian vegetation. *Reviews of Geophysics*, *51*, 1–36.

Camporeale, C, & Ridolfi, L. (2006). Riparian vegetation distribution induced by river flow variability: A stochastic approach. *Water resources research*, *42*(10).

Camporeale, C., Perona, P., & Ridolfi, L. (2019). Hydrological and geomorphological significance of riparian vegetation in drylands, In *Dryland ecohydrology*. Springer.

Camporeale, C., Zen, S., Bertagni, M., Caponi, F., Siviglia, A., Zolezzi, G., Bertoldi, W., & Perona, P. (2018). Stochastic modelling of organic carbon sequestration from river ecomorphodynamic processes, In *Egu general assembly conference abstracts*.

Cannon, W. A. (1949). A tentative classification of root systems. *Ecology*, *30*(4), 542–548.

Canter, L. W. (2018). *Environmental impact of water resource projects*. CRC Press.

Caponi, F., Koch, A., Bertoldi, W., Vetsch, D. F., & Siviglia, A. (2019). When does vegetation establish on gravel bars? Observations and modelling in the Alpine Rhine river. *Frontiers in Environmental Science*, *7*, 124.

Caponi, F., & Siviglia, A. (2018). Numerical modeling of plant root controls on gravel bed river morphodynamics. *Geophysical Research Letters*, *45*(17), 9013–9023.

Carollo, F., Ferro, V, & Termini, D. (2005). Flow resistance law in channels with flexible submerged vegetation. *Journal of Hydraulic Engineering*, *131*(7), 554–564.

Carter Johnson, W. (2000). Tree recruitment and survival in rivers: Influence of hydrological processes. *Hydrological Processes*, *14*(16-17), 3051–3074.

Castillo, E. (2012). *Extreme value theory in engineering*. Elsevier.

Choi, S.-U., Yoon, B., & Woo, H. (2005). Effects of dam-induced flow regime change on downstream river morphology and vegetation cover in the Hwang River, Korea. *River Research and Applications*, *21*(2-3), 315–325.

Church, M. (2006). Bed material transport and the morphology of alluvial river channels. *Annual Review of Earth and Planetary Sciences*, *34*(1), 325–354.

Claps, P, & Laio, F. (2003). Peak over threshold analysis of flood and rainfall frequency curves, In *Hydrological Risk: Recent Advances in Peak River Flow Modelling, Prediction and Real-time Forecasting. Assessment of the Impacts of Land-use and Climate Changes, Proceedings of the ESF LESC Exploratory Workshop, Bologna, Italy.*

Collison, A., & Anderson, M. (1996). Using a combined slope hydrology/stability model to identify suitable conditions for landslide prevention by vegetation in the humid tropics. *Earth surface processes and landforms*, *21*(8), 737–747.

Comiti, F, Lucía, A, & Rickenmann, D. (2016). Large wood recruitment and transport during large floods: A review. *Geomorphology*, *269*, 23–39.

Connell, B. S., & Yue, D. K. (2007). Flapping dynamics of a flag in a uniform stream. *Journal of fluid mechanics*, *581*, 33–67.

Cook, C. D., Gut, B. J., Rix, E. M., & Schneller, J. (1974). *Water plants of the world: A manual for the identification of the genera of freshwater macrophytes*. Springer Science & Business Media.

Corenblit, D., Tabacchi, E., Steiger, J., & Gurnell, A. (2007). Reciprocal interactions and adjustments between fluvial landforms and vegetation dynamics in river corridors: A review of complementary approaches. *Earth-Science Reviews*, *84*, 56–86.

Corenblit, D., Baas, A. C., Bornette, G., Darrozes, J., Delmotte, S., Francis, R. A., Gurnell, A., Julien, F., Naiman, R. J., & Steiger, J. (2011). Feedbacks between geomorphology and biota controlling earth surface processes and landforms: A review of foundation concepts and current understandings. *Earth-Science Reviews*, *106*(3-4), 307–331.

Corenblit, D., Vautier, F., González, E., & Steiger, J. (2020). Formation and dynamics of vegetated fluvial landforms follow the biogeomorphological succession model in a channelized river. *Earth Surface Processes and Landforms*.

Corless, R. M., Gonnet, G. H., Hare, D. E., Jeffrey, D. J., & Knuth, D. E. (1996). On the LambertW function. *Advances in Computational mathematics*, *5*(1), 329–359.

Coulthard, T. J. (2005). Effects of vegetation on braided stream pattern and dynamics. *Water Resources Research*, *41*(4).

Coutts, M. P. (1983). Root architecture and tree stability. *Plant and Soil*, *71*, 171–188.

Cramér, H., & Leadbetter, M. R. (2013). *Stationary and related stochastic processes: Sample function properties and their applications*. Courier Corporation.

Cronk, J. K., & Fennessy, M. S. (2016). *Wetland plants: Biology and ecology*. CRC press.

Crouzy, B., Edmaier, K., Pasquale, N., & Perona, P. (2013). Impact of floods on the statistical distribution of riverbed vegetation. *Geomorphology*, *202*, 51–58.

Crouzy, B., & Perona, P. (2012). Biomass selection by floods and related timescales. part 2: Stochastic modeling. *Adv. Water Res.*

Crouzy, B., Bärenbold, F., D'Odorico, P., & Perona, P. (2016). Ecomorphodynamic approaches to river anabranching patterns. *Advances in water resources*, *93*, 156–165.

Crouzy, B., Edmaier, K., & Perona, P. (2014). Biomechanics of plant anchorage at early development stage. *Journal of theoretical biology*, *363*, 22–29.

Da-Chuan, R., Quan-Hua, L., Zu-Hao, Z., Guo-Qing, W., & Zhang, X.-H. (2008). Sediment retention by check dams in the Hekouzhen-Longmen Section of the Yellow River. *International Journal of Sediment Research*, *23*(2), 159–166.

Daniels, H. E. (1945). The statistical theory of the strength of bundles of threads. I. *Proceedings of the Royal Society of London. Series A. Mathematical and Physical Sciences*, *183*(995), 405–435.

Daniels, M. D. (2006). Distribution and dynamics of large woody debris and organic matter in a low-energy meandering stream. *Geomorphology*, *77*(3-4), 286–298.

De Baets, S., Poesen, J., Gyssels, G., & Knapen, A. (2006). Effects of grass roots on the erodibility of topsoils during concentrated flow. *Geomorphology*, *76*(1-2), 54 –67.

De Marsily, G. (1986). *Quantitative hydrogeology* (tech. rep.). Paris School of Mines, Fontainebleau.

Décamps, H., & Naiman, R. J. (1990). *The ecology and management of aquatic-terrestrial ecotones* (Vol. 4). CRC Press.

Desrochers, V., Frenette-Dussault, C., Nissim, W. G., Brisson, J., & Labrecque, M. (2020). Using willow microcuttings for ecological restoration: An alternative method for establishing dense plantations. *Ecological Engineering*, *151*, 105859.

Dewit, L., & Reid, D. M. (1992). Branch abscission in balsam poplar (Populus balsamifera): characterization of the phenomenon and the influence of wind. *International Journal of Plant Sciences*, *153*(4), 556–564.

Dirr, M. A. (1987). *The reference manual of woody plant propagation: From seed to tissue culture; a practical working guide to the propagation of over 1100 species, varieties and cultivars* (tech. rep.).

Dixon, M. D., & Turner, M. G. (2006). Simulated recruitment of riparian trees and shrubs under natural and regulated flow regimes on the Wisconsin River, USA. *River Research and Applications*, *22*(10), 1057–1083.

Docker, B., & Hubble, T. (2008). Quantifying root-reinforcement of river bank soils by four australian tree species. *Geomorphology*, *100*(3-4), 401–418.

Dosskey, M. G., Vidon, P., Gurwick, N. P., Allan, C. J., Duval, T. P., & Lowrance, R. (2010). The role of riparian vegetation in protecting and improving chemical water quality in streams1. *JAWRA Journal of the American Water Resources Association*, *46*(2), 261–277.

Downs, P. W., & Simon, A. (2001). Fluvial geomorphological analysis of the recruitment of large woody debris in the Yalobusha River network, Central Mississippi, USA. *Geomorphology*, *37*(1-2), 65–91.

Doyle, M. W., Stanley, E. H., Strayer, D. L., Jacobson, R. B., & Schmidt, J. C. (2005). Effective discharge analysis of ecological processes in streams. *Water Resources Research*, *41*(11).

Du, E., Terrer, C., Pellegrini, A. F., Ahlström, A., van Lissa, C. J., Zhao, X., Xia, N., Wu, X., & Jackson, R. B. (2020). Global patterns of terrestrial nitrogen and phosphorus limitation. *Nature Geoscience*, *13*(3), 221–226.

Duan, J. G., Barkdoll, B., & French, R. (2006). Lodging velocity for an emergent aquatic plant in open channels. *Journal of Hydraulic Engineering*, *132*(10), 1015–1020.

Dupuy, L., Fourcaud, T., & Stokes, A. (2005). A numerical investigation into factors affecting the anchorage of roots in tension. *Europ. Journal of soil Science*, *56*, 319–327.

Dybala, K. E., Steger, K., Walsh, R. G., Smart, D. R., Gardali, T., & Seavy, N. E. (2019). Optimizing carbon storage and biodiversity co-benefits in reforested riparian zones. *Journal of applied ecology*, *56*(2), 343–353.

Easson, D., Pickles, S., & White, E. (1995). A study of the tensile force required to pull wheat roots from soil. *Annals of Applied Biology*, *127*(2), 363–373.

Edmaier, K. (2014). *Uprooting mechansims of juvenile vegetation by flow erosion* (Doctoral dissertation). EPFL.

Edmaier, K, Burlando, P., & Perona, P. (2011). Mechanisms of vegetation uprooting by flow in alluvial non-cohesive sediment. *Hydrology and Earth System Sciences*, *15*(5), 1615–1627.

Edmaier, K., Crouzy, B., Burlando, P., & Perona, P. (2012). Experimental characterization of root anchoring in non-cohesive sediment, In *River flow 2012*.

Edmaier, K, Crouzy, B, & Perona, P. (2015). Experimental characterization of vegetation uprooting by flow. *Journal of Geophysical Research: Biogeosciences*, *120*(9), 1812–1824.

Edmaier, K., Crouzy, B., Ennos, R., Burlando, P., & Perona, P. (2014). Influence of root characteristics and soil variables on the uprooting mechanics of Avena sativa and Medicago sativa seedlings. *Earth Surface Processes and Landforms*, *39*(10), 1354–1364.

EEA. (2015). The European Environment -State and Outlook 2015: synthesis report (EEA 2015). *EEA 2015*, 62.63.

Eichel, J., Corenblit, D., & Dikau, R. (2016). Conditions for feedbacks between geomorphic and vegetation dynamics on lateral moraine slopes: A biogeomorphic feedback window. *Earth Surface Processes and Landforms*, *41*(3), 406–419.

Einstein, A. (1905). Über die von der molekularkinetischen Theorie der Wärme geforderte Bewegung von in ruhenden Flüssigkeiten suspendierten Teilchen. *Annalen der Physik*, *322*(8), 549–560.

Ekanayake, J. C., Marden, M., Watson, A. J., & Rowan, D. (1997). Tree roots and slope stability: a comparison between Pinus radiata and kanuka. *New Zealand Journal of Forestry Science*, *27*(2), 216–233.

Ennos, A. R. (1993). The scaling of root anchorage. *Journal of Theoretical Biology*, *161*(1), 61 –75.

Ennos, A. R. (1989). The mechanics of anchorage in seedlings of sunflower, helianthus annuus l. *New Phytologist*, *113*(2), 185–192.

Ennos, A. R. (1990). The anchorage of leek seedlings: The effect of root length and soil strength. *Annals of Botany*, *65*(4), 409–416.

Ennos, A., & Pellerin, S. (2000). Plant anchorage, In *Root methods*. Springer.

Errico, A., Lama, G. F. C., Francalanci, S., Chirico, G. B., Solari, L., & Preti, F. (2019). Flow dynamics and turbulence patterns in a drainage channel colonized by common reed (Phragmites australis) under different scenarios of vegetation management. *Ecological engineering*, *133*, 39–52.

Erskine, W. D. (1985). Downstream geomorphic impacts of large dams: the case of Glenbawn Dam, NSW. *Applied Geography*, *5*(3), 195–210.

Eschner, T. R., Hadley, R. F., & Crowley, K. D. (1983). *Hydrologic and morphologic changes in channels of the Platte River Basin in Colorado, Wyoming, and Nebraska: a historical perspective*. US Government Printing Office Washington, DC.

Fan, Y., Miguez-Macho, G., Jobbágy, E. G., Jackson, R. B., & Otero-Casal, C. (2017). Hydrologic regulation of plant rooting depth. *Proceedings of the National Academy of Sciences*, *114*(40), 10572–10577.

Favre, V. (2004). Evolution of the Maggia floodplain, Analysis of an aerial photograph time series from 1962 to 2001. Laboratoire de Biologie de la Conservation, Université de Lausanne.

Fergus, T. (1997). Geomorphological response of a river regulated for hydropower: River Fortun, Norway. *Regulated Rivers: Research & Management: An International Journal Devoted to River Research and Management*, *13*(5), 449–461.

Fischer, J. R., & Claflin, T. O. (1995). Declines in aquatic vegetation in navigation pool no. 8, upper Mississippi River between 1975 and 1991. *Regulated Rivers: Research & Management*, *11*(2), 157–165.

Fisher, S. G., & Likens, G. E. (1972). Stream ecosystem: Organic energy budget. *BioScience*, *22*(1), 33–35.

Foglia, L, Birsan, M., Burlando, P, Hill, M., & Mehl, S. (2004). Calibration strategies for a groundwater model in a highly dynamic alpine floodplain, In *International conference on finite-element models, modflow, and more 2004*.

Francis, R. A. (2007). Size and position matter: Riparian plant establishment from fluvially deposited trees. *Earth Surface Processes and Landforms*, *32*(8), 1239–1243.

Francis, R. A., Gurnell, A. M., Petts, G. E., & Edwards, P. J. (2005). Survival and growth responses of populus nigra, salix elaeagnos and alnus incana cuttings to varying levels of hydric stress. *Forest Ecology and Management*, *210*(1-3), 291 –301.

Francis, R. A., Gurnell, A. M., Petts, G. E., & Edwards, P. J. (2006). Riparian tree establishment on gravel bars: Interactions between plant growth strategy and the physical environment, In *Braided rivers: Process, deposits, ecology and management*. Blackwell Oxford.

Francis, R. A., Tibaldeschi, P., & McDougall, L. (2008). Fluvially-deposited large wood and riparian plant diversity. *Wetlands Ecology and Management*, *16*(5), 371–382.

Fraser, A. I. (1962). The soil and roots as factors in tree stability. *Forestry*, *35*(2), 117–127.

Friedman, J. M., Osterkamp, W., & Lewis Jr, W. M. (1996). The role of vegetation and bed-level fluctuations in the process of channel narrowing. *Geomorphology*, *14*(4), 341–351.

Galloway, G., & Worrall, J. (1979). Cladoptosis: A reproductive strategy in black cottonwood? *Canadian Journal of Forest Research*, *9*(1), 122–125.

Garssen, A. G., Verhoeven, J. T., & Soons, M. B. (2014). Effects of climate-induced increases in summer drought on riparian plant species: A meta-analysis. *Freshwater Biology*, *59*(5), 1052–1063.

Gasser, E., Schwarz, M., Simon, A., Perona, P., Phillips, C., Hübl, J., & Dorren, L. (2019). A review of modeling the effects of vegetation on large wood recruitment processes in mountain catchments. *Earth-Science Reviews*.

Genet, M., Stokes, A., Salin, F., Mickovski, S., Fourcaud, T., Dumail, J.-F., & Beek, R. (2005). The influence of cellulose content on tensile strength in tree roots. *Plant and Soil*, *278*, 1–9.

Ghestem, M., Veylon, G., Bernard, A., Vanel, Q., & Stokes, A. (2014). Influence of plant root system morphology and architectural traits on soil shear resistance. *Plant and Soil*, *377*(1-2), 43–61.

Giadrossich, F., Schwarz, M., Cohen, D., Cislaghi, A., Vergani, C., Hubble, T., Phillips, C., & Stokes, A. (2017). Methods to measure the mechanical behaviour of tree roots: A review. *Ecological Engineering*, *109*, 256 –271.

Gibling, M. R., & Davies, N. S. (2012). Palaeozoic landscapes shaped by plant evolution. *Nature Geoscience*, *5*(2), 99–105.

Gibling, M., Davies, N., Falcon-Lang, H., Bashforth, A. R., DiMichele, W. A., Rygel, M., & Ielpi, A. (2014). Palaeozoic co-evolution of rivers and vegetation: A synthesis of current knowledge. *Proceedings of the Geologists' Association*, *125*(5-6), 524–533.

Gordon, E., & Meentemeyer, R. K. (2006). Effects of dam operation and land use on stream channel morphology and riparian vegetation. *Geomorphology*, *82*(3-4), 412–429.

Gorla, L., Signarbieux, C., Turberg, P., Buttler, A., & Perona, P. (2015). Transient response of Salix cuttings to changing water level regimes. *Water Resources Research*, *51*(3), 1758–1774.

Graf, W. L. (2006). Downstream hydrologic and geomorphic effects of large dams on american rivers. *Geomorphology*, *79*(3-4), 336–360.

Grams, P. E., & Schmidt, J. C. (2002). Streamflow regulation and multi-level flood plain formation: channel narrowing on the aggrading Green River in the eastern Uinta Mountains, Colorado and Utah. *Geomorphology*, *44*(3-4), 337–360.

Gran, K., & Paola, C. (2001). Riparian vegetation controls on braided stream dynamics. *Water Resources Research*, *37*(12), 3275–3283.

Gray, D. H., & Leiser, A. T. (1982). *Biotechnical slope protection and erosion control*. Van Nostrand Reinhold Company Inc.

Greenway, D. (1987). Slope stability, geotechnical engineering and geomorphology. chap vegetation and slope stability. Wiley, London.

Gregory, P. (2007). *Plant roots*. Wiley Online Library.

Gregory, P. (2006). *Plant roots, growth, activity and interaction with soils* (B. P. Ltd., Ed.). Blackwell Publishing Ltd.

Gregory, S. V., Meleason, M. A., & Sobota, D. J. (2003). Modeling the dynamics of wood in streams and rivers, In *American fisheries society symposium*. Citeseer.

Grimardias, D., Guillard, J., & Cattanéo, F. (2017). Drawdown flushing of a hydroelectric reservoir on the rhône river: Impacts on the fish community and implications for the sediment management. *Journal of environmental management*, *197*, 239–249.

Guilloy, H., González, E., Muller, E., Hughes, F. M., & Barsoum, N. (2011). Abrupt drops in water table level influence the development of Populus nigra and Salix alba seedlings of different ages. *Wetlands*, *31*(6), 1249–1261.

Gurnell, A, Edwards, P. J., Petts, G. E., & Ward, J. V. (2000). A conceptual model for alpine proglacial river channel evolution under changing climatic conditions. *Catena*, *38*(3), 223–242.

Gurnell, A., Tompson, K., Goodson, J., & Moggridge, H. (2008). Propagule deposition along river margins: Linking hydrology and ecology. *Journal of Ecology*, *96*, 553–565.

Gurnell, A., Downward, S., & Jones, R. (1994). Channel planform change on the River Dee meanders, 1876–1992. *Regulated rivers: research & management*, *9*(4), 187–204.

Gurnell, A., Piégay, H., Swanson, F., & Gregory, S. (2002). Large wood and fluvial processes. *Freshwater Biology*, *47*(4), 601–619.

Gurnell, A. (2014). Plants as river system engineers. *Earth Surface Processes and Landforms*, *39*(1), 4–25.

Gurnell, A., Tockner, K., Edwards, P., & Petts, G. (2005). Effects of deposited wood on biocomplexity of river corridors. *Frontiers in Ecology and the Environment*, *3*(7), 377–382.

Gurnell, A. M., Bertoldi, W., & Corenblit, D. (2012). Changing river channels: The roles of hydrological processes, plants and pioneer fluvial landforms in humid temperate, mixed load, gravel bed rivers. *Earth-Science Reviews*, *111*(1-2), 129–141.

Gyssels, G., Poesen, J., Bochet, E., & Li, Y. (2005). Impact of plant roots on the resistance of soils to erosion by water: A review. *Progress in physical geography*, *29*(2), 189–217.

Hadley, R. F., & Emmett, W. W. (1998). Channel changes downstream from a dam. *JAWRA Journal of the American Water Resources Association*, *34*(3), 629–637.

Hanson, G. (1990). Surface erodibility of earthen channels at high stresses part II-developing an in situ testing device. *Transactions of the ASAE*, *33*(1), 132–0137.

Hanson, G., & Simon, A. (2001). Erodibility of cohesive streambeds in the loess area of the midwestern USA. *Hydrological processes*, *15*(1), 23–38.

Helfield, J. M., & Naiman, R. J. (2001). Effects of salmon-derived nitrogen on riparian forest growth and implications for stream productivity. *Ecology*, *82*(9), 2403–2409.

Hey, R. D., & Thorne, C. R. (1986). Stable channels with mobile gravel beds. *Journal of Hydraulic engineering*, *112*(8), 671–689.

Hickin, E. J. (1984). Vegetation and river channel dynamics. *Canadian Geographer/Le Géographe canadien*, *28*(2), 111–126.

Hobbs, R. J., Higgs, E., & Harris, J. A. (2009). Novel ecosystems: Implications for conservation and restoration. *Trends in ecology & evolution*, *24*(11), 599–605.

Hortobágyi, B., Corenblit, D., Steiger, J., & Peiry, J.-L. (2018). Niche construction within riparian corridors. Part I: Exploring biogeomorphic feedback windows of three pioneer riparian species (Allier River, France). *Geomorphology*, *305*, 94–111.

Howell, J., Benson, D., & McDougall, L. (1994). Developing a strategy for rehabilitating riparian vegetation of the Hawkesbury-Nepean River, Sydney, Australia. *Pacific Conservation Biology*, *1*(3), 257–271.

Hsu, F., Nelson, C., & Chow, W. (1984). A mathematical model to utilize the logistic function in germination and seedling growth. *Journal of Experimental Botany*, *35*(11), 1629–1640.

Hughes, F. M. R. (1997). Floodplain biogeomorphology. *Progr. Phys. Geogr.*, *21*, 501–529.

Hughes, F. M., Harris, T., Richards, K., Pautou, G., El Hames, A., Barsoum, N., Girel, J., Peiry, J.-L., & Foussadier, R. (1997). Woody riparian species response to different soil moisture conditions: Laboratory experiments on alnus incana (l.) moench. *Global Ecology and Biogeography Letters*, 247–256.

Hungr, O., Evans, S., & Hutchinson, I. (2001). A review of the classification of landslides of the flow type. *Environmental & Engineering Geoscience*, *7*(3), 221–238.

Hupp, C. R. (1992). Riparian vegetation recovery patterns following stream channelization: A geomorphic perspective. *Ecology*, *73*(4), 1209–1226.

Hupp, C., & Osterkamp, W. (1996). Riparian vegetation and fluvial geomorphic processes. *Geomorphology*, *14*, 277–296.

Hwang, S.-K., & Jeong, G.-Y. (2006). Geology in drainage field of the Imha Dam and origins of high turbid water in the Imha Lake, Andong. *Economic and environmental geology*, *39*(6), 771–786.

Iroumé, A., Mao, L., Andreoli, A., Ulloa, H., & Ardiles, M. P. (2015). Large wood mobility processes in low-order chilean river channels. *Geomorphology*, *228*, 681–693.

Ishikawa, Y., Sakamoto, T., & Mizuhara, K. (2003). Effect of density of riparian vegetation on effective tractive force. *Journal of Forest Research*, *8*(4), 235–246.

Järvelä, J. (2002). Determination of flow resistance of vegetated channel banks and floodplains. In B. Zech (Ed.), *River flow 2002* (pp. 311–318). Swets & Zeitlinger, Lisse.

Johnson, W. C. (1998). Adjustment of riparian vegetation to river regulation in the Great Plains, USA. *Wetlands*, *18*(4), 608–618.

Johnson, W. C., Burgess, R. L., & Keammerer, W. R. (1976). Forest overstory vegetation and environment on the Missouri River floodplain in North Dakota. *Ecological Monographs*, *46*(1), 59–84.

Johnston, C. A., & Naiman, R. J. (1987). Boundary dynamics at the aquatic-terrestrial interface: The influence of beaver and geomorphology. *Landscape Ecology*, *1*(1), 47–57.

Jordanova, A. A., & James, C. (2003). Experimental study of bed load transport through emergent vegetation. *Journal of Hydraulic Engineering*, *129*(6), 474–478.

Kamchoom, V., Leung, A. K., & Ng, C. W. W. (2014). Effects of root geometry and transpiration on pull-out resistance. *Géotechnique Letters*, *4*(4), 330–336.

Karr, J. R. (1991). Biological integrity: A long-neglected aspect of water resource management. *Ecological applications*, *1*(1), 66–84.

Karrenberg, S., Blaser, S., Kollmann, J., Speck, T., & Edwards, P. (2003). Root anchorage of saplings and cuttings of woody pioneer species in a riparian environment. *Functional Ecology*, *17*, 170–177.

Kath, J, Reardon-Smith, K, Le Brocque, A., Dyer, F., Dafny, E, Fritz, L, & Batterham, M. (2014). Groundwater decline and tree change in floodplain landscapes: Identifying non-linear threshold responses in canopy condition. *Global Ecology and Conservation*, *2*, 148–160.

Keller, E. A., & Swanson, F. J. (1979). Effects of large organic material on channel form and fluvial processes. *Earth surface processes*, *4*(4), 361–380.

Kiley, D., & Schneider, R. (2005). Riparian roots through time, space and disturbance. *Plant and Soil*, *269*, 259–272.

Kirkil, G., & Constantinescu, G. (2010). Flow and turbulence structure around an in-stream rectangular cylinder with scour hole. *Water Resources Research*, *46*(11).

Knight, A. W., & Bottorff, R. L. (1984). The importance of riparian vegetation to stream ecosystems. *California riparian systems: ecology, conservation, and productive management. University of California Press, Berkeley, CA, USA*, 160–167.

Koch, C., & Kollmann, J. (2012). Clonal re-introduction of endangered plant species: the case of German false tamarisk in pre-Alpine rivers. *Environmental management*, *50*(2), 217–225.

Kondolf, G. M., Boulton, A. J., O'Daniel, S., Poole, G. C., Rahel, F. J., Stanley, E. H., Wohl, E., Bång, A., Carlstrom, J., Cristoni, C. Et al. (2006). Process-based ecological river restoration: Visualizing three-dimensional connectivity and dynamic vectors to recover lost linkages. *Ecology and society*, *11*(2).

Köstler, J., Brückner, E., & Bibelriether, H. (1968). *Die Wurzeln der Waldbäume*. Verlag Paul Parey.

Kostler, J. N., Bruckner, E, & Bibelriether, H. (1968). Die Wurzeln der Waldbaume. *Paul Parey, Hamburg*, *284*.

Kozlowski, T. T. Et al. (1984). *Flooding and plant growth*. Elsevier.

Kui, L., Stella, J., Lightbody, A., & Wilcox, A. C. (2014). Ecogeomorphic feedbacks and flood loss of riparian tree seedlings in meandering channel experiments. *Water Resour. Res.*

Laio, F, Porporato, A, Ridolfi, L., & Rodriguez-Iturbe, I. (2001). Mean first passage times of processes driven by white shot noise. *Physical Review E*, *63*(3), 036105.

Lake, P., Bond, N., & Reich, P. (2007). Linking ecological theory with stream restoration. *Freshwater biology*, *52*(4), 597–615.

Lassettre, N. S., Piégay, H., Dufour, S., & Rollet, A.-J. (2008). Decadal changes in distribution and frequency of wood in a free meandering river, the Ain River, France. *Earth Surface Processes and Landforms: The Journal of the British Geomorphological Research Group*, *33*(7), 1098–1112.

Latterell, J. J., Scott Bechtold, J, O'KEEFE, T. C., Van Pelt, R., & Naiman, R. J. (2006). Dynamic patch mosaics and channel movement in an unconfined river valley of the Olympic Mountains. *Freshwater Biology*, *51*(3), 523–544.

Leopold, L. B., & Wolman, M. G. (1957). *River channel patterns: Braided, meandering, and straight*. US Government Printing Office.

Lester, P. J., Mitchell, S. F., & Scott, D. (1994). Effects of riparian willow trees (Salix fragilis) on macroinvertebrate densities in two small Central Otago, New Zealand, streams. *New Zealand journal of marine and freshwater research*, *28*(3), 267–276.

Levine, C., & Stromberg, J. (2001). Effects of flooding on native and exotic plant seedlings: Implications for restoring south-western riparian forests by manipulating water and sediment flows. *Journal of Arid Environments*, *49*(1), 111–131.

Li, R., & Shen, H. W. (1973). Effect of tall vegetations on flow and sediment. *Journal of the hydraulics division*, *99*.

Li, S., Pezeshki, S., & Goodwin, S. (2004). Effects of soil moisture regimes on photosynthesis and growth in cattail (typha latifolia). *Acta Oecologica*, *25*(1), 17 –22.

Li, X., Liu, J. P., Saito, Y., & Nguyen, V. L. (2017). Recent evolution of the Mekong Delta and the impacts of dams. *Earth-Science Reviews*, *175*, 1–17.

Liang, T., Knappett, J. A., Leung, A., Carnaghan, A., Bengough, A. G., & Zhao, R. (2020). A critical evaluation of predictive models for rooted soil strength with application to predicting the seismic deformation of rooted slopes. *Landslides*, *17*(1), 93–109.

Lightbody, A. F., & Nepf, H. M. (2006). Prediction of velocity profiles and longitudinal dispersion in salt marsh vegetation. *Limnology and oceanography*, *51*(1), 218–228.

Likens, G. E., & Bormann, F. H. (1974). Linkages between Terrestrial and Aquatic Ecosystems. *BioScience*, *24*(8), 447–456.

Liu, Y., Gao, J., Lou, H., Zhang, J., & Cui, Q. (2011). The root anchorage ability of salix alba var. tristis using a pull-out test. *African Journal of Biotechnology*, *10*(73), 16501–16507.

Lloyd, N., Quinn, G., Thoms, M., Arthington, A., Gawne, B., Humphries, P., & Walker, K. (2004). Does flow modification cause geomorphological

and ecological response in rivers. *A literature review from an Australian perspective. CRC for Freshwater Ecology*, *57*.

Loades, K. W. (2010). *Quantifying soil reinforcement by fibrous roots* (Doctoral dissertation). University of Dundee.

Loheide, S. P., Butler Jr, J. J., & Gorelick, S. M. (2005). Estimation of groundwater consumption by phreatophytes using diurnal water table fluctuations: A saturated-unsaturated flow assessment. *Water resources research*, *41*(7).

López, F., & García, M. (1998). Open-channel flow through simulated vegetation: Suspended sediment transport modeling. *Water resources research*, *34*(9), 2341–2352.

Lytle, D. A., & Merrit, D. J. (2004). Hydrologic regimes and riparian forests: Astructure population model for cottonwood. *Ecology*, *85(9)*, 2493–2503.

Lytle, D. A., & Poff, N. L. (2004). Adaptation to natural flow regimes. *Trends in ecology & evolution*, *19*(2), 94–100.

MacVicar, B., & Piégay, H. (2012). Implementation and validation of video monitoring for wood budgeting in a wandering piedmont river, the Ain River (France). *Earth Surface Processes and Landforms*, *37*(12), 1272–1289.

Magilligan, F. J., & Nislow, K. H. (2005). Changes in hydrologic regime by dams. *Geomorphology*, *71*(1-2), 61–78.

Magilligan, F. J., Nislow, K. H., & Graber, B. E. (2003). Scale-independent assessment of discharge reduction and riparian disconnectivity following flow regulation by dams. *Geology*, *31*(7), 569–572.

Mahoney, J. M., & Rood, S. B. (1998). Streamflow requirements for cottonwood seedling recruitment-An integrative model. *Wetlands*, *18*(4), 634–645.

Maingi, J. K., & Marsh, S. E. (2002). Quantifying hydrologic impacts following dam construction along the Tana River, Kenya. *Journal of Arid Environments*, *50*(1), 53–79.

Malamy, J. (2005). Intrinsic and environmental response pathways that regulate root system architecture. *Plant, cell & environment*, *28*(1), 67–77.

Malanson, G. P. (1993). *Riparian landscapes*. Cambridge, Cambridge University Press.

Manes, C., & Brocchini, M. (2015). Local scour around structures and the phenomenology of turbulence. *Journal of Fluid Mechanics*, *779*, 309–324.

Mao, L., Andreoli, A., Iroumé, A., Comiti, F., & Lenzi, M. A. (2013). Dynamics and management alternatives of in-channel large wood in mountain basins of the southern Andes. *Bosque*, *34*(3), 319–330.

Marani, M., Belluco, E., Ferrari, S., Silvestri, S., D'Alpaos, A., Lanzoni, S., Feola, A., & Rinaldo, A. (2006). Analysis, synthesis and modelling of high-resolution observations of salt-marsh eco-geomorphological patterns in the Venice lagoon. *Estuarine, Coastal and Shelf Science*, *69*(3-4), 414–426.

Markesteijn, L., & Poorter, L. (2009). Seedling root morphology and biomass allocation of 62 tropical tree species in relation to drought-and shade-tolerance. *Journal of Ecology*, *97*(2), 311–325.

Martin, D. J., & Benda, L. E. (2001). Patterns of instream wood recruitment and transport at the watershed scale. *Transactions of the American Fisheries Society*, *130*(5), 940–958.

Masle, J. (2002). *High soil strength: Mechanical forces at play on root morphogenesis and in root: Shoot signaling, in plant roots: The hidden half* (Y. Waisel, A. Eshel, & U. Kafkafi, Eds.). Marcel Dekker.

Matzinger, A., Pieters, R., Ashley, K. I., Lawrence, G. A., & Wüest, A. (2007). Effects of impoundment on nutrient availability and productivity in lakes. *Limnology and Oceanography*, *52*(6), 2629–2640.

Melville, B. W., & Sutherland, A. (1988). Design method for local scour at bridge piers. *Journal Hydr Eng ASCE*, *114*, 1210–1226.

Merritt, D. M., & Wohl, E. E. (2002). Processes governing hydrochory along rivers: Hydraulics, hydrology, and dispersal phenology. *Ecological applications*, *12*(4), 1071–1087.

Mickovski, A., & Ennos, R. (2002). A morphological and mechanical study of the root systems of suppressed crown Scots pine *Pinus sylvestris*. *Trees*, *16*, 274–280.

Mickovski, S., Bengough, A., Bransby, M., Davies, M., Hallet, P., & Sonnenberg, R. (2007). Material stiffness, branching pattern and soil matric potential affect the pullout of model root systems. *Europ. Journal of Soil Science*, *58*, 1471–1481.

Mickovski, S., Hallett, P., Bransby, M., Davies, M., Sonnenberg, R., & Bengough, A. (2009). Mechanical reinforcement of soil by willow roots: Impacts of root properties and root failure mechanism in controlled laboratory tests. *Soil Science of America Journal*, *73*, 1276–1285.

Millar, R. G. (2000). Influence of bank vegetation on alluvial channel patterns. *Water Resour. Res.*, *36*(4), 1109–1118.

Molnar, P., Favre, V., Perona, P., Burlando, P., Randin, C., & Ruf, W. (2008). Floodplain forest dynamics in a hydrologically altered mountain river. *Peckiana*, *5*, 17–24.

Montgomery, D. R., Collins, B. D., Buffington, J. M., & Abbe, T. B. (2003). Geomorphic effects of wood in rivers, In *American fisheries society symposium*.

Mosner, E., Schneider, S., Lehmann, B., & Leyer, I. (2011). Hydrological prerequisites for optimum habitats of riparian salix communities–identifying suitable reforestation sites. *Applied Vegetation Science*, *14*(3), 367–377.

Moulin, B, & Piégay, H. (2004). Characteristics and temporal variability of large woody debris trapped in a reservoir on the River Rhone (Rhone): implications for river basin management. *River Research and Applications*, *20*(1), 79–97.

Müller, N., & Scharm, S. (2001). The importance of seed rain and seed bank for the recolonisation of gravel bars in alpine rivers. *Studies on the Vegetation of Alluvial Plains, Yokohama, In*, 127–140.

Munar-Martinez, M., Vargas-Luna, A., & Torres, A. (2019). Laboratory investigation on bed-shear stress partitioning in vegetated flows, In *E-proceedings of the 38th IAHR World Congress, Panama City, Panama.*

Musleh, F., & Cruise, J. (2006). Functional relationships of resistance in wide flood plains with rigid unsubmerged vegetation. *Journal of hydraulic engineering*, *132*(2), 163–171.

Naiman, R. J., Bilby, R. E., & Bisson, P. A. (2000). Riparian ecology and management in the pacific coastal rain forest. *BioScience*, *50*(11), 996–1011.

Naiman, R. J., & Decamps, H. (1997). The ecology of interfaces: Riparian zones. *Annual review of Ecology and Systematics*, *28*(1), 621–658.

Naiman, R. J., Decamps, H., & Pollock, M. (1993). The role of riparian corridors in maintaining regional biodiversity. *Ecological applications*, *3*(2), 209–212.

Nakamura, F., & Swanson, F. J. (1993). Effects of coarse woody debris on morphology and sediment storage of a mountain stream system in western Oregon. *Earth Surface Processes and Landforms*, *18*(1), 43–61.

Naumburg, E., Mata-Gonzalez, R., Hunter, R. G., Mclendon, T., & Martin, D. W. (2005). Phreatophytic vegetation and groundwater fluctuations: A review of current research and application of ecosystem response modeling with an emphasis on great basin vegetation. *Environmental Management*, *35*(6), 726–740.

Nepf, H. M. (2012). Hydrodynamics of vegetated channels. *Journal of Hydraulic Research*, *50*(3), 262–279.

Nepf, H. (1999). Drag, turbulence, and diffusion in flow through emergent vegetation. *Water Resouces Research*, *35*, 479–489.

Nilsson, C., & Berggren, K. (2000). Alterations of riparian ecosystems caused by river regulation: Dam operations have caused global-scale ecological changes in riparian ecosystems. How to protect river environments and human needs of rivers remains one of the most important questions of our time. *BioScience*, *50*(9), 783–792.

Nyssen, J., Poesen, J., Moeyersons, J., Luyten, E., Veyret-Picot, M., Deckers, J., Haile, M., & Govers, G. (2002). Impact of road building on gully erosion risk: a case study from the northern Ethiopian highlands. *Earth Surface Processes and Landforms: The Journal of the British Geomorphological Research Group*, *27*(12), 1267–1283.

Ogle, K., & Barber, J. J. (2008). Bayesian data-model integration in plant physiological and ecosystem ecology, In *Progress in botany*. Springer.

OHare, K. (1995). *Operation of glen canyon dam environmental impact statement* (tech. rep.). American Society of Civil Engineers, New York, NY (United States).

Okada, Y., & Kurokawa, U. (2015). Examining effects of tree roots on shearing resistance in shallow landslides triggered by heavy rainfall in Shobara in 2010. *Journal of forest research*, *20*(1), 230–235.

Oorschot, M. v., Kleinhans, M., Geerling, G., & Middelkoop, H. (2016). Distinct patterns of interaction between vegetation and morphodynamics. *Earth Surface Processes and Landforms*, *41*(6), 791–808.

Operstein, V, & Frydman, S. (2000). The influence of vegetation on soil strength. *Proceedings of the Institution of Civil Engineers-Ground Improvement*, *4*(2), 81–89.

Orellana, F., Verma, P., Loheide, S. P., & Daly, E. (2012). Monitoring and modeling water-vegetation interactions in groundwater-dependent ecosystems. *Reviews of Geophysics*, *50*(3).

Osterkamp, W., Scott, M. L., Auble, G. T. Et al. (1998). Downstream effects of dams on channel geometry and bottomland vegetation: Regional patterns in the great plains. *Wetlands*, *18*(4), 619–633.

Palmer, M. A., Hondula, K. L., & Koch, B. J. (2014). Ecological restoration of streams and rivers: Shifting strategies and shifting goals. *Annual Review of Ecology, Evolution, and Systematics*, *45*, 247–269.

Papanicolaou, A., Diplas, P, Evaggelopoulos, N, & Fotopoulos, S. (2002). Stochastic incipient motion criterion for spheres under various bed packing conditions. *Journal of Hydraulic Engineering*, *128*(4), 369–380.

Parker, G., Wilcock, P. R., Paola, C., Dietrich, W. E., & Pitlick, J. (2007). Physical basis for quasi-universal relations describing bankfull hydraulic geometry of single-thread gravel bed rivers. *Journal of Geophysical Research: Earth Surface*, *112*(F4).

Pasquale, N. (2012). *Quantification of vegetation root induced cohesion in non-cohesive river beds by experiments, monitoring and modeling* (Doctoral dissertation). Federal Instiutue of Technology Zürich, Switzerland.

Pasquale, N., Perona, P., Francis, R., & Burlando, P. (2014). Above-ground and below-ground Salix dynamics in response to river processes. *Hydrological Processes*, *28*, 5189–5203.

Pasquale, N., Perona, P, Francis, R, & Burlando, P. (2012). Effects of streamflow variability on the vertical root density distribution of willow cutting experiments. *Ecological Engineering*, *40*, 167–172.

Pasquale, N., Perona, P., Schneider, P., Shrestha, J., Wombacher, A., & Burlando, P. (2011). Modern comprehensive approach to monitor the morphodynamic evolution of a restored river corridor. *Hydrology and Earth System Sciences*, *15*(4), 1197–1212.

Penuelas, J., Poulter, B., Sardans, J., Ciais, P., Van Der Velde, M., Bopp, L., Boucher, O., Godderis, Y., Hinsinger, P., Llusia, J. Et al. (2013).

Human-induced nitrogen–phosphorus imbalances alter natural and managed ecosystems across the globe. *Nature communications*, *4*(1), 1–10.

Perona, P, & Crouzy, B. (2018). Resilience of riverbed vegetation to uprooting by flow. *Proceedings of the Royal Society A: Mathematical, Physical and Engineering Sciences*, *474*(2211), 20170547.

Perona, P., Molnar, P., Crouzy, B., Perucca, E., Jiang, Z., McLelland, S., Wüthrich, D., Edmaier, K., Francis, R., Camporeale, C., & Gurnell, A. (2012a). Biomass selection by floods and related timescales: Part 1. experimental observations. *Adv. Water Res.*

Perona, P, Porporato, A, & Ridolfi, L. (2007). A stochastic process for the interannual snow storage and melting dynamics. *Journal of Geophysical Research: Atmospheres*, *112*(D8).

Perona, P., Camporeale, C., Perucca, E., Savina, M., Molnar, P., Burlando, P., & Ridolfi, L. (2009). Modelling river and riparian vegetation interactions and related importance for sustainable ecosystem management. *Aquatic Sciences*, *71*(3), 266.

Perona, P., Daly, E., Crouzy, B., & Porporato, A. (2012b). Stochastic dynamics of snow avalanche occurrence by superposition of poisson processes. *Proceedings of the Royal Society A: Mathematical, Physical and Engineering Sciences*, *468*(2148), 4193–4208.

Perucca, E., Camporeale, C., & Ridolfi, L. (2007). Significance of the riparian vegetation dynamics on meandering river morphodynamics. *Water Resour. REs.*, *43*, W03430.

Peterjohn, W. T., & Correll, D. L. (1984). Nutrient dynamics in an agricultural watershed: Observations on the role of a riparian forest. *Ecology*, *65*(5), 1466–1475.

Petts, G. E. (1984). *Impounded rivers: Perspectives for ecological management*. Wiley.

Petts, G. E. (1987). Time-scales for ecological change in regulated rivers, In *Regulated streams*. Springer.

Pezeshki, S. R., Anderson, P. H., & Shields, F. D. (1998). Effects of soil moisture regimes on growth and survival of black willow (Salix nigra) posts (cuttings). *Wetlands*, *18*(3), 460–470.

Pezeshki, S. R., Li, S., Shields Jr, F. D., & Martin, L. T. (2007). Factors governing survival of black willow (Salix nigra) cuttings in a streambank restoration project. *ecological engineering*, *29*(1), 56–65.

Pinay, G., Bernal, S., Abbott, B. W., Lupon, A., Marti, E., Sabater, F., & Krause, S. (2018). Riparian corridors: A new conceptual framework for assessing nitrogen buffering across biomes. *Frontiers in Environmental Science*, *6*, 47.

Poff, N. L., Allan, J. D., Bain, M. B., Karr, J. R., Prestegaard, K. L., Richter, B. D., Sparks, R. E., & Stromberg, J. C. (1997). The natural flow regime. *BioScience*, *47*(11), 769–784.

Poff, N. L., & Zimmerman, J. K. (2010). Ecological responses to altered flow regimes: A literature review to inform the science and management of environmental flows. *Freshwater biology*, *55*(1), 194–205.

Pollen, N. (2007). Temporal and spatial variability in root reinforcement of streambanks: Accounting for soil shear strength and moisture. *Catena*, *69*(3), 197–205.

Pollen, N., & Simon, A. (2005). Estimating the mechanical effects of riparian vegetation on stream bank stability using a fiber bundle model. *Water Resouces Research*, *41*, W07025.

Pollen-Bankhead, N., & Simon, A. (2010). Hydrologic and hydraulic effects of riparian root networks on streambank stability: Is mechanical root reinforcement the whole story? *Geomorphology*, *116*, 353–362.

Pollen-Bankhead, N., Thomas, R., Gurnell, A., Liffen, T., Simon, A., & O'Hare, M. (2011). Quantifying the potential for flow to remove the emergent

aquatic macrophyte Sparganium erectum from the margins of low-energy rivers. *Ecological Engineering*, *37*(11), 1779 –1788.

Porto, L., McLaughlin, R., & Noakes, D. (1999). Low-head barrier dams restrict the movements of fishes in two Lake Ontario streams. *North American Journal of Fisheries Management*, *19*(4), 1028–1036.

Power, M. E., Sun, A., Parker, G., Dietrich, W. E., & Wootton, J. T. (1995). Hydraulic food-chain models: An approach to the study of food-web dynamics in large rivers. *BioScience*, *45*(3), 159–167.

Preti, F. (2013). Forest protection and protection forest: Tree root degradation over hydrological shallow landslides triggering. *Ecological Engineering*, *61*, 633–645.

Prosser, I. P., Dietrich, W. E., & Stevenson, J. (1995). Flow resistance and sediment transport by concentrated overland flow in a grassland valley. *Geomorphology*, *13*, 71–86.

Pu, J. H., Hussain, A., Guo, Y.-k., Vardakastanis, N., Hanmaiahgari, P. R., & Lam, D. (2019). Submerged flexible vegetation impact on open channel flow velocity distribution: An analytical modelling study on drag and friction. *Water Science and Engineering*, *12*(2), 121–128.

Pusey, B. J., & Arthington, A. H. (2003). Importance of the riparian zone to the conservation and management of freshwater fish: A review. *Marine and freshwater Research*, *54*(1), 1–16.

Ravanbakhsh, M., Sasidharan, R., Voesenek, L. A., Kowalchuk, G. A., & Jousset, A. (2017). Acc deaminase-producing rhizosphere bacteria modulate plant responses to flooding. *Journal of Ecology*, *105*(4), 979–986.

Ravazzolo, D, Mao, L., Picco, L, & Lenzi, M. (2015). Tracking log displacement during floods in the tagliamento river using rfid and gps tracker devices. *Geomorphology*, *228*, 226–233.

Richter, B., Baumgartner, J., Wigington, R., & Braun, D. (1997). How much water does a river need? *Freshwater biology*, *37*(1), 231–249.

Ridolfi, L., D'Odorico, P., & Laio, F. (2011). *Noise-induced phenomena in the environmental sciences*. Cambridge University Press.

Riestenberg, M. M. (1994). *Anchoring of thin colluvium by roots of sugar maple and white ash on hillslopes in Cincinnati* (Vol. 2059). US Government Printing Office.

Rigon, E, Comiti, F, & Lenzi, M. (2012). Large wood storage in streams of the Eastern Italian Alps and the relevance of hillslope processes. *Water Resources Research*, *48*(1).

Rodriguez-Iturbe, I., Porporato, A., Ridolfi, L., Isham, V., & Cox, D. (1999). Probabilistic modelling of water balance at a point: The role of climate, soil and vegetation. *Proc. R. Soc. Lond. A*, *455*, 3789–3805.

Rominger, J. T., Lightbody, A. F., & Nepf, H. M. (2010). Effects of added vegetation on sand bar stability and stream hydrodynamics. *Journal of Hydraulic Engineering*, *136*(12), 994–1002.

Rood, S. B., Kalischuk, A. R., & Mahoney, J. M. (1998). Initial cottonwood seedling recruitment following the flood of the century of the Oldman River, Alberta, Canada. *Wetlands*, *18*(4), 557–570.

Rood, S. B., Kalischuk, A. R., Polzin, M. L., & Braatne, J. H. (2003). Branch propagation, not cladoptosis, permits dispersive, clonal reproduction of riparian cottonwoods. *Forest Ecology and Management*, *186*(1-3), 227–242.

Rosenberg, D. M., McCully, P., & Pringle, C. M. (2000). Global-scale environmental effects of hydrological alterations: Introduction. *BioScience*, *50*(9), 746–751.

Rosso, R., Rulli, M. C., & Bocchiola, D. (2007). Transient catchment hydrology after wildfires in a mediterranean basin: Runoff, sediment and woody debris. *Hydrology and Earth System Sciences Discussions*, *11*(1), 125–140.

Roulound, A., Sumer, B. M, Fredsoe, J., & Michelsen, J. (2005). Numerical and experimental investigation of flow and scour around a circular pile. *J. Fluid Mech.*, *534*, 351–401.

Rubol, S., Battiato, I., & de Barros, F. P. J. (2016). Vertical dispersion in vegetated shear flows. *Water Resources Research*, *52*(10), 8066–8080.

Rubol, S., Ling, B., & Battiato, I. (2018). Universal scaling-law for flow resistance over canopies with complex morphology. *Scientific reports*, *8*(1), 1–15.

Ruf, W. (2007). *Numerical modelling of distributed river: Aquifer coupling in an alpine floodplain* (Doctoral dissertation). ETH Zurich.

Ruiz-Villanueva, V., Bladé Castellet, E., Díez-Herrero, A., Bodoque, J. M., & Sánchez-Juny, M. (2014). Two-dimensional modelling of large wood transport during flash floods. *Earth surface processes and landforms*, *39*(4), 438–449.

Ruiz-Villanueva, V., Piégay, H., Gurnell, A., Marston, R. A., & Stoffel, M. (2016). Recent advances quantifying the large wood dynamics in river basins: New methods and remaining challenges. *Reviews of Geophysics*, *54*(3), 611–652.

Ruiz-Villanueva, V., Wyżga, B., Zawiejska, J., Mikuś, P., Hajdukiewicz, H., Hajdukiewicz, M., & Stoffel, M. (2016). Large wood transport, deposition and remobilization during floods in the Czarny Dunajec River: outcomes from numerical modelling, In *Flood risk in the upper vistula basin*. Springer.

Sabater, S. (2000). Structure and architecture of a stromatolite from a mediterranean stream. *Aquatic Microbial Ecology*, *21*(2), 161–168.

Savina, M., Perona, P., Molnar, P., & Burlando, P. (2008). Ecomorphological changes in the Maggia River in the pre- and post impoundment periods. *Scientific Report of the Swiss National Science Foundation "MaVal" project. ETH Zurich, Zurich, CH*.

Schimpf, D., Flint, S., & Palmblad, I. (1977). Representation of germination curves with the logistic function. *Annals of Botany*, *41*(6), 1357–1360.

Schnauder, I., & Moggridge, H. (2009). Vegetation and hydraulic-morphological interactions at the individual plant, patch and channel scale. *Aquatic Sciences*, *71*, 318–330.

Schoneboom, T., Aberle, J., & Dittrich, A. (2010). Hydraulic resistance of vegetated flows: Contribution of bed shear stress and vegetative drag to total hydraulic resistance. *River Flow 2010*, 269–276.

Schumm, S. A. (1969). River metamorphosis. *Journal of the Hydraulics division*, *95*(1), 255–274.

Schwarz, M, Cohen, D, & Or, D. (2010a). Root-soil mechanical interactions during pullout and failure of root bundles. *Journal of Geophysical Research: Earth Surface*, *115*(F4).

Schwarz, M, Cohen, D, & Or, D. (2011). Pullout tests of root analogs and natural root bundles in soil: Experiments and modeling. *Journal of Geophysical Research: Earth Surface*, *116*(F2).

Schwarz, M., Giadrossich, F., & Cohen, D. (2013). Modeling root reinforcement using a root-failure Weibull survival function. *Hydrology and Earth System Sciences*, *17*, 4367–4377.

Schwarz, M., Lehmann, P., & Or, D. (2010b). Quantifying lateral root reinforcement in steep slopes-from a bundle of roots to tree stands. *Earth Surf. Proc. Land.*, *35*, 354–367.

Schwarz, M., Preti, F., Giadrossich, F., Lehmann, P., & Or, D. (2010c). Quantifying the role of vegetation in slope stability: A case study in Tuscany (Italy). *Ecological Engineering*, *36*, 285–291.

Sedell, J. R., & Froggatt, J. L. (1984). Importance of streamside forests to large rivers: The isolation of the Willamette River, Oregon, USA, from its floodplain by snagging and streamside forest removal. *Internationale Vereinigung für theoretische und angewandte Limnologie: Verhandlungen*, *22*(3), 1828–1834.

Seo, J. I., & Nakamura, F. (2009). Scale-dependent controls upon the fluvial export of large wood from river catchments. *Earth Surface Processes and Landforms*, *34*(6), 786–800.

Serlet, A. (2018). *Biomorphodynamics of river bars in channelized, hydropower-regulated rivers* (Doctoral dissertation). University of Trento.

Shafroth, P. B., Friedman, J. M., Auble, G. T., Scott, M. L., & Braatne, J. H. (2002a). Potential responses of riparian vegetation to dam removal: Dam removal generally causes changes to aspects of the physical environment that influence the establishment and growth of riparian vegetation. *BioScience*, *52*(8), 703–712.

Shafroth, P. B., Stromberg, J. C., & Patten, D. T. (2002b). Riparian vegetation response to altered disturbance and stress regimes. *Ecological applications*, *12*(1), 107–123.

Shields, A. (1936). Anwendung der Aehnlichkeitsmechanik und der Turbulenzforschung auf die Geschiebebewegung. *PhD Thesis Technical University Berlin*.

Shields, F., Knight, S., & Cooper, C. (1994). Effects of channel incision on base flow stream habitats and fishes. *Environmental Management*, *18*(1), 43–57.

Shields Jr, F. D., Knight, S., & Cooper, C. (1995). Rehabilitation of watersheds with incising channels. *JAWRA Journal of the American Water Resources Association*, *31*(6), 971–982.

Simon, A., & Collison, A. J. (2001). Quantifying root reinforcement of streambanks for some common riparian species: Are willows as good as it gets?, In *Wetlands engineering & river restoration 2001*.

Simon, A., & Collison, A. J. (2002). Quantifying the mechanical and hydrologic effects of riparian vegetation on streambank stability. *Earth surface processes and landforms*, *27*(5), 527–546.

Siviglia, A., & Crosato, A. (2016). Numerical modelling of river morphodynamics: Latest developments and remaining challenges. *Advances in Water Resources*, *93*(Part A), 1–3.

Smit, A. L., Bengough, A. G., Engels, C., van Noordwijk, M., Pellerin, S., & van de Geijn, S. C. (2013). *Root methods: A handbook*. Springer Science & Business Media.

Smolik, M., Dullinger, S, Essl, F, Kleinbauer, I, Leitner, M, Peterseil, J, Stadler, L.-M., & Vogl, G. (2010). Integrating species distribution models and interacting particle systems to predict the spread of an invasive alien plant. *Journal of Biogeography*, *37*(3), 411–422.

Stähly, S., Franca, M. J., Robinson, C. T., & Schleiss, A. J. (2019). Sediment replenishment combined with an artificial flood improves river habitats downstream of a dam. *Scientific reports*, *9*(1), 1–8.

Steffen, W., Richardson, K., Rockström, J., Cornell, S. E., Fetzer, I., Bennett, E. M., Biggs, R., Carpenter, S. R., De Vries, W., De Wit, C. A. Et al. (2015). Planetary boundaries: Guiding human development on a changing planet. *Science*, *347*(6223), 1259855.

Steiger, J., Tabacchi, E., Dufour, S., Corenblit, D., & Peiry, J.-L. (2005). Hydrogeomorphic processes affecting riparian habitat within alluvial channel–floodplain river systems: A review for the temperate zone. *River Research and Applications*, *21*(7), 719–737.

Stella, J. C., Rodríguez-González, P. M., Dufour, S., & Bendix, J. (2013). Riparian vegetation research in mediterranean-climate regions: Common patterns, ecological processes, and considerations for management. *Hydrobiologia*, *719*(1), 291–315.

Stokes, A, Ball, J, Fitter, A., Brain, P, & Coutts, M. (1996). An experimental investigation of the resistance of model root systems to uprooting. *Annals of Botany*, *78*(4), 415–421.

Stolzy, L. H., & Barley, K. P. (1968). Mechanical resistance encountered by roots entering compact soils. *Soil Science*, *105*, 297–301.

Stone, B. M., & Shen, H. T. (2002). Hydraulic resistance of flow in channels with cylindrical roughness. *Journal of hydraulic engineering*, *128*(5), 500–506.

Sturzenegger, M. (2005). *Changes in river morphology and vegetation caused by stream-flow regulation: a case study in the Maggia Valley, Switzerland* (Doctoral dissertation). Master s thesis, ETH/IHW.

Tabacchi, E., Lambs, L., Guilloy, H., Planty-Tabacchi, A.-M., Muller, E., & Decamps, H. (2000). Impacts of riparian vegetation on hydrological processes. *Hydrological processes*, *14*(16-17), 2959–2976.

Tabacchi, E., Planty-Tabacchi, A.-M., Salinas, M. J., & Décamps, H. (1996). Landscape structure and diversity in riparian plant communities: A longitudinal comparative study. *Regulated Rivers: Research & Management*, *12*(4-5), 367–390.

Tal, M., Gran, K. B., Murray, A. B., Paola, C., & Hicks, M. (2004). Riparian vegetation as a primary control on channel characteristics in multi-thread rivers. *Water Science and Application*, *8*, 43–58.

Tal, M., & Paola, C. (2007). Dynamic single-thread channels maintained by the interaction of flow and vegetation. *Geology*, *35*, 347–350.

Tal, M., & Paola, C. (2010). Effects of vegetation on channel morphodynamics: Results and insights from laboratory experiments. *Earth Surface Processes and Landforms*, *35*(9), 1014–1028.

Tambroni, N, da Silva, J. F., Duck, R., McLelland, S., Venier, C., & Lanzoni, S. (2016). Experimental investigation of the impact of macroalgal mats on the wave and current dynamics. *Advances in water resources*, *93*, 326–335.

Tanaka, N., & Yagisawa, J. (2009). Effects of tree characteristics and substrate condition on critical breaking moment of trees due to heavy flooding. *Landscape Ecol Eng*, *5*, 59–70.

Temmerman, S., Govers, G., Wartel, S, & Meire, P. (2003). Spatial and temporal factors controlling short-term sedimentation in a salt and freshwater tidal marsh, Scheldt estuary, Belgium, SW Netherlands. *Earth Surface Processes and Landforms: the Journal of the British Geomorphological Research Group*, *28*(7), 739–755.

Terwilliger, V. J. (1990). Effects of vegetation on soil slippage by pore pressure modification. *Earth Surface Processes and Landforms*, *15*(6), 553–570.

Theobald, D. M., Merritt, D. M., & Norman, J. B. (2010). *Assessment of threats to riparian ecosystems in the western US*. Colorado State University.

Thorne, C. R. (1990). Effects of vegetation on riverbank erosion and stability (J. B. Thornes, Ed.). In J. B. Thornes (Ed.), *Vegetation and erosion*. Wiley, Chichester.

Tockner, K., Ward, J. V., Arscott, D. B., Edwards, P. J., Kollmann, J., Gurnell, A., Petts, G. E., & Maiolini, B. (2003). The Tagliamento River: a model ecosystem of European importance. *Aquatic Sciences*, *65*(3), 239–253.

Todorovic, P. (1978). Stochastic models of floods. *Water Resources Research*, *14*(2), 345–356.

Todorovic, P. (1970). On some problems involving random number of random variables. *The Annals of Mathematical Statistics*, *41*(3), 1059–1063.

Tollner, E., Barfield, B., Vachirakornwatana, C, & Haan, C. (1977). Sediment deposition patterns in simulated grass filters. *Transactions of the ASAE*, *20*(5), 940–0944.

Tooth, S., & Nanson, G. C. (2000). The role of vegetation in the formation of anabranching channels in an ephemeral river, Northern plains, arid central Australia. *Hydrological processes*, *14*(16-17), 3099–3117.

Tosi, M. (2007). Root tensile strength relationships and their slope stability implications of three shrub species in the Nothern Apennines (Italy). *Geomorphology*, *87*, 268 –283.

Tron, S., Laio, F., & Ridolfi, L. (2014). Effect of water table fluctuations on phreatophytic root distribution. *Journal of theoretical biology*, *360*, 102–108.

Tron, S., Perona, P., Gorla, L., Schwarz, M., Laio, F., & Ridolfi, L. (2015). The signature of randomness in riparian plant root distributions. *Geophysical Research Letters*, *42*(17), 7098–7106.

Trubat, R., Cortina, J., & Vilagrosa, A. (2006). Plant morphology and root hydraulics are altered by nutrient deficiency in Pistacia lentiscus (L.) *Trees*, *20*(3), 334.

Trush, W. J., McBain, S. M., & Leopold, L. B. (2000). Attributes of an alluvial river and their relation to water policy and management. *Proceedings of the National Academy of Sciences*, *97*(22), 11858–11863.

Uhlenbeck, G. E., & Ornstein, L. S. (1930). On the theory of the brownian motion. *Physical review*, *36*(5), 823.

Ulloa, H., Iroumé, A., Picco, L., Korup, O., Lenzi, M. A., Mao, L., & Ravazzolo, D. (2015). Massive biomass flushing despite modest channel response in the Rayas River following the 2008 eruption of Chaitén volcano, Chile. *Geomorphology*, *250*, 397–406.

Van Rijn, L. (2013). Simple general formulae for sand transport in rivers, estuaries and coastal waters. *Retrieved from www. leovanrijn-sediment. com*, 1–16.

Vandersande, M. W., Glenn, E. P., & Walworth, J. L. (2001). Tolerance of five riparian plants from the lower Colorado River to salinity drought and inundation. *Journal of Arid Environments*, *49*(1), 147–159.

Vargas Luna, A. (2016). *Role of vegetation on river bank accretion* (Doctoral dissertation). TUDelft.

Vargas-Luna, A., Crosato, A., & Uijttewaal, W. S. (2015). Effects of vegetation on flow and sediment transport: Comparative analyses and validation of predicting models. *Earth Surface Processes and Landforms*, *40*(2), 157–176.

Vargas-Luna, A., Duró, G., Crosato, A., & Uijttewaal, W. (2019). Morphological adaptation of river channels to vegetation establishment: A laboratory study. *Journal of Geophysical Research: Earth Surface*, *124*(7), 1981–1995.

Västilä, K., Järvelä, J., & Aberle, J. (2013). Characteristic reference areas for estimating flow resistance of natural foliated vegetation. *Journal of hydrology*, *492*, 49–60.

Vaughan, I. P., Diamond, M, Gurnell, A., Hall, K., Jenkins, A, Milner, N., Naylor, L., Sear, D., Woodward, G, & Ormerod, S. J. (2009). Integrating ecology with hydromorphology: A priority for river science and management. *Aquatic Conservation: Marine and Freshwater Ecosystems*, *19*(1), 113–125.

Velasco, D., Bateman, A., Redondo, J. M., & DeMedina, V. (2003). An open channel flow experimental and theoretical study of resistance and turbulent characterization over flexible vegetated linings. *Flow, Turbulence and Combustion*, *70*(1-4), 69–88.

Verboom, W., & Pate, J. (2006). Bioengineering of soil profiles in semiarid ecosystems: The 'phytotarium' concept. a review. *Plant and Soil*, *289*(1-2), 71–102.

Vergani, C., Schwarz, M., Soldati, M., Corda, A., Giadrossich, F., Chiaradia, E. A., Morando, P., & Bassanelli, C. (2016). Root reinforcement dynamics in subalpine spruce forests following timber harvest: a case study in Canton Schwyz, Switzerland. *Catena*, *143*, 275–288.

Vesipa, R., Camporeale, C., & Ridolfi, L. (2017). Effect of river flow fluctuations on riparian vegetation dynamics: Processes and models. *Advances in Water Resources*, *110*, 29 –50.

Vigiak, O., Lutz, S., Mentzafou, A., Chiogna, G., Tuo, Y., Majone, B., Beck, H., de Roo, A., Malagó, A., Bouraoui, F. Et al. (2018). Uncertainty of modelled flow regime for flow-ecological assessment in Southern Europe. *Science of the Total Environment*, *615*, 1028–1047.

Waisel, Y., & Eshel, A. (2002). *Functional diversity of various constituents of a single root system, in plant roots: The hidden half* (Y. Waisel, A. Eshel, & U. Kafkafi, Eds.). Marcel Dekker.

Waldron, L., & Dakessian, S. (1981). Soil reinforcement by roots: Calculation of increased soil shear resistance from root properties. *Soil Science*, *132*, 427–435.

Wang, P., Li, X., Tong, Y., Huang, Y., Yang, X., & Wu, X. (2019a). Vegetation dynamics dominate the energy flux partitioning across typical ecosystem in the heihe river basin: Observation with numerical modeling. *Journal of Geographical Sciences*, *29*(9), 1565–1577.

Wang, W.-J., Peng, W.-Q., Huai, W.-X., Katul, G. G., Liu, X.-B., Qu, X.-D., & Dong, F. (2019b). Friction factor for turbulent open channel flow covered by vegetation. *Scientific reports*, *9*(1), 1–16.

Ward, J. (1998). Riverine landscapes: Biodiversity patterns, disturbance regimes, and aquatic conservation. *Biological conservation*, *83*(3), 269–278.

Ward, J. (1989). The four-dimensional nature of lotic ecosystems. *Journal of the North American Benthological Society*, *8*(1), 2–8.

Wardle, P. (1991). *Vegetation of New Zealand*. CUP Archive.

Watson, M. (1979). River plants: The macrophytic vegetation of watercourses. JSTOR.

Weinberger, I. C., Muff, S., Kranz, A., & Bontadina, F. (2019). Riparian vegetation provides crucial shelter for resting otters in a human-dominated landscape. *Mammalian Biology*, *98*(1), 179–187.

Welber, M., Bertoldi, W., & Tubino, M. (2012). The response of braided planform configuration to flow variations, bed reworking and vegetation: the case of the Tagliamento River, Italy. *Earth Surface Processes and Landforms*, *37*(5), 572–582.

Welty, J. J., Beechie, T., Sullivan, K., Hyink, D. M., Bilby, R. E., Andrus, C., & Pess, G. (2002). Riparian aquatic interaction simulator (RAIS): a model

of riparian forest dynamics for the generation of large woody debris and shade. *Forest Ecology and Management*, *162*(2-3), 299–318.

Wieder, W. R., Cleveland, C. C., Smith, W. K., & Todd-Brown, K. (2015). Future productivity and carbon storage limited by terrestrial nutrient availability. *Nature Geoscience*, *8*(6), 441–444.

Wilford, D. J., Cherubini, P., & Sakals, M. E. (2005). *Dendroecology: A guide for using trees to date geomorphic and hydrologic events*. British Columbia, Ministry of Forests, Forest Science Program.

Williams, G. P., & Wolman, M. G. (1984). *Downstream effects of dams on alluvial rivers* (Vol. 1286). US Government Printing Office.

Wilson, C. A. M. E., Stoesser, T., Bates, P., & Batemann Pinzen, A. (2003). Open channel flow through different forms of submerged flexible vegetation. *Journal of Hydraulic Engineering*, *129*(11), 847–853.

Winfield, M., & Hughes, F. M. (2002). Variation in Populus nigra clones: implications for river restoration projects in the United Kingdom. *Wetlands*, *22*(1), 33–48.

Wohl, E. (2011). Threshold-induced complex behavior of wood in mountain streams. *Geology*, *39*(6), 587–590.

Wohl, E. (2019). Forgotten legacies: Understanding and mitigating historical human alterations of river corridors. *Water Resources Research*, *55*(7), 5181–5201.

Wohl, E., Angermeier, P. L., Bledsoe, B., Kondolf, G. M., MacDonnell, L., Merritt, D. M., Palmer, M. A., Poff, N. L., & Tarboton, D. (2005). River restoration. *Water Resources Research*, *41*(10).

Wohl, E., & Scott, D. N. (2017). Wood and sediment storage and dynamics in river corridors. *Earth Surface Processes and Landforms*, *42*(1), 5–23.

Wohl, E. E. (2004). *Disconnected rivers: Linking rivers to landscapes*. Yale University Press.

Wolfe, J. (1992). Field plantings of four willow selections (1984–1989). *Project Rep*, (6).

Wong, M., & Parker, G. (2006). Reanalysis and correction of bed-load relation of meyer-peter and müller using their own database. *Journal of Hydraulic Engineering*, *132*(11), 1159–1168.

Wood, D. M. (1990). *Soil behaviour and critical state soil mechanics*. Cambridge university press.

Wu, T. (1979). Strength of tree roots and landslides on Prince of Wales Island, Alaska. *Canadian Geotech.*, *16*, 19–33.

Wyżga, B., Zawiejska, J., & Radecki-Pawlik, A. (2016). Impact of channel incision on the hydraulics of flood flows: Examples from Polish Carpathian rivers. *Geomorphology*, *272*, 10 –20.

Xie, Y., An, S., Wu, B., & Wang, W. (2006). Density-dependent root morphology and root distribution in the submerged plant Vallisneria Natans. *Environmental and Experimental Botany*, *57*(1-2), 195 –200.

Yagci, O, Tschiesche, U, & Kabdasli, M. (2010). The role of different forms of natural riparian vegetation on turbulence and kinetic energy characteristics. *Advances in water Resources*, *33*(5), 601–614.

Yagci, O., Celik, M. F., Kitsikoudis, V., Kirca, V. O., Hodoglu, C., Valyrakis, M., Duran, Z., & Kaya, S. (2016). Scour patterns around isolated vegetation elements. *Advances in Water Resources*, *97*, 251–265.

Yager, E., & Schmeeckle, M. (2013). The influence of vegetation on turbulence and bed load transport. *Journal of Geophysical Research: Earth Surface*, *118*(3), 1585–1601.

Yang, S., Milliman, J., Xu, K., Deng, B, Zhang, X., & Luo, X. (2014). Downstream sedimentary and geomorphic impacts of the Three Gorges Dam on the Yangtze River. *Earth-Science Reviews*, *138*, 469–486.

Yen, C. (1987). Tree root patterns and erosion control, In *Proceedings of the international workshop on soil erosion and its countermeasures. soil and water conservation society of thailand, bangkok.*

Yoshioka, H., Shimizu, E., Fukuoka, N., Fujiwara, T., & Sato, F. (1998). Evaluation of Rooting Ability in Cabbage Plug Seedlings by Drag Resistance (Resistance to Uprooting). *Journal of the Japanese Society for Horticultural Science*, *67*, 589–594.

Zen, S., & Perona, P. (2020). Biomorphodynamics of river banks in vegetated channels with self-formed width. *Advances in Water Resources*, *135*, 103488.

Zen, S., Zolezzi, G., Toffolon, M., & Gurnell, A. M. (2016). Biomorphodynamic modelling of inner bank advance in migrating meander bends. *Advances in Water Resources*, *93*, 166 –181.

Zischg, A., Galatioto, N., Deplazes, S., Weingartner, R., & Mazzorana, B. (2018). Modelling spatiotemporal dynamics of large wood recruitment, transport, and deposition at the river reach scale during extreme floods. *Water*, *10*(9), 1134.